Studies with Muons in ATLAS: TileCal Level-2 Trigger and MSSM Higgs Discovery Reach

Aránzazu Ruiz Martínez

Departament de Física Atòmica, Molecular i Nuclear and IFIC
(CSIC - Universitat de València)

13 November 2009

CERN-THESIS-2009-131
13/11/2009

Declaration

This dissertation is the result of my own work, except where explicit reference is made to the work of others, and has not been submitted for another qualification to this or any other university. This dissertation does not exceed the word limit for the respective Degree Committee.

Aránzazu Ruiz Martínez

Preface

This thesis was carried out in the years previous to the LHC start-up, i.e. during the ATLAS detector commissioning phase. It contains an introductory part about the detector and its expected physics performance and two main parts about the development of a Level-2 trigger for muons and a study of the MSSM Higgs discovery reach with simulated data, which are briefly described below.

CERN history and highlights as well as a general description of the LHC, the ATLAS experiment and its main parts are presented in Chapter 1. In particular, a detailed explanation of the TileCal front-end and back-end electronics is also given in order to help in the understanding of the muon trigger developments described in Chapter 3.

An overview of the current status of the high-energy physics field and the theoretical basis behind is provided in Chapter 2. The chapter contains a brief description of the Standard Model. New physics beyond the Standard Model, expected at the TeV energy scale, is also discussed.

Chapter 3 is devoted to TileMuId, the muon identication algorithm based on TileCal whose main goal is to be used as a Level-2 trigger of low-p_{T} muons. A second version of TileMuId (ROD-based) has been implemented to run in the TileCal ROD DSPs. This involved developments in the DSP firmware and in the Athena framework, described in the chapter. In addition, studies of the algorithm performance in terms of efficiency and fraction of fakes have been done. Developments and studies to match the TileCal muon candidates with the Inner Detector tracks (provided by ID reconstruction algorithms) have been performed and two new trigger chains combining TileCal and ID have been created. Both TileMuId versions are fully integrated in the Muon Trigger Slice Working Group and have been

running in High Level Trigger during cosmics data taking periods and are included in the trigger menu of $\mathscr{L} = 10^{31}$ cm^{-2}s^{-1}.

In Chapter 4, the ATLAS discovery potential of the MSSM neutral Higgs boson in the dimuon decay channel, $h/A/H \to \mu^+\mu^-$, for a center-of-mass energy of 14 TeV is explored with simulated data. This analysis was done in collaboration with the Higgs Working Group at CERN. For this analysis, we used the official event selection cuts agreed by the collaboration with the only exception of not requiring b-tagging for the jets. Since jet flavor tagging is not required in the analysis, it can be performed with low integrated luminosity, even before the b-tagging in the experiment reaches its optimal performance. Discovery significances and exclusion limits for several Higgs masses (110 GeV to 400 GeV) and $\tan\beta$ values (10 to 60) are evaluated using a maximum likelihood fit formalism based on toy Monte Carlo experiments at different integrated luminosities. Our results show that the MSSM parameter space can be significantly constrained with this analysis at 1 fb^{-1} (a 95% CL exclusion can be established for $m_A = 130$ GeV and $\tan\beta > 30$) and discovery is feasible at 10 fb^{-1} (5σ significance can be achieved for $m_A = 130$ GeV and $\tan\beta > 35$).

Finally, a summary containing the main conclusions and some final remarks is presented at the end of the thesis.

Valencia, October 2009.

Contents

List of Figures

List of Tables

"Genius is one percent inspiration, ninety-nine percent perspiration."
— Thomas Edison (1847-1931)

1 The ATLAS Experiment

"Assignment of the Science is not to open a door to endless knowledge, but to set a barrier to the endless ignorance."
— Galileo Galilei (1564 - 1642)

1.1 CERN

In 1949, to redress the balance and restore a strong European scientific community after the Second World War, the French physicist and Nobel prize-winner Louis de Broglie proposes the creation of a European science laboratory. Founded in 1954, the laboratory was one of Europe's first joint ventures by 12 states. It was provisionally named *Conseil Européen pour la Recherche Nucléaire* (European Council for the Nuclear Research, CERN) and sited astride the Franco-Swiss border near Geneva. The name has changed in two more occasions to European Organization for Nuclear Research and the current European Laboratory for Particle Physics, but the acronym lasts until today. Nowadays CERN is the world's largest particle physics center. Figures 1.1 and 1.2 show two aerial views of CERN's location.

Currently, CERN includes 20 European member states: Austria, Belgium, Bulgaria, the Czech Republic, Denmark, Finland, France, Germany, Greece, Hungary, Italy, the Netherlands, Norway, Poland, Portugal, the Slovak Republic, Spain, Sweden, Switzerland and the United Kingdom. However, many non-European countries are also involved in different ways. More than 6500 scientists (about half the world's particle physics community) collaborate in experiments conducted at

CERN for their research. In particular, Spain joined CERN in 1961, withdrew eight years later and joined again in November 1983 with more than 400 people involved currently.

Figure 1.1: Aerial view of the region with the CERN accelerator complex.

Since its foundation, great discoveries have been possible at CERN. In 1968 the invention of multiwire proportional chambers and drift chambers revolutionized the domain of electronic particle detectors. In 1992, Georges Charpak from CERN was awarded the Nobel Prize for Physics for this work.

Figure 1.2: CERN Meyrin site.

In 1976 the operation of the Super Proton Synchrotron (SPS) started. On 25 January 1983, a historic press conference announced the observation of W particles in the UA1 experiment at CERN, and was followed by another in May when

Z particles were found. The proton-antiproton collisions in the SPS led confirmed the unification of weak and electromagnetic forces as predicted by theory in 1968. In recognition of these efforts, Carlo Rubbia, head of the UA1 project, and Simon van der Meer, inventor of the stochastic cooling technique, were awarded the Nobel Prize for Physics in 1984. It was the first Nobel Prize awarded for research conducted at CERN.

At the beginning of the 1980's, CERN embarked on the enormous Large Electron-Positron Collider (LEP) construction project. The excavation of the 27-kilometer LEP tunnel was a huge technical challenge. LEP had 5176 magnets, 128 accelerating cavities (to re-accelerate the energy lost in the bends of the ring) and 4 enormous detectors: ALEPH, DELPHI, L3 and OPAL. The first collisions took place in August 1989 and only two months after, extremely accurate measurements of the Z particle showed that the fundamental building blocks of matter consist of three, and only three, families of particles. LEP operated at 100 GeV for seven years and produced Z particles. In 1995, LEP was upgraded for a second phase of operation known as LEP2, and spent the rest of its career operating at almost twice its original energy (over 200 GeV). This led to the production of W^+W^- pairs, the other two vectors of the weak force. After 11 years of successful research, LEP was closed down on 2 November 2000 to make way for the construction of the LHC (see Section 1.2), which will continue to challenge the Standard Model.

In addition, the LHC injectors have their own experimental hall, where their beams are used for experiments at lower energies. A scheme of the CERN accelerators is shown in Figure 1.3. Some of these experimental facilities are truly unique:

- **AD:** Antiproton Decelerator, is an antimatter factory. Its aim is to produce antihydrogen atoms for the particle physicists to study their spectroscopy and test fundamental symmetries.
- **CTF3:** Clic Test Facility, aims to demonstrate the technical feasibility of the key concepts of the novel CLIC RF power source for the future multi-TeV electron-positron linear collider.
- **CNGS:** CERN Neutrinos to Gran Sasso, sends a high intensity neutrino beam to a detector located near Rome, 800 km away from CERN.

- **ISOLDE:** Isotope Separator OnLine DEvice, produces radioactive nuclei for a number of applications covering nuclear, atomic, molecular and solid state physics, but also biology and astrophysics.
- **LEIR:** Low Energy Ion Ring, is a central part of the injector chain to supply lead ions to the LHC. It will transform long pulses from LINAC 3 into short and dense bunches.
- **LINAC:** LINear ACcelerators, where all of CERN's particles begin their travels. The 50-MeV Alvarez LINAC 2 produces proton beams and 4.2-MeV/u LINAC 3 produces heavy ion beams.
- **n-ToF:** Neutrons Time Of Flight, produces neutrons in an energy range covering more than eight orders of magnitude (between 1 eV and ∼250 MeV) for experiments in nuclear physics. The time of arrival of the particle at the experiment is a measure of the energy.

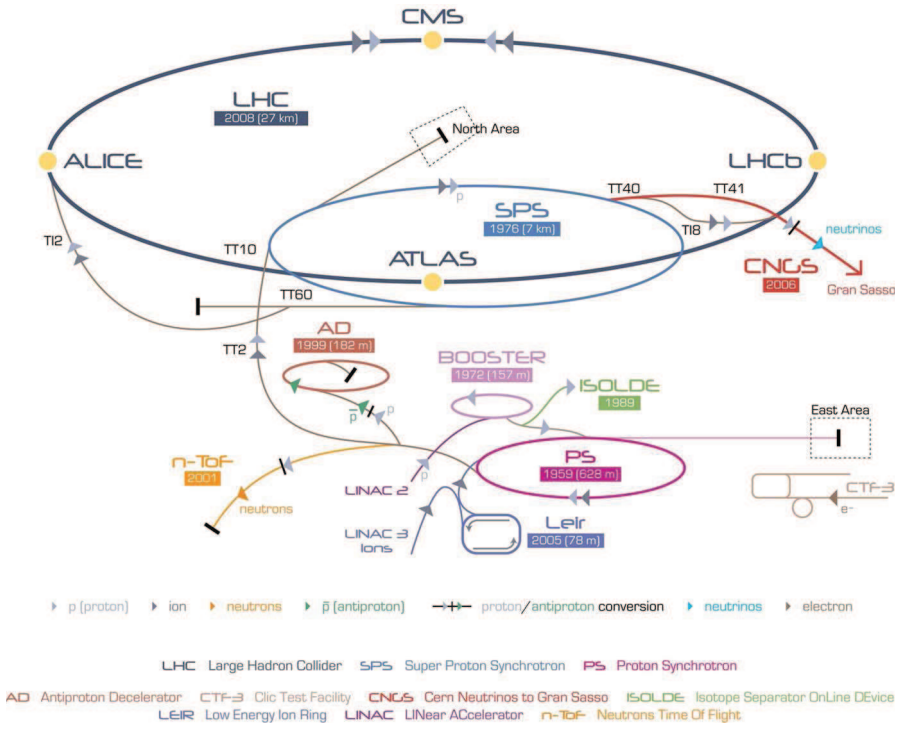

Figure 1.3: CERN accelerator complex.

Apart from pure scientific discoveries, great technological developments have been done at CERN. For instance, the World Wide Web (WWW) was proposed by CERN as a distributed information system based on “hypertext”. Nowadays, the GRID project is developing an architecture for large scale computing based on the use of many computers connected by a network.

As CERN is a pioneer institution, innovative technologies developed at CERN find many applications in different fields. Cancer therapy, medical and industrial imaging, radiation processing, electronics and measuring instruments are some examples.

1.2 The Large Hadron Collider

The next research instrument in Europe’s particle physics armoury is the Large Hadron Collider (LHC) [1]. In keeping CERN’s cost-effective strategy of building on previous investments, it is designed to share the 100-meter underground and 27-kilometer LEP tunnel, and be fed by existing particle sources and pre-accelerators. For instance the SPS accelerator was first upgraded into a proton-antiproton collider, then a heavy ion accelerator, later a lepton injector for LEP and now a high density proton injector for LHC. Figure 1.4 shows the LHC magnets in the tunnel.

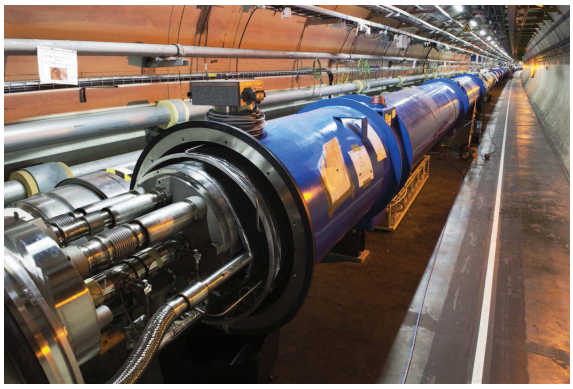

Figure 1.4: Picture of the LHC in the tunnel.

The two proton beams will collide with a center-of-mass energy of 14 TeV and beams of heavy ions such as lead with a total collision energy in excess of 1250 TeV. The resulting large beam current (I_b = 0.53 A) is a particular challenge in a machine made of delicate superconducting magnets operating at cryogenic temperatures. To bend 7 TeV protons around the ring, the LHC dipoles must be able to produce fields of 8.36 T, almost 10^5 times the Earth's magnetic field. LHC magnet coils are made of copper-clad niobium-titanium cables and are operated at 1.9 K. Figure 1.5 shows the different parts of the LHC magnets.

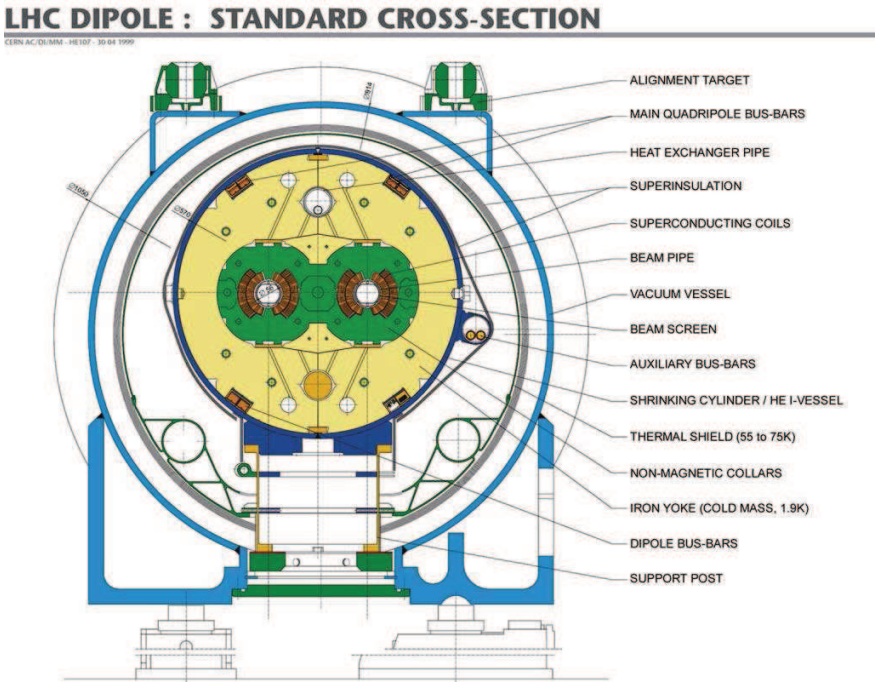

Figure 1.5: LHC dipole magnet diagram.

The proton beams will contain 2808 bunches of 10^{11} particles each, separated 7.5 millimeters, achieving a luminosity of 10^{34} $cm^{-2}s^{-1}$. It will work at a 40 MHz rate, that is, bunch crossings will be produced each 25 ns. Table 1.1 summarizes the LHC main parameters.

Table 1.1: LHC beam parameters for proton and lead ion collisions.

	p ⟷ p	**Pb ⟷ Pb**
Energy at injection	450 GeV	1.774 TeV/u
Energy at collision	7 TeV	2.76 TeV/u
Center-of-mass energy	14 TeV	1250 TeV
Luminosity	10^{34} cm^{-2}s^{-1}	10^{31} cm^{-2}s^{-1}
Number of particles per bunch	1.15×10^{11}	7×10^{7}
Number of bunches	2808	592
Bunch separation	25 ns	100 ns
Number of collision points	4	
Number of insertions	8	
Ring Circumference	26658.883 m	
Number of main bends	1232	
Length of main bends	14.3 m	
Field of main bends at injection	0.535 T	
Field of main bends at collision	8.33 T	

Figure 1.6 shows the placement of the LHC underground structures, as well as the surroundings of the CERN laboratory in the Geneva region.

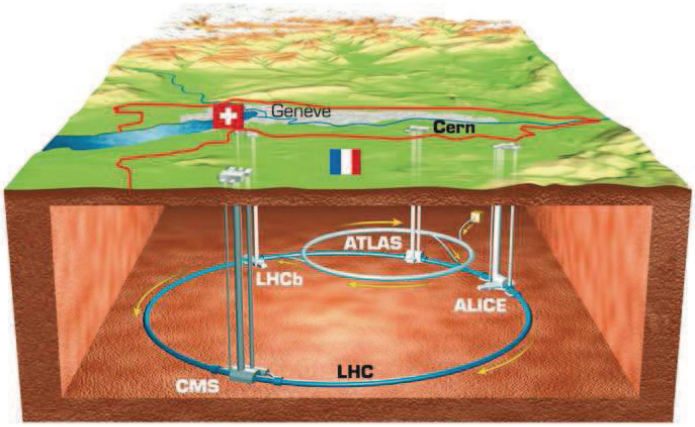

Figure 1.6: LHC schematic layout.

The first proton beams were circulated around the LHC on 10 September 2008. The event was opened to the media and broadcasted world wide live. At 10:25 am (Geneva time), after only an hour of tuning the beam, it successfully circulated all the way around the 27 km ring. Figure 1.7 shows the cross-section of the beam pipe after the first beam turn, showing the position of the beam when it was injected and once arrived to the same point.

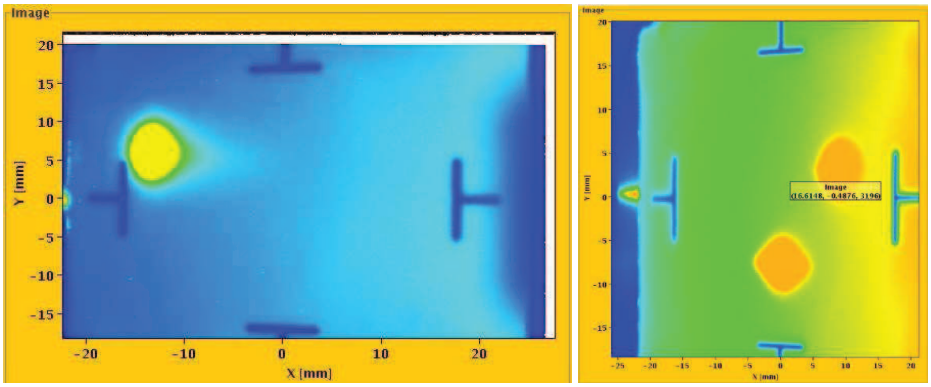

Figure 1.7: On the left, first beam injected in the LHC, during synchronization tests, on 8 August 2008. The yellow spot shows a bunch of protons arriving at point 3 of the LHC ring. On the right, position of the proton beam after the first circulation in LHC on 10 September 2008: one dot was the injection into the ring and a second dot was the beam returning to that same location.

After the successful start-up, on September 19, during commissioning (without beam) of the final LHC sector at high current for operation at 5 TeV, an incident occurred. The initial malfunction was caused by a faulty electrical connection between two of the accelerator magnets. This resulted in mechanical damage and release of helium from the magnet cold mass into the tunnel. A total of 53 magnet units had to be removed from the tunnel for cleaning or repair. The last repaired magnet was lowered to the LHC tunnel on 30 April 2009. Due to this incident and the corresponding reparation, LHC operation was delayed and the first collisions are foreseen for autumn 2009.

1.3 The LHC Experiments

The LHC experiments have been designed to look for theoretically predicted phenomena. However, they must also be prepared, as far as possible, for surprises. Six experiments are involved in the LHC:

ALICE (A Large Ion Collider Experiment) [2], shown in Figure 1.8(a), is a dedicated heavy-ion detector to study the physics of strongly interacting matter at extreme energy densities, where the formation of a new phase of matter, the quark-gluon plasma, is expected.

ATLAS (A Toroidal LHC ApparatuS) [3] is one of the two LHC general-purpose experiments. The detector is 44 meters long, 22 meters diameter and weights about 7000 tons. It is described in detailed in Section 1.4 and it is shown in Figure 1.8(b).

CMS (Compact Muon Solenoid) [4] is designed as a general-purpose experiment. The completed detector will be cylindrical, 21 meters long and 16 meters diameter and weight approximately 12 500 tons. The main highlight features of the detector are: its relatively small size, the powerful solenoid which will produce a 4-tesla magnetic field and its optimization for tracking muons. The detector layout is shown in Figure 1.8(c).

LHCb (the Large Hadron Collider beauty experiment) [5], shown in Figure 1.8(d), is an experiment to study specifically B-physics and *CP* violation.

LHCf (the Large Hadron Collider forward experiment) [6] uses forward particles created inside the LHC as a source to simulate cosmic rays in laboratory conditions. Studying how collisions inside the LHC cause similar cascades of particles will help scientists to interpret and calibrate large-scale cosmic-ray experiments that can cover thousands of kilometers. It will have detectors at 140 meters from the ATLAS collision point.

TOTEM (TOTal Elastic and diffractive cross-section Measurement) [7] studies forward particles to focus on physics that is not accessible to the general-purpose experiments. Among a range of studies, it will measure the effective

size of the proton and also monitor accurately the LHC's luminosity. Eight Roman pots will be placed in pairs at four locations near the collision point of the CMS experiment.

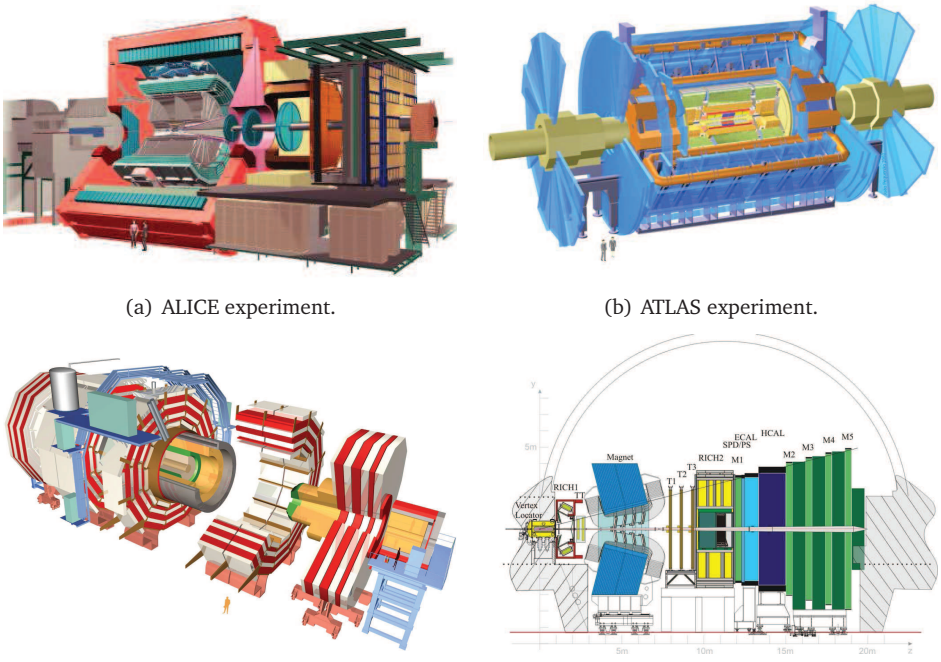

(a) ALICE experiment. (b) ATLAS experiment.

(c) CMS experiment. (d) LHCb experiment.

Figure 1.8: The four main LHC experiments.

1.4 ATLAS

ATLAS (A Toroidal LHC ApparatuS), shown in Figure 1.9, is a general-purpose pp detector which is designed to exploit the full discovery potential of the LHC. The LHC offers a large range of physics opportunities, among which the origin of the mass at the electroweak scale is a major focus of interest for ATLAS. The detector optimization is therefore guided by physics issues such as sensitivity to the largest possible Higgs mass range. Other important goals are the searches for

supersymmetric particles, for compositeness of the fundamental fermions, as well as the investigation of *CP* violation in B-decays, and detailed studies of the top quark (see Chapter 2). The ability to cope well with a broad variety of possible physics processes is expected to maximize the detector's potential or the discovery of new, unexpected physics.

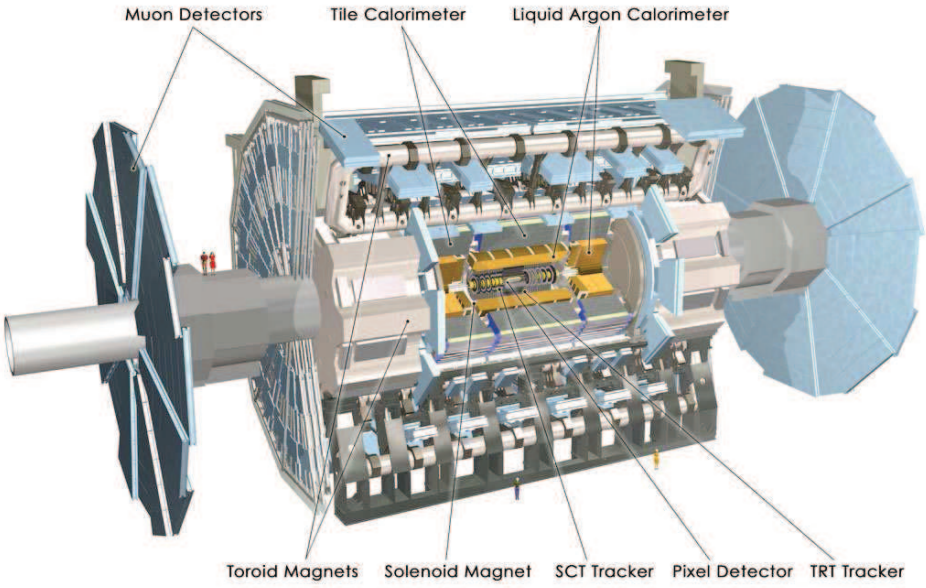

Figure 1.9: Simulation of the ATLAS experiment.

The ATLAS detector consists of four major components:

- Inner Detector, which is composed of three subdetectors (the Pixel Detector, the SemiConductor Tracker and the Transition Radiation Tracker) and measures the momentum of each charged particle.
- Calorimeter, which is divided in an electromagnetic and a hadronic part and measures the energy carried by the particles.
- Muon Spectrometer, which identifies and measures muons.
- Magnet system, which bends charged particles for momentum measurements.

The interactions of the particles created in the LHC proton collisions going through the ATLAS detectors will create an enormous data flow. To digest these data we need:

- The trigger system
- The data acquisition system
- The computing system

Figure 1.10 shows the typical behaviour of several particles in the different parts of ATLAS, which are described in the following Sections.

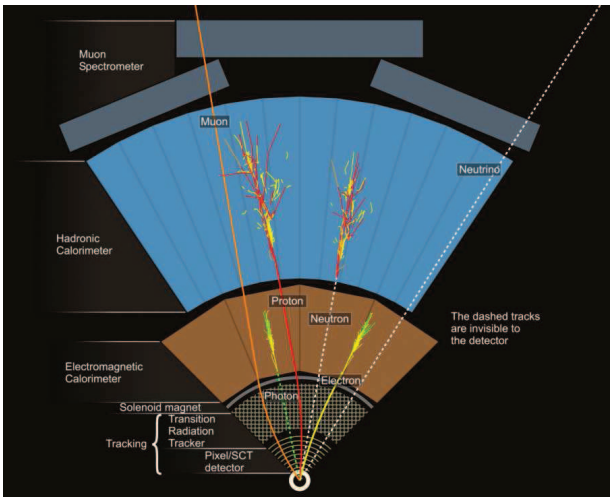

Figure 1.10: A slice of the ATLAS detector. Note the typical tracks left by the different particles going through the detector.

Figure 1.11 shows the event display for the first event recorded in the ATLAS experiment with the proton beam circulated in the LHC accelerator on 10 September 2008.

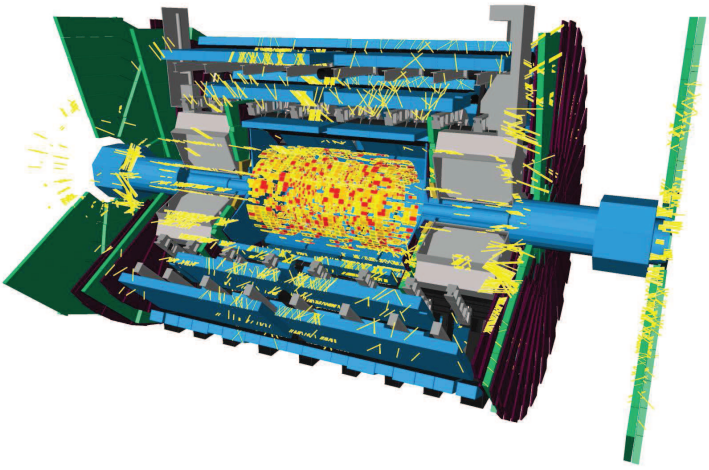

Figure 1.11: Display of the first beam event seen in the ATLAS experiment.

1.4.1 Inner Detector

The task of the Inner Detector (ID) [8] is to reconstruct the tracks and vertices in the event from the LHC beam pipe to the electromagnetic calorimeter system with high efficiency. The ID is shown in Figure 1.12, its main parameters are summarized in Table 1.2 and its parts are described below.

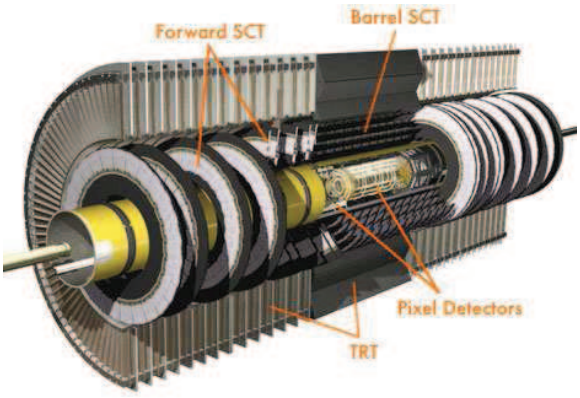

Figure 1.12: Three-dimensional view of the Inner Detector.

Table 1.2: Parameters of the Inner Detector.

System	Position	Area (m^2)	Resolution σ (μm)	Channels (10^6)	Coverage in $\lvert\eta\rvert$
Pixels	1 removable barrel layer	0.2	$(R\phi, z) = (12, 66)$	16	2.5
	2 barrel layers	1.4	$(R\phi, z) = (12, 66)$	81	1.7
	4 end-cap disks on each side	0.7	$(R\phi, z) = (12, 77)$	43	1.7 - 2.5
SCT	4 barrel layers	34.4	$(R\phi, z) = (16, 580)$	3.2	1.4
	9 end-cap wheels on each side	26.7	$(R\phi, z) = (16, 580)$	3.0	1.4 - 2.5
TRT	Axial barrel straws		170 (per straw)	0.1	2.5
	Radial end-cap straws		170 (per straw)	0.32	0.7 - 2.5

Pixel Detector

The Pixel Detector is designed to provide a very high granularity, high precision set of measurements as close to the interaction point as possible. The system consists of three barrels at average radii of ∼4 cm, 11 cm and 14 cm, and four disks on each side, between radii of 11 cm and 20 cm, which complete the angular coverage. The system is designed to be highly modular, containing approximately 1500 identical barrel modules and 1000 identical disk modules.

SemiConductor Tracker (SCT)

The SemiConductor Tracker (SCT) is designed to provide four precision measurements per track in the intermediate radial range, contributing to the measurement of momentum, impact parameter and vertex position, as well as providing good pattern recognition by the use of high granularity. The SCT is based upon silicon microstrip detector technology. The detector contains 61 m^2 of silicon detectors, with 6.2 million read-out channels. The spatial resolution is 16 μm in $R\phi$ and 580 μm in z.

Transition Radiation Tracker (TRT)

The Transition Radiation Tracker (TRT) is based on the use of straw detectors. The barrel contains about 50 000 straws and the end-caps contain 320 000 radial straws. The total number of electronic channels is 420 000.

1.4.2 Calorimetry

The tasks of the calorimeters [9] at hadron colliders are: accurate measurement of the energy and position of electrons and photons; measurement of the energy and direction of jets and of the event missing transverse momentum; particle identification (for instance, separation of electrons and photons from hadrons and jets, and τ hadronic decays from jets) and event selection at the trigger level.

In ATLAS, the central cryostat contains the barrel electromagnetic calorimeter and the 2-tesla superconducting solenoid. Each end-cap cryostat houses an electromagnetic and two hadronic wheels, and one forward calorimeter. The barrel and end-cap cryostats are built out of aluminum, and are vacuum insulated. The total weight of the calorimeter system is about 4000 tons. The ATLAS calorimeters are shown in Figure 1.13 and their main parameters summarized in Table 1.3.

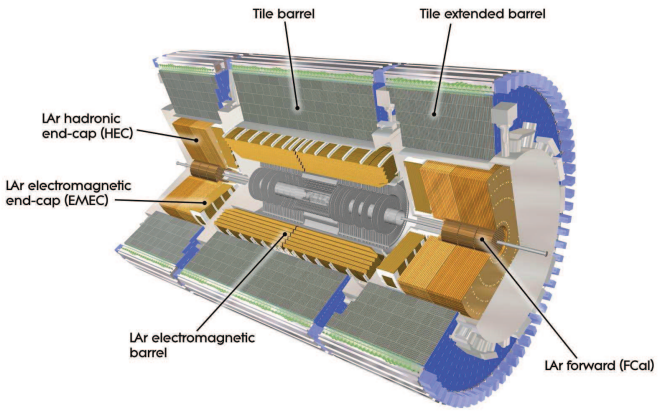

Figure 1.13: Three-dimensional view of the ATLAS calorimeters.

Table 1.3: Coverage, longitudinal segmentation and granularity of the ATLAS calorimeters.

EM CALORIMETER	**Barrel**	**End-Cap**	
Coverage	$\|\eta\|<1.475$	$1.375<\|\eta\|<3.2$	
Longitudinal segmentation	3 samplings	3 samplings	$1.5<\|\eta\|<2.5$
		2 samplings	$1.375<\|\eta\|<1.5$
			$2.5<\|\eta\|<3.2$
Granularity ($\Delta\eta \times \Delta\phi$)			
Sampling 1	0.003×0.1	0.025×0.1	$1.375<\|\eta\|<1.5$
		0.003×0.1	$1.5<\|\eta\|<1.8$
		0.004×0.1	$1.8<\|\eta\|<2.0$
		0.006×0.1	$2.0<\|\eta\|<2.5$
		0.1×0.1	$2.5<\|\eta\|<3.2$
Sampling 2	0.025×0.025	0.025×0.025	$1.375<\|\eta\|<2.5$
		0.1×0.1	$2.5<\|\eta\|<3.2$
Sampling 3	0.05×0.025	0.05×0.025	$1.5<\|\eta\|<2.5$
PRESAMPLER	**Barrel**	**End-Cap**	
Coverage	$\|\eta\|<1.52$	$1.5<\|\eta\|<1.8$	
Longitudinal segmentation	1 sampling	1 sampling	
Granularity ($\Delta\eta \times \Delta\phi$)	0.025×0.1	0.025×0.1	
HADRONIC TILE	**Barrel**	**Extended Barrel**	
Coverage	$\|\eta\|<1.0$	$0.8<\|\eta\|<1.7$	
Longitudinal segmentation	3 samplings	3 samplings	
Granularity ($\Delta\eta \times \Delta\phi$)			
Samplings 1 and 2	0.1×0.1	0.1×0.1	
Sampling 3	0.2×0.1	0.2×0.1	
HADRONIC LAr		**End-Cap**	
Coverage		$1.5<\|\eta\|<3.2$	
Longitudinal segmentation		3 samplings	
Granularity ($\Delta\eta \times \Delta\phi$)		0.1×0.1	$1.5<\|\eta\|<2.5$
		0.2×0.2	$2.5<\|\eta\|<3.2$
FORWARD CALORIMETER		**End-Cap**	
Coverage		$3.1<\|\eta\|<4.9$	
Longitudinal segmentation		3 samplings	
Granularity ($\Delta\eta \times \Delta\phi$)		$\sim 0.2 \times 0.2$	

Liquid Argon Calorimeter (LAr)

The Liquid Argon [10] sampling calorimeter technique with "accordion-shaped" electrodes is used for all electromagnetic calorimetry covering the pseudorapidity interval $|\eta| < 3.2$. The layout of this system can be seen in Figure 1.14.

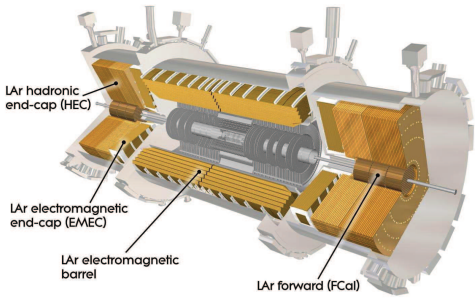

Figure 1.14: Three-dimensional view of the LAr calorimeters inside the cryostat.

Each hadronic end-cap calorimeter (HEC) uses copper as passive medium and liquid argon as active medium. It consists of two independent wheels: HEC1 and HEC2.

The forward calorimeter (FCAL) is composed of three modules; the electromagnetic (FCAL1) and two hadronic modules (FCAL2 and FCAL3). The passive medium in the electromagnetic modules is copper composition and in the hadronic modules is tungsten and sintered tungsten alloy.

Tile Calorimeter (TileCal)

The Tile Calorimeter [11], shown in Figure 1.15, is a large hadronic sampling calorimeter which makes use of steel as the absorber material and scintillating plates read out by wavelength shifting (WLS) fibers as the active medium. The new feature of its design is the orientation of the scintillating tiles which are placed in planes perpendicular to the colliding beams and are staggered in depth as Figure 1.16 shows.

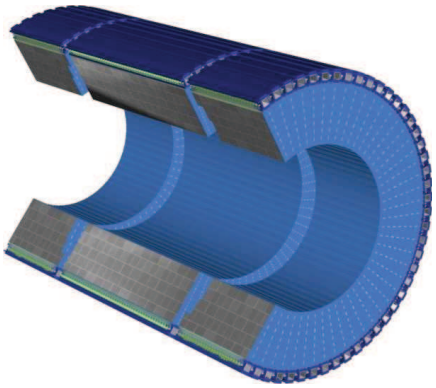

Figure 1.15: Three-dimensional view of the Tile Calorimeter. Note the long barrel and the two extended barrels as well as the 64 modules in the azimuthal direction.

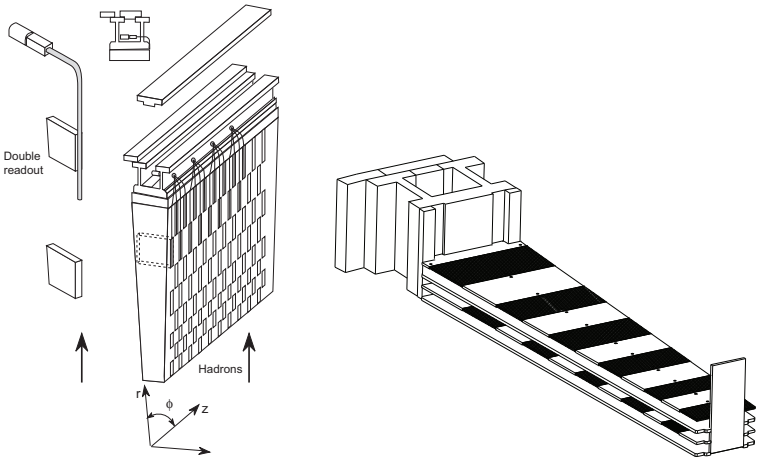

(a) The principle of the Tile Calorimeter design.

(b) Scheme of a TileCal period. The scintillating tiles are shown in black and the iron parts in white.

Figure 1.16: TileCal design.

The Tile Calorimeter is designed as one Long Barrel (LB) and two Extended Barrel (EB) parts, covering the $|\eta| < 1.7$ region. The calorimeter consists of a cylindrical structure with inner and outer radius of 2280 mm and 4230 mm respectively. The barrel part is 5640 mm in length along the beam axis, while each of the extended barrel cylinders is 2910 mm long. Each detector cylinder is built

of 64 independent wedges along the azimuthal direction. Between the barrel and the extended barrels there is a gap of about 600 mm, which is needed for the Inner Detector and the Liquid Argon cables, electronics and services. Part of this gap contains an extension of the extended barrel: the Intermediate Tile Calorimeter (ITC), which is a structure stepped in order to maximize the volume of active material in this region, while still leaving room for the services and cables.

All TileCal read-out electronics (front-end and back-end) are described in detail in Sections 1.5, 1.6 and 1.7. The knowledge of the TileCal electronics will help in the understanding of Chapter 3.

1.4.3 Muon Spectrometer

The layout of the Muon Spectrometer [12] is shown in Figure 1.17. For the precise measurement of muon tracks in the principal bending direction of the magnetic fields, Monitored Drift Tube (MDT) chambers are used except in the innermost ring of the inner station of the end-caps, where particle fluxes are highest. In this region, covering the pseudorapidity range $2 < |\eta| < 2.7$, Cathode Strip Chambers (CSCs) are employed.

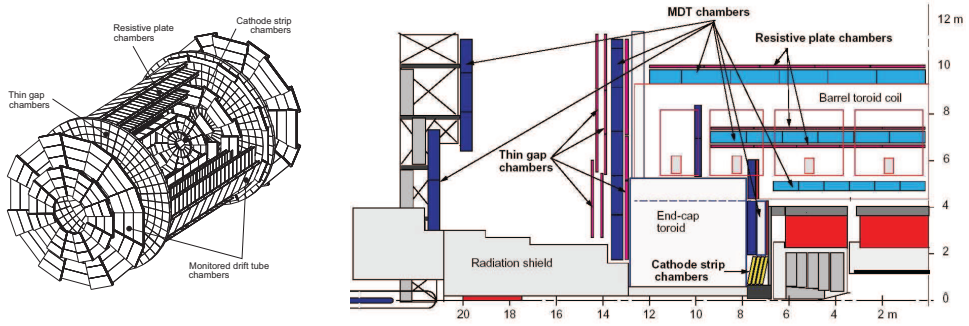

(a) Three-dimensional view of the Muon Spectrometer instrumentation indicating the areas covered by the four different chamber technologies.

(b) Two-dimensional xy view of the Muon Spectrometer with the 4 types of chambers in use labeled.

Figure 1.17: Muon Spectrometer layout.

The trigger function in the barrel is provided by three stations of Resistive Plate Chambers (RPCs). They are located on both sides of the middle MDT station, and either directly above or directly below the outer MDT station. In the end-caps, the trigger is provided by three stations of Thin Gap Chambers (TGCs) located near the middle MDT station. See Table 1.4 for detailed information about the Muon Spectrometer chambers.

Table 1.4: Overview of the Muon Spectrometer.

	Precision chambers		**Trigger chambers**	
	CSC	**MDT**	**RPC**	**TGC**
Number of chambers	32	1194	596	192
Number of read-out channels	67 000	370 000	355 000	440 000
Area covered (m^2)	27	5500	3650	2900

1.4.4 Magnet System

An essential part of the ATLAS detector setup is the magnet system [13] which provides the bending power required for the momentum measurement of charged particle tracks. It consists of an arrangement of a Central Solenoid (CS) servicing the Inner Detector trackers with an axial magnetic field, surrounded by a system of three large scale air-core toroids generating a tangential magnetic field for the Muon Spectrometer: one Barrel Toroid (BT) and two End-Cap Toroids (ECTs). Each of the three toroids consists of eight coils.

The magnet system assembly has an overall dimension of 25 meters length by 20 meters in diameter. It has a total weight of 1300 tons, is cooled by liquid helium at 4.8 K and stores a magnetic energy of 1600 MJ. Figure 1.18 shows a scheme of the magnet system, Figure 1.19 shows pictures of its different parts and Table 1.5 summarizes its main parameters.

The Central Solenoid is designed to provide a 2-tesla strong magnetic field in the central tracking volume. It is a conduction-cooled superconducting solenoid based on a thin-walled construction for minimum thickness to decrease particle scattering effects. In order to reduce material build-up and enhance particle trans-

parency, the solenoid shares its cryostat with the Liquid Argon calorimeter. The solenoid is made as a single layer coil.

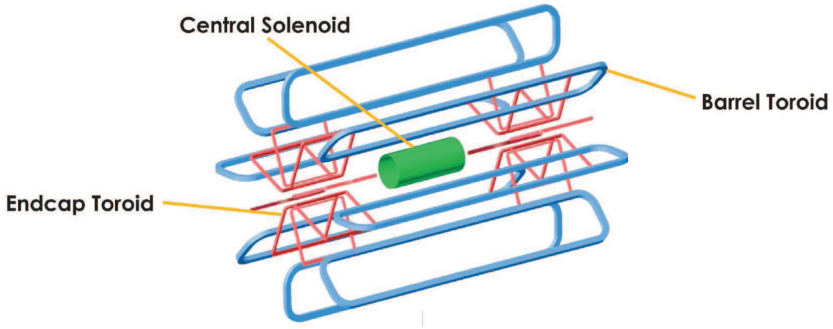

Figure 1.18: Scheme of the magnet system. Note the central solenoid and the three toroids.

The Barrel Toroid consists of eight flat race-track coils each of them consisting of two double pancake windings housed in a common aluminum casing 25 meters long and 5 meters wide. It generates the magnetic field for the central region of the muon detector. The coils are grouped in a torus shape maintained by a system of 16 supporting rings.

Two End-Cap Toroids are positioned inside the Barrel Toroid, one at each end of the Central Solenoid. They provide the magnetic field in the forward regions of the ATLAS detector across a radial span of 1.7 to 5 meters. The eight coils of each End-Cap Toroid are assembled as a single unit inside one large cryostat.

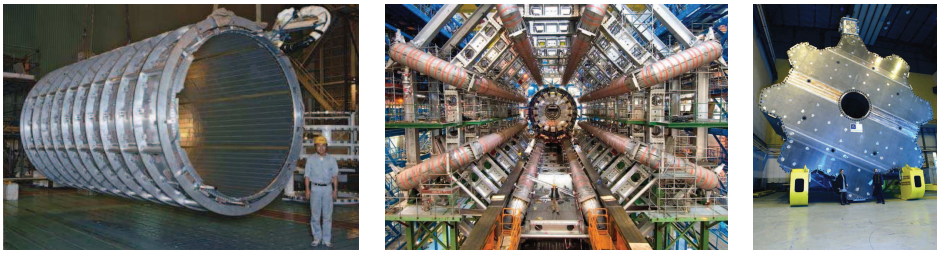

(a) Central Solenoid. (b) Barrel Toroid. (c) Endcap Toroid.

Figure 1.19: Parts of the ATLAS magnet system.

Table 1.5: Overview of the magnet system parameters.

	Barrel Toroid	End-Cap Toroid	Central Solenoid
Overall Dimensions			
inner diameter	9.4 m	1.65 m	2.46 m
outer diameter	20.1 m	10.7 m	2.63 m
axial length	25.3 m	5.0 m	5.30 m
number of coils	8	2×8	1
Mass			
conductor	118 tons	2×20.5 tons	3.8 tons
cold mass	370 tons	2×160 tons	5.4 tons
total assembly	830 tons	2×239 tons	5.7 tons
Coil			
central field			2.0 T
field integral	2 - 6 T m	4 - 8 T m	

1.4.5 Trigger and Data Acquisition System

The ATLAS trigger and data acquisition (DAQ) system [14] is based on three levels of online event selection, as shown in Figure 1.20. Each trigger level refines the decisions made at the previous level and, where necessary, applies additional selection criteria. Starting from an initial bunch-crossing rate of 40 MHz (interaction rate $\sim 10^9$ Hz at a luminosity of 10^{34} cm^{-2}s^{-1}) the final rate of selected events must be reduced to $\sim$100 Hz for permanent storage.

The Level-1 trigger is hardware-based and makes an initial selection based on reduced-granularity information from a subset of detectors. For instance, high transverse momentum (high-p_{T}) muons are identified using only the so-called trigger chambers (RPCs in the barrel and TGCs in the end-caps). The calorimeter selections are based on reduced-granularity information from all the ATLAS calorimeters. Objects searched for by the calorimeter trigger are high-p_{T} electrons and photons, jets, and taus decaying into hadrons, as well as large missing and total transverse energy. In the case of the electron/photon and hadron/tau triggers, isolation can be required.

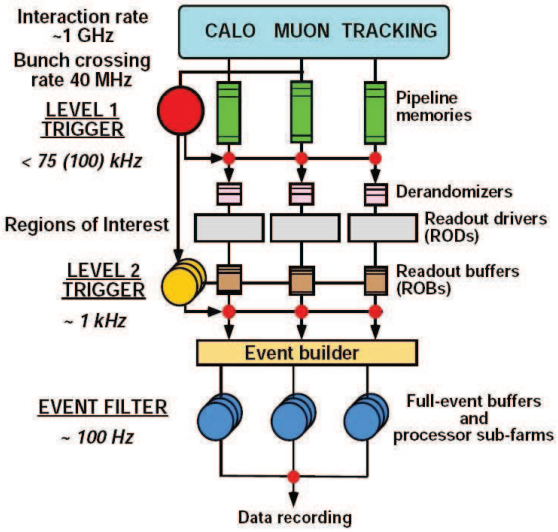

Figure 1.20: Block diagram of the Trigger/DAQ system.

When the Level-1 selection criteria are fulfilled potentially interesting objects may be present. Then, we say we have a Level-1 Accept (L1A) and information about the Region of Interest (RoI) is sent to the next level using a dedicated data path. This information includes the position (η and ϕ) and p_{T} range of candidate objects (high-p_{T} muons, electrons/photons, hadrons/taus, jets) and energy sums (missing E_{T} vector and scalar E_{T} value, where E_{T} is transverse energy).

The Level-1 trigger makes RoI information available for all of the objects that contributed to the event being selected; these are called primary RoIs. Furthermore, in order to allow additional requirements to be made at Level-2, the Level-1 trigger can provide RoI information for objects that did not contribute to the selection of the event. Such RoIs, typically for objects of relatively low p_{T}, are called secondary RoIs.

The Level-1 maximum rate is 75 kHz (upgradable to 100 kHz) with a 2.5 μs Level-1 detector latency, that is, the time required for each subdetector to provide a trigger decision. It is defined as the time measured from the pp collision until the trigger decision is available to the detector front-end for data transmission.

The Level-2 trigger is software-based and makes use of RoI information provided by the Level-1 trigger. It selectively accesses data from the Read-Out Buffers (ROBs), moving on the data that are required in order to make the Level-2 decision. The Level-2 trigger has access to all of the event data, if necessary with the full precision and granularity.

After Level-2, a last stage of selection is performed in the Event Filter (EF). Here the algorithms will be based on offline code. The EF must reduce the rate to a level suitable for permanent storage, currently assumed to be ∼100 Hz for full events of size ∼1 Mb.

The software-based trigger levels (Level-2 and EF) are commonly known as High Level Trigger (HLT).

1.5 TileCal Front-End Electronics

The light produced by the particles going through the scintillating tiles is collected by the WLS fiber bundles, which route it to the photomultiplier tubes (PMTs), first stage of the front-end electronics. Figure 1.21 shows the different elements mentioned above.

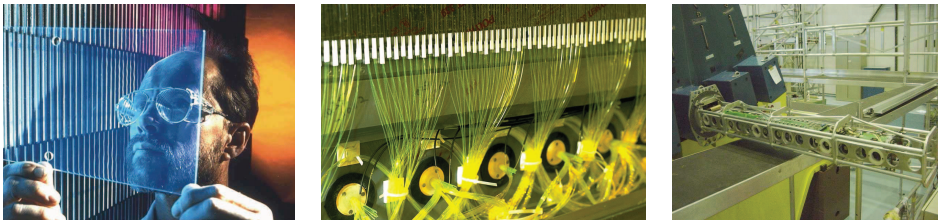

(a) A scintillating tile. (b) WLS fiber bundles. (c) View of a drawer.

Figure 1.21: Different parts of a TileCal module.

All front-end electronics in TileCal are placed in compact structures called drawers. Two physical drawers are coupled from the electronics point of view forming a new structure called superdrawer. The superdrawers are located inside the back-beam region of the Tile Calorimeter modules and contain the PMT blocks, the

pipelines and the HV distributors. There are 256 superdrawers in TileCal. There is a superdrawer per each half barrel module and per each extended barrel module.

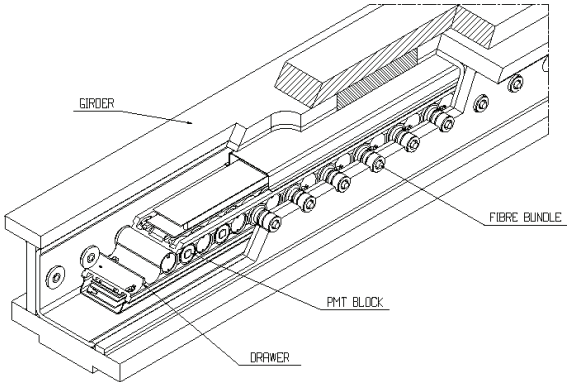

Figure 1.22: Scheme of the drawer inside the girder with all the parts labeled.

1.5.1 PMT Block

The function of a PMT block is to convert light signals from the calorimeter cells into electronic signals. Each PMT block contains a photomultiplier tube, a light mixer, a high voltage divider and a 3-in-1 card, as Figure 1.23 shows.

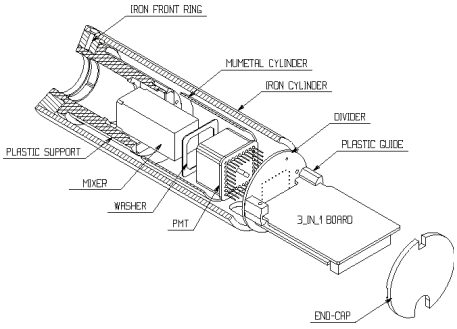

(a) Arrangement of a PMT block.

(b) The components of a PMT block before assembly.

Figure 1.23: PMT block.

There is one PMT block assigned to each of the 10 010 fiber bundles in the Tile Calorimeter and each PMT corresponds to one channel for read-out. The output of the PMT block is a shaped electronic signal which is subsequently digitized by the electronics inside the superdrawer.

Photomultiplier Tube

The conversion of the light signals from the fiber bundles to electrical charge is done by the photomultipliers in the PMT blocks. After several studies, the Hamamatsu R7877 PMT was the chosen model to equip the TileCal PMTs. From 2000 to 2003, the TileCal-Valencia group characterized and tested at IFIC about 1750 photomultipliers which are being employed in TileCal.

Light Mixer

The role of this light guide is to mix the light coming from the fibers so that there is no correlation between the position of a fiber and the area of the photocathode which receives its light.

HV Divider

The primary purpose of the HV divider is to partition the high voltage between the dynodes of the PMT. The Tile Calorimeter divider also serves as a socket allowing connection of the PMT to the front-end electronics without any interconnecting wires. This design minimizes the capacitance between the PMT and the electronics, and is important to reduce noise and unreliable connections.

3-in-1 Board

This board provides three basic functions: pulse shaping and accommodation of the large dynamic range, charge injection calibration and slow integration of the PMT signals for monitoring and calibration.

1.5.2 Analog Trigger Tower Adders

Analog summation is used to build the trigger signals from the TileCal, which are to be used in the Level-1 trigger system of ATLAS. Specific cards for such purpose are placed in the drawers, just below the digitizers. The trigger signals are built taking as input the shaped signals provided by the 3-in-1 cards from the PMT blocks in each trigger tower.

1.5.3 Digitizer System

Figure 1.24 shows a block diagram of this device, in which fast pulse signals from the 3-in-1 cards are digitized in the digitizer boards and sent down a digital pipeline. On receipt of a L1A, the digitizer boards capture an event frame consisting of a string of digitizations. The events (data frames) are stored locally and queued for transmission to the interface link.

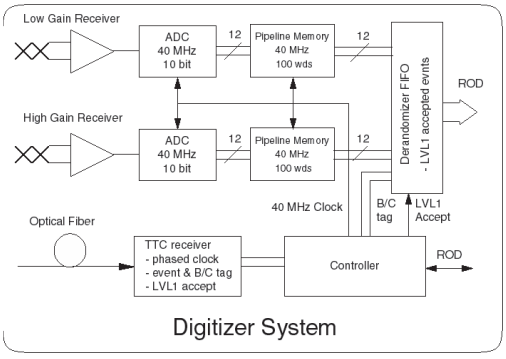

Figure 1.24: Digitizer system for a single channel. Note the high and low gain inputs.

The data presented to the digitizer boards by the 3-in-1 system are delivered with two versions of each signal, a high and a low gain version (being 64 the gain ratio). The data are converted to discrete time format in digitizers formed mainly by commercial ADCs, TTCrx [15] for Trigger and Timing Control (TTC) [16] information receipt and custom Application Specific Integrated Circuit (ASIC) chip TileDMU (Data Management Unit) [17]. The criteria used to decide which set of data (high or low gain) remains is the saturation of the samples.

The TileDMU is responsible for reformatting and reordering the digitized data and for sending them to the interface links. Each TileDMU manages 3 ADCs, and each digitizer board has 2 TileDMUs. Therefore there are 8 digitizer boards for LB superdrawers (up to 48 channels, only 45 are needed), and 6 for EB superdrawers (36 possible channels, only 32 are needed). Figure 1.25 shows a scheme of the digitizer boards in a LB superdrawer and a picture of the TileDMU chip.

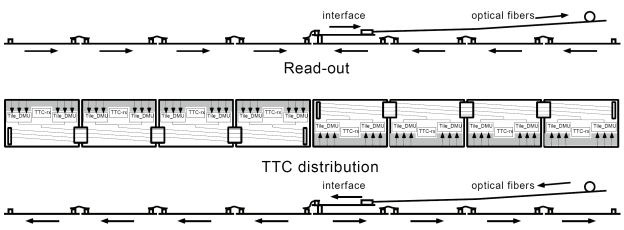

(a) Scheme of the 8 digitizer boards corresponding to a LB superdrawer.

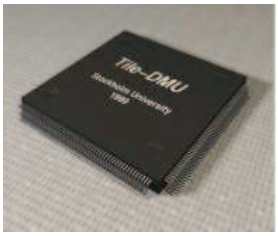

(b) TileDMU chip picture.

Figure 1.25: Components of the digitizer system.

1.5.4 Interface Links

Figure 1.26 shows a diagram of the interface links. There is one interface board per superdrawer and it provides two main functionalities:

- Receives the TTC information (two fibers) and sends it to digitizers equipped with the TTCrx chip (8 Low Voltage Differential Signaling - LVDS - signals).
- Receives the data (also LVDS) from the up to 8 digitizer boards in a superdrawer, deserializes them and sends them through an optical link to the input stage of the Read-Out Drivers (RODs).

The actual design of the interface links is based in S-Link protocol over HP G-Link chips as a physical layer. The implementation is an integrated G-Link Link Source Card (LSC) (640 Mbit/s) working at 16 bits in 40 MHz mode (chip HDMP1032). Dual channel read-out is implemented to provide redundancy.

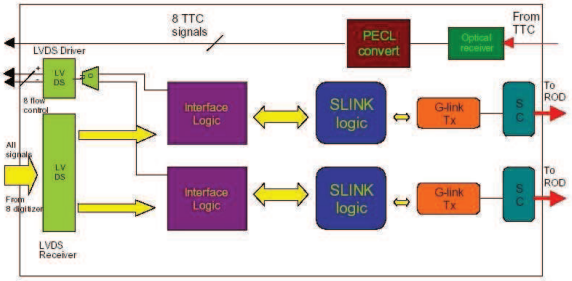

Figure 1.26: Diagram of the interface card. Note the redundant dual output to the ROD.

1.6 TileCal Back-End Electronics

The main element in the back-end electronics is the Read-Out Driver. A total number of 38 RODs (32 + 6 spares) have been produced in the TileCal-Valencia laboratory during 2006. They are placed in 4 ROD crates in the underground counting room USA15 corresponding to the 4 TileCal partitions for data acquisition (EBA, LBA, LBC and EBC). Figure 1.27 shows schematically the DAQ structure for TileCal with its 4 partitions.

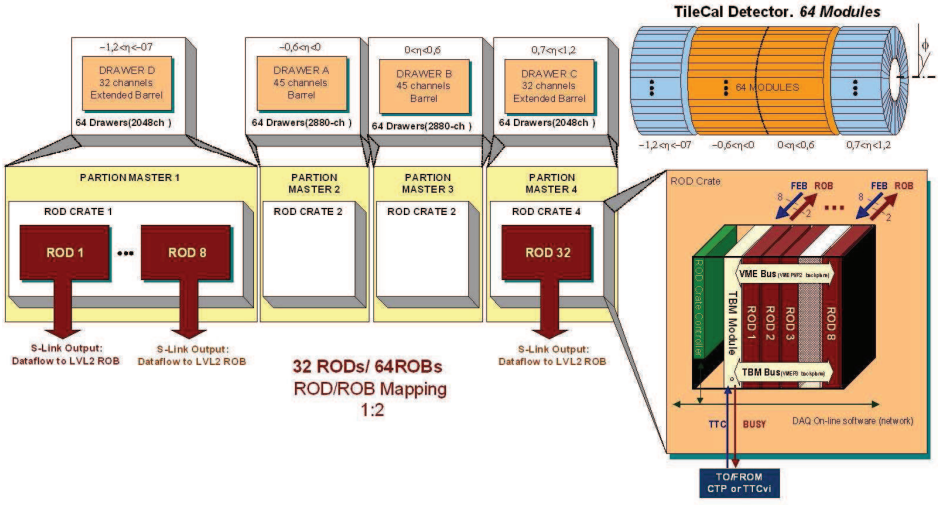

Figure 1.27: Scheme of the TileCal partitions and the corresponding ROD crates.

Each partition is managed by the so-called TTC crate which is equipped by standard TTC modules for the LHC experiments. In the following Sections, all back-end modules are described.

1.6.1 ROD Crate

The ROD crate is a standard ATLAS 9U crate with remote water cooling power supply. This crate has standard P1 and P2 VME64x backplanes and a custom P3 backplane which allow communication between the ROD Crate Controller (RCC), master module, and all the other slave VME modules in the crate: Trigger and Busy Module (TBM) and 8 ROD motherboards. Each ROD crate can hold up to 21 VME modules. It is planned to include 8 Optical Multiplexer Boards (OMBs) for each ROD crate in the final system setup. Each ROD motherboard is associated with a Transition Module (TM) at the back of the crate. A diagram of a ROD crate is shown in Figure 1.28.

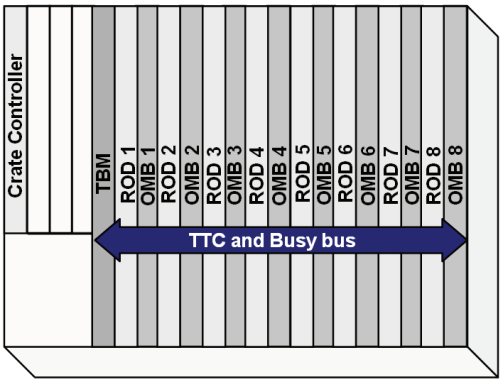

Figure 1.28: Scheme of a TileCal ROD crate.

ROD Crate Controller (RCC)

The RCC is a 6U VME module with a CPU for the initialization of the modules as well as monitoring and support of the VME access (for configuration and data transfer). The VP-110 crate controller from Concurrent Technologies [18] is the

standard one accepted by the ATLAS collaboration. The next generation of crate controllers by Concurrent Technologies (VP-315 and VP-317) may also be used during the life of the experiment. A picture of the VP-110 crate controller is shown in Figure 1.29(a).

Trigger and Busy Module (TBM)

The TBM [19] is a 9U VME module which manages TTC and busy signals in the ROD crate. The TBM must be placed in slot #5 in the ROD crate since it is a VME master module and receives the TTC signals from the trigger system, does the optical to electrical conversion and distributes them to all the ROD modules in the crate through the P3 backplane.

The TBM also receives the busy signals from the 8 RODs in the crate through the P3 backplane. These signals are meant to stop the data reception when the ROD is processing previous data. The TBM produces a logical OR of the 8 ROD busy signals to generate a crate busy signal. Figure 1.29(b) shows a picture of this board.

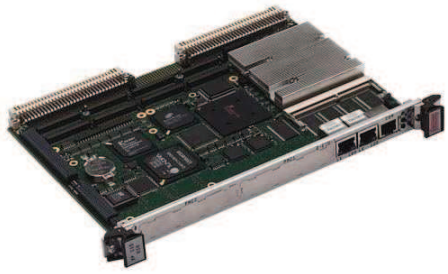

(a) ROD Crate Controller.

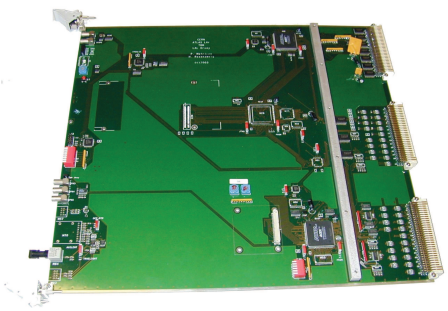

(b) Trigger and Busy Module.

Figure 1.29: ROD Crate Controller and Trigger and Busy Module pictures.

Read-Out Driver (ROD)

The ROD motherboard [20] is a 9U VME module which can read up to 8 optical fibers from the front-end electronics with the information from a single module each. It can have up to 4 mezzanine cards, called Processing Units (PUs), to process the data online before sending them to the Transition Module installed at the back of the VME crate. In the current setup, two DSP PUs are placed in the PU slots #1 and #3 to process the data. Figure 1.30(a) shows a picture of a ROD module equipped with two DSP PUs. The ROD functionalities and components are described in Section 1.7.

Transition Module (TM)

The TM boards [21] are placed just behind each ROD module. The ROD module sends the data through the P2 and P3 backplanes to the TM which transmits them via optical fibers using up to 4 S-Link mezzanine LSCs [22] to the Read-Out System (ROS) computer (the next step in the read-out chain). Serializer and deserializer chips are located in ROD and TM respectively to allow this functionality due to the limited number of pins in P2 and custom P3. Figure 1.30(b) shows a picture of a TM equipped with two HOLA LSCs and Figure 1.31 shows the component diagram and data flow for the ROD and the TM.

Optical Multiplexer Board (OMB)

The TileCal front-end data are transmitted with redundancy, i.e., two fibers carry the same data from the Interface Cards to the ROD (see Section 1.5.4). In such a radiation hard environment and in a long-lived experiment as ATLAS, this redundancy is mandatory in order to prevent the effect of the malfunctions in the front-end electronics due to radiation damage.

To exploit this redundancy, an Optical Multiplexer Board [23] is being produced by the TileCal-Valencia group in collaboration with the DSDC group at the *Dpto. Ingeniería Electrónica, Universitat de València*. This 9U VME module will receive

the two fibers carrying the same data, check possible errors in them and provide a single optical link carrying correct data to the ROD as input. In another operation mode, this module can generate data so that it may also be used as ROD injector in absence of front-end data or for test purposes.

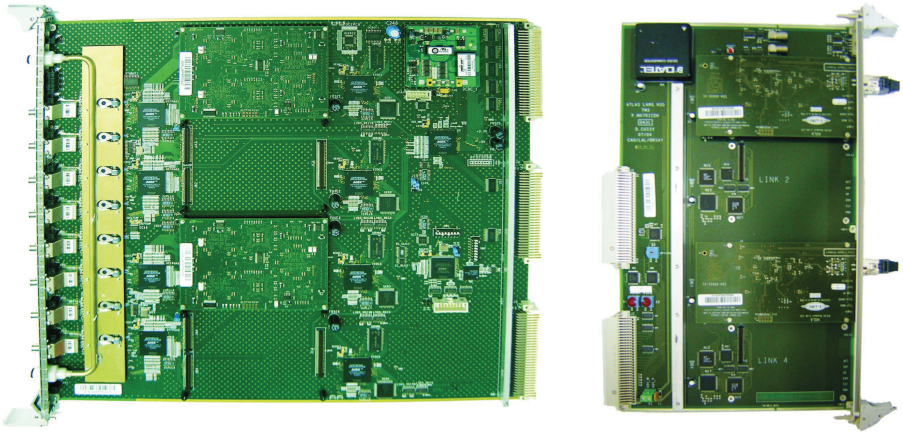

(a) ROD motherboard. (b) Transition Module

Figure 1.30: Read-Out Driver and Transition Module pictures. Note that there are only 2 DSP PUs in the ROD motherboard and 2 HOLA LSCs in the Transition Module, as needed in the default operation mode.

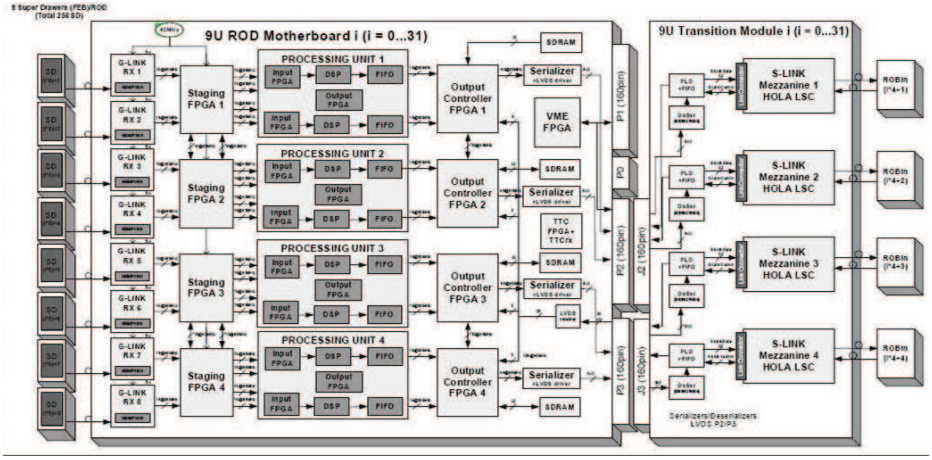

Figure 1.31: Read-Out Driver and Transition Module scheme.

Figure 1.32 shows a picture of the OMB board together with a diagram of its components. The OMB has 16 inputs to receive data from 8 superdrawers, with 8 output fibers to the RODs. In consequence, one of these OMB boards can provide data to one ROD module and therefore 32 OMBs are needed for the whole calorimeter.

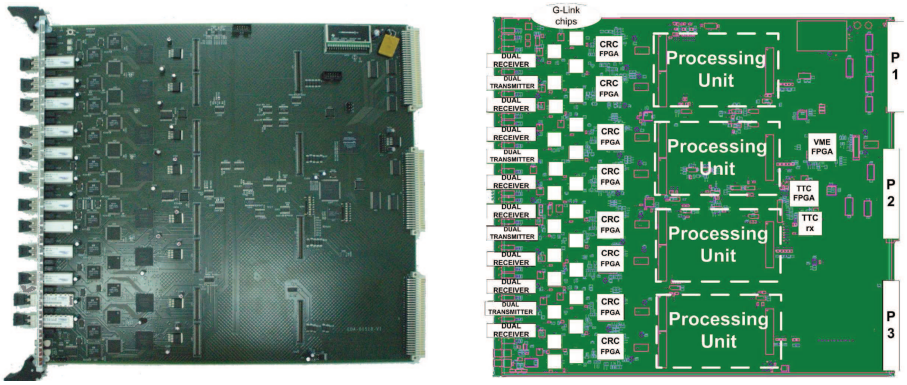

Figure 1.32: Picture of the Optical Multiplexer Board (left) and diagram of its components (right).

To handle the optical input and output fibers, 8 dual receivers and 4 dual transmitters are needed. The data checking operations are performed in dedicated FPGAs by means of CRC checks. The OMBs are equipped with a TTCrx chip to receive TTC information which allows the possibility to perform additional BCID checks. The design is completed with two FPGAs providing the TTC and VME interface and four PMC connectors for mezzanine boards which can eventually be used in future upgrades.

1.7 ROD Description

In the following Sections, the components of the ROD are described. The ROD main functionalities are:

- **Data processing:** raw data gathering from the first level de-randomizers at the L1A event rate of 100 kHz. The ROD provides the energy, timing

and a quality factor to the next trigger level by processing the data with the algorithms implemented in the PUs (see Chapter 3). Depending on the DAQ constraints (pile-up, high energy events, ...) there is also the possibility to send a fraction or all the raw data without processing.

- **Trigger:** TTC signals will be present (with a latency $\sim$2 μs after L1A) at each module, providing ROD L1ID (Level-1 Identifier), BCID (Bunch Crossing Identifier) and Ttype (Trigger type).
- **Error detection:** the ROD checks that the owner BCID and L1ID numbers match with the numbers received from the front-end. If a mismatch is detected, an error flag is set with some error code.
- **Data links:** at a L1A event rate of 100 kHz the ROD sends the data to the next step in the acquisition chain (ROBs) using the standard ATLAS Read-Out Links (ROLs).
- **Busy generation:** the TBM provides a busy signal which stops the L1A generation, performing an OR operation with the ROD busy signals coming from all the RODs in a partition.
- **Local monitoring:** part of the data can be read through VME for monitoring tasks without introducing dead-time or additional latency.

1.7.1 Optical Receivers and G-Link Chips

The ROD motherboard has up to 8 optical receivers (ORXs). These ORXs are mezzanine boards that receive the optical signals coming from the front-end electronics. Then 8 G-Link chips (HDMP-1024) deserialize the incoming data and send them to the Staging Field Programmable Gate Arrays (FPGAs).

1.7.2 Staging FPGAs

Four Staging FPGAs (ACEX EP1k50) are used in the ROD motherboard. Each one receives deserialized data from two G-Link chips. The main functionalities of this device are to route the external input data to the PU, monitor the G-Link temperature, generate internal event data and send them to the PU for tests.

The Staging FPGA is responsible for receiving the incoming data into the ROD from two different G-Link chips and route them to the PU. In the default operation mode, called staging mode, the data coming from four G-Links are sent to a single PU (using a bus between each pair of Staging FPGAs). There is also the possibility to work in the so-called full mode, where the data from two G-Links are sent to a single PU.

1.7.3 Output Controller FPGAs

An ACEX EP1k100 is used as Output Controller (OC) FPGA [24]. There are 4 OCs in a ROD motherboard. The OC reads the data from the FIFOs of the Processing Units and sends them either to a SDRAM to read the data through the VME protocol or to a serializer chip to send the data to the TM.

1.7.4 VME FPGA

The VME interface is implemented in a FPGA ACEX EP1k100 [25]. The ROD module is considered as a VME slave module and can be accessed by the RCC. The data bus is D32 (32-bit data words) and the addressing is A32 (32-bit address words) for data transfer.

1.7.5 TTC Controller FPGA

The TTC FPGA [26] is an APEX EP1k30 and gets the LHC clock from the backplane via the TBM to distribute it to the ROD.

The TTC FPGA is responsible for providing the ROD with all the TTC signals and information for the different trigger operation modes. The TTC information sent by the TBM is received by the TTCrx chip in the ROD and recovered by the TTC Controller FPGA, which distributes it to all PUs.

1.7.6 Processing Units (PUs)

Online data processing is done by the so-called Processing Units which are 120 mm × 85 mm mezzanine cards which are connected to the ROD motherboard via 3 connectors. Each ROD motherboard can hold up to 4 PU daughterboards.

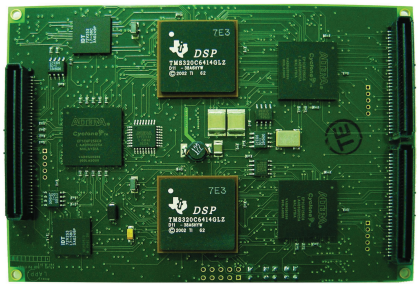

(a) ROD DSP PU picture. Note that the front-end input data come from right to left.

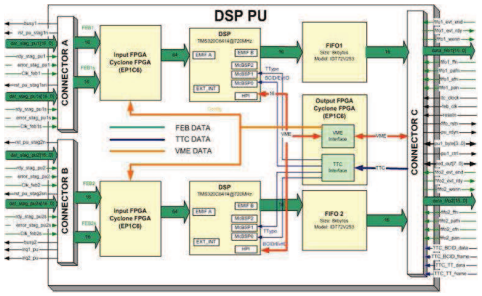

(b) ROD DSP PU scheme. Note the arrows according to the data flow.

Figure 1.33: ROD DSP PU.

DSP PU

The Digital Signal Processor (DSP) PU [27] is composed of two blocks, each one with an input FPGA Cyclone EP1C6, a TMS320C6414 DSP from Texas Instruments and an external output FIFO. The DSP PU also contains an output FPGA Cyclone EP1C6 used for the VME and TTC interface. A picture of this device and its layout are shown in Figure 1.33. The input FPGAs and the DSPs can be programmed by uploading the corresponding code through the VME interface.

The main functions of the DSP PU are:

- Data flow management
- Data formatting
- TTC reception
- Buffering and synchronization

- Data processing with online algorithms
- Online histogramming
- Error detection, several checks can be performed like the presence of the start and the end of an event, the parity of each word, etc.

2 Physics Motivations

"If I have seen further it is only by standing on the shoulders of giants."
— Isaac Newton (1643 - 1727)

This Chapter tries to give an overall impression on which is the status of the field of high-energy physics on the verge of the LHC era. It starts by briefly describing the Standard Model of particle physics and how successful it is in describing the experimental data, as well as what other new physics theories can be confirmed or discarded at the TeV energy scale.

The last two Sections contain a summary of the challenging ATLAS physics program, divided in Standard Model and Beyond the Standard Model searches.

2.1 High Energy Physics Overview

2.1.1 Standard Model Review

The Standard Model (SM) [28] is a very successful description of the interactions of the components of matter at the smallest scales ($<10^{-18}$ m) and highest energies ($\sim$200 GeV) available. It is a quantum field theory which describes the interaction of spin-1/2, point-like fermions, whose interactions are mediated by spin-1 gauge bosons. The bosons arise when local gauge invariance is applied to the fermion fields, and are a manifestation of the symmetry group of the theory,

which for the Standard Model is SU(3)⊗SU(2)⊗U(1). The fundamental fermions are leptons and quarks. There are three generations of fermions, each identical except for mass. The origin of this generational structure, and the breaking of generational symmetry (i.e. the different masses of each generation) remains a mystery. Corresponding to the three generations, there are three leptons with electric charge -1, the electron (e), the muon (μ) and the tau (τ), and three electrically neutral leptons (the neutrinos ν_e, ν_μ and ν_τ). Similarly there are three quarks with electric charge $+2/3$, up (u), charm (c) and top (t), and three with electric charge -1/3, down (d), strange (s) and bottom (b). There is mixing between the three generations of quarks, which in the SM is parametrized (but not explained) by the Cabibbo-Kobayashi-Maskawa (CKM) matrix.

The quarks are triplets of the SU(3) gauge group and so they carry an additional "charge", referred to as color, which is responsible for their participating in the strong interaction (quantum chromodynamics or QCD). Eight vector gluons mediate this interaction; they carry color charges themselves, and are thus self-interacting. This implies that the QCD coupling α_s is small for large momentum transfers but large for soft processes, and leads to the confinement of quarks inside color-neutral hadrons (like protons and neutrons). Attempting to free a quark produces a jet of hadrons through quark-antiquark pair production and gluon bremsstrahlung.

In the SM, the SU(2)⊗U(1) symmetry group, which describes the so-called electroweak interaction, is spontaneously broken through the existence of a (postulated) Higgs field with non-zero expectation value. This leads to the emergence of massive vector bosons, the $W^\pm$ and the Z, which mediate the weak interaction, while the photon of electromagnetism remains massless. One physical degree of freedom remains in the Higgs sector, which could be manifest most simply as a neutral scalar boson H^0, which is presently unobserved. Figure 2.1 shows graphically all the particles in the SM.

The basics of the SM were proposed in the 1960's and 1970's. Increasing experimental evidence of the correctness of the model accumulated through the 1970's and 1980's. Deep inelastic scattering experiments at SLAC showed the existence of point-like scattering centers inside nucleons, later identified with quarks. The c and b quarks were observed and neutral weak currents (Z exchange) were iden-

tified. Three-jet final states (from gluon bremsstrahlung) were observed in e^+e^- and hadron-hadron collisions, and the W and Z were directly observed at the CERN SPS collider. Following these discoveries, the 1990's decade was largely an era of consolidation. Even more precise experiments were carried out at LEP and SLC which provided verification of the couplings of quarks and leptons at the level of 1-loop radiative corrections - O(10^{-3}). The top quark was discovered at FNAL in 1995, and it was found to have an unexpectedly large mass (175 GeV). After the discovery in 2000 of the ν_τ in the DONUT experiment also at FNAL, only one particle of the SM has yet to be observed: the Higgs boson. The last, but the most important as it holds the key to the generation of W, Z, quark and lepton masses.

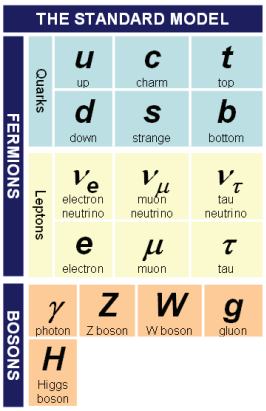

Figure 2.1: Standard Model elementary particles.

2.1.2 Beyond the Standard Model

The successes of the Standard Model have drawn increased attention to its limitations. In its simplest version, the SM has 19 parameters - three coupling constants, nine quark and lepton masses, the mass of the Z boson which sets the scale of the weak interaction, four CKM mixing parameters, and one (small) parameter describing the scale of CP violation in the strong interaction. The remaining parameter is associated with the mechanism responsible for the breakdown of the electroweak SU(2)⊗U(1) symmetry to U(1) of electromagnetism ("electroweak symmetry breaking" or EWSB). This can be taken as the mass of the Higgs bo-

son, the couplings of the Higgs are determined once its mass is given. Within the model we have no guidance on the expected mass of the Higgs boson. The current experimental lower bound from LEP2 is about 115 GeV, and the upper limit from global fits to electroweak parameters is about 470 GeV. As its mass increases, the self-couplings of the W and Z grow, and so the mass must be less than about 800 GeV, or the strong dynamics of WW and ZZ interactions will reveal new structure. It is this simple argument that sets the energy scale that must be reached to guarantee that an experiment will be able to provide information on the nature of electroweak symmetry breaking, which is the central goal of the Large Hadron Collider.

The presence of a single elementary scalar boson is distasteful to many theorists. If the theory is part of some more fundamental theory with a larger mass scale (such as the scale of grand unification, or the Planck scale) then radiative corrections will result in the Higgs mass being driven up to this large scale unless some delicate cancellations are engineered. There are two ways out of this problem which both result in new physics on the scale of 1 TeV. New strong dynamics could enter that provide the scale of the W mass or new particles could appear which would cancel the divergences in the Higgs boson mass. In any of these eventualities - Standard Model, new dynamics or new particles - something must be discovered at the TeV scale, i.e. at the LHC.

Supersymmetry (SUSY) is an appealing concept for which there is at present no experimental evidence. It offers the only presently known mechanism for incorporating gravity into the quantum theory of particle interactions and provides an elegant cancellation mechanism for the divergences affecting the Higgs mass, while retaining all the successful predictions of the Standard Model and allowing a unification of the three couplings of the gauge interactions at a high scale. Supersymmetric models postulate the existence of superpartners for all the presently observed particles. There are bosonic superpartners of fermions (squarks and sleptons), and fermionic superpartners of bosons (gluinos and gauginos). There are also multiple Higgs bosons: h, H, A and $H^{\pm}$. There is thus a large spectrum of presently unobserved particles, whose exact masses, couplings and decay chains are calculable in the theory given certain parameters. Unfortunately these parameters are unknown; but if supersymmetry has anything to do with EWSB, the

masses should be in the region 100 GeV - 1 TeV. Figure 2.2 shows a diagram of the Minimal Supersymmetric Standard Model (MSSM) particles.

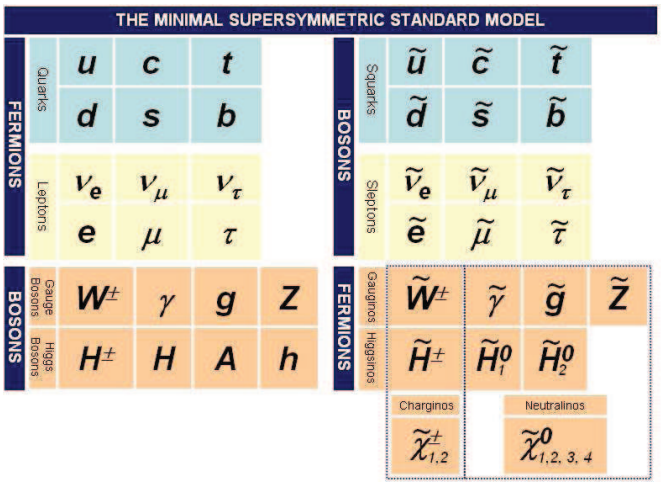

Figure 2.2: Minimal Supersymmetric Standard Model elementary particles.

An example of the strong coupling scenario is “technicolor” models based on dynamical symmetry breaking. An elegant implementation of these ideas is lacking. Nonetheless, if the dynamics has anything to do with EWSB, we would expect new states in the region 100 GeV - 1 TeV and most models predict a large spectrum. At the very least, there must be structure in the WW scattering amplitude at around 1 TeV center-of-mass energy.

There are also other possibilities for new physics that are not necessarily related to the scale of EWSB. There could be neutral or charged gauge bosons with masses larger than the Z or W. There could be new quarks, charged leptons or massive neutrinos or quarks and leptons might turn out not to be elementary objects. While we have no definite expectations for the masses of such particles, the LHC must be able to search for them over its entire available energy range.

2.2 Standard Model Physics at ATLAS

2.2.1 Physics of Electroweak Gauge Bosons

Gauge bosons and gauge-boson pairs will be abundantly produced at the LHC. The large statistics and the high center-of-mass energy will allow several precision measurements to be performed. Indeed, the study of the production of W and Z events at the LHC is fundamental in several aspects.

First, the calculation of higher order corrections to these simple, color singlet final states is very advanced, with a residual theoretical uncertainty smaller than 1%. Such precision makes W and Z production a stringent test of QCD.

Secondly, more specifically for Z production, the clean and fully reconstructed leptonic final states will allow a precise measurement of the transverse momentum and rapidity distributions. The transverse momentum distribution will provide more constraints on QCD, most significantly on non-perturbative aspects related to the resummation of initial parton emissions, while the rapidity distribution is a direct probe of the parton density functions (PDFs) of the proton. The high expected counting rates will bring significant improvement on these aspects, and this improvement translates to virtually all physics at the LHC, where strong interaction and PDF uncertainties are a common factor.

From the experimental point of view, the precisely measured properties of the Z boson provide strong constraints on the detector performance. Its mass, width and leptonic decays can be exploited to measure the detector energy and momentum scale, its resolution, and lepton identification efficiency very precisely.

Finally, a number of fundamental electroweak parameters can be accessed through W and Z final states (M_W, through the W boson decay distributions; $\sin^2\theta_W$, via the Z forward-backward asymmetry; lepton universality, by comparing electron and muon cross-sections). These measurements are long term applications where the understanding of the hadronic environment at the LHC is crucial, and to which the above-mentioned measurements are necessary inputs.

Figure 2.3 shows the expected transverse mass distribution for $W \to \mu\nu$ and the invariant mass distribution in the $Z \to \mu\mu$ channel, both for an integrated luminosity of 50 pb^{-1}.

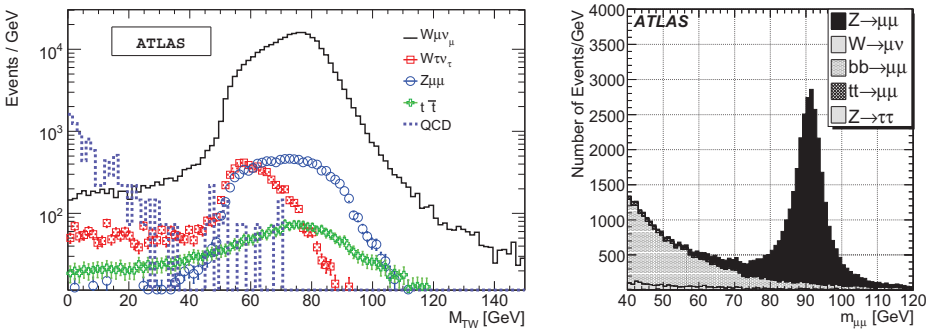

Figure 2.3: On the left, transverse mass distribution in the $W \to \mu\nu$ channel for 50 pb^{-1}. On the right, dimuon invariant mass distribution in the $Z \to \mu\mu$ channel for 50 pb^{-1}.

Diboson Physics

The analysis of diboson production (W^+W^-, $W^\pm Z$, ZZ, $W^\pm\gamma$, $Z\gamma$) using lepton and photon final states at the LHC provides an important test of the high energy behavior of electroweak interactions setting limits on anomalous triple gauge boson couplings (TGC).

Any theory predicting physics beyond the Standard Model while maintaining the Standard Model as a low-energy limit may introduce deviations in the gauge couplings at some high energy scale. Precise measurements of the couplings will not only provide stringent tests of the Standard Model, but will also probe for new physics in the bosonic sector. These tests will provide complementary information to other direct searches for new physics at the LHC.

2.2.2 Top Quark Physics

The LHC will be a top quark factory, producing millions of $t\bar{t}$ pairs in a sample of 10 fb^{-1}, which is expected to be collected during the first years of LHC operation. Non-Standard Model physics could first manifest itself in non-standard couplings of the top quark which show up as anomalies in top quark production and decays.

Top Quark Production

The determination of the top quark pair production cross-section is one of the measurements that will be carried out once the first data samples are available at the ATLAS experiment. It casts light on the intrinsic properties of the top quark and its electroweak interactions. Cross-section measurements are also an important test of possible new production mechanism, as non Standard Model top quark production can lead to a significant increase of the cross-section.

The production cross-section for $t\bar{t}$ system can be measured by its decay both into a single electron or muon with associated jets, or two electrons or muons with jets. With only 100 pb^{-1} of accumulated data, top-quark signals can be observed and its production cross-section measured. Various methods have been proposed and prospects show that the overall uncertainties are of the order of (5 - 10)% and are dominated by systematics.

Single Top

The DØ [29] and CDF [30] collaborations at the Fermilab Tevatron collider reported 5σ evidence for single top quark production and a first direct measurement of the CKM matrix element V_{tb} in 2009. At the LHC the production of single top quark events accounts for about a third of the $t\bar{t}$ production, which leads to about 2.5 million events per year when running at 10^{32} cm^{-2}s^{-1}. A precise determination of single top quark cross-sections can be achieved for a few fb^{-1} and V_{tb} can also be measured with high precision.

Similarly to the situation at the Tevatron, the selection of single top quark events will suffer from the presence of both W+jets and $t\bar{t}$ backgrounds, which are produced at much higher rates. In a context of low signal over background ratio, the use of sophisticated analysis techniques is required.

Once the single top quark signal has been established, detailed measurements of the process will follow, for example of the top quark polarization, ratios of cross-sections, and charge asymmetries.

Top Quark Measurements

In contrast to earlier measurements of the top quark mass, which concentrated on preserving as much of the signal as possible in order to minimize the statistical uncertainty, the LHC will produce so many top quark pairs that rather stringent requirements can be imposed, to restrict the measurement to regions in which the systematic uncertainties can be well controlled. The precision on the top quark mass relies mainly on the jet energy scale uncertainty: a precision of the order of 1 to 3.5 GeV should be achievable with 1 fb^{-1}, assuming a jet energy scale uncertainty of 1 to 5%.

Several properties of the top quark have already been explored by the Tevatron experiments, such as the mass, charge and lifetime, the rare decays through flavor changing neutral currents (FCNC) and the production cross-sections.

The electric charge of the top quark is one of its fundamental properties and will be probed with high statistics at the LHC. The measurement of the top quark charge can be performed either by identifying the charge of its decay products in the main decay channel $t \rightarrow bW$ or by studying radiative top quark processes. At the Tevatron the DØ and CDF collaborations have already initiated the study of the top quark charge and, with the available statistics, they showed that the data gives preference to the Standard Model top quark hypothesis (with a charge of +2/3) over the scenario with an exotic quark of charge -4/3 and mass of ∼170 GeV, fully consistent with the present precision electroweak data. Already with 0.1 fb^{-1} it is possible to distinguish with a 5σ significance, between the b-jet charges associated

with leptons of opposite charges, which allows to distinguish the Standard Model from an exotic scenario.

As the top quark decays before it can form hadronic bound states, a consequence of its high mass, the spin information of the top quark is propagated to its decay products. This unique behavior among quarks allows direct top quark spin studies, as spin properties are not washed out by hadronization. Through the measurement of the angular distributions of the decay products the information of the top quark spin can be reconstructed. Top quark spin polarization and correlations in $t\bar{t}$ events produced at the LHC are precisely predicted by the Standard Model and are sensitive to the fundamental interactions involved in the top quark production and decay.

2.2.3 B-Physics

The rate of B-hadron production at the LHC is enormous thanks to the large hadronic cross-section for b-quark production and the high luminosity of the machine: about one collision in every hundred will produce a b-quark pair. The B-event rate will be higher than in any accelerator in operation before the start-up of the LHC.

In ATLAS, the main B-physics measurements will be made with an instantaneous luminosity of around 10^{33} cm^{-2}s^{-1}; however, the B-physics potential begins during early data taking at low luminosity (10^{31} cm^{-2}s^{-1}). With an integrated luminosity of 10 pb^{-1} ATLAS will already be able to register about 1.3×10^{5} events containing $J/\psi \rightarrow \mu\mu$ selected by the low luminosity trigger menu.

In ATLAS, an inclusive-muon trigger with a p_{T} threshold of 6 GeV will make an initial selection of B-events. Using this inclusive selection, about 25% of the muon-trigger events will contain b-quarks.

Although the main focus of the ATLAS physics program is the search for and study of physics beyond the Standard Model, through the production and decay of new types of particles, an important range of B-physics studies is planned. In fact, an important aim of the B-physics work is to test the SM through precision mea-

surements of B-hadron decays that together will over-constrain the CKM matrix, possibly giving indirect evidence for new physics.

Heavy Quarkonium Physics with Early Data

The number of $J/\psi \to \mu\mu$ and $\Upsilon \to \mu\mu$ decays produced at the LHC is expected to be quite large. Their importance for ATLAS is threefold: first, being narrow resonances, they can be used as tools for alignment and calibration of the trigger, tracking and muon systems. Secondly, understanding the details of the prompt quarkonia production is a challenging task and a good testbed for various QCD calculations, spanning both perturbative and non-perturbative regimes. Last, but not the least, heavy quarkonium states are among the decay products of heavier states, serving as good signatures for many processes of interest, some of which are quite rare. These processes have prompt quarkonia as a background and, as such, a good description of the underlying quarkonium production process is crucial to the success of these studies.

Figure 2.4 illustrates the quarkonium signal and main background invariant mass distributions in the mass range 2 - 12 GeV, for those events which satisfy the mu6mu4 trigger requirements. Peaks from the J/ψ and $\Upsilon(1S)$ clearly dominate the background. The dotted line indicates the level of the background continuum before the analysis cuts.

During the initial run of the LHC, the integrated luminosity of 1 pb^{-1} with the mu6mu4 trigger would mean about 15000 J/ψ and 2500 Υ recorded events. If the mu4mu4 trigger is used, these numbers would increase up to 17000 and 20000 respectively, with these additional events mainly concentrated at the lower end of the quarkonium transverse momenta.

With these statistics, the p_T dependence of the cross-section for both J/ψ and Υ should be measured reasonably well, in a wide range of transverse momenta ($10 < p_T < 50$ GeV). The precision of J/ψ polarisation measurement can reach 0.02 - 0.06 (depending on the level of polarisation itself), while the expected error on Υ polarisation is unlikely to be better than about 0.2.

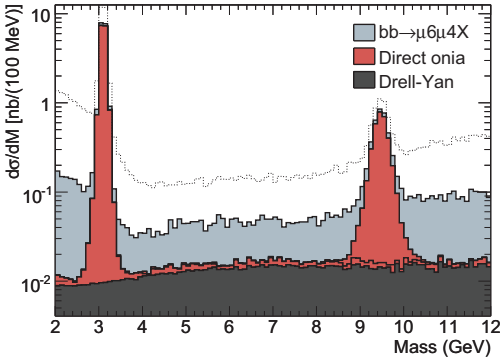

Figure 2.4: The cumulative plot of the invariant mass of dimuons from various sources, reconstructed with a mu6mu4 trigger, with the requirement that both muons are identified as coming from the primary vertex and with a pseudo-proper time cut of 0.2 ps. The dotted line shows the cumulative distribution without vertex and pseudo-proper time cuts.

At this stage, first attempts may be made to understand the performance of the electromagnetic calorimetry at low photon energies, and to try and reconstruct $c\bar{c}$ states from their radiative decays. With an integrated luminosity of 100 pb^{-1}, the transverse momentum spectra are expected to reach about 100 GeV and possibly beyond, for both J/ψ and Υ. With several million J/ψ and more than 500000 of Υ decays, and a good understanding of the detector, high precision polarisation measurements, at the level of few percent, should become possible for both J/ψ and Υ. $\chi_b \to \Upsilon\gamma$ decays could become observable, while other measurements mentioned above will become increasingly precise.

CP Violation in B-Meson Decays

Within the Standard Model, *CP* violation in weak decays is introduced by the phase of the CKM quark-mixing matrix. The unitarity of this matrix is used to derive triangle relation between the matrix elements, defining the so-called unitary triangle which has 3 angles denoted as α, β and γ. Figure 2.5 shows the updated constraints for the angles and sides of the CKM triangle with the currently available data (see Ref. [31] for details).

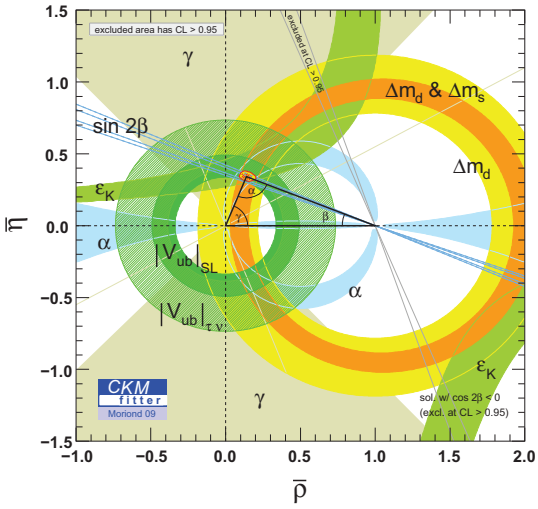

Figure 2.5: Current boundaries on the CKM unitary triangle. The red blob represents the constraints obtained with the world average data.

The most important channels to study *CP* violation in ATLAS are the following:

- $B_d^0 \to \mathrm{J}/\psi\, K_s^0$, with $\mathrm{J}/\psi \to \mu\mu$ or $\mathrm{J}/\psi \to ee$ and $K_s^0 \to \pi^+\pi^-$:
  This channel can provide a clean measurement of the angle β of the unitary matrix. The asymmetry in this channel depends only on the mass difference in the B_d^0 - $\overline{B_d^0}$ system (Δm_d) and the angle β, without any contribution from penguin diagrams. Furthermore, it is experimentally a very clean channel with relatively low backgrounds.

- $B_s^0 \to \mathrm{J}/\psi\, \phi$, with $\mathrm{J}/\psi \to \mu\mu$ and $\phi \to KK$:
  Only a very small asymmetry is predicted for this channel in the SM, but an observation of a sizeable effect would be a clear sign of new physics. In addition, some SM parameters can be measured in this channel, such as the width difference in the B_s^0 - $\overline{B_s^0}$ system.

- $B_d^0 \to D^0 K^{*0}$:
  The study of the decay amplitude in this channel would be used to determine the angle γ of the unitary matrix.

Summing up, high-statistics studies of *CP* violation in these channels will give measurements of the unitary triangle angles and will search for deviations from the Standard Model.

Measurements of B_s^0 Oscillations

The observed B_s^0 and $\overline{B_s^0}$ states are linear combinations of two mass eigenstates, denoted here as H and L. Due to the non-conservation of flavor in charged weak-current interactions, transitions between B_s^0 and $\overline{B_s^0}$ states occur with a frequency proportional to $\Delta m_s = m_H - m_L$. In the B_d^0 - $\overline{B_d^0}$ system, the oscillations have been directly observed and precisely measured (the current value of this mass difference is $\Delta m_d = (0.563^{+0.068}_{-0.076})$ ps^{-1}). Simulations show that it will be possible to measure Δm_s at LHC with a good sensitivity.

Rare B-Decays

Certain decays, such as $B_{s,d} \to \mu\mu$(X), involve flavor changing neutral currents (FCNC) and are strongly suppressed in the Standard Model, with predicted branching ratios typically in the range 10^{-5} to 10^{-10}.

These decay modes are forbidden at the tree level in the SM, so the decays involve loop diagrams. In non-standard models of electroweak interactions, FCNC processes can be allowed at the tree level and thus, the branching ratios of these rare decays would not be so suppressed. In addition, in the presence of new physics, additional particles may be present in the loops again enhancing the decay probability. Due to the very low SM predictions for the branching fractions for purely muonic decays, a significant enhancement in measured branching fractions would clearly demonstrate the effects of new physics.

2.2.4 Higgs Hunting

While the Standard Model of electroweak and strong interactions is in excellent agreement with the numerous experimental measurements, the dynamics responsible for electroweak symmetry breaking is still unknown. Within the Standard Model, the Higgs mechanism is invoked to break the electroweak symmetry. A doublet of complex scalar fields is introduced, of which a single neutral scalar particle, the Higgs boson, remains after symmetry breaking. Many extensions of this minimal version of the Higgs sector have been proposed, mostly discussed a scenario with two complex Higgs doublets as realized in the MSSM. Details on the MSSM Higgs sector are given in Chapter 4 which is devoted to the ATLAS MSSM neutral Higgs boson discovery potential in the dimuon channel.

As mentioned above, within the Standard Model the Higgs boson is the only particle that has not been discovered so far. The direct search at the LEP collider has led to a lower bound on its mass of 114.4 GeV. Indirectly, high precision electroweak data constrain the mass of the Higgs boson via their sensitivity to loop corrections. Assuming the overall validity of the Standard Model and the lower mass bounds, a global fit to all electroweak data leads to the 95% CL $m_H < 182$ GeV.

On the basis of the present theoretical knowledge, the Higgs sector in the Standard Model remains largely unconstrained. While there is no direct prediction for the mass of the Higgs boson, an upper limit of $\sim$1 TeV can be inferred from unitarity arguments.

Further constraints can be derived under the assumption that the Standard Model is valid only up to a cutoff energy scale Λ, beyond which new physics becomes relevant. Requiring that the electroweak vacuum is stable and that the Standard Model remains perturbative allows to set upper and lower bounds on the Higgs boson mass. For a cutoff scale of the order of the Planck mass, the Higgs boson mass is required to be in the range $130 < m_H < 180$ GeV. If new physics appears at lower mass scales, the bound becomes weaker, e.g., for $\Lambda = 1$ TeV the Higgs boson mass is constrained to be in the range $50 < m_H < 800$ GeV.

Direct searches for the Standard Model Higgs boson at the Tevatron include looking for its production via gluon fusion and subsequent decay to WW^*. The

observed 95% CL limit by CDF (with an integrated luminosity of 3.6 fb^{-1} analyzed) is about 1.6 times the Standard Model prediction for $m_H = 160$ GeV. Similarly the DØ collaboration excludes at 95% CL the production of this boson with a cross-section about 2.4 times the one predicted by the Standard Model ($\sigma^{WW}_{\rm SM}$). Searches at low mass are done studying Higgs bosons produced in association with the W and Z, and looking for $H \to b\bar{b}$ with leptonic W and Z decays (e, μ). CDF sets a 95% CL limit to $8.2\sigma^{b\bar{b}}_{\rm SM}$, while the one from DØ is $11\sigma^{b\bar{b}}_{\rm SM}$, for $m_H = 115$ GeV. Preliminary results on the combination of the results from these two experiments excluded with a 95% CL the SM Higgs boson in the $160 < m_H < 170$ GeV with a limit on the production cross-section to about $2.15\sigma_{\rm SM}$ for $m_H = 115$ GeV [32].

Figure 2.6 shows the production cross-section and decay branching ratios for the Standard Model Higgs boson.

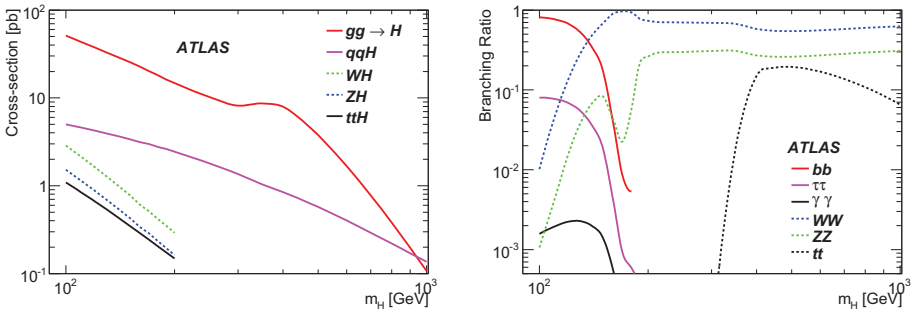

Figure 2.6: On the left, cross-sections for the five production channels of the Standard Model Higgs boson at the LHC at 14 TeV. On the right, branching ratios for the relevant decay modes of the Standard Model Higgs boson as a function of its mass.

Some of the most promising channels for Higgs discovery at LHC are the following:

- $pp \to H \to \gamma\gamma$ either in direct production or from the associated production WH, ZH and $t\bar{t}H$
- $pp \to H \to 4\ell$ (mediated by 2 virtual Z bosons)
- $pp \to H \to \ell\nu\ell\nu$, $\ell\nu qq$ (mediated by 2 virtual W bosons)

- $pp \to t\bar{t}H \to t\bar{t}b\bar{b}$ from the associated production WH, ZH and ttH
- $pp \to qqH \to qq\tau\tau$
- $pp \to t\bar{t}H \to t\bar{t}WW$
- $pp \to ZH \to \ell\ell WW$

Figure 2.7 shows the estimated discovery potential for these channels in the ATLAS experiment for a Higgs mass range from 100 GeV to 1 TeV for an integrated luminosity of 10 fb^{-1}.

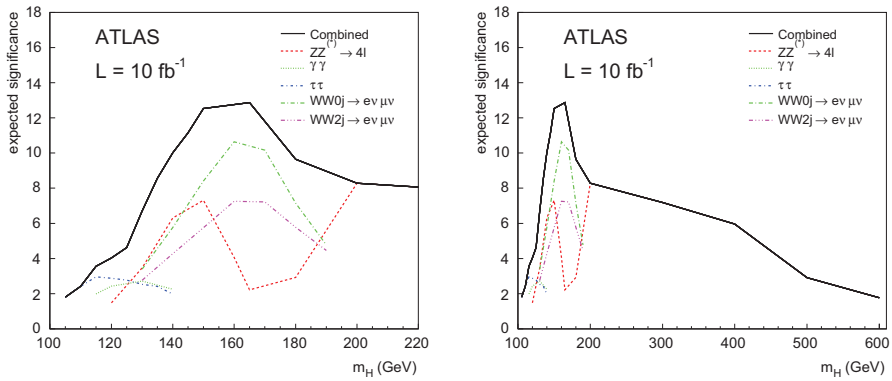

Figure 2.7: The median discovery significance for the various channels and the combination with an integrated luminosity of 10 fb^{-1} for the lower mass range (left) and for masses up to 600 GeV (right).

2.3 Physics Beyond the Standard Model at ATLAS

2.3.1 Supersymmetry

Supersymmetry is a generalization of the space-time symmetries of quantum field theory that transforms fermions into bosons and vice versa. Supersymmetry also provides a framework for the unification of particle physics and gravity, which is

governed by the Planck energy scale, $M_{\rm Pl} \sim 10^{19}$ GeV (where the gravitational interactions become comparable in magnitude to the gauge interactions). In particular, it is possible that supersymmetry will ultimately explain the origin of the large hierarchy of energy scales from the W and Z masses to the Planck scale, the so-called gauge hierarchy. The stability of the gauge hierarchy in the presence of radiative quantum corrections is not possible to maintain in the SM, but can be maintained in supersymmetric theories.

If supersymmetry were an exact symmetry of nature, then particles and their superpartners (which differ in spin by half a unit) would be degenerate in mass. Since superpartners have not (yet) been observed, supersymmetry must be a broken symmetry. Nevertheless, the stability of the gauge hierarchy can still be maintained if the supersymmetry breaking is *soft*, and the corresponding SUSY-breaking mass parameters are no larger than a few TeV.

Another argument which supports the existence of SUSY is the fact that there are experimental evidences that about 90% of the matter of the universe is dark. Furthermore, the large scale structure of the universe may be accommodated supposing two kinds of dark matter. One kind is composed of particles which were relativistic at the time of the structure formation. This is called Hot Dark Matter (HDM). The other kind is composed of particles which were non-relativistic at the time of structure formation. These constitute the Cold Dark Matter (CDM) component of the universe. In any case the CDM component of the universe is at least 60%.

The existence of dark matter cannot be explained within the Standard Model of particle physics. It is tempting to attribute the dark matter to the existence of a neutral stable thermal relic (i.e., a particle that was in thermal equilibrium with all other fundamental particles in the early universe at temperatures above the particle mass). Remarkably, the existence of such a particle could yield the observed density of dark matter if its mass and interaction rate were governed by new physics associated with the TeV-scale. The lightest supersymmetric particle is a promising (although not the unique) candidate for the dark matter.

Minimal Supersymmetric Standard Model

The Minimal Supersymmetric Standard Model is the SUSY model with the minimal particle content. Each left-handed and right-handed fermion of the SM is postuled to have its own bosonic superpartner with equal mass and coupling strengths. Similarly, each SM boson would have its own fermionic superpartner with equal mass and couplings.

The Higgs sector consists of two complex doublets of Higgs fields, leading to five physical states: one *CP*-odd neutral pseudoscalar (A), two neutral *CP*-even scalars (h and H) and two charged bosons ($H^{\pm}$). The superpartners of the SM fermions are denoted with the prefix s- (so there would be a slepton, squark, etc) and the superpartner of the SM bosons have the suffix -ino (photino, zino, wino, etc.). In shorthand notation, these superpartners are denoted with a tilde ($\tilde{e}$, $\tilde{g}$, $\tilde{q}$, $\tilde{Z}$, etc.). The partners of the gauge and Higgs bosons are called gauginos and higgsinos, respectively. Note that the charged (neutral) gauginos and higgsinos are mixed to give physical mass eigenstates called charginos (neutralinos).

As a consequence of barion-lepton number invariance, the MSSM has a multiplicative R-parity invariance, $R=(-1)^{3(B-L)+2S}$ where B, L, and S are the baryon number, lepton number and spin. Note that this implies that all the ordinary Standard Model particles have even R parity, whereas the corresponding supersymmetric partners have odd R parity. The conservation of R parity in scattering and decay processes has a crucial impact on supersymmetric phenomenology. For example, starting from an initial state involving ordinary (R-even) particles, it follows that supersymmetric particles must be produced in pairs. In general, these particles are highly unstable and decay into lighter states. However, R-parity invariance also implies that the Lightest Supersymmetric Particle (LSP) is absolutely stable, and must eventually be produced at the end of a decay chain initiated by the decay of a heavy unstable supersymmetric particle.

In order to be consistent with cosmological constraints, a stable LSP is almost certainly electrically and color neutral. Consequently, the LSP in an R-parity-conserving theory is weakly interacting with ordinary matter, i.e., it behaves like a stable heavy neutrino and will escape collider detectors without being directly observed. Thus, the canonical signature for conventional R-parity-conserving su-

persymmetric theories is missing transverse energy ($E_{\mathrm{T}}^{\mathrm{miss}}$) due to the escape of the LSP.

In the MSSM there are a total of 105 new parameters in addition to the Standard Model ones. Clearly it is not possible to explore the complete parameter space of the MSSM and in the absence of experimental help some theoretical prejudice must be imposed. Hence, with additional assumptions on top of the MSSM, several models have been developed such as supergravity (SUGRA), minimal supergravity (mSUGRA), Gauge Mediated Supersymmetry Breaking (GMSB), *R*-parity violating scenarios, etc. Even if the general MSSM is correct, none of these scenarios is likely to be the whole truth, but they do provide self-consistent frameworks in which to test the ability of the ATLAS detector to study supersymmetry at the LHC.

Several analysis strategies have been developed to cover all the possible signatures coming from supersymmetric models. For instance, in mSUGRA models the analysis is based on the selection of multiple jets, either isolated leptons or a lepton veto and $E_{\mathrm{T}}^{\mathrm{miss}}$, with good prospects for an early discovery at the LHC. Figure 2.8 shows the discovery reach for an integrated luminosity of 1 fb^{-1} in the mSUGRA parameter space for several analysis branches.

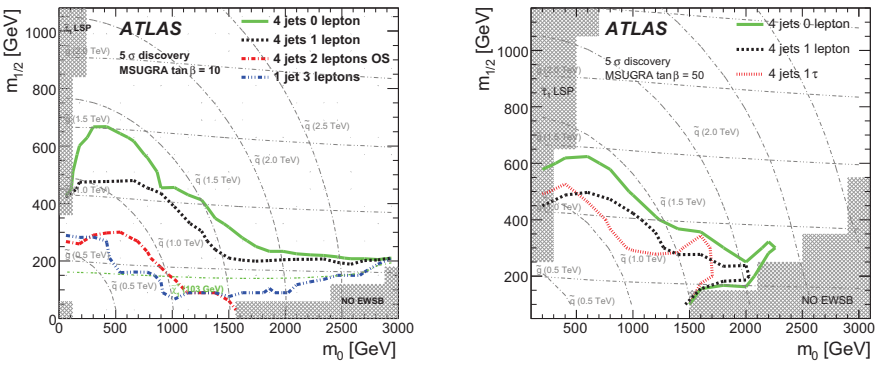

Figure 2.8: 5σ reach contours for the jets plus $E_{\mathrm{T}}^{\mathrm{miss}}$ analyses with 1 fb^{-1} for various lepton requirements for mSUGRA as a function of m_0 and $m_{1/2}$ for $\tan\beta = 10$ (left) and $\tan\beta = 50$ (right). The horizontal and curved grey lines indicate gluino and squark mass contours respectively in steps of 500 GeV.

2.3.2 Extra-Dimensions

Theories involving extra spatial dimensions have been developed to find mechanisms to unify gravity with quantum mechanics and/or the M_W-$M_{\rm Pl}$ hierarchy problem and can have direct implications for collider experiments.

Let us consider a D-dimensional spacetime (called "bulk") with $D{=}4{+}\delta$, where δ is the number of extra spatial dimensions. Standard Model fields are assumed to be localized on a (3+1)-dimensional subspace (called "brane"). This assumption can be realized in field theory, but it is most natural in the setting of string theory, so that gauge and matter fields can be confined to live on branes.

On the other hand, gravity, which according to general relativity is described by the spacetime geometry, extends to all D dimensions and gravitons are allowed to propagate in the bulk. These particles lead to the appearance in the brane of a tower of massive particles: Kaluza-Klein (KK) excitations with the same properties as the original particle but with a mass proportional to the size of the extra-dimensions (R).

Since the produced gravitons interact with matter only with rates suppressed by inverse powers of $M_{\rm Pl}$, they will remain undetected leaving a $E_{\rm T}^{\rm miss}$ signature. The D-dimensional graviton can then be recast as a tower of KK states with increasing mass. Since R^{-1} is smaller than the typical energy resolution in collider experiments, the mass distribution of KK gravitons is practically continuous.

Although each KK graviton has a purely gravitational coupling suppressed by $M_{\rm Pl}^{-1}$, inclusive processes in which we sum over the large number of available gravitons have cross-sections suppressed only by powers of the effective gravitational scale (M_D), which is then connected to the Planck scale through:

$$M_{\rm Pl}^2 \sim M_D^{2+\delta} R^{\delta}. \tag{2.1}$$

Processes involving gravitons are therefore detectable in collider experiments if M_D is in the TeV region. The current combined LEP 95% CL limits are $M_D > 1.60$, 1.20, 0.94, 0.77, 0.66 TeV for $\delta = 2, \ldots, 6$ respectively. The most promising channels for extra-dimensions discovery are $pp \to \text{jet} + E_{\rm T}^{\rm miss}$ and $pp \to \gamma + E_{\rm T}^{\rm miss}$ [33].

2.3.3 Other Physics Beyond the Standard Model

- **Fourth generation of quarks and leptons:** data from LEP imply the existence of only three SM families with light neutrinos. However, extra generations with heavy neutrinos are not excluded, and models which include them have been proposed. The current experimental limits on fourth family leptons and quarks are $m_\ell > 80$ GeV and $m_q > 128$ GeV.

- **Compositeness:** if quarks and leptons are made of constituents, at the scale of constituent binding energies, new interactions among quarks and leptons should appear. At energies much below the compositeness scale (Λ), these interactions are suppressed by inverse powers of Λ. Another typical consequence of compositeness is the appearance of excited leptons and quarks (ℓ^* and q^*). Phenomenologically, an excited lepton is defined to be a heavy lepton which shares leptonic quantum number with one of the existing leptons (an excited quark is defined similarly).

  The replication of three generations of quarks and leptons suggests the possibility that they are composite structures made up of more fundamental constituents.

- **New vector bosons:** the W' (Z') boson is a hypothetical massive particle of electric charge ± 1 and spin 1 (electrically-neutral and color-singlet particle of spin 1), which are predicted in various extensions of the Standard Model. The discovery of the W' could be performed in ATLAS via its leptonic decays (such as $W' \to e\nu$, as Figure 2.9 shows), $W' \to \bar{t}b$ or $W' \to WZ \to (\ell\nu)(\ell\ell)$. Promising channels for the Z' discovery are ee, $\mu\mu$, $e\mu$, $\tau\tau$ and $t\bar{t}$. Figure 2.9 shows the mass spectrum for the $W' \to e\nu$ and $Z' \to ee$ channels.

- **Leptoquarks:** Leptoquarks (LQs) are hypothetical particles carrying both baryon number and lepton number. Leptoquark states are a generic prediction of Grand Unified Theories (GUTs), of composite models, of technicolor schemes, of supersymmetry with R-parity violation, etc. At LHC, scalar leptoquarks can be produced via gg fusion and $q\bar{q}$ annihilation. If the two LQs are assumed to decay to a charged lepton and a quark, a topology with two high-p_{T} leptons and two high-E_{T} jets is provided. In the case that both LQs are assumed to decay to a neutrino and a quark, events will present a topology with two high-E_{T} jets and large $E_{\mathrm{T}}^{\mathrm{miss}}$.

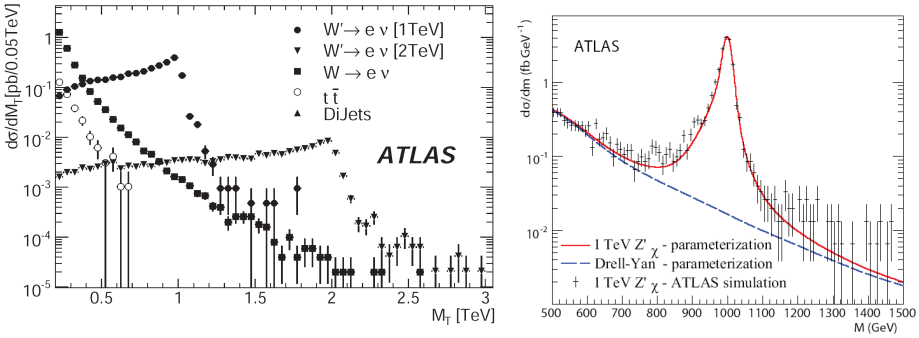

Figure 2.9: On the left, transverse mass spectrum for a $m_{W'}$=1, 2 TeV in the $W' \rightarrow e\nu$ channel. On the right, invariant mass spectrum for a $m_{Z'}$=1 TeV in the $Z' \rightarrow ee$ channel.

- **Technicolor:** Technicolor theory provides a dynamical means of breaking electroweak symmetry. It assumes the existence of technifermions possessing a technicolor charge and interacting strongly at a high scale. The ATLAS detector will be sensitive to these new resonances predicted in technicolor theory, up to the TeV range. Although the parameter space is very large, the number of potential channels allows for combinations of signatures to help in understanding the nature of the resonances, and determine the possible existence of techniparticles.

3 TileCal Muon Level-2 Trigger

"I, at any rate, am convinced that He does not throw dice."
— Albert Einstein, letter to Max Born (4 December 1926)

As mentioned in Chapter 2, a lot of interesting Standard Model physics studies are based on low-p_{T} muons. The possibility to detect muons with the Tile Calorimeter was explored already in the 90's [34, 35] and the calorimeter can certainly contribute to the overall ATLAS muon identification in the p_{T} and η range where the Muon Spectrometer is not fully efficient. The algorithm responsible for tagging muons in TileCal is known as TileMuId [36, 37] and was developed as a contribution to the Level-2 trigger aiming to be used in B-physics studies.

This Chapter describes in first place the muon reconstruction strategy in ATLAS and introduces the foundations of the TileMuId algorithm. The technical developments done towards a full integration in both the offline and HLT framework are presented, together with the TileMuId performance with Monte Carlo and real cosmics data.

3.1 Muon Reconstruction in ATLAS

The identification of muons in the ATLAS experiment is based on three different track reconstruction strategies:

- Stand-alone: the muon track reconstruction is based only on the Muon Spectrometer data in the $|\eta| < 2.7$, as defined by the spectrometer acceptance.

- Combined: this makes use of the combination of a Muon Spectrometer track with an Inner Detector track in the $|\eta| < 2.5$, as defined by the Inner Detector acceptance.
- Segment tag: combination of an Inner Detector track and a Muon Spectrometer segment, that is, a straight line track in an inner muon station.

Track segments are defined as straight lines in a single MDT or CSC station. Track candidates are built from segments, starting from the outer and middle stations and extrapolating back through the magnetic field to the segments reconstructed in the other stations. Each time a reasonable match is found, the segment is added to the track candidate. The final track-fitting procedure takes into account, in full detail, the geometrical description of the traversed material and the magnetic field inhomogeneities along the muon trajectory.

The Muon Spectrometer track parameters are determined at the inner stations, which yield the first set of measurements in the Muon Spectrometer. The track is then propagated back to the interaction point and the momentum is corrected for the energy loss in the calorimeters (and in the Inner Detector).

The combination of the stand-alone tracks reconstructed in the Muon Spectrometer with tracks reconstructed in the Inner Detector is performed in the region $|\eta| < 2.5$, which corresponds to the geometrical acceptance of the Inner Detector. This combination will considerably improve the momentum resolution for tracks with $p_{\mathrm{T}} < 100$ GeV, but will also suppress to a certain extent backgrounds from pion punch-through and from pion or kaon decays in flight.

In the case of segment tags, Inner Detector tracks are extrapolated to the inner muon stations and associated to reconstructed muon segments. The muons reconstructed through this procedure provide an important improvement to the stand-alone muon reconstruction for three main reasons:

- at momenta below typically 6 GeV, muon tracks do not always reach the middle and outer muon stations, as Figure 3.1 shows;
- in the barrel/end-cap transition region with $1.1 < |\eta| < 1.7$, the middle stations are missing for the initial data taking and the stand-alone reconstruction efficiency is therefore reduced in this region;

- in the difficult regions at $|\eta| \approx 0$ and in the feet, the geometrical acceptance of the muon stations is considerably reduced.

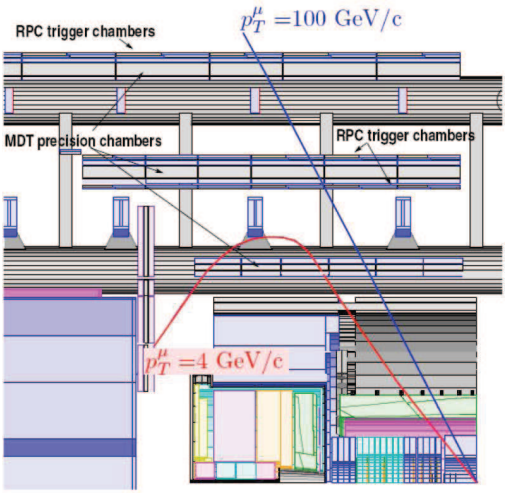

Figure 3.1: Sketch of a low-p_T and a high-p_T muon in ATLAS. Note how the magnetic field bends the low-p_T muon trajectory so that it only goes through the innermost Muon Spectrometer stations.

Figure 3.2 shows the single muon reconstruction efficiency for stand-alone and combined reconstruction, and for the overall combination of these with the segment tags as a function of $|\eta|$ for muons with $p_T = 100$ GeV and as a function of p_T. In this case, the efficiency is defined as the fraction of simulated muons which are reconstructed within a cone of size $\Delta R = 0.2$ of the initial muon.

The efficiency for stand-alone tracks drops to very low values in the region with $|\eta| \approx 0$ because of the large gap for services, in which there are very few muon stations. The stand-alone efficiency also drops substantially close to $|\eta| \approx 1.2$, which corresponds to the barrel/end-cap transition region where several stations are missing. The efficiency for combining stand-alone muon tracks with the Inner Detector is very high in the central region, starts to drop for $|\eta| > 2.0$ and decreases rapidly to 0 for $|\eta| > 2.4$. The segment tags contribute only to a limited extent to the overall efficiency for $1.4 < |\eta| < 2.0$ for muons with high p_T, but as expected, their contribution is substantial for lower p_T values.

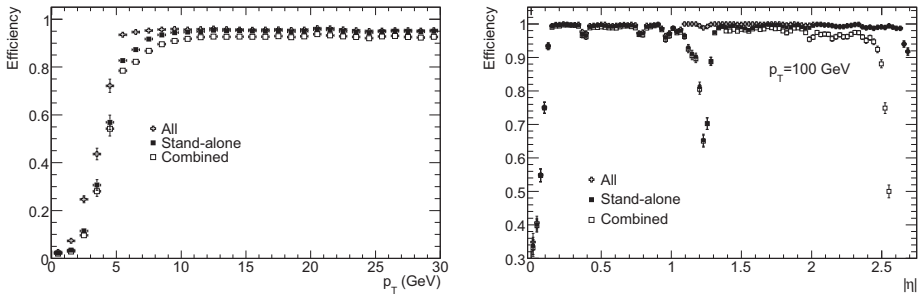

Figure 3.2: Efficiency for reconstructing muons as a function of p_{T} (left) and as a function of $|\eta|$ for $p_{\mathrm{T}} = 100$ GeV (right). The results are shown for stand-alone reconstruction, combined reconstruction and for the combination of these with the segment tags.

3.2 TileMuId Description

The algorithm proposed here for muon identification in TileCal is based on the typical MIP-like energy deposition in the calorimeter together with its geometrical segmentation. As mentioned in Chapter 1, TileCal is divided in three longitudinal samplings (known as A, BC and D layers) and in η-projective towers, as shown in Figure 3.3.

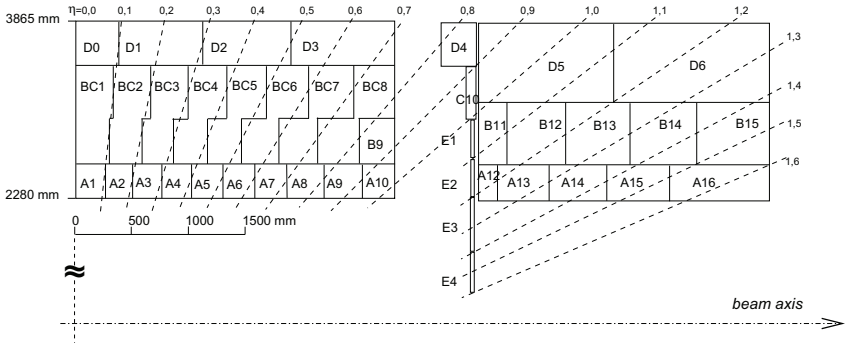

Figure 3.3: Segmentation in depth and η of the TileCal modules.

Since the granularity in the outermost layer is $\Delta\eta \times \Delta\phi = 0.2 \times 0.1$, each cell in the D layer is associated to two different towers in the A and BC layers. Note that

the projectivity of the towers in the extended barrel is not ideal and that the D0 cell is split between the two partitions in the long barrel.

The strategy used to find muons in the calorimeter starts in the outermost layer since this is where cleaner signatures are expected due to the screening effects of the inner layers against low energy hadrons and minimum bias pile-up. If the energy deposition in a D-layer cell is compatible with a MIP, a muon candidate is defined. The condition applied to select whether a MIP-like deposition is found consists of requiring that the cell energy is comprised between a lower and a higher energy thresholds:

$$Thr_{\text{lower}} < E_{\text{cell}} < Thr_{\text{higher}}. \tag{3.1}$$

The lower energy threshold (Thr_{lower}) is meant to discard noise fluctuations or minimum bias pile-up. It is set to three times the electronics noise RMS in the cell. On the contrary, the higher energy threshold (Thr_{higher}) is meant to discard hadronic showers and tails. Due to their different sizes, it is obtained individually for each cell using Monte Carlo data.

The search continues to the BC-layer cells in the two towers associated to the D-cell where the muon candidate is found. In case the condition in Eq. (3.1) is also fulfilled in the BC layer, the corresponding A-layer cell is also checked for a muon-like energy deposition. Finally, if cells in the three layers are found in a projective pattern whose energy depositions can be described by Eq. (3.1), the muon is tagged. The η and ϕ coordinates of the tagged muon are assigned to be the average of the three cells used in the algorithm.

In some cases the muon can go through the transition between the cells in the η direction and therefore leave signal in more than one tower. In consequence, a mechanism is implemented in TileMuId to prevent the same physical muon to be tagged twice in adjacent towers.

Although in TileMuId the condition in Eq. (3.1) is applied by default in the three TileCal layers (approach known as “tight selection”), the user can select to use the so-called “loose selection” instead. In this case, the energy in the three layers is required to be $E_{\text{cell}} > Thr_{\text{lower}}$, but the condition $E_{\text{cell}} < Thr_{\text{higher}}$ is only imposed in

two of the three cells. This way, muons which deposit a large amount of energy in a small volume can be recovered.

3.3 TileMuId Implementation in the ROD DSP

Taking advantage of the high computing capabilities of the ROD DSPs, the TileMuId algorithm has been implemented inside these processors. This way, the algorithm is executed for all the events accepted by Level-1 trigger and its results are encoded in the output data format in a dedicated fragment. Specific software developed inside the Level-2 trigger retrieves the information in those fragments to use it in the HLT environment (see Section 3.4). Although the implementation of the algorithm in the DSP introduces some limitations, its main advantage is the reduction in the computing time required at Level-2.

Due to the fact that each DSP processes only the information from 2 superdrawers sequentially, the main limitation of the ROD-based approach of the algorithm is that in principle it will only be possible to execute it separately in each single superdrawer. Therefore, the algorithm cannot use adjacent superdrawers in the ϕ direction and the LB and EB cells with the same ϕ cannot be combined to tag muons either.

In the DSP, the routine responsible for TileMuId uses the channel energy previously computed inside the processor using the Optimal Filtering algorithm [38]. The cell energy is computed as the sum of the energy in its two PMTs. The fact that the energy is computed in the DSP with a 0.5 MeV and 32 MeV precision for high and low gain, respectively, is taken into account when computing the cell energy.

Bad channels as stored in the TileCal conditions database are used in such a way that if one of the two PMTs in a cell is known to have problems (noisy channels, etc.), the cell energy is estimated to be twice the energy of the remaining PMT. In particular, the two PMTs in the D0 cell are read out by different superdrawers and at the DSP level only one of them can be accessed. In consequence, the D0 cell energy is also estimated to be twice the energy in the available PMT.

TileMuId is then executed using the cell energy computed in the DSP as described in the previous Section and the output is packed in the raw data with the format described below.

3.3.1 Output ROD Data Format Description

After the algorithms are processed inside the ROD DSP, their output is formatted according to the ATLAS data format requirements described in Ref. [39] and sent to the next step in the data acquisition chain. Each DSP PU builds a ROD fragment which is formed by several subfragments containing different types of data and framed by a header and a trailer blocks. The subfragments present in a ROD fragment depends on the run type, in particular the output from the muon tagging algorithm is present by default for Physics runs. Each ROD fragment contains the information from up to 4 superdrawers.

Table 3.1 shows the TileCal ROD fragment used during the detector commissioning phase for cosmics runs. As shown, the present subfragments contain the raw data (Digitizer fragments), the online reconstructed energy (Reco fragments), data quality checks (Status fragments) and the output of the trigger-oriented algorithms for Level-2 (L2 fragments). Apart from TileMuId, the computation of the total transverse energy per superdrawer may also be executed in the DSP for trigger purposes. All the subfragments contain the information corresponding to a single superdrawer, except the L2 fragments which hold the data from the 2 superdrawers processed by the same DSP to allow a faster data access in HLT.

Each of those subfragments starts with a header composed of three 32-bit words. The first word in the header, known as header marker, is set to 0xff1234ff. The second word contains the fragment size (number of words in the whole subfragment, including the header words) and the last word in the header is the fragment identifier which holds the type of fragment and the superdrawers processed.

In the default DSP operation mode, called staging mode, the data coming from 2 superdrawers are processed by a single DSP. There is also the possibility to work in the so-called full mode, where the data from only one superdrawer are processed by a single DSP. Therefore, depending on whether both trigger-oriented algorithms

are selected to be executed or just one of them and the ROD operation mode (staging or full), there are 4 different types of L2 fragments where TileMuId is executed:

- Fragment type 0x10: TileMuId and transverse energy computation enabled, staging mode.
- Fragment type 0x11: TileMuId and transverse energy computation enabled, full mode.
- Fragment type 0x12: TileMuId enabled, staging mode.
- Fragment type 0x13: TileMuId enabled, full mode.

Table 3.1: TileCal ROD fragment data format during commissioning for Physics runs.

Header
Reco fragment (type 0x4) #1
Digitizer fragment (type 0x0) #1
Status fragment (type 0xa) #1
Reco fragment (type 0x4) #2
Digitizer fragment (type 0x0) #2
Status fragment (type 0xa) #2
L2 fragment (type 0x12) #1 #2
Reco fragment (type 0x4) #3
Digitizer fragment (type 0x0) #3
Status fragment (type 0xa) #3
Reco fragment (type 0x4) #4
Digitizer fragment (type 0x0) #4
Status fragment (type 0xa) #4
L2 fragment (type 0x12) #3 #4
Trailer

These four fragments will only be present in the output data if the corresponding algorithms are enabled to be executed online. They are variable-size fragments

sending two 32-bit words per muon found. If the transverse energy computation is also enabled, an additional word per superdrawer with this information is added before the muon data words. Note that the fragments which only store the information from the TileMuId algorithm (0x12 and 0x13) are not present in the bytestream (not even their header) unless muons are actually found. Hence, if one muon is found in the superdrawers read out by one DSP, the fragment will contain 5 words. Table 3.2 shows the structure of one of those fragments.

Table 3.2: Description of a L2 fragment (only TileMuId enabled).

Fragment header (0xff1234ff)
Fragment size ($3+2\times n$)
Fragment identifier
Muon 1, data word 1
Muon 1, data word 2
...
Muon n, data word 1
Muon n, data word 2

Tables 3.3 and 3.4 show the bit field for the fragment identifier word for staging mode and full mode fragments respectively. In both cases the 16 most significant bits (MSB) are dedicated to encode the fragment type (0x10 to 0x13) and the 16 least significant bits (LSB) are used for the TileCal partition (1 for LBA, 2 for LBC, 3 for EBA and 4 for EBC) and the 1 or 2 superdrawers processed. Note that in staging mode, the 6 LSB are used for the first superdrawer and the next 6 bits for the second superdrawer proccessed by the same DSP.

Table 3.3: Bit field for the fragment identifier 32-bit word for staging mode (0x10 and 0x12).

Fragment type	Partition	Drawer #2	Drawer #1
bits 31:16	bits 15:12	bits 11:6	bits 5:0

Table 3.4: Bit field for the fragment identifier 32-bit word for full mode (0x11 and 0x13).

Fragment type	Partition	Drawer
bits 31:16	bits 15:8	bits 7:0

Table 3.5: Description of the first muon data word.

QF	D	Muon pattern	Energy in 3rd layer
bit 31	bit 30	bits 29:25	bits 24:0

Table 3.6: Description of the second muon data word.

Energy in 2nd layer	Energy in 1st layer
bits 31:16	bits 15:0

The bit fields for the two 32-bit muon data words are shown in detail in Tables 3.5 and 3.6. The variables encoded in the muon data words are the following:

- **Quality factor (QF)**: this variable is set to 0 if the muon has been tagged following the tight selection criteria and is set to 1 if tagged following the loose selection criteria, as defined in Section 3.2. The most significant bit in the first muon data word is used to encode this quality factor in the output data format.
- **Superdrawer (D)**: since each DSP can process up to 2 superdrawers, one bit in the muon data words is used to identify in which superdrawer the muon has been found. This bit is set to 0 if the muon has been tagged in the first superdrawer processed by the DSP (i.e., in the Drawer #1 specified in the fragment identifier, see Table 3.3) or it is set to 1 if found in the second superdrawer (Drawer #2 in the fragment identifier, see Table 3.3).
- **Muon pattern**: taking into account the geometrical segmentation of TileCal, a muon produced at the interaction point can go through the calorimeter

following several trajectories. Furthermore, as the projectivity in the cell segmentation is not ideal, cells in different towers can be hit by the same muon. Therefore, we define different projective patterns as a combination of 3 cells, one per layer, as shown in Tables 3.7 and 3.8. The pattern in which the muon has been found is encoded using 5 bits in the first muon data word. During the fragment decoding, the muon η coordinate is computed as the average of the η coordinates from the 3 cells in the pattern. This way, knowing the superdrawer and the muon pattern, the (η, ϕ) position of the muon is perfectly determined.

- **Energy deposited by the muon in each layer**: in addition, this fragment contains the energy released in all the 3 cells used to tag the muon using 25 bits in the first muon data word and the whole second muon data word. The energy stored in those words is expressed in MeV and scaled by a factor 2 in order to have a precision of 0.5 MeV using a fixed-point processor.

Table 3.7: Projective patterns defined in the LB superdrawers. Note that the $\pm N$ references to the N-th η tower.

Muon pattern	D cell	BC cell	A cell	$<\|\eta\|>$
0	D0	BC±1	A±1	0.033
1	D±1	BC±2	A±2	0.167
2	D±1	BC±3	A±3	0.233
3	D±2	BC±4	A±4	0.367
4	D±2	BC±5	A±5	0.433
5	D±2	BC±6	A±6	0.500
6	D±3	BC±6	A±6	0.567
7	D±3	BC±7	A±7	0.633
8	D±3	BC±8	A±8	0.700

Table 3.8: Projective patterns defined in the EB superdrawers. Note that the $\pm N$ references to the N-th η tower.

Muon pattern	D cell	BC cell	A cell	$<\|\eta\|>$
0	D±5	B±11	A±12	1.067
1	D±5	B±12	A±12	1.100
2	D±5	B±12	A±13	1.133
3	D±5	B±13	A±12	1.133
4	D±5	B±13	A±13	1.167
5	D±5	B±13	A±14	1.200
6	D±6	B±11	A±12	1.133
7	D±6	B±12	A±12	1.167
8	D±6	B±12	A±13	1.200
9	D±6	B±13	A±12	1.200
10	D±6	B±13	A±13	1.233
11	D±6	B±13	A±14	1.267
12	D±6	B±14	A±13	1.267
13	D±6	B±14	A±14	1.300
14	D±6	B±14	A±15	1.333
15	D±6	B±15	A±14	1.333
16	D±6	B±15	A±15	1.367

3.4 TileMuId Software Developments

Offline computing in ATLAS covers all processing from storing raw data up to the final analysis, as well as Monte Carlo generation, detector simulation and event display. Athena [40] is the general framework for the ATLAS offline software, based upon the Gaudi [41] architecture. ATLAS software is organized into a hierarchical structure of projects and packages. All packages are stored in an official Subversion (SVN) code management system repository. A project consists of a complete collection of tagged packages and it is identified with a release number.

The StoreGate, which is the ATLAS tool to access the Transient Data Store (TDS), is the main channel of communication among different Athena modules. Each algorithm can create Data Objects (hits, tracks, digits, etc.) and save them into the

StoreGate and any algorithm is able to retrieve data from the StoreGate. Objects are stored in the StoreGate using containers.

The main developments in Athena related to TileMuId are described in this Section and are present in the TileCalorimeter and Trigger container packages.

3.4.1 Developments in TileCalorimeter Package

They include object class definition, fully offline implementation of the algorithm (TileLookForMuAlg) and dedicated code for unpacking the TileMuId information computed at the ROD level.

TileEvent Package

This package contains the two classes developed to hold the TileMuId information:

- **TileMu**: this is the class meant to hold the output from TileMuId computed completely at the offline level. Its data members contain the information for muon coordinates, energy deposited in TileCal and quality factor.
- **TileL2**: this is the class developed to keep the information from the Level-2 algorithms executed in the Tile DSP. One instance of TileL2 is created for each superdrawer in TileCal. It holds variables for the ϕ coordinate of the superdrawer and its fragment identifier from the bytestream, the muon η coordinate, the energy released in each of the TileCal layers and the quality of the identification. It also stores the values of the 32-bit muon data words. Dedicated methods are also provided to obtain the E_{x} and E_{y} from the total E_{T} in the superdrawer.

TileMuId Package

This package was created to run TileMuId offline for muon identification. The main algorithm in this package is the following:

- **TileLookForMuAlg**: this algorithm performs the TileMuId search fully at the offline level, taking as input a TileCellContainer, applying the muon search with those cells and storing the output TileMu objects in a TileMuContainer.
- **CBNTAA_TileMu**: this algorithm is used to store the information in TileMu objects in ROOT ntuples.

TileL2Algs Package

This package is devoted to the algorithms processed at the TileCal ROD DSP for Level-2 trigger purposes, that is, TileMuId and E_{T} computation. The algorithms related to TileMuId which are present in this package are the following:

- **TileL2Builder**: this AlgTool emulates the algorithms processed at the TileCal ROD DSP level to contribute to the Level-2 trigger for simulation studies. It creates TileL2 objects from TileRawChannel (with the energy and time for every channel) and can be called either by TileRawChannelToL2 or TileROD_Decoder (see below). The "process" method is responsible for creating TileL2 objects and store them in a TileL2Container.
- **TileRawChannelToL2**: this algorithm takes as input the TileRawChannelContainer, creates TileL2 objects and stores them in a TileL2Container. It makes use of the TileL2Builder tool to fill the TileL2Container and records it in the Athena StoreGate.
- **CBNTAA_TileMuROD**: this algorithm is used to store the information in TileL2 objects in ROOT ntuples.

TileByteStream Package

This package contains all the software used to decode and encode TileCal bytestream. The pieces of code related to TileMuId are the following:

- **TileL2ContByteStreamCnv**: this converter contains methods to do the conversion from bytestream format to TileL2 objects stored in a TileL2Container and vice versa.

- **TileL2ContByteStreamTool**: this AlgTool, which is called by TileL2ContByteStreamCnv, is used for encoding into bytestream the TileL2 objects stored in a TileL2Container making use of the TileROD_Encoder class (see below).

- **TileROD_Decoder**: this class decodes the different TileCal ROD subfragments present in the bytestream data and fills TileDigitsContainer, TileRawChannelContainer, TileL2Container, etc. In particular, the methods "unpack_frag10", "unpack_frag11", "unpack_frag12" and "unpack_frag13" are used to extract the data in the 0x10, 0x11 0x12 and 0x13 fragment types and with that information creates TileL2 objects to be stored in a TileL2Container. The method called "fillCollectionL2", which is called directly by the trigger algorithm TrigTileRODMuAlg (see below), accesses the ROB fragments and call the corresponding "unpack_fragXX" methods to extract the muon information processed at the DSP. If the input Monte Carlo data used don't contain the TileL2 information, TileL2 objects are created on the fly by means of the TileL2Builder AlgTool.

- **TileROD_Encoder**: this class encodes TileDigits, TileRawChannel and TileL2 objects into bytestream data (fragment types 0x1, 0x2, 0x3, 0x4 and 0x10). In particular, the fragment 0x10 is encoded by means of the method "fillROD10". The purpose of this encoding capabilities is to create bytestream files containing the information from objects present in the StoreGate, for instance, to run HLT algorithms on them.

3.4.2 Developments in Trigger Package

The ATLAS trigger menus are built based on elemental trigger objects (electrons, photons, taus, muons, jets, b-tagged jets, B-physics objects, $E_{\mathrm{T}}^{\mathrm{miss}}$, etc.). Each of these basic objects are defined using a chain of algorithms that are executed sequentially. The algorithms are grouped in two big families:

- **Feature Extraction (FEX) algorithms**: build objects as calorimeter clusters, tracks, etc. They do not reject any event.
- **Hypothesis (HYPO) algorithms**: perform the selection applying cuts on the objects built by the FEX algorithms. The execution of a chain is stopped when a hypothesis algorithm is not satisfied, and the event would be rejected unless it has successfully passed the selection in some other chain.

A chain of algorithms that defines a trigger object is called a "slice" (Egamma trigger slice, Jet trigger slice, etc.). Typically there is a FEX algorithm followed by a hypothesis algorithm. For a given slice the threshold values used to define the cuts are programmable.

Equivalently to the offline case, two different implementations of the TileMuId algorithm are used for trigger within the ATLAS collaboration: TrigTileLookForMuAlg, which is fully executed at Level-2, and TrigTileRODMuAlg, which extracts the muons tagged at the ROD DSPs present in the bytestream for the selection at Level-2. Dedicated code has been developed in three different packages to be used at HLT.

TrigMuonEvent Package

This package contains all the Feature classes for the Muon Trigger Slice. In particular, the classes related to TileMuId are:

- **TileMuFeature**: this class is used to store the TileCal muon candidates provided by TrigTileLookForMuAlg and TrigTileRODMuAlg (see below).
- **TileTrackMuFeature**: this class is used to store the muon candidates obtained from the combination of TileCal and the Inner Detector performed in TrigTileMuFex (see below).

In particular, the TileMuId information in these classes is stored in a TileMuFeatureContainer and a TileTrackMuFeatureContainer, respectively.

TrigTileMuId Package

The implementation of TileMuId to run at the trigger level is done in this package which is part of the TrigAlgorithms container package. In particular, the following algorithms are used:

- **TrigTileLookForMuAlg**: this algorithm, also known as TileLookForMu, inherits from AllTEAlgo base class and uses the RegionSelector service to access the TileCell objects around the Level-1 RoIs over which the TileMuId algorithm is applied. The output of this algorithm is a TileMuFeature containing the information from the muons tagged.
- **TrigTileRODMuAlg**: this algorithm, also known as TileRODMu, inherits from AllTEAlgo base class and accesses the ROB fragments around the Level-1 RoIs to extract the TileMuId information computed at the ROD level. This is done by means of the TileROD_Decoder "fillCollectionL2" method and the corresponding TileMuFeature objects are created.
- **TrigTileMuFex**: this algorithm inherits from FexAlgo base class and is used to combine the TileCal information provided by TrigTileLookForMuAlg or TrigTileRODMuAlg with the Inner Detector tracks provided by ID trigger algorithms such as TrigIDSCAN [42] and TrigSiTrack [43]. The tracks are extrapolated from the ID to the TileCal radius (see below) and are stored in a TileTrackMuFeature object in a TileTrackMuFeatureContainer.

TrigMuonHypo Package

This package contains all the Hypothesis classes for the Muon Trigger Slice holding the final trigger decision. In particular, for TileMuId this is done by:

- **TileMuHypo**: this class, which inherits from the HypoAlgo base class, gets the TileMuFeatureContainer or TileTrackMuFeatureContainer and takes the final trigger decision after applying a p_{T} cut.

3.5 TileMuId Integration in the Muon Slice

The Muon Trigger Slice [44] covers Level-1 trigger simulation as well as Level-2 and EF trigger algorithms. The Muon Trigger Slice is shown schematically in Figure 3.4.

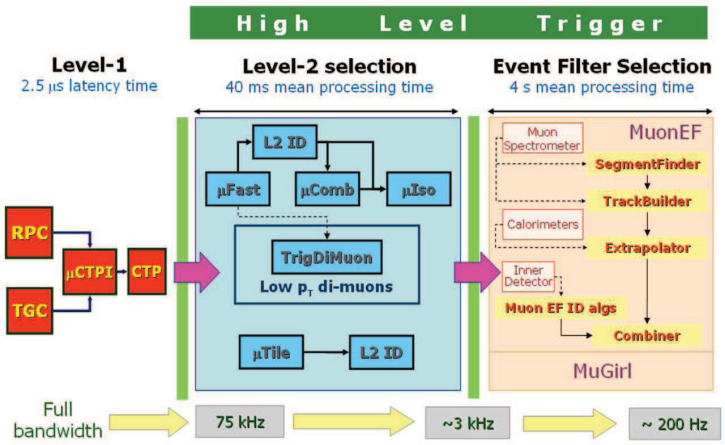

Figure 3.4: Diagram of the Muon Trigger Slice.

The Level-2 algorithms which compose the Muon Trigger Slice are the following:

- **muFast**: this algorithm, which is seeded by the Level-1 RoIs provided by the RPCs and TGCs, reconstructs the muon tracks using the Muon Spectrometer stand-alone information.
- **muComb**: this algorithm, which is seeded by muFast, combines the Muon Spectrometer tracks reconstructed by muFast with the Inner Detector tracks, finds the best matching and improves the η, ϕ and p_{T} resolution. It is used to enhance the accuracy of the muon reconstruction at Level-2 and for K/π rejection.
- **muIso**: this algorithm, which can be seeded either by muFast or muComb, selects isolated muon tracks making use of the calorimeter or Inner Detector information in a cone around the muon direction. It can be used to reject muons from beauty and charm semileptonic decays.

- **muTile**: this algorithm, also known as TileMuId as described in the present Chapter, is seeded by the Level-1 RoIs provided by the RPCs and TGCs, identifies low-p_{T} projective muons in TileCal and performs a matching with the Inner Detector tracks. It is meant for the selection of B-physics channels, like J/ψ and Υ.

The EF algorithms which are part of the Muon Trigger Slice are the following:

- **MuonEF**: this algorithm refines the Level-2 hypotheses using muon offline reconstruction tools starting from the Muon Spectrometer.
- **MuGirl**: this algorithm reconstructs muon candidates in the Muon Spectrometer extrapolating the Inner Detector tracks. One of the aims of this algorithm is the selection of slow particle candidates.

3.6 Overall Performance with Monte Carlo Data

The performance of TileMuId in its two implementations (TrigTileLookForMuAlg and TrigTileRODMuAlg) has been studied with single muon samples and the inclusive $b\bar{b} \rightarrow \mu(6)$X process, where there is at least one muon with $p_{\mathrm{T}} > 6$ GeV in the final state.

The geometrical acceptance of the muon tagging algorithm is limited by the coverage of the TileCal third layer, $|\eta| = 1.4$. For this reason, in this analysis only muons generated in $|\eta| < 1.4$ are considered.

3.6.1 Spatial Resolution

The algorithm spatial resolution has been defined using a sample of single muon events with 2 GeV $\leq p_{\mathrm{T}} \leq$ 15 GeV. In order to compare the reconstructed muon ϕ coordinates with the information from the Monte Carlo truth, which is defined at the vertex, the latter is extrapolated to the TileCal radius, to take into account the

bending by the solenoid magnetic field, using the following parametrization:

$$\phi_{\text{Tile}}(\mu^{\pm}) = \phi_{\text{Truth}}(\mu^{\pm}) \mp 0.000123 \mp \frac{0.507}{p_{\text{T}}(\mu^{\pm})} \tag{3.2}$$

where p_{T} is expressed in GeV and ϕ in rad. This parametrization is extracted using single muon events at different transverse momenta. The numerical factors in Eq. (3.2) are obtained from a fit of $(\phi_{\text{Tile}} - \phi_{\text{Truth}})$ as a function of the muon p_{T}. The average shift with p_{T} in the distribution of residuals $(\phi_{\text{Tile}} - \phi_{\text{Truth}})$ is thus cancelled, as shown in Figure 3.5.

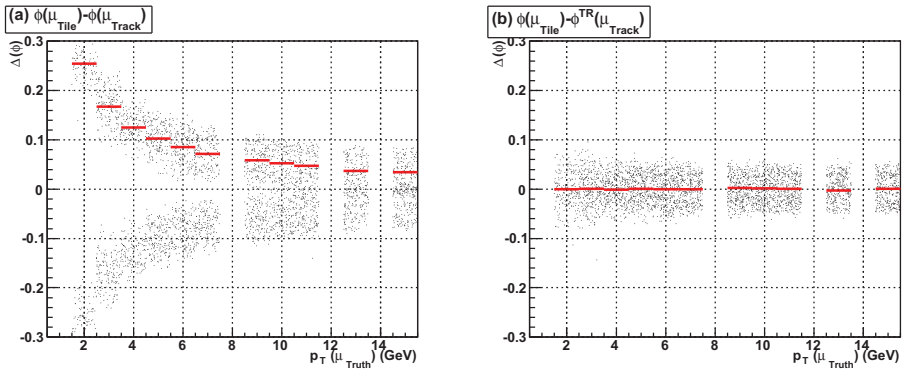

Figure 3.5: Difference between the muon ϕ coordinate provided by TileMuId (ϕ_{Tile}) and the ϕ coordinate of the muon in the truth (left) and after having been extrapolated to the TileCal Radius (ϕ_{TR}) using Eq. (3.2) (right) as a function of the truth muon p_{T}.

The final distributions of residuals, $(\eta_{\text{Tile}} - \eta_{\text{Truth}})$ and $(\phi_{\text{Tile}} - \phi_{\text{Truth}})$, for muons with different momenta are shown in Figure 3.6 for both algorithms, TrigTileLookForMuAlg and TrigTileRODMuAlg. These distributions are used to define the spatial resolution of the algorithm.

Note that the η distribution for TrigTileLookForMuAlg is biased toward positive values due to an unexpected feature of the algorithm, that results in an asymmetry between the positive and negative side. The muons tagged at $|\eta| \simeq 1.4$ are split among two search paths due to the coarse granularity of the detector and the lack of projectivity in the segmentation. Since the direction in the detector scan is fixed from negative to positive η, we pick up mostly one rather than the other of the

two different (but equivalent, since the splitting) paths in the two detector sides. This feature is being corrected for the new releases.

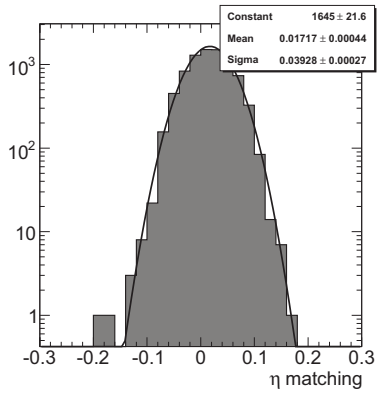

(a) Distribution of residuals in η for TrigTileLookForMuAlg.

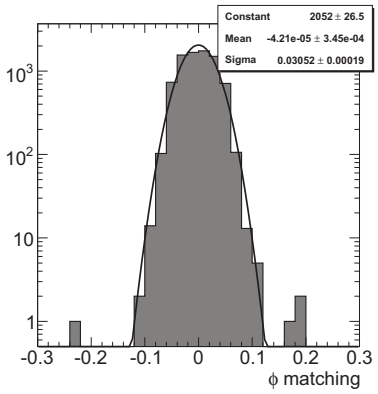

(b) Distribution of residuals in ϕ for TrigTileLookForMuAlg.

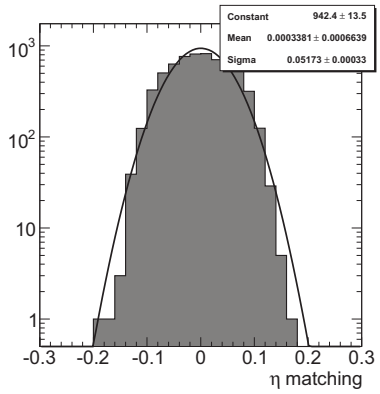

(c) Distribution of residuals in η for TrigTileRODMuAlg.

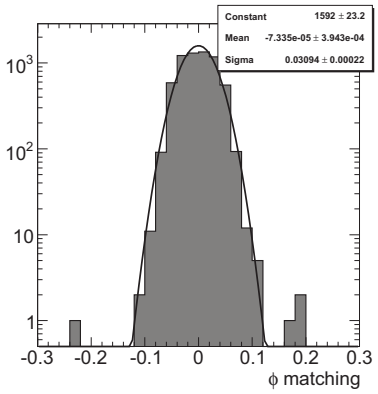

(d) Distribution of residuals in ϕ for TrigTileRODMuAlg.

Figure 3.6: Distribution of residuals between the coordinates of the muons identified by both TileMuId algorithms and the truth muons in the Monte Carlo.

The distributions are fitted with a Gaussian to define an acceptance region (4σ) that will be used to characterize the performance of the algorithm with physics events. Hence, we define an acceptance cone of $\Delta\eta \times \Delta\phi = 0.16 \times 0.12$ for TrigTileLookForMuAlg and of $\Delta\eta \times \Delta\phi = 0.2 \times 0.12$ for TrigTileRODMuAlg. For this analysis and to be able to compare their performance, we use a same cone

size of $\Delta\eta \times \Delta\phi = 0.2 \times 0.12$ for both algorithms. Note that the η resolution is better for TrigTileLookForMuAlg because if the muon energy is also deposited in the neighbouring cells, these cells are taken into account to compute the average η assigned to the tagged muon.

3.6.2 Efficiency

The μ-tagging efficiency is simply defined as the ratio between the number of tagged muons which match a Monte Carlo muon (N_{tag}) over the number of generated muons (N_{gen}):

$$\epsilon = \frac{N_{\text{tag}}}{N_{\text{gen}}}. \tag{3.3}$$

The algorithm efficiency has been computed with Monte Carlo samples of single muons at different values of p_{T} and $b\bar{b} \rightarrow \mu(6)\text{X}$.

The cells in the towers split between TileCal long and extended barrels belong to different partitions and hence are processed by different ROD DSPs. In consequence the muon tagging algorithm cannot be applied at the ROD level for these particular towers. For this reason, as Figure 3.7(a) shows, the TrigTileRODMuAlg efficiency is lower than TrigTileLookForMuAlg at $0.8 \leq |\eta| \leq 1.1$ and therefore its average efficiency is slightly smaller as well. Different performance is also observed for $\eta \sim 0$, as the 2 PMTs reading out the central cell in the outermost layer (D0 cell) are processed by different ROD DSPs. Except for the gap and central regions, both algorithms show an efficiency of $\sim 85\%$ with good agreement. Since TileCal is homogeneous in ϕ, the efficiency is uniform as a function of this coordinate, see Figure 3.7(b).

As shown in Figure 3.7(c), the efficiency decreases as the muon p_{T} decreases for $p_{\text{T}} < 3$ GeV and is about 58% (42%) for TrigTileLookForMuAlg (TrigTileRODMuAlg) at $p_{\text{T}} = 2$ GeV. In fact, most of the muons with $p_{\text{T}} \leq 2$ GeV are stopped in TileCal. For $p_{\text{T}} \geq 4$ GeV, the efficiency is constant in p_{T} with a value of 75% (60%) for TrigTileLookForMuAlg (TrigTileRODMuAlg).

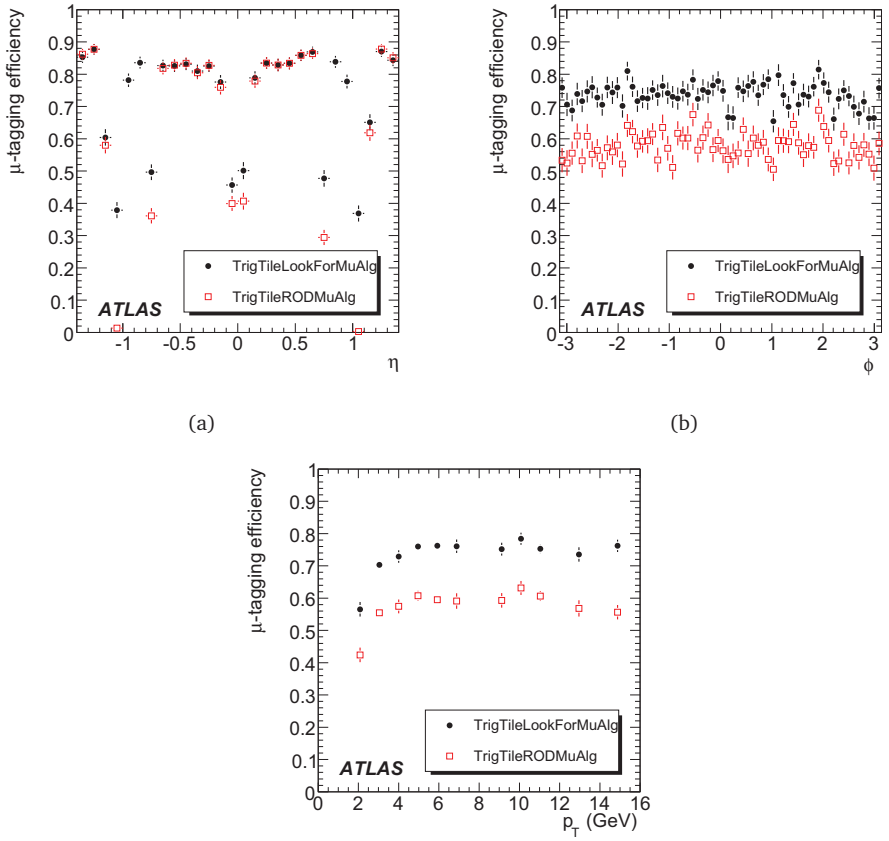

Figure 3.7: Muon tagging efficiency (tight selection) as a function of η, ϕ and p_{T} for single muon events. The performance of TrigTileLookForMuAlg (filled circles) and TrigTileRODMuAlg (open squares) is shown.

Figure 3.8 shows the comparison between the efficiencies of both algorithms for a $b\bar{b} \rightarrow \mu(6)\mathrm{X}$ sample, using the tight selection criteria, as a function of η and p_{T}. Similarly to the single muons case, differences between the efficiency of the algorithms are found in the gap region, leading to a smaller average efficiency in the case of TrigTileRODMuAlg. Figure 3.9 shows the efficiency as a function of the η coordinate and the muon p_{T} for the TrigTileRODMuAlg algorithm distinguishing the cases when the tight and loose selection criteria are used. As expected, the

efficiency increases when applying the loose selection, since the muons with large depositions in a single layer are also identified in this approach. This way, in the region $0.2 \leq |\eta| \leq 0.6$ the efficiency reaches 90%, with no special dependence on the p_T of the particle. Figure 3.10 shows the efficiency of TrigTileLookForMuAlg for this $b\bar{b} \rightarrow \mu(6)X$ process without minimum bias pile-up events and at low luminosity.

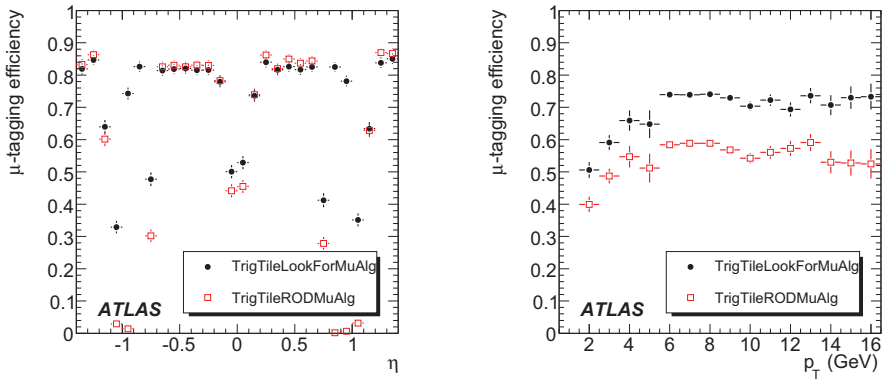

Figure 3.8: Muon tagging efficiency (tight selection) as a function of η (left) and p_T (right) for $b\bar{b} \rightarrow \mu(6)X$ events. The performance of TrigTileLookForMuAlg (filled circles) and TrigTileRODMuAlg (open squares) is shown.

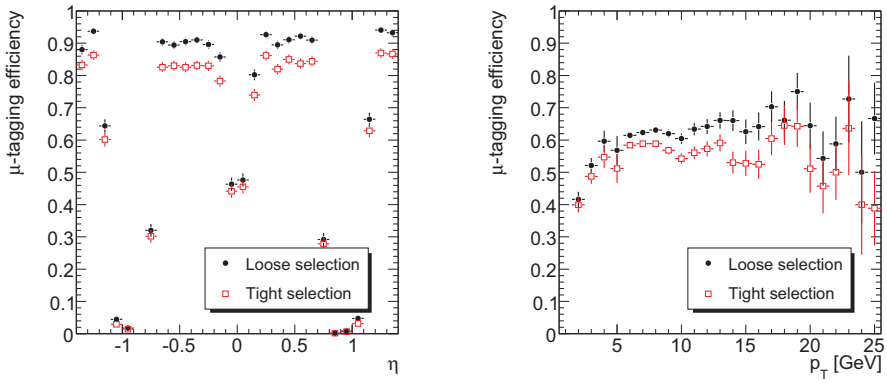

Figure 3.9: Muon tagging efficiency (TrigTileRODMuAlg) as a function of η (left) and p_T (right) for $b\bar{b} \rightarrow \mu(6)X$ events. The performance of the loose selection (filled circles) and the tight selection criteria (open squares) is shown.

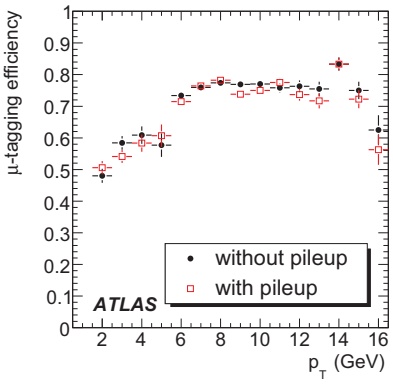

Figure 3.10: Muon tagging efficiency (TrigTileLookForMuAlg) as a function of p_T for $b\bar{b} \rightarrow \mu(6)X$ events. The performance without pile-up (filled circles) and with $\mathscr{L} = 10^{33}$ cm^{-2}s^{-1} minimum bias pile-up (open squares) is shown.

3.6.3 Fraction of Fakes

The fraction of fakes given by the algorithm is computed as:

$$\text{Fraction of fakes} = \frac{\text{Number of misidentified muons}}{\text{Number of events}}. \tag{3.4}$$

Figure 3.11 shows the fraction of fakes as a function of η and ϕ for the inclusive process $b\bar{b} \rightarrow \mu(6)X$, for both algorithms and tight muon identification criteria. Both algorithms present an average fraction of fakes less than 0.12% per tower in the long barrel region ($|\eta| < 0.7$). The largest fraction of fakes corresponds to the extended barrel region, where the cells are bigger and the projectivity is worse. In particular, TrigTileLookForMuAlg shows a significant contribution coming from the gap region, where TrigTileRODMuAlg cannot be applied, leading to a larger average fraction of fakes for the former. As expected, the fraction of misidentified muons as a function of ϕ is a flat distribution.

Figure 3.12 shows the fraction of fakes for TrigTileRODMuAlg for the loose and tight selection criteria as a function of the η and ϕ coordinates. Larger fraction of fakes is found with the loose selection in all calorimeter towers and modules, but especially in the extended barrel region. In consequence, the improvement in

the efficiency obtained with the loose selection is shown to be associated with an increase in the fraction of fakes. Results on the fakes induced by $t\bar{t}$ samples are discussed in Section 3.7.1.

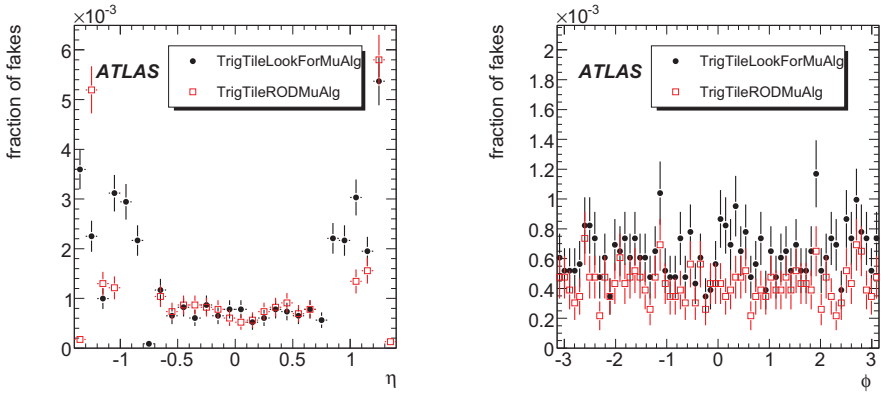

Figure 3.11: Fraction of fakes (tight selection) as a function of η (left) and ϕ (right) for $b\bar{b} \rightarrow \mu(6)$X events. The comparison between TrigTileLookForMuAlg (filled circles) and TrigTileRODMuAlg (open squares) is shown.

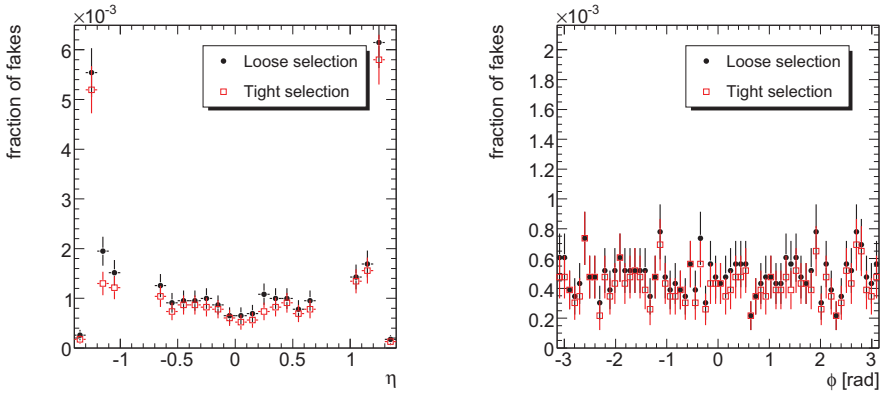

Figure 3.12: Fraction of fakes (TrigTileRODMuAlg) as a function of η (left) and ϕ (right) for $b\bar{b} \rightarrow \mu(6)$X events. The comparison between the loose selection (filled circles) and the tight selection criteria (open squares) is shown.

Figure 3.13 compares the fraction of mistags for TrigTileLookForMuAlg using the tight selection criteria without pileup and the same results with minimum bias pileup at low luminosity.

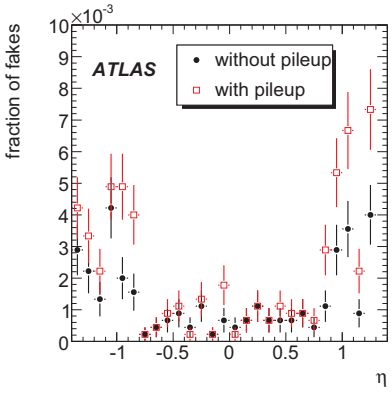

Figure 3.13: Fraction of fakes (TrigTileLookForMuAlg) as a function of η for $b\bar{b} \rightarrow \mu(6)$X events. The performance without pile-up (filled circles) and with $\mathscr{L} = 10^{33}$ cm^{-2}s^{-1} minimum bias pile-up (open squares) is shown.

3.6.4 Summary

The overall performance of the Tile muon tagging algorithm has been presented in this Section for both implementations of the algorithm (TrigTileLookForMuAlg and TrigTileRODMuAlg) and the two selections defined (tight and loose) using Monte Carlo samples of single muons and the inclusive $b\bar{b} \rightarrow \mu(6)$X process. Table 3.9 summarizes the efficiencies and fraction of fakes found for this B-physics process for both algorithms.

Table 3.9: Performance of both algorithms for the inclusive process $b\bar{b} \rightarrow \mu(6)$X.

	Efficiency (%)		Fraction of fakes (%)	
	Tight selection	Loose selection	Tight selection	Loose selection
TileLookForMu	71.8 ± 0.4	82.5 ± 0.3	4.08 ± 0.14	5.96 ± 0.17
TileRODMu	56.9 ± 0.4	61.6 ± 0.4	2.74 ± 0.11	3.14 ± 0.12

3.7 High Level Trigger Performance with Monte Carlo Data

All the results shown so far have been obtained making use of the information from the whole calorimeter to detect muons with TileMuId. Nevertheless, the HLT framework is designed to run over Regions of Interest (RoIs) found at Level-1. This Section will discuss the performance of TileMuId in this execution mode as well as in combination with the Inner Detector. Results obtained under minimum bias pile-up are also shown. Finally, the TileMuId trigger chains defined in the trigger menu are described.

3.7.1 Data Access

The Level-1 trigger in the Muon Spectrometer is based on the Resistive Plate Chambers (RPCs) in the barrel and Thin Gap Chambers (TGCs) in the end-caps. The RPC-based system covers the pseudorapidity range $|\eta| < 1.05$, while the TGC-based system covers $1.05 < |\eta| < 2.4$.

As illustrated in Figure 3.14, the Level-1 trigger is based on three trigger stations. Two stations are used for low-p_{T} muon triggers (threshold range approximately 6-10 GeV), while the third station is used in addition for high-p_{T} triggers (threshold range approximately 8-35 GeV).

As mentioned in Chapter 1, the reconstruction at Level-2 trigger is seeded by Level-1 RoIs with access to the full detector granularity. The size of the RoI is determined by the Level-2 algorithms depending on the type of object to be triggered. Level-2 requests only require a small fraction of the detector data, reducing the network data traffic and the bandwidth needed. This way, the RoI mechanism is used to minimize the amount of data needed to successfully provide trigger decisions. Within each RoI, Level-2 algorithms reconstruct physics objects using fast algorithms which use detector information from individual subsystems. Therefore, additional rejection and higher purity can be obtained with the combination of data from different subdetectors.

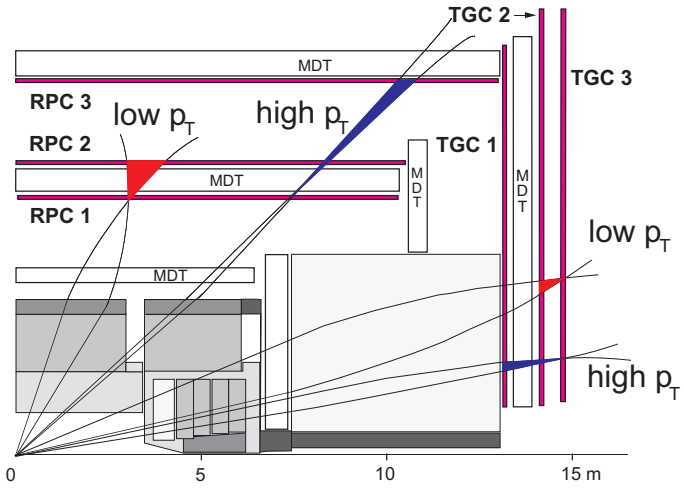

Figure 3.14: Longitudinal view of the end-cap and barrel muon trigger systems.

As already mentioned, the data processed in each ROD are sent to a ROB. The ROBs store the data fragments until they are requested by Level-2 or the Event Builder (EB). While Level-2 only requests a limited amount of data fragments, the EB will request fragments from the whole detector for events approved by Level-2 for subsequent processing in the EF computer nodes.

In full scan mode the TileMuId algorithms access the fragments from all the Tile ROBs on receipt of a Level-1 accept. Unfortunately, the fact that data from the whole detector are requested can cause network load problems when running online in the HLT. In order to access a limited amount of cells or Tile ROB fragments, information only from Level-1 muon RoIs can be used.

As said in Section 3.4.2, TrigTileLookForMuAlg extracts the TileCells information in the Tile ROBs with the RegionSelector package which provides access to the detector data in a given region of $\eta_{\mathrm{RoI}} \pm \Delta\eta$ and $\phi_{\mathrm{RoI}} \pm \Delta\phi$. Since low-$p_{\mathrm{T}}$ charged particles are strongly affected by the magnetic field, as shown in Section 3.6.1, a safe value of $\Delta\phi = 0.2$ rad is chosen. Optimization studies showed that a value of $\Delta\eta = 0.3$ provides similar efficiency to the full scan mode. Therefore an RoI size of $\Delta\eta \times \Delta\phi = 0.3 \times 0.2$ is chosen for this algorithm.

On the contrary, TrigTileRODMuAlg extracts the information from Tile ROB fragments, where one ROB fragment contains four Tile superdrawers. Therefore the minimum accessible granularity when requesting Tile ROB fragments is 0.4 rad in ϕ with the η range covering a whole TileCal partition ($0 \leq |\eta| \leq 0.9$ for LBA and LBC, and $0.7 \leq |\eta| \leq 1.7$ for EBA and EBC). In this case, the $\Delta\eta \times \Delta\phi = 0.1 \times 0.1$ is used for ROB requests, noting that the actual portion of the detector data accessed is much larger.

Figures 3.15 and 3.16 show the number of Level-1 muon RoIs and Tile ROB fragments accessed for different physics processes ($b\bar{b} \rightarrow \mu(4)$X and $t\bar{t}$). As shown, more RoIs are opened in the $t\bar{t}$ case since more muons can be produced from W or b decays. Note that the number of events with no muon RoI (44%) corresponds well to the expected 43% of the cases where no muon is present in the final state for the $t\bar{t}$ decay process. In consequence, the number of ROB fragments accessed by TrigTileRODMuAlg is higher for $t\bar{t}$ (2.6 in average) than for $b\bar{b} \rightarrow \mu(4)$X (1.8).

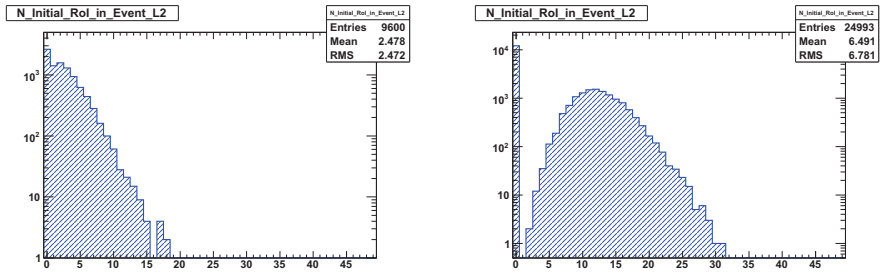

Figure 3.15: Level-1 RoI multiplicity in $b\bar{b} \rightarrow \mu(4)$X (left) and $t\bar{t}$ (right) events.

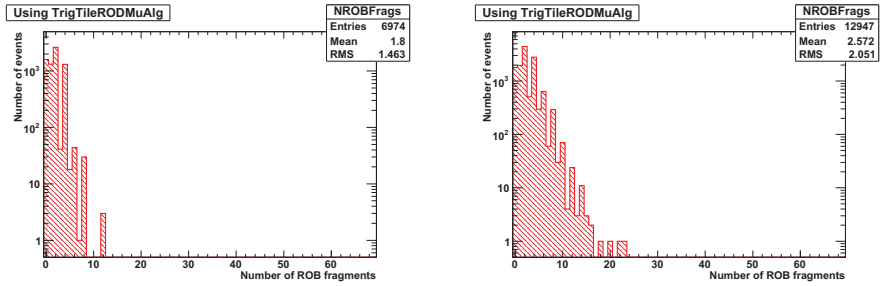

Figure 3.16: Number of Tile ROB fragments accessed by TrigTileRODMuAlg in $b\bar{b} \rightarrow \mu(4)$X (left) and $t\bar{t}$ (right) events.

Figure 3.17 shows the (η, ϕ) coordinates of the RoIs for the muons triggered at Level-1 which are not tagged by TileMuId for $b\bar{b} \rightarrow \mu(6)$X events. Level-1 RoIs cannot be confirmed by TrigTileRODMuAlg in the gap region $0.8 \leq |\eta| \leq 1.1$ and at $|\eta| > 1.4$. Regarding the RoIs in the central barrel region, $|\eta| < 0.7$, ~83% of events were accepted by TileMuId. It is also observed that the fraction of fakes when running seeded by Level-1 RoIs is a 17.4% lower than in full scan mode for $t\bar{t}$ events, while the difference between the two running modes is negligible for $b\bar{b} \rightarrow \mu(6)$X events.

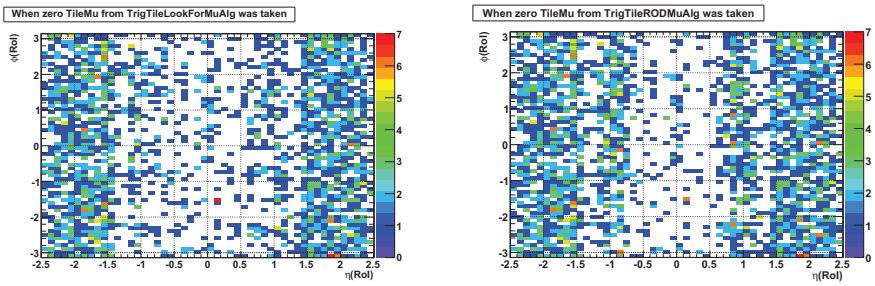

Figure 3.17: Correlation between the η_{RoI} and ϕ_{RoI} coordinates for the RoIs where no muon is found by TrigTileLookForMuAlg (left) and TrigTileRODMuAlg (right) for $b\bar{b} \rightarrow \mu(6)$X events.

Figures 3.18 and 3.19 shows the correlation in η and ϕ between the Level-1 muon RoIs and the muons tagged by the two TileMuId versions, showing a very good agreement. Again in this case, the efficiency of muons tagged by TrigTileRODMuAlg is affected in the gap region between LB and EB.

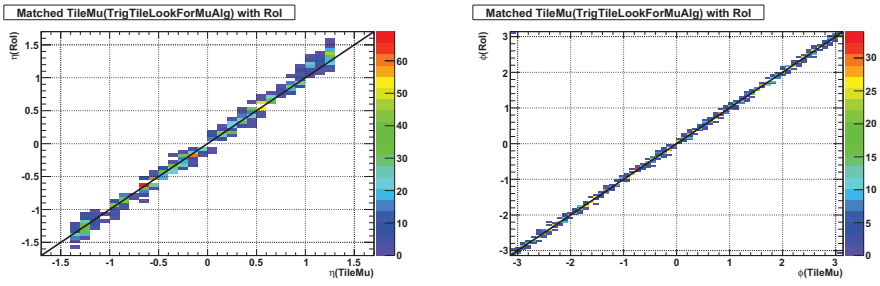

Figure 3.18: Correlation between the coordinates of the Level-1 muon RoIs and the muons tagged by TrigTileLookForMuAlg for $b\bar{b} \rightarrow \mu(6)$X events.

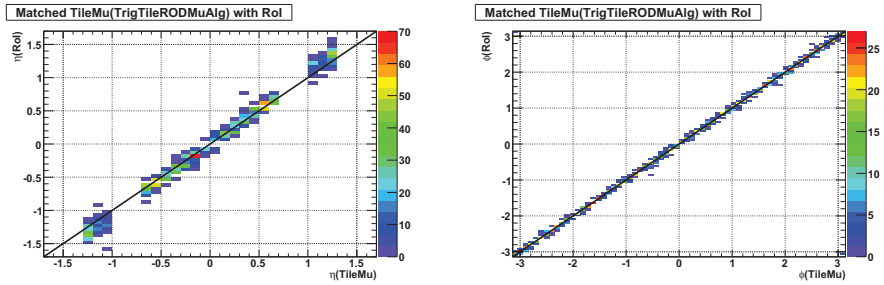

Figure 3.19: Correlation between the coordinates of the Level-1 muon RoIs and the muons tagged by TrigTileRODMuAlg for $b\bar{b} \rightarrow \mu(6)$X events.

Figures 3.20 and 3.21 shows the difference between running the algorithm performing a full scan search and seeded by Level-1 RoIs for $b\bar{b} \rightarrow \mu(4)$X and $t\bar{t}$ events. The number of muons tagged as a function of η and ϕ is shown.

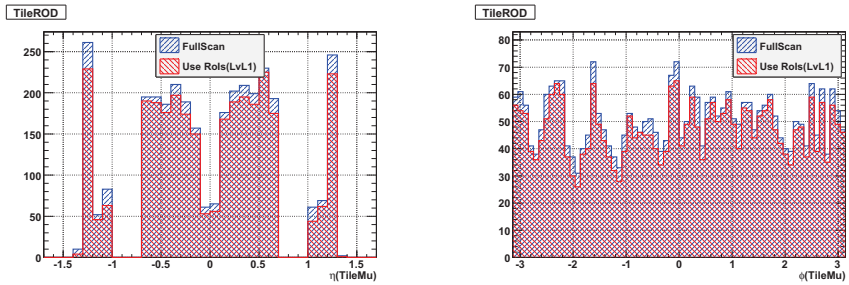

Figure 3.20: Number of muons tagged by TrigTileRODMuAlg as a function of η (left) and ϕ (right) for $b\bar{b} \rightarrow \mu(4)$X events.

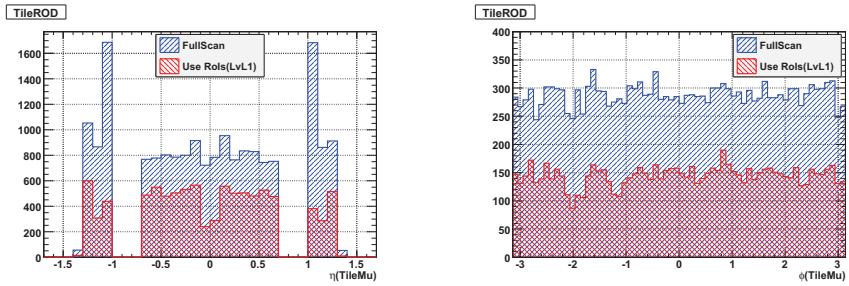

Figure 3.21: Number of muons tagged by TrigTileRODMuAlg as a function of η (left) and ϕ (right) for $t\bar{t}$ events.

As shown in the figures, significant differences are observed between $b\bar{b} \rightarrow \mu(4)$X and $t\bar{t}$ events. Only 4% of the muons found performing a full scan search fail to be detected when the algorithm is run seeded by Level-1 RoIs in $b\bar{b} \rightarrow \mu(4)$X events, but this fraction increases to about 24% in $t\bar{t}$ events . Indeed, the muons which are only detected in full scan mode are predominantly from the loose selection, as shown in Figures 3.22 and 3.23.

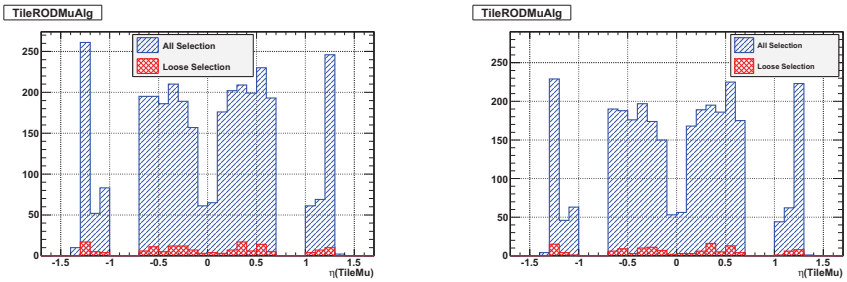

Figure 3.22: Number of muons tagged by TrigTileRODMuAlg as a function of η running on full scan mode (left) and seeded by Level-1 RoIs (right) for $b\bar{b} \rightarrow \mu(4)$X events.

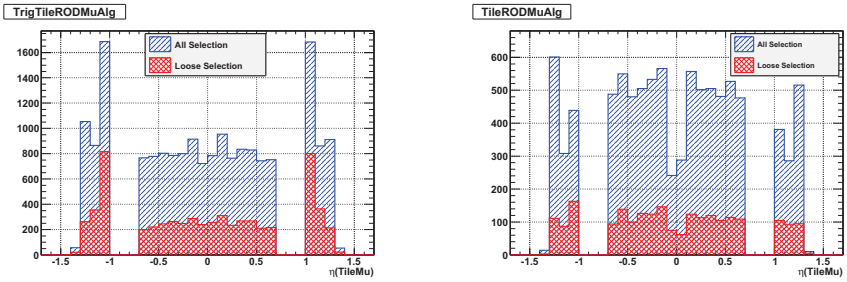

Figure 3.23: Number of muons tagged by TrigTileRODMuAlg as a function of η running on full scan mode (left) and seeded by Level-1 RoIs (right) for $t\bar{t}$ events.

The reduction in the number of events triggered when the algorithm is run seeded by Level-1 RoIs comes from a reduction of the fake tags in the algorithm originated from the hadronic activity in the $t\bar{t}$ process. Therefore, the search based on Level-1 RoIs, since it is not only based on TileCal, can reduce the fraction of

fake muons finally obtained with the algorithm. Note that the number of muons obtained running on the RoIs is relatively smaller at $\eta \approx 0$ (where the Muon Spectrometer efficiency is reduced) and at $-2.3 \leq \phi \leq -1.7$ rad and $-1.4 \leq \phi \leq -0.9$ rad (where the magnet support structures are and therefore some RPC stations are missing).

In summary, very similar performance is obtained when running on the Level-1 RoIs instead of running with a full scan search for the $b\bar{b}$ sample, with a reduced fraction of fakes. Most of the difference between both running modes comes from the loose selection, as shown with the $t\bar{t}$ sample. In consequence, muon search based on Level-1 RoIs is selected for the TileMuId trigger chains considering only the tight muon selection criteria.

3.7.2 Combination with the Inner Detector

As mentioned above, TrigTileMuFex compares the TileCal muon candidates with the Inner Detector tracks. This FEX algorithm looks at all the tracks within a cone around the muon tagged in TileCal. Once the correction in Eq. (3.2) is applied to the track ϕ to extrapolate it to the TileCal radius, the closest track is selected as the best matched track for a muon tagged in TileCal.

Figure 3.24 shows the ID track multiplicity within the matching cone for $b\bar{b}$ events without pile-up and with $\mathscr{L} = 10^{33}$ cm^{-2}s^{-1} minimum bias pile-up. When comparing different $\Delta\phi$ values in Figure 3.24(left), note that for the case with $\Delta\phi = 0.1$ rad the chances to miss the muon track are higher since more events show no track within the matching cone compared to $\Delta\phi = 0.2$ rad. Regarding $\Delta\eta$, the increase from $\Delta\eta = 0.1$ to $\Delta\eta = 0.2$ does not improve the track matching performance. Therefore, with a cone size of $\Delta\eta \times \Delta\phi = 0.1 \times 0.2$ dominantly a single track within the matching cone is found and the ambiguity which could be introduced by the presence of several tracks is minimized. As shown in Figure 3.24(right) the number of tracks is not strongly affected by the presence of minimum bias pile-up.

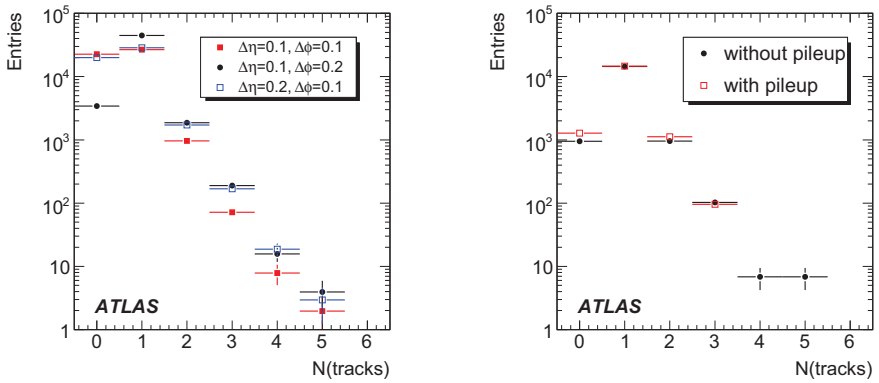

Figure 3.24: On the left, number of ID tracks found within the matching cone for different cone sizes in $b\bar{b} \rightarrow \mu(4)$X events. On the right, number of ID tracks found within the matching cone for a fixed cone size ($\Delta\eta \times \Delta\phi = 0.1 \times 0.2$) in $b\bar{b} \rightarrow \mu(6)$X events without pile-up and with $\mathscr{L} = 10^{33}$ cm^{-2}s^{-1} minimum bias pile-up.

However, if this study is repeated for dijet samples (see Figure 3.25), higher track multiplicities are obtained with respect to $b\bar{b}$ processes for a fixed cone size. Track multiplicity also increases significantly with the matching cone size and the p_{T} of the leading jet as well.

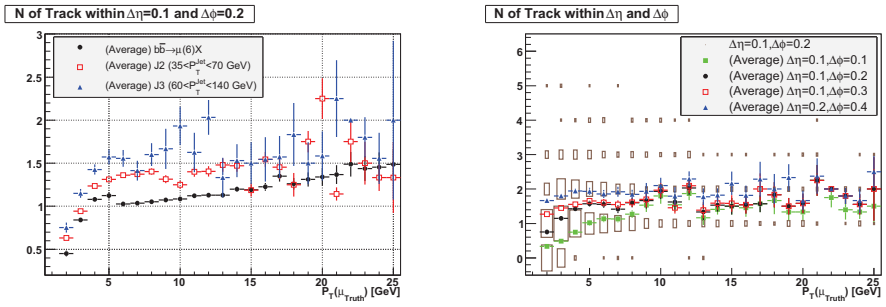

Figure 3.25: Average track multiplicity as a function of $p_{\mathrm{T}}(\mu_{\mathrm{Truth}})$ in $b\bar{b} \rightarrow \mu(6)$X and dijet samples for a fixed matching cone size of $\Delta\eta \times \Delta\phi = 0.1 \times 0.2$ (left) and for variable cone size in J3 ($70 < p_{\mathrm{T}}^{\mathrm{jet}} < 140$ GeV) sample (right).

Figure 3.26 shows the muon tagging efficiency of TrigTileLookForMuAlg stand-alone and in combination with the Inner Detector for two different matching cone sizes: $\Delta\eta \times \Delta\phi = 0.1 \times 0.1$ and $\Delta\eta \times \Delta\phi = 0.1 \times 0.2$.

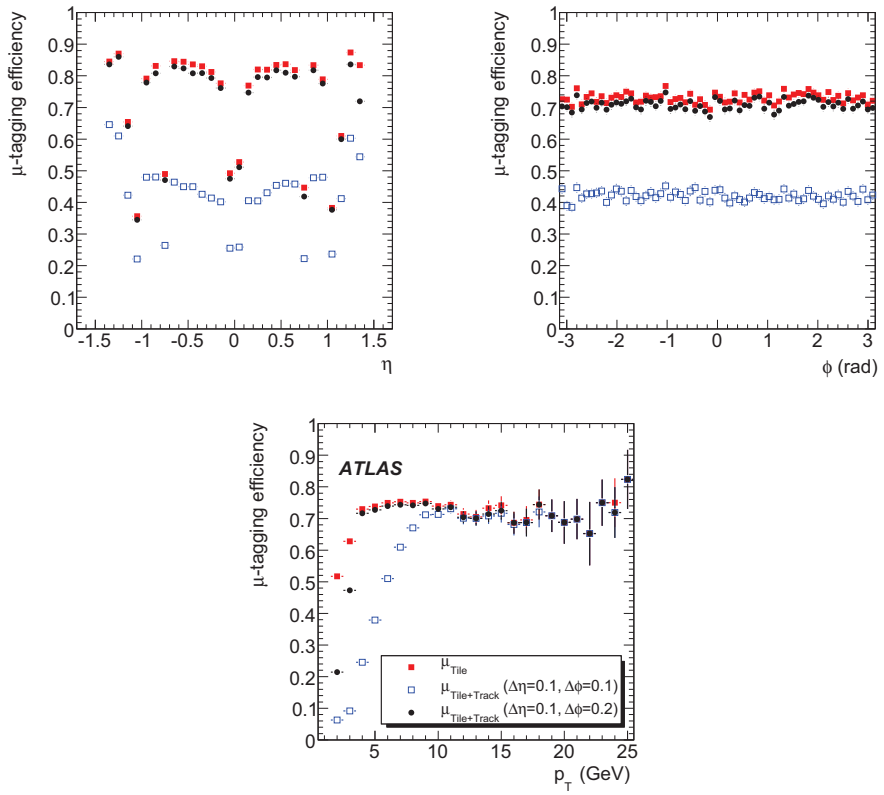

Figure 3.26: Efficiencies as a function of η (top-left), ϕ (top-right) and p_{T} (bottom) for $b\bar{b} \rightarrow \mu(4)\mathrm{X}$ events. Results are shown for TrigTileLookForMuAlg stand-alone (tight selection) and in combination with the Inner Detector tracks for a matching cone size of $\Delta\eta \times \Delta\phi = 0.1 \times 0.1$ and $\Delta\eta \times \Delta\phi = 0.1 \times 0.2$.

The efficiency obtained when matching ID tracks with $\Delta\phi = 0.1$ rad is significantly lower than before the matching for $p_{\mathrm{T}} < 10$ GeV as expected from Figure 3.24. However the efficiency for $\Delta\phi = 0.2$ rad is very similar to TileCal stand-alone with discrepancies only for $p_{\mathrm{T}} < 3.5$ GeV. No bias is found as a function of η or ϕ.

Table 3.10 summarizes the efficiency, fraction of unmatched tags and purity using different matching cone sizes for each process. The fraction of unmatched tags is defined as:

$$\text{Fraction of unmatched tags} = \frac{\text{Number of tags not matched to ID tracks}}{\text{Number of tagged muons}} \tag{3.5}$$

and the purity is defined as:

$$\text{Purity} = \frac{\text{Number of tags matched to MC truth}}{\text{Number of tagged muons}}. \tag{3.6}$$

As shown in the Table, the efficiency and purity are significantly improved when moving from $\Delta\phi = 0.1$ to $\Delta\phi = 0.2$ rad, but no additional improvement is obtained if $\Delta\phi = 0.3$ rad is used. The deterioration caused by minimum bias pile-up is observed to be only about 2-3%.

Table 3.10: Trigger performance in terms of efficiency, fraction of unmatched tags and purity for TrigTileLookForMuAlg and different matching cone sizes in $b\bar{b} \rightarrow \mu(6)$X samples.

	Matching cone size ($\Delta\eta \times \Delta\phi$)		
	(0.1×0.1)	(0.1×0.2)	(0.1×0.3)
$b\bar{b} \rightarrow \mu(6)$X			
Efficiency (%)	59.59 ± 0.19	71.21 ± 0.17	72.43 ± 0.17
Unmatched μ_{Tile} (%)	18.68 ± 0.21	2.81 ± 0.08	1.15 ± 0.05
Efficiency for $p_{\text{T}} > 6$ GeV (%)	63.44 ± 0.19	73.55 ± 0.17	73.70 ± 0.17
Purity for $p_{\text{T}} > 6$ GeV (%)	98.92 ± 0.71	98.90 ± 0.66	98.85 ± 0.66
$b\bar{b} \rightarrow \mu(6)$X with $\mathscr{L} = 10^{33}$ cm^{-2}s^{-1} pile-up			
Efficiency (%)	57.92 ± 0.83	67.94 ± 0.79	68.93 ± 0.78
Unmatched μ_{Tile} (%)	16.86 ± 0.90	2.49 ± 0.32	1.06 ± 0.21
Efficiency for $p_{\text{T}} > 6$ GeV (%)	61.32 ± 0.86	70.08 ± 0.80	70.39 ± 0.80
Purity for $p_{\text{T}} > 6$ GeV (%)	99.16 ± 3.22	99.05 ± 2.98	99.05 ± 2.99

Summing up, taking into account the performance which can be obtained and in order to minimize, on one hand, the processing time needed to reconstruct the tracks within the selected cone and, on the other hand, the ambiguity from the

presence of several tracks, a cone size of $\Delta\eta \times \Delta\phi = 0.1 \times 0.2$ is selected for Inner Detector track matching with TileMuId muon candidates.

Results Combining Different Inner Detector Trigger Algorithms

Two algorithms have been developed by the ATLAS collaboration for track reconstruction in the HLT environment. The first one, TrigSiTrack, makes use of a combinatorial pattern recognition approach to reconstruct tracks starting from space points formed in the SCT while the second, TrigIDSCAN, also includes the information from the Pixel Detector.

Table 3.11 shows the average track multiplicity, track matching efficiency and p_{T} resolution for $b\bar{b}$ and $t\bar{t}$ samples at different luminosity scenarios.

Table 3.11: Average track multiplicity, track matching efficiency and p_{T} resolution for TrigTileLookForMuAlg using TrigIDSCAN and TrigSiTrack algorithms in $b\bar{b} \rightarrow \mu(4)$X and $t\bar{t}$ samples.

	$< N_{\mathrm{Tracks}} >$	$\mathrm{Efficiency}_{\mathrm{Track}}$	$p_{\mathrm{T}}^{\mathrm{Track}} - p_{\mathrm{T}}^{\mathrm{Truth}}$ (GeV)
$b\bar{b} \rightarrow \mu(4)$X			
TrigIDSCAN	1.27 ± 0.66	0.94 ± 0.27	0.006 ± 0.35
TrigSiTrack	1.29 ± 0.73	0.90 ± 0.30	0.004 ± 0.27
$t\bar{t}$ (14 TeV) without pile-up			
TrigIDSCAN	2.34 ± 2.08	0.91 ± 0.29	1.14 ± 2.35
TrigSiTrack	3.03 ± 2.82	0.90 ± 0.31	1.16 ± 2.40
$t\bar{t}$ (10 TeV) with pile-up (450 ns)			
TrigIDSCAN	2.29 ± 2.02	0.89 ± 0.32	1.03 ± 2.16
TrigSiTrack	3.07 ± 2.96	0.90 ± 0.30	1.03 ± 2.16
$t\bar{t}$ (10 TeV) with pile-up (75 ns)			
TrigIDSCAN	2.41 ± 2.13	0.85 ± 0.36	1.11 ± 2.33
TrigSiTrack	3.20 ± 3.09	0.88 ± 0.32	1.16 ± 2.36
$t\bar{t}$ (10 TeV) with pile-up (25 ns)			
TrigIDSCAN	2.50 ± 2.09	0.77 ± 0.42	1.17 ± 2.42
TrigSiTrack	3.38 ± 3.12	0.86 ± 0.35	1.19 ± 2.44

As shown, TrigSiTrack provides more tracks within the cone and therefore introduces higher ambiguity for the proper track selection. Although TrigSiTrack matching efficiency is higher for $t\bar{t}$ samples, their p_{T} resolution is slightly worse due to tracks wrongly matched. For $b\bar{b}$ samples, these two algorithms provide similar efficiency and performance. Therefore, as default, the TrigIDSCAN algorithm is selected to be used in combination with TileMuId for the LHC initial run.

3.7.3 Trigger Chains Based on TileMuId

The trigger chains based on TileMuId, which are included in the early running menu ($\mathscr{L} = 10^{31}$ cm^{-2}s^{-1}), are summarized in Table 3.12. The mu4_tile chain is based on TrigTileLookForMuAlg and mu4_trod is based on TrigTileRODMuAlg. Except for the TileMuId algorithm used, the rest of the elements in the trigger sequence are the same in both cases. At Level-2, muons from TileCal are matched with the Inner Detector tracks. Therefore, the trigger result from EF_mu4_tile or EF_mu4_trod implies the global matching muons with TileCal, Inner Detector and the Muon System.

Table 3.12: TileMuId trigger sequences included in the $\mathscr{L} = 10^{31}$ cm^{-2}s^{-1} trigger menu.

	mu4_tile	mu4_trod
L1	L1_MU4	L1_MU4
L2	TrigTileLookForMuAlg_L2	TrigTileRODMuAlg_L2
	TrigIDSCAN_Tile	TrigIDSCAN_TROD
	TrigTileMuFex_900GeV	TrigTileMuFex_900GeV_TROD
	TileMuHypo_900GeV_4GeV	TileMuHypo_900GeV_4GeV_TROD
EF	EFID_mu4_tile	EFID_mu4_trod
	MS_mu4_tile	MS_mu4_trod
	TB_mu4_tile	TB_mu4_trod
	SA_mu4_tile	SA_mu4_trod
	EF_mu4_tile	EF_mu4_trod

3.7.4 Rates

The rates for the trigger sequences are estimated at a luminosity of 10^{31} cm^{-2}s^{-1} using 10 TeV "enhanced" bias samples with Athena releases 14.5.0.3 (running on full scan mode) and 15.0.0 (running seeded by Level-1 RoIs). The enhanced bias sample contains minimum bias events with a filter using the Level-1 trigger so that a reduced dataset is produced to compute the rates more efficiently. The values obtained for the rates are summarized in Tables 3.13 and 3.14. With a prescale factor of 5 for Level-2 and 50 for EF, their rates are readjusted to ∼1 Hz which is suitable for the timing latency of TDAQ.

Table 3.13: Trigger rates computed for 3×10^6 10 TeV enhanced bias events at $\mathscr{L} = 10^{31}$ cm^{-2}s^{-1} using release 14.5.0.3 (running on full scan mode).

Signature	Prescale	# Evts accepted	Rate (Hz)
L1_MU4	1	5456	1200 ± 16
L2_mu4_tile	5	397	17.4 ± 0.9
L2_mu4_trod	5	349	15.3 ± 0.8
EF_mu4_tile	50	306	1.34 ± 0.08
EF_mu4_trod	50	282	1.24 ± 0.07

Table 3.14: Trigger rates computed for 3×10^6 10 TeV enhanced bias events at $\mathscr{L} = 10^{31}$ cm^{-2}s^{-1} using release 15.0.0 (running seeded by Level-1 RoIs).

Signature	Prescale	# Evts accepted	Rate (Hz)
L1_MU4	1	4880	1060 ± 15
L2_mu4_tile	5	329	14.3 ± 0.8
L2_mu4_trod	5	262	11.4 ± 0.7
EF_mu4_tile	50	297	1.29 ± 0.07
EF_mu4_trod	50	234	1.01 ± 0.07

3.7.5 Performance with Pile-up and Cavern Background

As luminosity increases, larger contributions from the minimum bias pile-up and cavern background are expected and the number of muons tagged by TileMuId in-

creases due to the fake muons from the hadronic activity involved. These muons will more likely fail to match the related ID tracks and therefore, the track matching efficiency decreases for the samples affected by a harder minimum bias environment.

Figure 3.27 shows the number of events tagged for $t\bar{t}$ processes including minimum bias pile-up and cavern background. The events are simulated for $\mathscr{L} = 10^{32}$ cm^{-2}s^{-1} with a bunch crossing of 450 ns, for $\mathscr{L} = 10^{33}$ cm^{-2}s^{-1} with a bunch crossing of 75 ns and for $\mathscr{L} = 2 \times 10^{33}$ cm^{-2}s^{-1} with a bunch crossing of 25 ns.

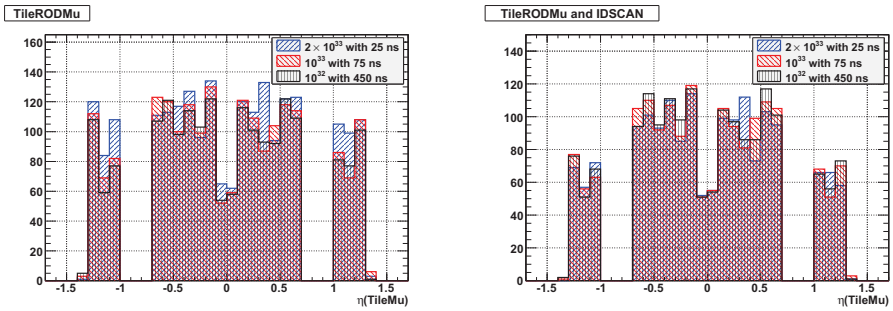

Figure 3.27: Number of muons tagged by TrigTileRODMuAlg stand-alone (left) and in combination with TrigIDSCAN (right) for $t\bar{t}$ at different luminosity scenarios.

Considering the fraction of the total events which give a positive trigger, as shown in Table 3.15, it increases about 4% due to the minimum bias pile-up and cavern background contribution for TileMuId stand-alone but the use of the Inner Detector tracks in the L2_mu4_trod trigger chain helps to reduce this effect significantly.

Table 3.15: Ratio of events tagged by TileMuId with respect to the total number of events.

	$N_{\text{TrigTileRODMuAlg}}/N_{\text{Total}}$	$N_{\text{L2\_mu4\_trod}}/N_{\text{Total}}$
$t\bar{t}$ (14 TeV) without pile-up	0.292 ± 0.003	0.273 ± 0.003
$t\bar{t}$ (10 TeV) with pile-up (450 ns)	0.304 ± 0.007	0.280 ± 0.006
$t\bar{t}$ (10 TeV) with pile-up (75 ns)	0.316 ± 0.007	0.278 ± 0.006
$t\bar{t}$ (10 TeV) with pile-up (25 ns)	0.334 ± 0.007	0.271 ± 0.006

Therefore, TileMuId is shown not to be very sensitive to this kind of backgrounds and therefore it will be a good option also for next phases of LHC running.

3.8 Performance with Cosmics Data

The performance of the TileMuId algorithm at the TileCal ROD DSPs has been tested with real data from detector commissioning in which dedicated data acquisition runs were performed using cosmic rays. These data are very useful since, on one hand, the algorithm is proved to be integrated and operative for global data acquisition in the experiment and, on the other hand, its performance can be tested in the real ATLAS conditions in terms of noise, detector status, etc.

Nevertheless, the topology of cosmic rays is not optimal for muon detection with this algorithm, since it is meant to tag muons from collision data, that is, coming from the interaction point. The present Section will discuss the results provided by TrigTileRODMuAlg during commissioning. In particular, the cosmics runs 91060 (magnetic field off) and 91900 (magnetic field on), acquired during cosmic data taking period in 2008, are used. The cosmic Monte Carlo samples used in this study were simulated with Athena release 14 and the geometry ATLAS-GEONF-04-00-00. The simulation step in these samples required that the cosmic rays go through either the TRT barrel or the Pixels detector.

3.8.1 Performance of TileMuId Stand-alone

The results shown in this Section have been obtained with cosmics run 91060 and only the events triggered by the L1Calo [45], which requires the deposition in a calorimeter tower to exceed a given threshold, have been considered due to the high statistics available in this data stream. Moreover, the results presented here have been obtained using the same lower energy threshold for all the cells, set to 300 MeV.

Figure 3.28 shows the number of muons found per cosmics event. In most of the events no muon is found by the algorithm, as expected from their non-projectivity.

However, in a sizeable fraction of the events one or two muons are found by the algorithm, with still some cases with three muons tagged. The properties of the events with two muon tags, since the top-down coincidence can be related to a better projectivity in the tagged muons, are discussed below.

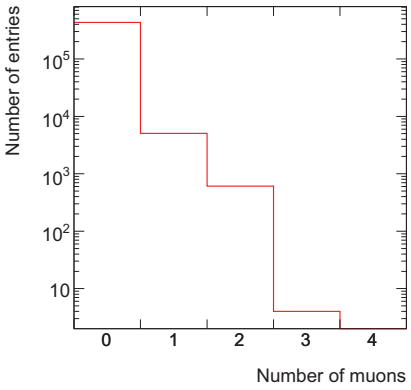

Figure 3.28: Multiplicity of muons found by TrigTileRODMuAlg for the cosmics run 91060.

Figure 3.29 shows the energy deposited by the cosmic muons as the sum of the three TileCal layers with real and Monte Carlo data. As expected, the energy released in the calorimeter by the muons follows a Landau-like shape with turn-on at 900 GeV (three times the lower energy threshold, corresponding to the case where the three cells used in the algorithm are just above the threshold). The energy deposition is compatible with the behavior of a MIP in TileCal: the distribution has its maximum in 2 GeV in agreement with Monte Carlo simulations and shows a long tail for the cosmic muons which deposit a large amount of their energy in a single cell. Note that the real noise environment makes the energy distribution wider compared with the Monte Carlo results.

The distributions for the ϕ coordinate in cosmic muons tagged by the algorithm for real and simulated data is shown in Figure 3.30. For both cases, more events are found in the ϕ coordinate corresponding to the up-down direction, as expected for the cosmics ray dependence on $\cos\theta$ [46], using the coordinate convention under which a vertical downward-going muon has $\theta = 0$.

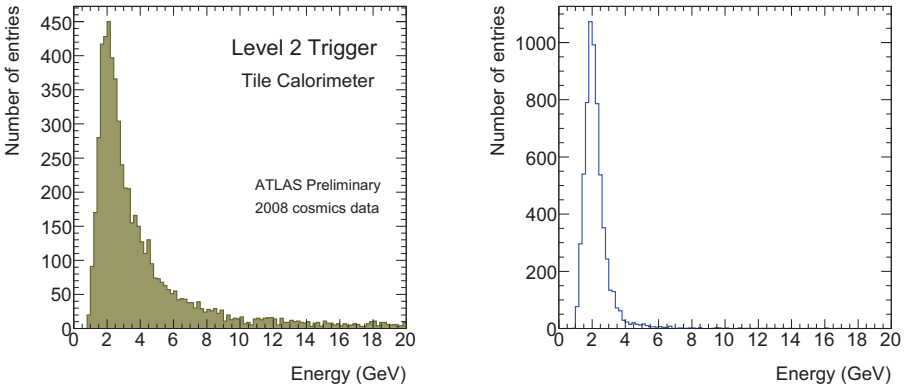

Figure 3.29: Energy deposited in TileCal by the muons for the cosmics run 91060 (left) and Monte Carlo cosmics data (right).

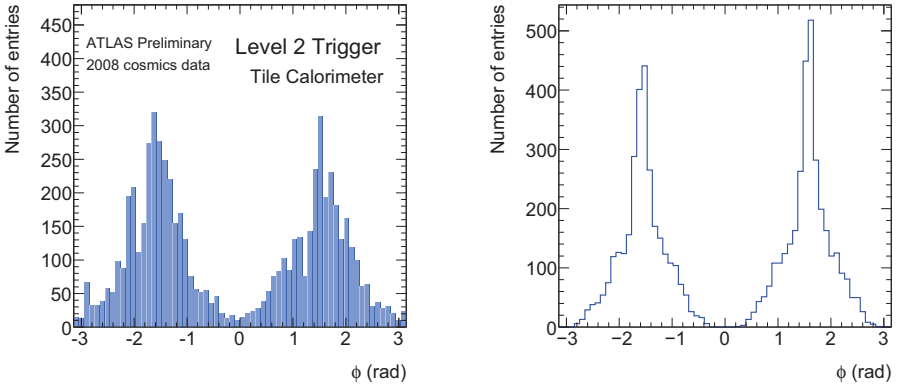

Figure 3.30: Number of muons tagged as a function of ϕ for the cosmics run 91060 (left) and Monte Carlo cosmics data (right).

Symmetrical distributions are obtained for the η coordinate and a clear structure for the long barrel and the extended barrels is observed (see Figure 3.31). Nevertheless, we can observe a disagreement between real data and Monte Carlo, most likely due to the different noise description in the simulation. It is known that the real noise in TileCal increases towards patch-panel connections leading to a noise dependence on η [47] as shown in Figure 3.32, but the electronics noise in the simulations was assumed to be flat on η.

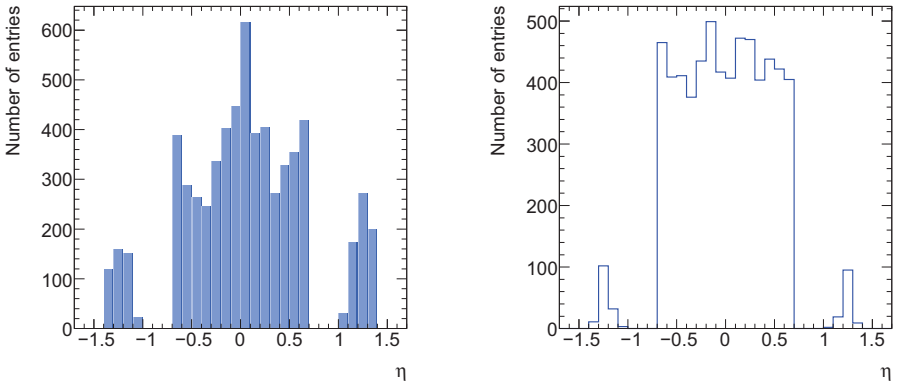

Figure 3.31: Number of muons tagged as a function of η for the cosmics run 91060 (left) and Monte Carlo cosmics data (right).

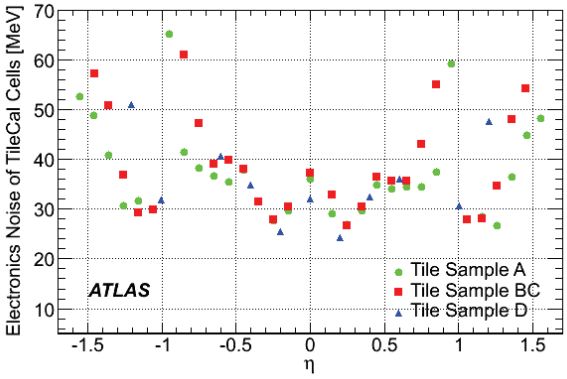

Figure 3.32: RMS of the cell electronics noise distribution of TileCal as measured from a cosmic run taken the 28th September 2008 and triggered by the RNDM trigger. The η dependence is very likely due to the power distribution of TileCal (sharp rise in $|\eta| \sim 1$ & 1.5).

For low values of $Thr_{\text{lower}}/\sigma^{\text{cell}}_{\text{noise}}$ the algorithm efficiency increases and also the fraction of fakes. Therefore, constant Thr_{lower} is a good approach for Monte Carlo data ($Thr_{\text{lower}}/\sigma^{\text{cell}}_{\text{noise}} = \text{constant}$) but in real data this leads to a non-uniform efficiency in η. The next implementation of the algorithm will include the usage of the database to store the lower energy thresholds. This way different lower energy thresholds for each cell depending of their noise level will be applied instead of

the same threshold for all of them, obtaining a double effect: efficiency increase in the regions with lower noise level and an important reduction of the fraction of fake muons coming from electronics noise. This can qualitatively explain the discrepancy in Figure 3.31.

Back-to-back Muon Analysis

In the events where two muon tags are provided by the TileMuId algorithm, they more likely correspond to two tracks from the same cosmic muon left in the calorimeter when it follows a quasi-projective pattern.

The assumption that these events correspond to back-to-back tracks by a single muon following an almost projective trajectory can be checked looking at the relation between the track coordinates, as shown in Figure 3.33. An ideally projective muon will present a $\eta(\mu_1)+\eta(\mu_2)=0$ and $\phi(\mu_1)-\phi(\mu_2)=\pi$ once detected with back-to-back tracks in TileCal. As shown, the majority of the events are concentrated in $\phi(\mu_1)-\phi(\mu_2)\sim\pi$, showing that the up-down coincidence is fulfilled with a good approximation. Nevertheless, few events are characterized by $\Delta\phi\approx 0$, in which more likely several parallel muons coming from the cosmic ray shower have been detected.

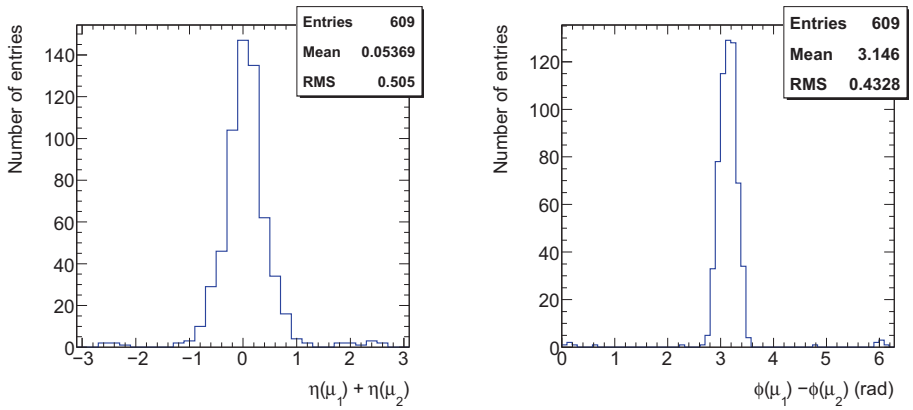

Figure 3.33: Distribution in $\eta(\mu_1)+\eta(\mu_2)$ (left) and $\phi(\mu_1)-\phi(\mu_2)$ (right) for the 2-tag events in cosmics run 91060.

Finally, the $\eta(\mu_1)+\eta(\mu_2)$ also shows that most of the tracks found are symmetric in the left-right direction $\eta(\mu_1) = -\eta(\mu_2)$, although long tails are also present. This can be better understood looking at the correlation between $\eta(\mu_1) + \eta(\mu_2)$ and $\phi(\mu_1) - \phi(\mu_2)$ in Figure 3.34. Most of the events are concentrated in $\phi(\mu_1) - \phi(\mu_2) \approx \pi$ and $\eta(\mu_1) + \eta(\mu_2) = 0$ and therefore correspond to quasi-projective muons as discussed above. Few cases show $\phi(\mu_1) - \phi(\mu_2) \approx \pi$ but large $\eta(\mu_1) + \eta(\mu_2)$, corresponding to single muons detected in a top-down geometry but with $\eta(\mu_1) \neq -\eta(\mu_2)$, i.e., not passing through the interaction point.

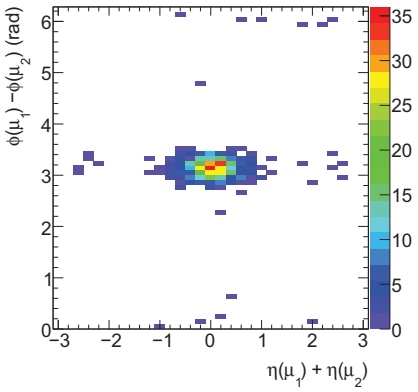

Figure 3.34: Correlation between $\eta(\mu_1) + \eta(\mu_2)$ and $\phi(\mu_1) - \phi(\mu_2)$ for the 2-tag events in cosmics run 91060.

Figure 3.35 shows the correlation between the ϕ coordinates of the two muon tags, where the up-down pattern is clearly seen even for the cases where the muon comes almost from the horizontal direction ($\phi \approx 0$) but it is still tagged twice and correctly with $\phi(\mu_1) - \phi(\mu_2) \approx \pi$, also note the cases where $\phi(\mu_1) \approx \phi(\mu_2)$ as discussed above.

Summing up, despite the limitations in the usage of cosmics data for testing the TileMuId performance, the algorithm shows very encouraging results in the real ATLAS running conditions. Taking into account the angular distribution of the arriving cosmic rays and the efficiency of the algorithm as shown in Monte Carlo studies, the η and ϕ distributions of the tagged muons are sensible with more events at $\eta \approx 0$ and $|\phi| \approx \pi/2$. Furthermore, in the 2-tag events, these tags

correspond to a single quasi-projective muon which is identified by its back-to-back energy depositions in the calorimeter.

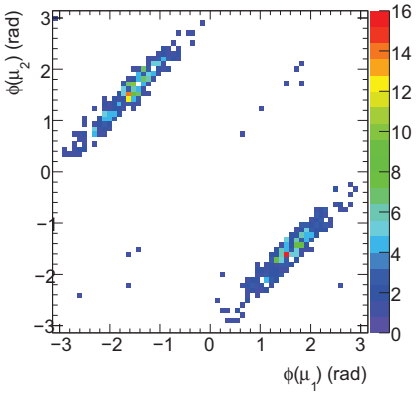

Figure 3.35: Correlation between the ϕ coordinates for the 2-tag events in cosmics run 91060.

3.8.2 Performance of TileMuId Combined with the Inner Detector

The plots shown here were extracted from the HLT monitoring histograms in cosmic run 91900 where the magnetic field was switched on. TrigTileRODMuAlg was running in combination with TrigIDSCAN to match the TileCal muon candidates with the Inner Detector tracks at Level-2 trigger.

Figure 3.36 shows the difference between the muon ϕ coordinate provided by TileMuId (ϕ_{Tile}) and the ϕ coordinate of the matched track in the Inner Detector provided by TrigIDSCAN (ϕ_{ID}) as a function of the muon p_{T} measured by TrigIDSCAN before applying extrapolation in Eq. (3.2).

Similarly to the Monte Carlo case illustrated in Figure 3.5, two branches are observed, corresponding to muons with different charge with worse agreement between ϕ_{Tile} and ϕ_{ID} in the low-p_{T} region.

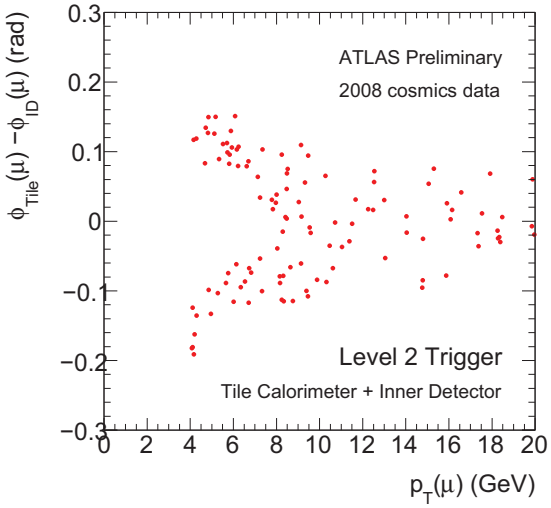

Figure 3.36: Difference between the muon ϕ coordinate provided by TileMuId (ϕ_{Tile}) and the ϕ coordinate of the associated track found in the Inner Detector by TrigIDSCAN (ϕ_{ID}) as a function of the muon p_{T} measured by TrigIDSCAN before applying extrapolation in Eq. (3.2).

Figure 3.37 shows the difference between the muon ϕ coordinate provided by TileMuId (ϕ_{Tile}) and the ϕ coordinate of the matched track in the Inner Detector provided by TrigIDSCAN and extrapolated to the TileCal Radius (ϕ_{TR}) using Eq. (3.2) as a function of the muon p_{T} measured by TrigIDSCAN.

Note that the maximum deviation obtained $|\phi_{\text{Tile}} - \phi_{\text{TR}}| \sim 0.05$ rad is exactly half the granularity that can be achieved in the ϕ measurement by TileCal. Therefore, the dispersion of ~ 0.1 rad, which is the TileCal granularity in ϕ ($2\pi/64$), confirms that the extrapolated ID track pointed to the TileCal module where the muon was found. In consequence, we can conclude that the parameters computed with Monte Carlo data to extrapolate the muon ϕ coordinate to the TileCal Radius due to its bending by the magnetic field are working fine for real data.

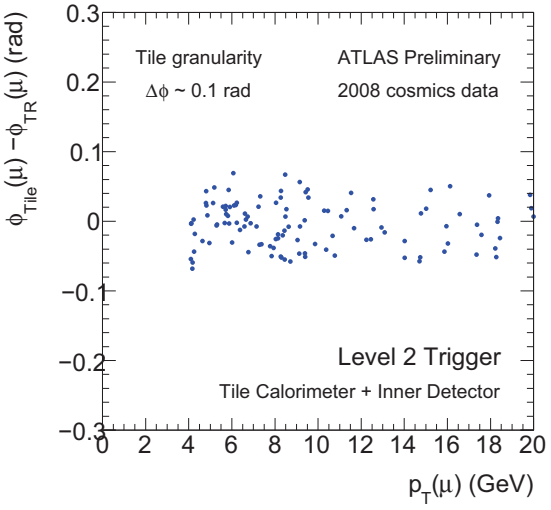

Figure 3.37: Difference between the muon ϕ coordinate provided by TileMuId (ϕ_{Tile}) and the ϕ coordinate of the associated track found in the Inner Detector by TrigIDSCAN after having been extrapolated to the TileCal Radius (ϕ_{TR}) using Eq. (3.2) as a function of the muon p_{T} measured by TrigIDSCAN.

3.9 Conclusions

TileMuId is a low-p_{T} muon tagging algorithm based on the energy deposited in TileCal, which takes advantage of its projective segmentation. Its purpose is to complement the ATLAS Muon Spectrometer in the regions with reduced geometrical acceptance and in the very low-p_{T} range. Note that low-p_{T} muons may not reach the middle and outer muon stations due to the magnetic field bending.

This algorithm has been implemented in the ROD DSPs so that it is processed online for all the events passing Level-1 trigger and the TileMuId information is present in the raw data to be accessed at Level-2 trigger. This ROD-based implementation is known as TrigTileRODMuAlg.

Dedicated code has been developed in the offline software framework for a fully offline version of TileMuId (TrigTileLookForMuAlg) which makes use of the cell

energy computed at the offline level. For the ROD-based version of the algorithm, software for decoding-encoding has been provided.

HLT algorithms have also been developed to use the TileMuId information at Level-2 trigger. Two trigger chains have been defined in the $\mathscr{L} = 10^{31}$ cm^{-2}s^{-1} trigger menu, which make use of a Muon Spectrometer Level-1, combine the muons tagged in TileCal with Inner Detector tracks and uses this information to feed EF algorithms. This trigger chains are meant to confirm the Level-1 muon RoIs and therefore reduce the trigger fake rate, as well as trigger muons which would not pass Level-2 and EF with the Muon Spectrometer information only.

In terms of performance with Monte Carlo data, in Full Scan mode a 75% (60%) efficiency for $p_{\mathrm{T}} > 6$ GeV is obtained for TrigTileLookForMuAlg (TrigTileRODMuAlg). In the HLT environment and seeded by Level-1 RoIs a ∼70% efficiency can be obtained in $b\bar{b}$ processes. TileMuId in its two implementations is fully operational and in use during ATLAS commissioning with cosmic rays. Although not being the optimal data source for testing the algorithm, very encouraging results are obtained even in combination with Inner Detector tracks.

In short, the low-p_{T} muon tagging strategy in TileCal is used now to find muons in commissioning and in good shape to be used at Level-2 trigger with the first collision data in ATLAS.

4 MSSM Higgs Search in ATLAS

"The way that the background fields generates mass is rather like the way in which when light passes through a transparent medium like glass or water, it gets slowed down. It no longer travels with the fundamental velocity of light c. And that's the way to think of the generation of mass."

— Peter Higgs, b. 1929.

This Chapter is devoted to the discovery analysis for the neutral MSSM Higgs boson in the dimuon decay channel. The main motivations for such analysis is the high momentum resolution and identification achievable with the ATLAS detector, which compensate to some extend for the suppression of the branching ratio compared to the ditau decay mode. Indeed, in this channel a full reconstruction of the Higgs boson final state is possible, which allows a direct mass measurement.

Although the discovery feasibility of this channel has been traditionally explored with a dimuon+b-jets signature, the original contribution of the analysis described here is that the search is performed without any b-tagging requirement.

4.1 General Introduction

The Minimal Supersymmetric Standard Model contains two complex Higgs doublets, leading to five physical Higgs bosons after electroweak symmetry breaking: three neutral (two *CP*-even h and H, and one *CP*-odd A) and a pair of charged Higgs bosons $H^{\pm}$.

As mentioned in Section 2.3.1, the MSSM may be constrained by the assumption that the sfermion masses, the gaugino masses and the trilinear Higgs-fermion couplings must unify at the Grand Unification scale (GUT). In one of the possible constrained models the chosen parameters are:

- M_{SUSY}: common mass for all sfermions at the electroweak scale.
- M_2: common $\mathrm{SU}(2)_L$ gaugino mass at the electroweak scale.
- μ: strength of the supersymmetric Higgs mixing.
- $\tan\beta$: ratio of the vacuum expectation values of the two Higgs fields.
- $A = A_t = A_b$: common trilinear Higgs-squarks coupling at the electroweak scale. It is assumed to be the same for up-type and down-type squarks.
- m_A: mass of the *CP*-odd Higgs boson.
- $m_{\tilde{g}}$: gluino mass.

Three of these parameters define the stop and sbottom mixing parameters $X_t = A_t - \mu\cot\beta$ and $X_b = A_b - \mu\cot\beta$.

Whereas the particle spectrum depends on all the parameters mentioned above, at tree level, the Higgs sector of the MSSM is fully specified by two parameters, generally chosen to be m_A and $\tan\beta$.

Radiative corrections modify the tree-level relations significantly. This is of particular interest for the mass of the lightest *CP*-even Higgs boson, which at tree level is constrained to be below the mass of the Z boson. Loop corrections are sensitive to the mass of the top quark, to the mass of the scalar particles and in particular to mixing in the stop sector.

Among all possible *CP*-conserving scenarios [48], the so-called m_h^{max} scenario corresponds to the maximum value of the stop mixing parameter $X_t = A_t - \mu\cot\beta = 2M_{\mathrm{SUSY}}$. The parameters are chosen such that the maximum possible Higgs-boson mass as a function of $\tan\beta$ is obtained. The theoretical bound on m_h is highest and the experimental limits are less constraining.

The no-mixing benchmark scenario is the same as the m_h^{max} scenario, but with vanishing mixing in the stop sector and with a higher SUSY mass scale. In this case, the highest value of m_h can be 114 GeV.

The large-μ scenario is designed such that the h boson does not decay into b-quark pairs due to large corrections from SUSY loop processes. The dominant decay modes are to $c\bar{c}$, gg, W^+W^- and $\tau^+\tau^-$. The highest value of m_h can be 108 GeV in this scenario.

Table 4.1 shows the parameters for these three scenarios. Unless otherwise stated, this Chapter only considers the $m_h^{\max}$ scenario since it is the most promising for the search of the h boson due to their relative high mass value.

Table 4.1: Parameters for some benchmark MSSM scenarios used in ATLAS.

Parameter	$m_h^{\max}$	no mixing	large μ
$M_{\rm SUSY}$ (GeV)	1000	2000	400
μ (GeV)	-200	-200	1000
M_2 (GeV)	200	200	400
$X_t = A_t - \mu\cot\beta$	$2M_{\rm SUSY}$	0	-300
$m_{\tilde{g}}$ (GeV)	$0.8M_{\rm SUSY}$	$0.8M_{\rm SUSY}$	200
m_A (GeV)	0.1-1000	0.1-1000	0.1-400
$\tan\beta$	0.4-50	0.4-50	0.7-50

In this scenario, if the full one-loop and the dominant two-loop contributions are included, the upper bound on the mass of the light Higgs boson h is expected to be around 135 GeV. While the light neutral Higgs boson may be difficult to distinguish from its Standard Model counterpart, the other heavier Higgs bosons are a distinctive signal of physics beyond the Standard Model. The masses of the heavier Higgs bosons H, A and $H^\pm$ are often almost degenerate.

Direct searches at LEP have given lower bounds of 92.9 (93.3) GeV and 93.4 (93.3) GeV on the masses of the lightest *CP*-even Higgs boson h and the *CP*-odd Higgs boson A within the $m_h^{\max}$ (no-mixing) scenario. Given the LEP results, the $\tan\beta$ regions of $0.9 < \tan\beta < 1.5$ and $0.4 < \tan\beta < 5.6$ are excluded at 95% confidence level for the $m_h^{\max}$ and the no-mixing scenarios, respectively. However, it should be noted that the exclusions in $\tan\beta$ depend critically on the exact value of the top-quark mass. In the LEP analysis $m_t = 179.3$ GeV has been assumed. With decreasing top mass the theoretical upper bound on m_h decreases and hence

the exclusions in $\tan\beta$ increase, while for m_t of about 183 GeV, or higher, the exclusions in $\tan\beta$ vanish.

Direct searches at the Tevatron [49, 50] have been performed looking to the τ-pair and b-pair production. With an integrated luminosity of 1.8 fb^{-1} no excess of events has been observed, and exclusion limits on production cross-section times branching fraction to tau pairs for a Higgs boson mass in the range from 90 to 250 GeV have been set. The expected reach of this search, assuming MSSM Higgs production, extends below $\tan\beta = 40$ for m_A in the mass range $m_A = 120$ to 160 GeV. Figure 4.1 shows the most recent results on the 95% CL exclusion in the $(m_A, \tan\beta)$ plane for the Tevatron experiments.

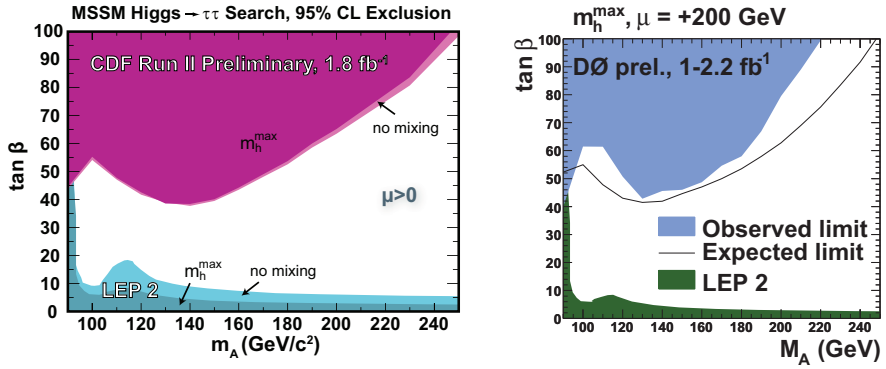

Figure 4.1: Excluded regions in the $\tan\beta$ vs m_A in the $m_h^{\max}$ scenario obtained by the Tevatron experiments CDF (left) and DØ (right). Both plots include the region already excluded by the LEP experiments. Note that the left plot also quotes the results for the no-mixing scenario.

The charged Higgs boson mass ($m^2_{H^\pm}$) is related to m_A via the tree-level relation $m^2_{H^\pm} = m^2_W + m^2_A$ and it is less sensitive to radiative corrections. Direct searches for charged Higgs bosons in the decay modes $H^\pm \to \tau\nu$ and $H^\pm \to cs$ have been carried out at LEP, yielding a lower bound of 78.6 GeV on $m_{H^\pm}$ independent of the $H^\pm \to \tau\nu$ branching ratio. At the Tevatron, the CDF and DØ experiments have performed direct and indirect searches for the charged Higgs bosons through the process $p\bar{p} \to t\bar{t}$ with at least one top quark decaying via $t \to H^\pm b$. These searches have excluded the small and large $\tan\beta$ regions for $H^\pm$ masses up to ~160 GeV.

The high collision energy of the LHC will allow the search for Higgs bosons to be extended into unexplored mass regions. The experiments have a large discovery potential for Higgs bosons in both the Standard Model and in the MSSM over the full parameter range. If the Higgs boson be light, i.e. have a mass in the range favoured by the precision electroweak measurements, the experiments at the Tevatron might also get indications of the existence of a Higgs boson.

4.1.1 Production of the Neutral Higgs Boson

The production of neutral Higgs bosons and their decays are different from those in the Standard Model. While decays into ZZ or WW are dominant in the Standard Model for Higgs boson masses above $m_H > 2m_W$, for high values of $\tan\beta$ these decay modes are either suppressed in case of the h and H or even absent in the case of the A. Instead, the coupling of the Higgs bosons to third generation fermions are strongly enhanced for large regions of the MSSM parameter space.

The Higgs boson production proceeds via two different mechanisms, the direct and the b quark associated production, as described below. In the following ϕ stands for either of the three neutral Higgs bosons: A, H, and h.

- **Direct production:** the diagram for this process is depicted in Figure 4.2(a). It dominates in the range of low $\tan\beta$ and its rates are significantly larger than for the Standard Model. For the range of higher $\tan\beta$ it is still dominant for low m_A. The cross-section for this process has been calculated at NLO accuracy.
- **Associated production:** different approaches have been followed by theorists to calculate the cross-section for Higgs boson production in association with b quarks, each of them assuming one of the diagrams depicted in Figure 4.2(b-e) as their leading order (LO) contribution:
  - $gg \rightarrow b\bar{b}\phi$
  - $b\bar{b} \rightarrow \phi$
  - $gb \rightarrow b\phi$
  - $q\bar{q} \rightarrow b\bar{b}\phi$

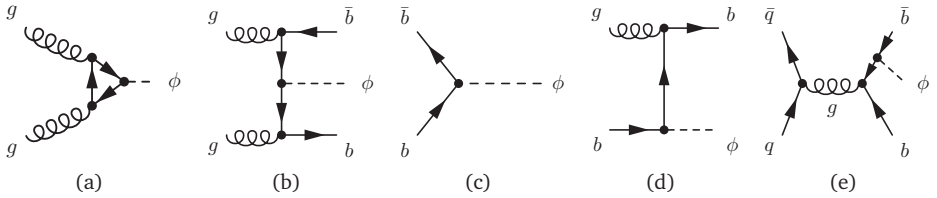

Figure 4.2: Feynman diagrams contributing to the MSSM Higgs boson production. Diagram (a) is called 'direct production', diagrams (b) to (e) contribute to the b quark associated production. In the above diagrams ϕ represents either of the neutral Higgs bosons in the MSSM, h, H, or A.

The cross-sections are calculated using FeynHiggs-2.6.2 [51] and HIGLU [52] yielding the cross-section for a Standard Model Higgs boson. The cross-sections in the MSSM are then obtained by scaling them by the ratio of partial widths into $b\bar{b}$:

$$\sigma^{\phi}_{\mathrm{MSSM}}(m_A, \tan\beta) = \sigma_{\mathrm{SM}}(m_\phi)\frac{\Gamma^{\mathrm{MSSM}}_{b\bar{b}\phi}(m_A, \tan\beta)}{\Gamma^{\mathrm{SM}}_{b\bar{b}\phi}(m_\phi)} \tag{4.1}$$

The production cross-sections for all Higgs boson masses considered here in the m_h^{max} scenario are summarized in Table 4.2 for $\tan\beta = 20$.

Table 4.2: Mass, cross-section for direct and b-associated production, for Higgs bosons in the m_h^{max} scenario and for $\tan\beta = 20$. All values were obtained using FeynHiggs-2.6.2 and HIGLU.

Mass (GeV)			$\sigma^{\mathrm{direct}}_{h,\,H,\,A}$ (fb)			$\sigma^{\mathrm{associated}}_{h,\,H,\,A}$ (fb)		
A	H	h	A	H	h	A	H	h
110	129.8	109.0	-	-	-	314810	7579	310707
130	134.2	124.7	92517	93941	43545	189602	92897	99992
160	160.8	128.0	32148	34706	44561	97480	93102	6650
200	200.5	128.4	9847	11377	45957	45685	45095	2188
300	300.4	128.6	955	1451	46986	10312	10253	979
450	449.8	128.6	-	-	-	2019	2035	723

The production cross-sections of A/H bosons increase approximately quadratically with increasing $\tan\beta$, while the h boson production is $\tan\beta$ dependent only

for $m_A < 130$ GeV. Similarly, the branching ratio to a dimuon pair increases for A/H with increasing values of $\tan\beta$, while for the h boson it depends little on these parameters.

4.2 Neutral Higgs Boson Dimuon Decay Mode

The Higgs boson decay into a $\mu^+\mu^-$ pair is strongly suppressed within single doublet Higgs sector of the Standard Model. However, as mentioned above, in the context of the MSSM, the A and H boson decays to muons are strongly enhanced for large values of $\tan\beta$ and, furthermore, they provide a very clean experimental signature. Therefore, this channel can provide a feasible discovery at LHC or, at least, new limits could be drawn on the (m_A, $\tan\beta$) parameter space. For $m_A > 150$ GeV the A and H bosons are approximately degenerate in mass (see Table 4.2), so that their signal rates can be added obtaining a two times stronger resonance. Table 4.3 shows the branching ratio of MSSM neutral Higgs bosons into $\tau^+\tau^-$ and $\mu^+\mu^-$ final states in the $m_h^{\max}$ scenario for $\tan\beta = 20$.

Table 4.3: Branching ratios into $\tau^+\tau^-$ and $\mu^+\mu^-$ final states for Higgs bosons in the $m_h^{\max}$ scenario and for $\tan\beta = 20$. All values were obtained using FeynHiggs-2.6.2 and HIGLU.

m_A	BR(h, H, $A \to \tau^+\tau^-$) (%)			BR(h, H, $A \to \mu^+\mu^-$) (%)		
(GeV)	A	H	h	A	H	h
110	8.86	9.11	8.88	0.031	0.032	0.031
130	9.11	9.23	9.00	0.032	0.033	0.032
160	9.42	9.46	8.40	0.033	0.033	0.030
200	9.57	9.72	7.49	0.034	0.034	0.027
300	8.22	9.51	6.27	0.029	0.034	0.022
450	6.07	6.24	5.68	0.021	0.022	0.020

Although often $h/A/H \to \mu\mu$ analysis relies on the selection of b-jets in an event [53,54], this Chapter is devoted to an alternative analysis with no b-tagging requirements for the event selection. This is especially convenient during the first phases of ATLAS data taking, where the performance of the b-tagging algorithm will still be characterized by a relatively large uncertainty. The feasibility

of the presented analysis is demonstrated even for a low integrated luminosity of 1-10 fb^{-1}.

4.2.1 Background Production

The main backgrounds to be considered for this analysis are due to $Z/\gamma^* \rightarrow \mu\mu$ (Drell-Yan production or associated with light or b-jets), $t\bar{t} \rightarrow (W^+b)(W^-\bar{b}) \rightarrow (\mu^+\nu b)(\mu^-\bar{\nu}\bar{b})$, ZZ and WW diboson production, whose production mechanisms are shown in Figure 4.3.

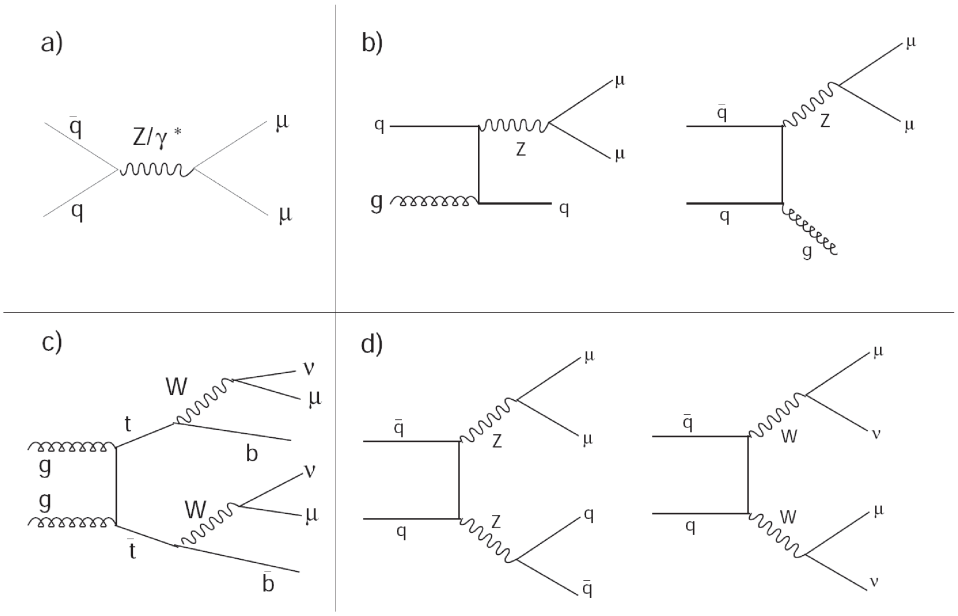

Figure 4.3: Tree-level Feynman diagrams for the dominant background processes with two isolated muons in the final state: a) Drell-Yan Z-boson production, b) Z-boson production in association with jets, c) $t\bar{t}$ production and d) ZZ and WW production.

The Drell-Yan Z production with subsequent decays into two muons is one of the most important backgrounds to be considered and even at high m_A the tail of the Z resonance represents the dominant background. On the other hand, the $t\bar{t}$ background, characterized by a high jet activity and large $E_{\mathrm{T}}^{\mathrm{miss}}$ tails due

to the neutrinos in the final state, can be strongly suppressed by establishing a cut in the $E_{\mathrm{T}}^{\mathrm{miss}}$ and also requiring less than 2 jets in the final event selection. The contribution of the ZZ and WW backgrounds, with lower production rates, is easily reduced after applying all the event selection criteria, as described in Section 4.6.

4.3 Likelihood Formalism

Fequentist statistical methods are used in this Chapter for a proper data treatment and correct estimation of significance and exclusion limits, where the effects of systematic uncertainties are incorporated by use of the profile likelihood ratio.

In this kind of searches the measurement corresponds to a histogram of a variable, e.g. the mass of the reconstructed Higgs candidate. The number of entries in bin i, n_i, is modeled as a Poisson variable with mean value

$$E[n_i] = \mu L \varepsilon_i \sigma_i \mathscr{B} + b_i \equiv \mu s_i + b_i, \tag{4.2}$$

where L is the integrated luminosity, ε_i, σ_i and $\mathscr{B}$ are the signal efficiency, Higgs cross-section, and branching ratio, and b_i is the expected number of background events. Here μ is a signal strength parameter defined such that $\mu = 0$ corresponds to the absence of a signal; $\mu = 1$ gives the signal rate s_i expected from the Standard Model. If we consider a fixed Higgs mass m_H, the only parameter of interest is μ. All other adjustable parameters needed to specify the model are called *nuisance parameters*.

For the ith bin of a histogram of a discriminating variable x, the expected signal and background can be written

$$s_i = s_{\mathrm{tot}} \int_{\mathrm{bin}\ i} f_s(x;\theta_s)dx, \tag{4.3}$$

$$b_i = b_{\mathrm{tot}} \int_{\mathrm{bin}\ i} f_b(x;\theta_b)dx, \tag{4.4}$$

where s_{tot} and b_{tot} are the total expected numbers of events in the histograms, $f_s(x;\theta_s)$ and $f_b(x;\theta_b)$ are the probability density functions (pdfs) of x for signal and background, and θ_s and θ_b represent sets of *shape parameters*.

The parametric forms of the pdfs $f_s(x;\theta_s)$ and $f_b(x;\theta_b)$ are determined from Monte Carlo simulations or data control samples. In the following we will use $\theta = (\theta_s, \theta_b, b_{\text{tot}})$ to refer to all of the nuisance parameters. The signal normalization s_{tot} here is not an adjustable parameter, but rather is fixed equal to the Standard Model prediction.

In addition to the measured histogram **n**, some search channels also make use of a set of subsidiary measurements $\mathbf{m}=(m_1, \ldots, m_M)$ in control regions where one expects mainly background events. These can be modeled as being Poisson distributed with mean values

$$E[m_i] = u_i(\theta), \tag{4.5}$$

where the u_i are calculable quantities depending on a set of parameters, at least some of which are the same as those entering into the predictions for s_i and b_i above.

The likelihood function is the product of Poisson probabilities for all bins:

$$L(\mu,\theta) = \prod_{j=1}^{N} \frac{(\mu s_j + b_j)^{n_j}}{n_j!} e^{-(\mu s_j + b_j)} \prod_{k=1}^{M} \frac{u_k^{m_k}}{m_k!} e^{-u_k}. \tag{4.6}$$

Equivalently the log-likelihood is

$$\ln L(\mu,\theta) = \sum_{j=1}^{N} (n_j \ln(\mu s_j + b_j) - (\mu s_j + b_j)) + \sum_{k=1}^{M} (m_k \ln u_k - u_k) + C, \tag{4.7}$$

where C represents terms that do not depend on the parameters and thus can be dropped. Here and in Eq. (4.6) the parameters θ enter through Eqs. (4.3), (4.4) and (4.5).

To test a hypothesized value of μ we construct the profile likelihood ratio,

$$\lambda(\mu) = \frac{L(\mu, \hat{\hat{\theta}})}{L(\hat{\mu}, \hat{\theta})}. \tag{4.8}$$

Here $\hat{\hat{\theta}}$ in the numerator denotes the value of θ that maximizes L for the specified μ, i.e., it is the conditional maximum-likelihood estimator (MLE) of θ (and thus is a function of μ). The denominator is the maximized (full) likelihood function, i.e., $\hat{\mu}$ and $\hat{\theta}$ are the MLEs.

From the definition of the profile likelihood ratio one can see that $0 \leq \lambda \leq 1$, with $\lambda(\mu) = 1$ implying good agreement between the data and the hypothesized value of μ. Equivalently it is convenient to work with the quantity

$$q_\mu = -2 \ln \lambda(\mu), \tag{4.9}$$

so that high values of q_μ correspond to poor agreement between the data and the hypothesized μ. The statistic q_μ will have a sampling distribution $f(q_\mu|\mu')$. Here μ refers to the strength parameter used to define the statistic q_μ, entering in the numerator of the likelihood ratio, and μ' is the value used to define the data generated to obtain the distribution (i.e., the 'true' value).

The level of compatibility between data that give an observed value $q_{\mu,\text{obs}}$ for q_μ and a hypothesized value of μ is quantified by giving the p-value

$$p_\mu = \int_{q_{\mu,\text{obs}}}^{\infty} f(q_\mu|\mu) dq_\mu. \tag{4.10}$$

This is the probability, under the assumption of μ, of seeing data with equal or greater incompatibility, as measured by q_μ, relative to the data actually obtained.

4.3.1 Significance Computation

One can define the *significance* corresponding to a given p-value as the number of standard deviations Z at which a Gaussian random variable of zero mean would give a one-sided tail area equal to p. That is, the significance Z is related to the

p-value by

$$p = \int_Z^\infty \frac{1}{\sqrt{2\pi}} e^{-x^2/2} dx = 1 - \Phi(Z), \tag{4.11}$$

where Φ is the cumulative distribution for the standard (zero mean, unit variance) Gaussian. Equivalently one has

$$Z = \Phi^{-1}(1-p), \tag{4.12}$$

where Φ^{-1} is the quantile of the standard Gaussian (inverse of the cumulative distribution). The relation between Z and p is illustrated in Figure 4.4.

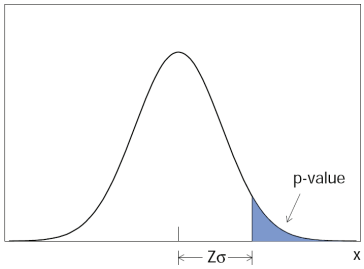

Figure 4.4: Illustration of the correspondence between the significance Z and a p-value.

A significance of $Z = 5$ corresponds to $p = 2.87 \times 10^{-7}$. Note that according to the definition in Eq. (4.12), a p-value of 0.05 corresponds to $Z = 1.64$. This should not be confused with a 1.96σ fluctuation of a Gaussian variable that gives 0.05 for the two-sided tail area.

The significance of a discovery Z depends on the data obtained. To quantify our ability to discover a hypothesized signal in advance of seeing the data, we report the *median* significance under the assumption that the signal is present at the Standard Model rate, $\mu = 1$. Since Z is a monotonic function of p_0, and p_0 is also a monotonic function of q_0, we have for the median significance,

$$Z_{\text{med}} = \Phi^{-1}(1 - p_{0_{\text{med}}}) = \Phi^{-1}(1 - p_0(q_{0_{\text{med}}})). \tag{4.13}$$

This can be obtained from the median value of q_0 found using data generated under the assumption of $\mu = 1$.

4.3.2 Computation of Limits

In addition to establishing discovery by rejecting the $\mu = 0$ hypothesis, we can consider the alternative hypothesis of some non-zero μ and try to reject it. A p-value is computed for each μ, and the set of μ values for which the p-value is greater than or equal to a fixed value $1 - \mathrm{CL}$ form a confidence interval for μ, where typically one takes a confidence level $\mathrm{CL} = 95\%$. The upper end of this interval μ_{up} is the upper limit (i.e., $\mu \leq \mu_{\mathrm{up}}$ at 95% CL).

For purposes of computing limits we redefine q_μ to be

$$q_\mu = \begin{cases} -2\ln\lambda(\mu) & \hat{\mu} \leq \mu, \\ 0 & \text{otherwise.} \end{cases} \tag{4.14}$$

Using the new definition 4.14, the p-value is given by the integral of $f(q_\mu|\mu)$ from the observed value $q_{\mu,\mathrm{obs}}$ to infinity as in Eq. (4.10). The p-value is computed in this manner for all values of μ, and the upper limit μ_{up} at 95% confidence level is the largest value of μ for which the p-value is at least 0.05.

4.4 Data Samples

All data samples used in the present Chapter have been simulated using Athena release 12 as a part of the central ATLAS Monte Carlo production with a center-of-mass energy of 14 TeV. The same data have also been used for the ATLAS performance studies in the Computing System Commissioning (CSC) notes [54]. In particular, the simulated data samples which have been used in this Chapter are summarized in Tables 4.4 and 4.5 for signal[1] and background samples, respectively. The procedure to compute the cross-sections can be found in Ref. [55–58].

[1] Note that the $gg \to h/A/H$ production has not been considered since its contribution to the overall cross-section is very small for $\tan\beta \geq 20$.

Table 4.4: Signal data samples for different values of A-boson mass (m_A) and $\tan\beta = 30$. Cross-sections are computed at next-to-leading order.

Dataset	Process (m_A, $\tan\beta$)	Generator	$\sigma \times$ BR (fb)	Filter efficiency	Number of events	Simulation type
6337	$b\bar{b}A(110, 30)$	PYTHIA	221.24	0.827	3200	full sim.
6340	$b\bar{b}A(130, 30)$	PYTHIA	134.00	0.839	3750	full sim.
6341	$b\bar{b}A(150, 30)$	PYTHIA	86.62	0.841	3750	full sim.
5351	$b\bar{b}A(200, 30)$	PYTHIA	31.48	0.876	4500	full sim.
6342	$b\bar{b}A(300, 30)$	PYTHIA	6.85	0.908	2750	full sim.
6343	$b\bar{b}A(400, 30)$	PYTHIA	1.93	0.922	4500	full sim.

As shown in the table, fully simulated data for different Higgs masses have been generated using the PYTHIA [59] event generator. A generator filter requiring at least two muons with $p_{\mathrm{T}} > 5$ GeV and $|\eta| < 2.7$ is applied to each event for all signal samples, after showering and before writing out the events into permanent storage.

Table 4.5: Background data samples. Cross-sections are computed at next-to-leading order.

Dataset	Process	Generator	$\sigma \times$ BR (pb)	Filter efficiency	Number of events	Simulation type
6356	$ZZ \to b\bar{b}\mu\mu$	PYTHIA	0.151	0.724	8000	full sim.
5985	WW	PYTHIA	116.8	0.35	50000	full sim.
6900	$t\bar{t}$, no filter	MC@NLO	833.0	1.0	2675000	Atlfast
6396	$(Z \to \mu\mu)$+ 0-3 light jets	SHERPA	1165.9	0.855	29000000	Atlfast
6397	$(Z \to \mu\mu)$+ 0-3 b-jets	SHERPA	52.3	0.914	1000000	Atlfast

PYTHIA has also been used for the ZZ and WW diboson backgrounds. SHERPA [60] has been used for the $Z \to \mu\mu$ backgrounds (in Drell-Yan production and in association with light and b-jets) and MC@NLO [61] has been used for the $t\bar{t}$ sample. The large statistics $Z \to \mu\mu$ and $t\bar{t}$ samples are produced with Atlfast [62] simulation, while full simulation is used for the remaining samples. Corrections obtained from comparison studies between Atlfast and full simulation are applied

to Atlfast samples to provide consistency with full simulation. These corrections are described in Ref. [54] and are applied to the muon detection efficiency and momentum resolution, missing transverse energy resolution and jet reconstruction efficiency.

All mentioned data samples have been simulated assuming there are no additional pp-interactions per event. However, at luminosities of 10^{33} cm^{-2}s^{-1} one expects to have 2-3 such pile-up interactions superimposed to the hard scattering. In addition, the neutron and photon background of the Muon Spectrometer (so-called cavern background) may increase the muon trigger rate and degrade the muon reconstruction performance [54]. In order to study the impact of the minimum bias pile-up and cavern background on the analysis performance (see Section 4.5.3), dedicated $b\bar{b}$, $t\bar{t}$ and $Zb\bar{b}$ data samples have been simulated with the realistic pile-up and cavern background contribution. The simulated cavern background is assumed to be five times higher than the prediction of GCALOR [63] and FLUKA [64] simulations, to account for the uncertainty of the calculation.

4.5 Detector Performance

The performance of the reconstruction algorithms is shortly described in this Section, concentrating on the key objects for the analyses: muon identification, jet reconstruction and the measurement of the missing transverse energy ($E_{\mathrm{T}}^{\mathrm{miss}}$). The definition of these objects and the results obtained in absence of pile-up and cavern background in the detector are shown. These are subsequently compared to the results obtained when both pile-up and cavern background are taken into account.

4.5.1 Object Definition

The high level reconstruction objects used in this analysis have been selected following the common conventions agreed in ATLAS for particle identification. This Section reviews these objects (jets, electrons, muons, etc.) together with the selection criteria and algorithms used to identify them.

Muons

The muons were reconstructed using the Staco algorithm [65], based on the statistical combination of a standlone Muon Spectrometer track with an Inner Detector track, as recommended by the muon performance group.

A loose selection is applied on the track segment match χ^2, which is required to be smaller than 100. If more than one Inner Detector track matched one track from the Muon Spectrometer, only the one with smallest $\Delta R = \sqrt{(\Delta\eta)^2 + (\Delta\phi)^2}$ is kept. Calorimeter isolation is obtained by requiring the energy in $\Delta R < 0.2$ cone to be less than 10 GeV and muons found within a distance $\Delta R < 0.4$ of a jet are discarded since they are likely associated to a decay of a jet particle.

Jets

The algorithm used to reconstruct jets here is called Cone4Tower [54] with a cone size of 0.4. Jets matching within a cone of $\Delta R < 0.2$ an isolated electron passing the reconstruction cuts described below are discarded. This procedure (*overlap removal*) prevents the same object to be reconstructed both as an electron and as a jet.

Electrons

The eGamma algorithm [54] was used for the electron identification and reconstruction, with the "medium" identification cuts recommended by the electron combined performance studies [54] for the Athena release 12.

The transverse isolation energy in a cone of $\Delta R < 0.2$ around the electron, computed using the calorimetric information, is used to select isolated electrons. This variable is required to be smaller than 10 GeV. In the available Monte Carlo datasets for Athena release 12 this variable is incorrectly calculated, but only a small bias is introduced by this problem, except for the crack region $1.37 < |\eta| < 1.52$.

In the region $1.37 < |\eta| < 1.52$, besides the problem with the isolation variable described above, the electron identification and measurement are degraded because of the large amount of material in front of the calorimeter and the crack between the barrel and extended barrel of the calorimeters. Therefore events with an electron candidate with $p_T > 10$ GeV, passing the medium eGamma cuts and with a pseudorapidity in the crack region are rejected.

Missing Transverse Energy

For the studies presented here, the output of the most refined algorithm for the reconstruction of the E_T^{miss}, known as MET_RefFinal [54], was used.

4.5.2 Reconstruction Performance without Pile-up and Cavern Background

Apart from the Staco algorithm mentioned above, the MuTag [54] reconstruction package is also used in this study. The average muon reconstruction efficiency for signal samples is $(97.15 \pm 0.04)\%$. This is reduced to $(95.44 \pm 0.05)\%$ if a match between the Muon Spectrometer track and the Inner Detector track is required. The momentum resolution of low-p_T muons is mostly dominated by the Inner Detector performance, while the high-p_T muon reconstruction is more sensitive to the Muon Spectrometer performance. The average muon momentum resolution is better than 3%, which allows for an excellent dimuon mass resolution.

Another important reconstruction object is the E_T^{miss}, which allows for the suppression of the $t\bar{t}$ background. In the signal processes, there is no neutrino contribution, such that the measured $E_{x,y}^{miss}$ value is dominated by the experimental resolution. The reconstruction algorithm for the calculation of the missing transverse energy is described in detail in Ref. [54]. The distributions of E_T^{miss} components in the signal samples have a Gaussian part with a width $\sigma = (7.8 \pm 0.1)$ GeV, while the non-Gaussian tails (above 5σ) are found to contribute less than 1.5% to the overall distribution. E_T^{miss} is sensitive to pile-up effects, as will be described in the next Section.

4.5.3 Reconstruction Performance under Influence of Pile-up and Cavern Background

In the following, the detector performance related to the analysis is evaluated in dependence on the pile-up at luminosities of 10^{33} cm^{-2}s^{-1} and cavern background (five times higher than the expectation). In Figure 4.5, the efficiency and the fake rate of the muon reconstruction is shown for the $b\bar{b}A$ signal sample simulated without and with the pile-up contribution as a function of the pseudorapidity. The corresponding momentum resolution is shown in Figure 4.5(middle). Similar results are obtained also for the background samples.

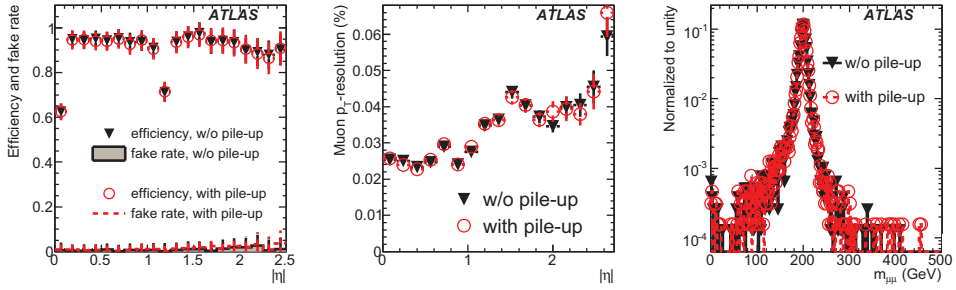

Figure 4.5: Efficiency and the fake rate (left) and resolution (middle) of the muon reconstruction as a function of the $|\eta|$ (for $p_{\mathrm{T}} > 20$ GeV), with and without the pile-up contribution in the $b\bar{b}A$ signal sample with $m_A = 200$ GeV. The right plot shows the corresponding dimuon mass distribution.

As shown in the plots, muon reconstruction is only marginally influenced by pile-up. Consequently, the dimuon invariant mass also remains unaffected, as shown in Figure 4.5(right) for $m_A = 200$ GeV.

On the contrary, the reconstruction of the missing transverse energy is substantially affected by pile-up in the calorimeter. The degradation of the $E_{\mathrm{T}}^{\mathrm{miss}}$ resolution mainly affects the selection of events with a small true missing energy (signal and the Z background) as shown in Figure 4.6(left); $t\bar{t}$ events, characterized by a large missing energy, are rather insensitive to pile-up, see Figure 4.6(right). This effect must be taken into account during the optimization of the event selection criteria. For instance, an event selection cut at $E_{\mathrm{T}}^{\mathrm{miss}} < 30$ GeV, which is reasonable without

pile-up, would reject too many signal events, once the pile-up contribution is included. Therefore, this analysis cut should rather be set to at least 40 GeV in the realistic LHC environment.

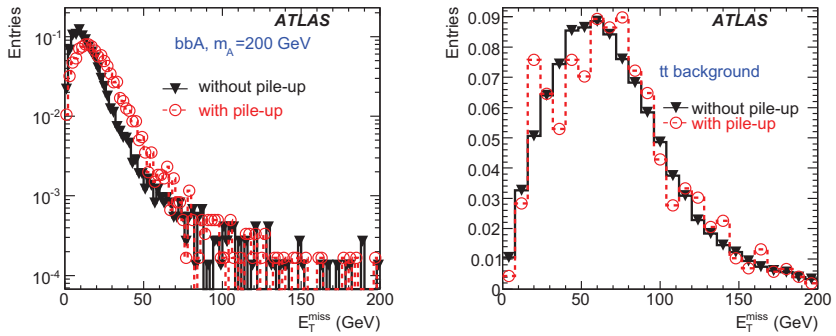

Figure 4.6: Missing transverse energy distribution for the $b\bar{b}A$ signal at 200 GeV (left) and the $t\bar{t}$ background (right), with and without pile-up.

The change of the calorimeter response under the influence of pile-up affects also the jet reconstruction. Due to a higher calorimeter activity, one expects an increase in the number of reconstructed jets. This can be observed in Figure 4.7, showing the jet multiplicity in the $Zb\bar{b}$ background events.

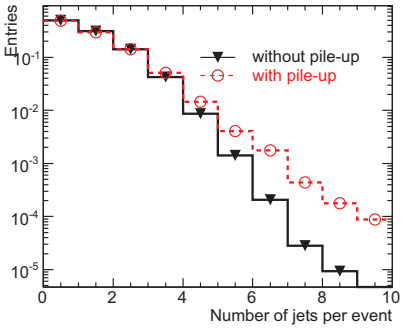

Figure 4.7: Total number of jets per event in the $Zb\bar{b}$ background sample, with and without the pile-up contribution.

4.6 Event Selection

In order to compare with the results obtained using the b-tagging approach [54], the same selection cuts have been applied in this analysis with the only exception that the jet flavor is not considered.

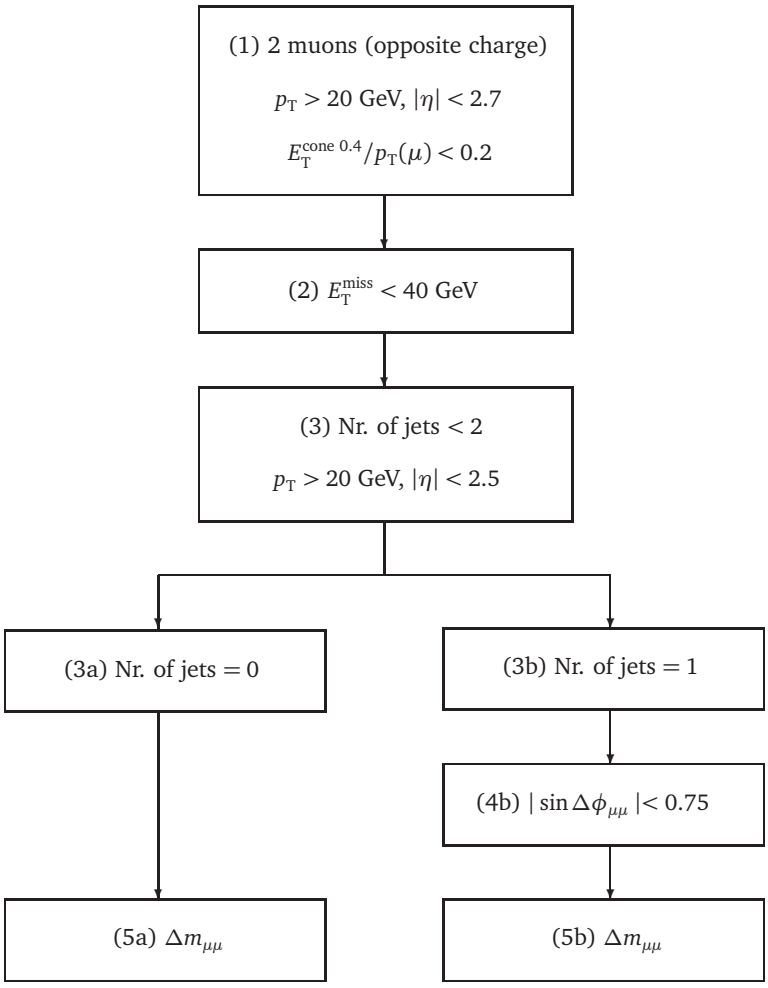

Figure 4.8: Analysis diagram. The analysis is split in two branches, considering 0 or 1 jets in the final state with no constraint on the jet flavor.

Figure 4.8 shows a diagram of the event selection used in the analysis, with cuts on muon multiplicity, $|\eta|$ and transverse momentum, muon isolation, $E_{\mathrm{T}}^{\mathrm{miss}}$ and jet multiplicity, $|\eta|$ and transverse momentum. Specifically, these are the cuts employed in the analysis:

1. Events with at least two muons with opposite charge, $p_{\mathrm{T}} > 20$ GeV and $|\eta| < 2.7$ are selected. This way, high-p_{T} muons potentially coming from the $h/A/H$ decay are considered. Figure 4.9 shows the muon multiplicity for signal and background events separately. The most important backgrounds after applying this cut are Z production in association with light jets and $t\bar{t}$. Note that an important fraction of the background is already rejected with this simple cut, which turns out to be very efficient in the rejection of the two dominant backgrounds.

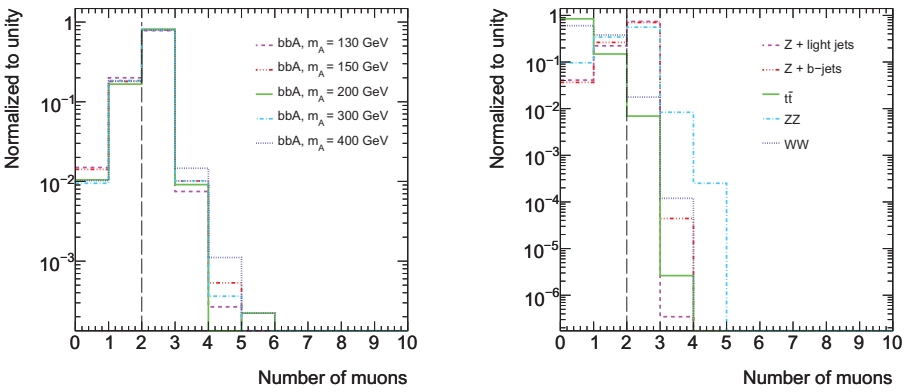

(a) Signal data samples.

(b) Background data samples.

Figure 4.9: Number of muons ($p_{\mathrm{T}} > 20$ GeV and $|\eta| < 2.7$) before applying any cut. The vertical dashed lines indicate the muon multiplicity value used to define cut 1.

Muon isolation is also required, limiting the energy deposition in a cone around the selected muons (see Figure 4.10). The energy deposited in the calorimeter cells in a cone of dimensions $\Delta R = 0.4$ around the muon normalized by the muon p_{T} is required to be $E_{\mathrm{T}}^{\mathrm{cone}\,0.4}/p_{\mathrm{T}}(\mu) < 0.2$. This cut is used to discard the muons coming from hadronic showers. The transverse energy in the cone is computed as $\Sigma_{\mathrm{Cells}}^{\Delta R<0.4} E_{\mathrm{T}} - E_{\mu}^{\mathrm{loss}}$. With this cut, events with muons

overlapped with jets are removed from the analysis. It is especially efficient for rejecting $t\bar{t}$ background where muons can be produced in b-quark decays.

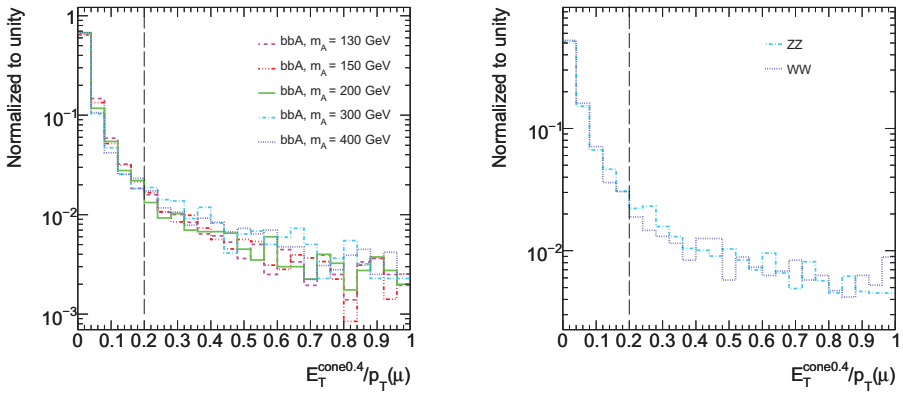

(a) Signal data samples.

(b) ZZ and WW diboson samples.

Figure 4.10: Muon isolation cut. The vertical dashed lines indicate the $E_{\mathrm{T}}^{\mathrm{cone}\ 0.4}/p_{\mathrm{T}}(\mu)$ value used to define cut 1. In the $t\bar{t}$ and $Z \to \mu\mu$ Atlfast data samples, the muons are a priori isolated, no isolation variable is available.

2. Events with $E_{\mathrm{T}}^{\mathrm{miss}} < 40$ GeV are selected. This cut rejects mostly the $t\bar{t}$ background, characterized by high $E_{\mathrm{T}}^{\mathrm{miss}}$ coming from the neutrinos involved in the top-quark decay. Figure 4.11 shows the $E_{\mathrm{T}}^{\mathrm{miss}}$ distributions for signal and background samples before applying this cut (i.e., after cut 1). The signals are clearly peaked at low $E_{\mathrm{T}}^{\mathrm{miss}}$ values while, for the $t\bar{t}$ distribution a plateau is observed at $E_{\mathrm{T}}^{\mathrm{miss}} > 40$ GeV, coinciding with the applied cut value. The same is true also for WW but the rest of the backgrounds remain almost unaffected by this cut. Note that Z+jets is now the dominant background after the two first cuts, which indeed removed a large fraction of the $t\bar{t}$ background.

3. Events with less than two jets ($p_{\mathrm{T}} > 20$ GeV and $|\eta| < 2.5$) are selected. This cut rejects most of the remaining $t\bar{t}$ and Z backgrounds. Figure 4.12 shows the jet multiplicity for signal and background samples. Although an important fraction of the signal has also two or more jets, the loss of the signal efficiency is compensated by the background reduction. Note that at this stage of the analysis the jet multiplicity for the $t\bar{t}$ sample peaks at 2-3 jets and therefore most of the $t\bar{t}$ events are removed here. One should remark

a possible sensitivity of this cut with respect to the additional jets from the pile-up, resulting in a degradation of the signal efficiency. However, as mentioned above, at the early stage of the data taking the pile-up contribution is expected to be small.

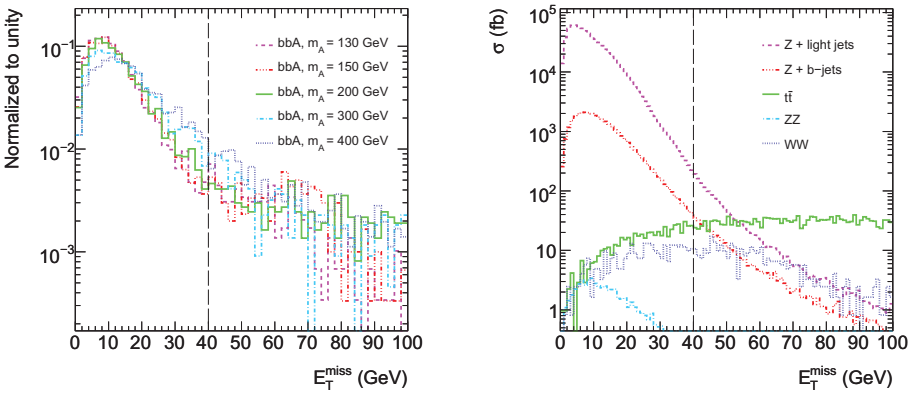

(a) Signal data samples. (b) Background data samples.

Figure 4.11: Distribution of $E_{\mathrm{T}}^{\mathrm{miss}}$ after cut 1 is applied. The vertical dashed lines indicate the $E_{\mathrm{T}}^{\mathrm{miss}}$ value used to define cut 2.

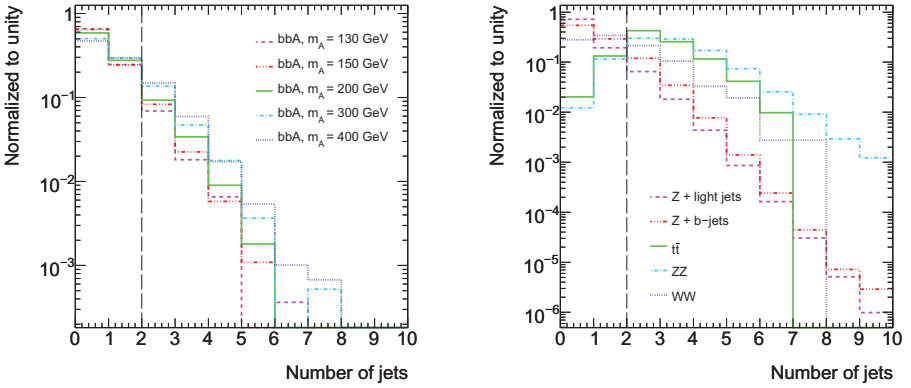

(a) Signal data samples. (b) Background data samples.

Figure 4.12: Number of jets ($p_{\mathrm{T}} > 20$ GeV and $|\eta| < 2.5$) after applying cut 2. The vertical dashed lines indicate the jet multiplicity value used to define cut 3.

Figure 4.13 shows the muon p_T spectrum for all the events passing the already described cuts. Harder muons are found for signal samples with increasing Higgs mass, although muons with low p_T are still present even at high m_A. In all the background events muons are concentrated in the low-p_T region with tails in the high momentum region.

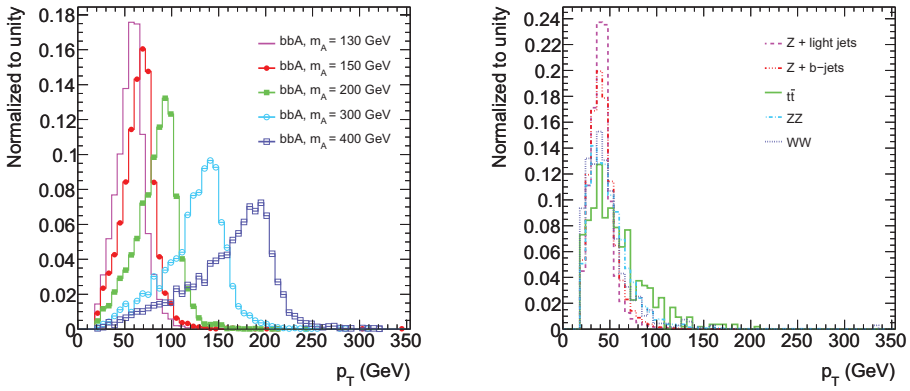

(a) Signal data samples.

(b) Background data samples.

Figure 4.13: Normalized muon transverse momentum distributions for signal and background data samples after applying cut 3.

At this point, the analysis is split in two different branches according to the number of jets, distinguishing between 0-jet and 1-jet events, regardless of the jet flavor. Note that the background level mainly produced by the Z+light jets is about a factor of 3 higher for the 0-jet case but the amount of signal events is also larger by a factor of 2-4 compared to the 1-jet case.

4. An additional cut on the angular separation between the two muons is required only in the 1-jet analysis. Due to the fact that two muons from the decay of the same particle tend to be emitted back-to-back and that if they come from two different particles their directions are not correlated, this variable can be used for background rejection. Figure 4.14 shows the $\sin\Delta\phi_{\mu\mu}$ distribution for signal and background samples. The condition applied is $|\sin\Delta\phi_{\mu\mu}| < 0.75$. Signal events are concentrated close to $\sin\Delta\phi_{\mu\mu} \sim 0$ and this cut has small impact on them. The $\sin\Delta\phi_{\mu\mu}$ distributions for background samples are quite flat, but a slight accumulation of events at $|\sin\Delta\phi_{\mu\mu}| \sim 1$

is seen. Hence, with this cut, more than 25% of the background can be removed.

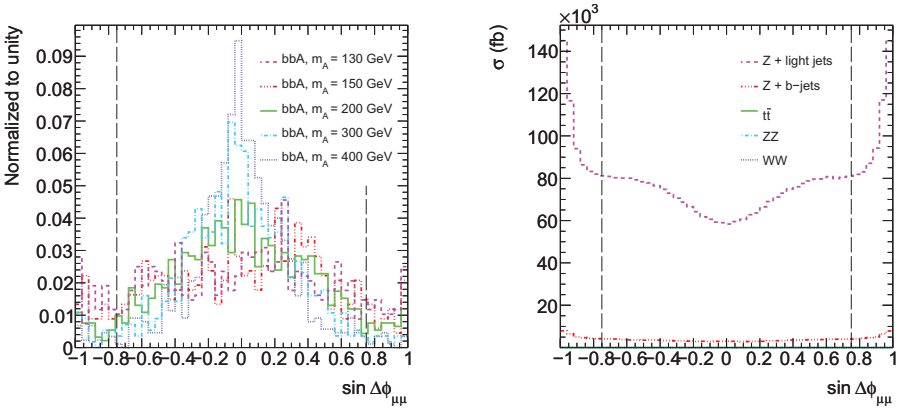

(a) Signal data samples.

(b) Background data samples.

Figure 4.14: Distributions of $\sin\Delta\phi_{\mu\mu}$ for signal and background samples after applying cut 3. The vertical dashed lines indicate the value used to define cut 4.

5. Finally, the last cut selects the events with dimuon invariant mass in a mass window four times larger than the A-boson reconstructed width, that is $\Delta m_{\mu\mu} = m_A \pm 2\sigma_{\mu\mu}$. In order to evaluate the width of the Higgs resonance, due to natural width and the detector resolution, a Gaussian is fitted to the invariant mass distributions for signal samples, as Figure 4.15 shows.

The results obtained after applying all the cuts described above are summarized in Tables 4.6-4.8, which show the cut flow for signal and background samples. The signal samples used in Table 4.6 correspond to several values of m_A, always with $\tan\beta = 30$. In the background case, apart from the total number of events in the whole mass range (Table 4.7), the events in a $\Delta m_{\mu\mu}$ window around the signal mass are also shown (Table 4.8).

The first conclusion to draw from the tables is that only 50% of the signal is lost through the event selection procedure, while the backgrounds are reduced by a factor ranging from 2.5 to 10^4, depending on the sample considered. The most reduced sample is $t\bar{t}$, since only 1% of the events contains a final state with two muons, and in those cases $E_{\mathrm{T}}^{\mathrm{miss}}$ from the semileptonic W decay is also present.

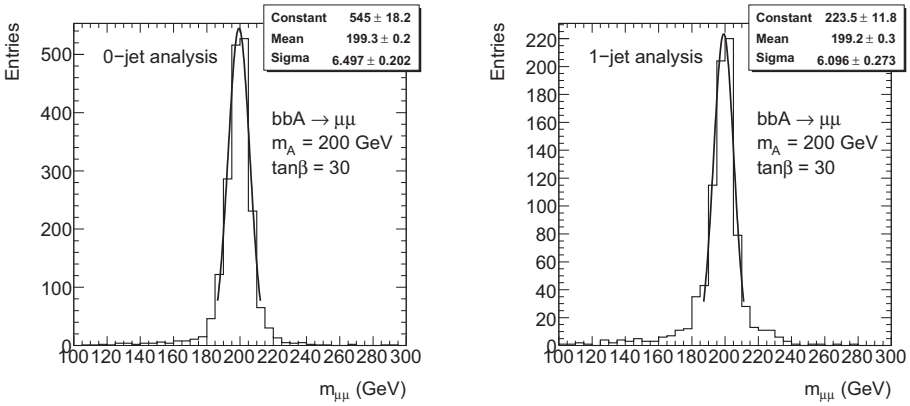

Figure 4.15: Dimuon invariant mass distributions for the $b\bar{b}A \to \mu\mu$ process after applying the selection cuts in the 0-jet and 1-jet analyses, where the A boson has $m_A = 150$ GeV and $\tan\beta = 30$. The distributions have been fitted with a single Gaussian.

Table 4.6: Effective cross-section for the signal processes (in fb) for different values of m_A and $\tan\beta = 30$ after each selection cut, obtained for the analysis without the use of the b-tagging requirement.

Cut	$b\bar{b}A \to \mu\mu$ (fb)					
	110 GeV	130 GeV	150 GeV	200 GeV	300 GeV	400 GeV
0.	182.97	112.43	72.85	27.58	6.22	1.78
1.	141.23	88.09	58.47	22.59	4.99	1.43
2.	133.34	82.51	53.62	20.40	4.33	1.17
3.	121.79	74.74	47.60	17.58	3.44	0.90
3a.	92.40	54.36	34.50	11.95	2.17	0.55
5a.	78.16	46.50	27.51	10.12	1.89	0.48
3b.	29.39	20.39	13.09	5.63	1.27	0.35
4b.	23.27	16.61	11.19	5.15	1.20	0.33
5b.	18.13	13.67	8.94	4.02	0.96	0.28

The processes which have been less affected by the event selection are processes containing a Z boson, although most of the remaining events in these samples will be populating the resonance peak at 90 GeV, away from the high-m_A signal region. Indeed, only a small fraction of the total background lies within the $\Delta m_{\mu\mu}$ window around the Higgs signals.

Table 4.7: Effective cross-section for the background processes (in fb) after each selection cut, obtained for the analysis without the use of the b-tagging requirement.

Cut	Z+light jets (fb)	Z+b-jets (fb)	$t\bar{t}$ (fb)	$ZZ \to b\bar{b}\mu\mu$ (fb)	WW (fb)
0.	996845	47802	833000	109.324	40880
1.	733960	33523	5648	60.948	673
2.	732441	33146	1354	55.837	298
3.	667670	27724	228	26.169	276
3a.	526455	18006	28.65	7.243	204.40
3b.	141215	9718	199.30	18.927	71.95
4b.	93022	6116	117.40	10.768	49.87

Table 4.8: Effective cross-section for the background processes (in fb) in the $\Delta m_{\mu\mu}$ windows around the signal points in Table 4.6.

m_A (GeV)	Z+light jets (fb)	Z+b-jets (fb)	$t\bar{t}$ (fb)	$ZZ \to b\bar{b}\mu\mu$ (fb)	WW (fb)
110	7857	227.63	2.18	0.164	15.53
130	2420	60.80	2.18	0.041	14.72
150	1035	22.56	1.25	0.014	19.62
200	373	4.68	1.87	0.014	11.45
300	107	1.05	0.93	<0.014	0.82
400	45	0.57	0.31	0.014	1.64
110	613	28.87	9.65	0.191	4.91
130	613	28.87	9.65	0.096	<0.82
150	291	13.34	8.41	0.027	4.09
200	126	4.59	4.05	<0.014	3.27
300	44	1.10	2.49	<0.014	0.82
400	20	0.24	0.31	0.014	<0.82

Figure 4.16 shows the dimuon invariant mass distributions for all backgrounds and three selected signal samples. After the analysis cuts explained above, the most significant background over the whole mass range is Z+light jets (even 200 GeV away from the Z peak), with Z+b-jets more than one order of magnitude below for the two analysis branches considered. Note that in Table 4.6 the number of signal events available is reduced as the Higgs mass increases. Therefore, although the background level is strongly suppressed for high $m_{\mu\mu}$, the reduction in the number of signal events will still make the signal discovery difficult. The

Z+light jet background in the 1-jet final state can be substantially reduced (by a factor of 10) by the b-tagging requirement, while other background contributions remain rather similar.

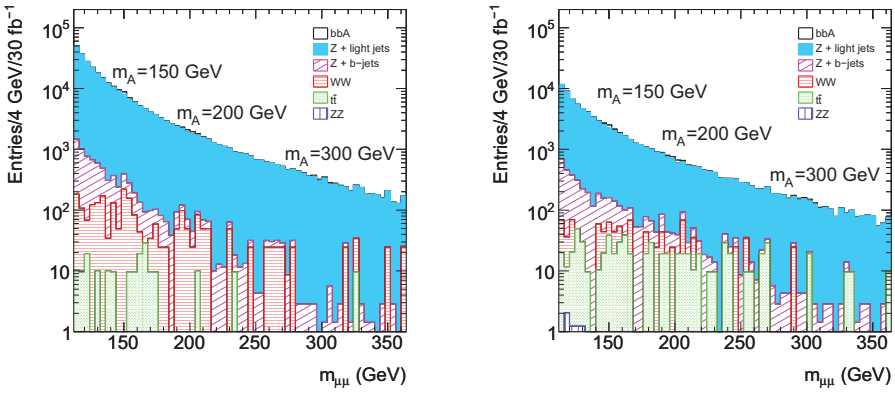

Figure 4.16: Dimuon invariant mass distributions for the sum of the main backgrounds and A-boson signal at $m_A = 150$, 200 and 300 GeV ($\tan\beta = 30$) for an integrated luminosity of 30 fb^{-1} for 0-jet (left) and 1-jet (right) analysis. Note that the signal production rates have been summed due to the A/H mass degeneracy.

4.7 Parametrization of the Background-Only Distribution

Fits are performed to the background-only (BO) distribution, that is, the dimuon invariant mass distribution resulting of the sum of all the backgrounds involved in the analysis. The function used for these fits is the following:

$$f_B(x) = \frac{a_1}{x}\left[\frac{1}{(x^2 - M_Z^2) + M_Z^2\Gamma_Z^2} + a_2\, e^{-a_3 x}\right] \tag{4.15}$$

where x stands for the dimuon invariant mass. This function contains a Breit-Wigner term to describe the Z resonance in the low-mass region and an exponential term to properly describe the high-mass region. The M_Z and Γ_Z variables correspond to the Z mass and width respectively, characterizing the Z-boson res-

onance. The fit is performed with three free parameters a_1, a_2 and a_3, where the first two parameters increase with the luminosity and the third parameter a_3 regulates the exponential slope.

Figure 4.17 shows the results of the fit performed for the case of 0 and 1 jets in the final state for an integrated luminosity of 1 fb^{-1}. A good agreement is found in the $m_{\mu\mu}$ window between 100 GeV and 500 GeV, proving that the function selected can model the actual background distributions correctly.

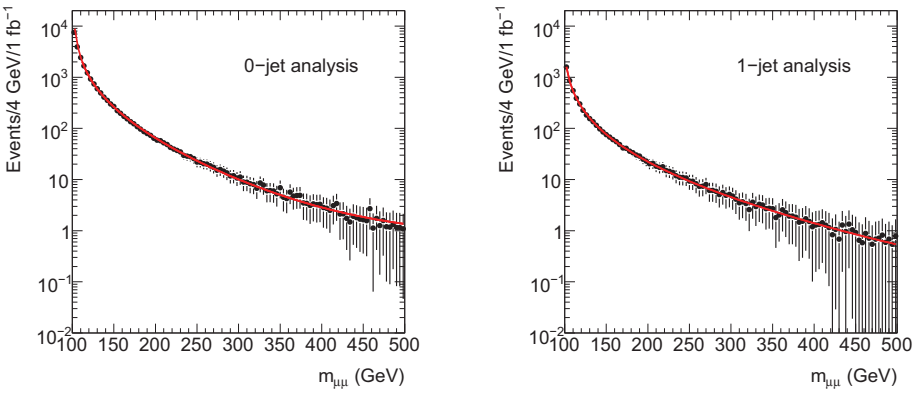

Figure 4.17: Fits performed on the background-only distributions in a mass window from 100 to 500 GeV, obtained for the 0-jet (left) and 1-jet (right) analysis for an integrated luminosity of 1 fb^{-1}. Fit results (compare Eq. (4.15)) are shown with a red line.

Two strategies have been developed in ATLAS to estimate the backgrounds contributions from the measured data. The first method makes use of the fact that the branching ratio for A/H boson decays into two electrons is negligible compared to the dimuon decay channel. Therefore, since one doesn't expect any signal in the dielectron final state, one can use this signature to determine the total background contribution [66].

Additionally, the signatures with one electron and one muon in the final state provide the contribution of the $t\bar{t}$ background alone, since the Z+jet processes do not contribute to this final state. Thus, one can separately measure the two background contributions. The background estimation based on the e^+e^- channel has been discussed in detail in Ref. [66]. Good agreement has been demonstrated

between the dilepton invariant mass distributions for the $Z \to \mu\mu$ and the $Z \to ee$ processes. The total number of background events selected in each of the two final states will be different due to different reconstruction efficiencies for muons and electrons. However, since these efficiencies can be experimentally measured with an accuracy of few percent.

The parameters $a_{2,3}$ describing the exponential part in Eq. (4.15) can be determined by the fit on the background estimated from data, as described above.

4.7.1 Estimation of the Background Fluctuations

The statistical uncertainty in the background should be evaluated in order to properly compute the discovery significance. Statistical fluctuations in the background level represented by the fits in Figure 4.17 are the main source of the background uncertainty, although the errors in the fit parameters representing the exponential part of the background (a_2 and a_3) can also be significant, especially at high $m_{\mu\mu}$. Additional sources of systematics in the shape and normalization are jet energy scale and muon resolution uncertainties.

The estimation of the background uncertainty due to statistical fluctuations has been performed by means of a large number of Monte Carlo pseudoexperiments (10^5) at different integrated luminosities (from 3 to 15 fb^{-1}). For each pseudoexperiment, the integral of the fit to the background shape obtained within a $m_A \pm 2\sigma_A$ window (fitted background) is compared with the integral of the fit in Figure 4.17 (expected background) since this was the function used to generate the toy Monte Carlo.

Figures 4.18 and 4.19 show the relative background difference for an integrated luminosity of 3 fb^{-1} and 15 fb^{-1} and both analysis branches considered. The fluctuations in the background are at the level of few percent and, as expected, are reduced as the luminosity increases due to the fact that more events are present in the distribution. At a fixed integrated luminosity, the fluctuations are smaller for the 0-jet analysis due the much higher background level in this case.

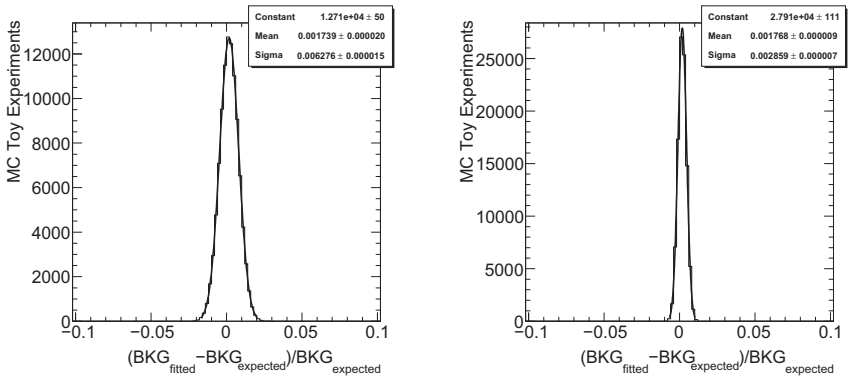

Figure 4.18: Relative difference between the background levels obtained from the fit to Figure 4.17(left) ($BKG_{expected}$) and to Monte Carlo pseudoexperiments (BKG_{fitted}) for an integrated luminosity of 3 fb^{-1} (left) and 15 fb^{-1} (right) in the 0-jet analysis.

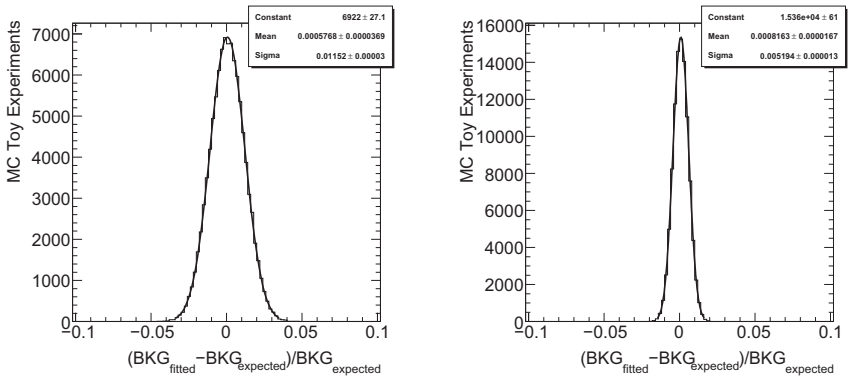

Figure 4.19: Relative difference between the background levels obtained from the fit to Figure 4.17(right) ($BKG_{expected}$) and to Monte Carlo pseudoexperiments (BKG_{fitted}) for an integrated luminosity of 3 fb^{-1} (left) and 15 fb^{-1} (right) in the 1-jet analysis.

The background uncertainty for a given luminosity is taken as the σ of the Gaussian fit to the distributions in Figures 4.18 and 4.19. Indeed, these uncertainties follow a $1/\sqrt{\mathscr{L}}$ dependence, as shown in Figure 4.20. With these results, the background uncertainty can be parametrized as $\sim 1\%/\sqrt{\mathscr{L}(\mathrm{fb}^{-1})}$ for the 0-jet analysis and $\sim 2\%/\sqrt{\mathscr{L}(\mathrm{fb}^{-1})}$ for the 1-jet analysis.

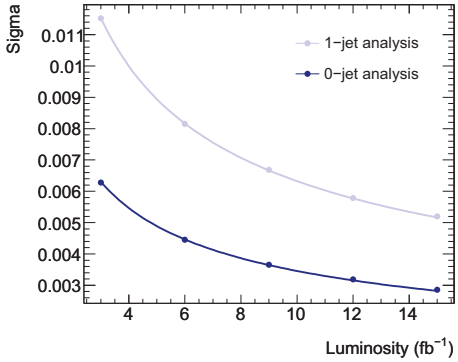

Figure 4.20: Background uncertainty as a function of the integrated luminosity for 0-jet and 1-jet analysis. $1/\sqrt{\mathscr{L}}$ function is fitted to the data points.

4.8 Parametrization of the Signal-plus-Background Distribution

Once a functional form for the background has been obtained together with its expected uncertainty as a function of the luminosity, a fit should also be obtained for the signal-plus-background (SpB) distributions. The function selected in this case is based on Eq. (4.15) and has the following form:

$$f_{\mathrm{SB}}(x) = f_{\mathrm{B}} + p_1 f_{\mathrm{S}} = f_{\mathrm{B}} + p_1 \frac{1}{\sigma_A \sqrt{2\pi}} \exp\left(-\frac{(x-m_A)^2}{2\sigma_A^2}\right) \tag{4.16}$$

where x stands for the dimuon invariant mass, f_{B} is the background term described by Eq. (4.15) and the excess created by the Higgs boson signal is modeled by f_{S}, which is a Gaussian centered in the A-boson mass (m_A) and characterized by its reconstructed width (σ_A).

The fits performed for $m_A = 150$ GeV, $\tan\beta = 60$ and for 0 and 1 jets in the final state are shown in Figure 4.21 for an integrated luminosity of 1 fb^{-1}. Although the A/H peak can hardly be seen in Figure 4.16, fits which distinguish those tiny signals from the background can be performed.

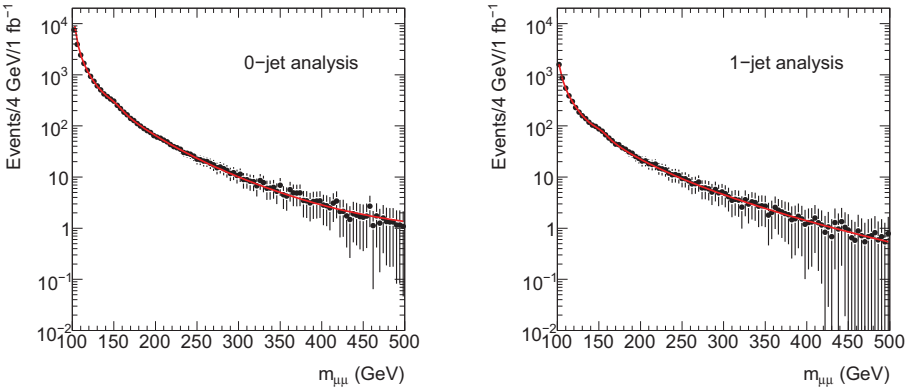

Figure 4.21: Fits performed on the signal-plus-background distributions in a mass window from 100 GeV to 500 GeV, obtained for the 0-jet (left) and 1-jet (right) analysis for an integrated luminosity of 1 fb^{-1}, $m_A = 150$ GeV and $\tan\beta = 60$. Fit results (compare Eq. (4.16)) are shown with a red line.

4.9 Significance Estimation

The statistical significance of an expected signal can be evaluated in several ways, and two different approaches will be used in the present Chapter. Both of them take advantage of the knowledge of the expected signal and background spectra and evaluates the log Likelihood Ratio of the background-only and signal-plus-background hypothesis by means of toy Monte Carlo pseudoexperiments [54]. In the first case, the mass of the resonance is assumed to be known and fixed in the analysis to the values used for the data generation (fixed-mass approach). In the second case, the mass of the resonance is assumed to be unknown and therefore this parameter is a free fit parameter (floating-mass approach).

4.9.1 Results with Fixed-Mass Fits

The significance of the $h/A/H$ signal at a given luminosity can be evaluated making use of the fits performed in Sections 4.7 and 4.8. The mass degeneracy for the signal is taken into account by summing up the contributions of A and H resonances for masses $m_A > 130$ GeV. In first place, a large number of toy Monte Carlo

pseudoexperiments are generated using the background-only function. The number of generated events is given by the Poisson distribution centered in the integral of the background-only invariant mass distribution in 100 GeV$< m_{\mu\mu} <$ 500 GeV, after scaling by the corresponding luminosity.

In each pseudoexperiment, the resulting distribution is fitted with the background-only function (Eq. (4.15)), as well as the signal-plus-background function (Eq. (4.16)), obtaining the corresponding log Likelihood values in both cases. The log Likelihood Ratio is then computed as the difference between the two log Likelihood values. The same procedure is repeated for pseudoexperiments generated with the signal-plus-background distribution, obtaining the log Likelihood Ratio for signal-plus-background distributions.

The mass of the resonance can be set to a constant value during the fitting procedure (fixed-mass approach) if the signal mass is well known. Nevertheless, it can also be a free parameter in the fit (floating-mass approach), although additional constraints are also imposed to the rest of the parameters in this case (see Section 4.9.2). As an example, Figure 4.22 shows the invariant mass distributions in two of those pseudoexperiments at an integrated luminosity of $\mathscr{L} = 30$ fb^{-1}, fitted to background-only and signal-plus-background models, respectively.

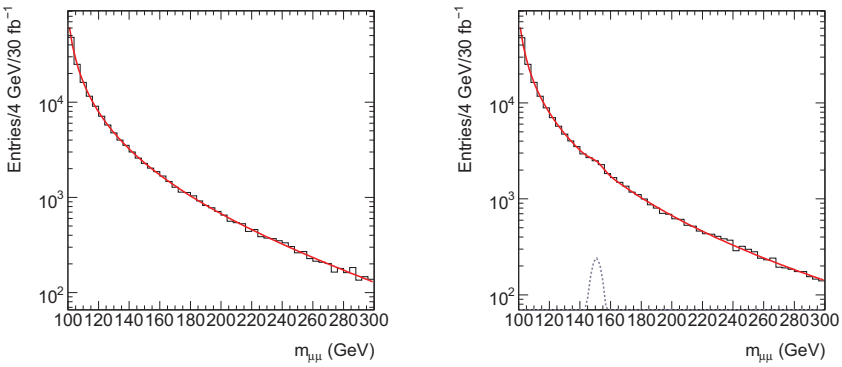

Figure 4.22: Example of a background-only (left) and a signal-plus-background (right) pseudoexperiments for $m_A = 150$ GeV and $\tan\beta = 30$ at $\mathscr{L} = 30$ fb^{-1} (1-jet analysis). Fits are performed with the same function used for the toy Monte Carlo generation. The signal component in the signal-plus-background case is shown with a dashed line.

The probability of a Type-II error is obtained as the fraction of background-only pseudoexperiments whose log Likelihood Ratio is larger than the median of the log Likelihood Ratio for signal-plus-background pseudoexperiments. This p-value is then transformed into significance of an observation (number of sigmas, $S = n\sigma$) following the conventions explained in Section 4.3.

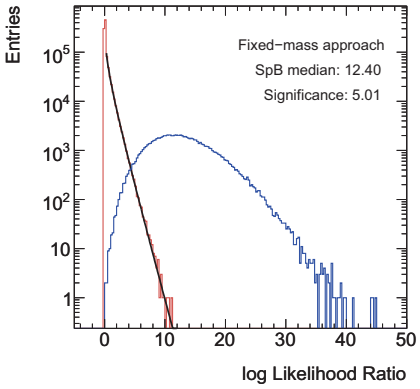

(a) $m_A = 130$ GeV, $\mathscr{L} = 30$ fb^{-1}, 0-jet analysis.

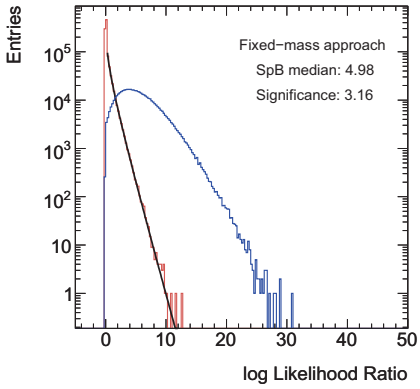

(b) $m_A = 130$ GeV, $\mathscr{L} = 30$ fb^{-1}, 1-jet analysis.

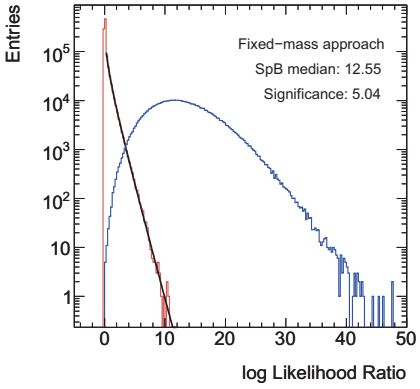

(c) $m_A = 150$ GeV, $\mathscr{L} = 40$ fb^{-1}, 0-jet analysis.

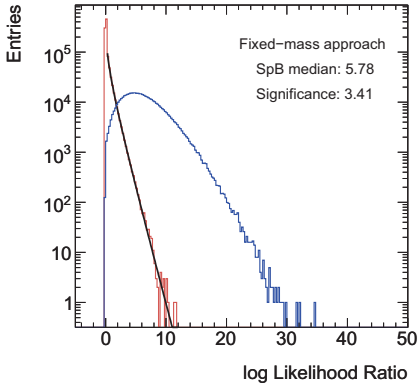

(d) $m_A = 150$ GeV, $\mathscr{L} = 40$ fb^{-1}, 1-jet analysis.

Figure 4.23: Log Likelihood Ratio distributions for background-only (red line) and signal-plus-background (blue line) pseudoexperiments computed for the 0-jet (left) and 1-jet (right) analysis using the fixed-mass approach. The background-only distributions are fitted to a χ^2 distribution for one degree of freedom to extrapolate the end of the tail and provide an accurate estimation of the signal significance.

Figure 4.23 shows the log Likelihood Ratio distributions for $m_A = 130$ GeV, $\tan\beta = 30$ at $\mathscr{L} = 30$ fb^{-1} and $m_A = 150$ GeV, $\tan\beta = 30$ at $\mathscr{L} = 40$ fb^{-1}, respectively. To obtain these results, 10^6 toy Monte Carlo pseudoexperiments have been generated for background-only and 10^5 for signal-plus-background. For both mass points, the outcome from background-only experiments is concentrated at very low values of the Likelihood Ratio since they are more likely described by the background-only model. On the other hand the log Likelihood Ratio for signal-plus-background pseudoexperiments for $m_A = 130$ at $\tan\beta = 30$ and the 1-jet case, although also concentrated in the low log Likelihood Ratio region, extends to higher values with the distribution median situated at 4.98, leading to a significance of 3.16. In the 0-jet case, for $m_A = 130$ GeV at $\tan\beta = 30$, the signal-plus-background log Likelihood Ratios are spread up to values of 40, having its median in 12.40 which leads to a significance of 5.01.

Figure 4.24 shows the log Likelihood Ratio distributions obtained for the signal-plus-background pseudoexperiments, in particular for $m_A = 150$ GeV and $\tan\beta = 30$, at different luminosities. Note how the signal-plus-background distribution is getting more symmetrical as the luminosity increases.

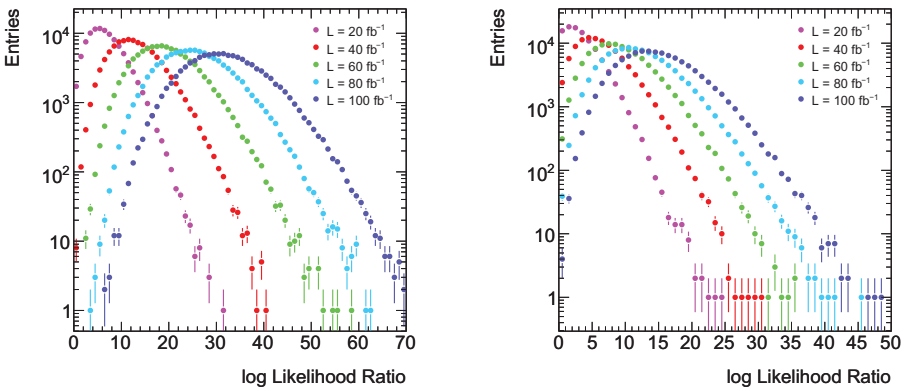

Figure 4.24: Log Likelihood Ratio distributions for signal-plus-background pseudoexperiments computed for $m_A = 150$ GeV and $\tan\beta = 30$ at different integrated luminosities for the 0-jet (left) and 1-jet (right) analysis.

The dependence of the significance with the $\tan\beta$ parameter can be found in Figure 4.25 for two different values of m_A and an integrated luminosity of $\mathscr{L} =$

10 fb^{-1}. The results obtained for $\tan\beta = 30$ have been scaled to different $\tan\beta$ values by considering that the production cross-section and the resonance width are approximately proportional to $\tan^2\beta$. The significance increases as a function of $\tan\beta$ because the larger amount of background events due to the increasing mass windows is compensated by the enhancement in the signal cross-section.

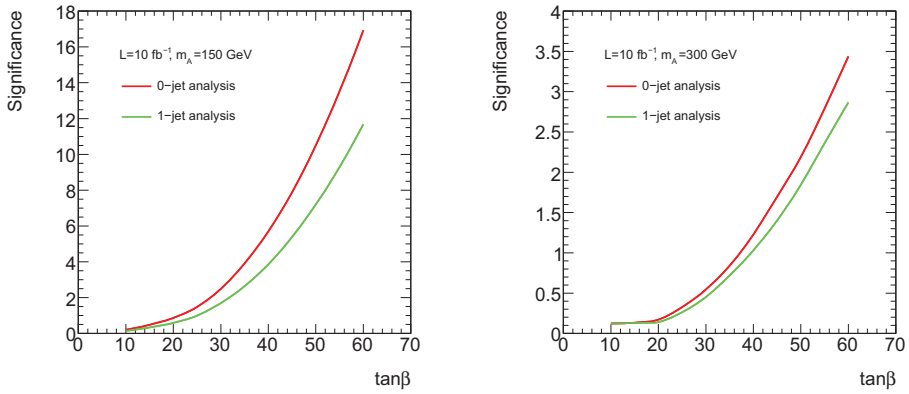

Figure 4.25: Signal significances obtained for $m_A = 150$ GeV (left) and $m_A = 300$ GeV (right) at different values of $\tan\beta$ using an integrated luminosity of 10 fb^{-1} for the 0-jet (red line) and 1-jet (green line) analysis.

Figure 4.26 shows the signal significance obtained as a function of the luminosity for different values of m_A and constant $\tan\beta = 30$ in both analysis branches using the fixed-mass approach. As expected, the significance increases smoothly with the luminosity. Note that in both cases, the earliest discovery could be achieved for $m_A = 130$ GeV. In particular, a 5σ discovery can be reached for $m_A = 130$ GeV at 30 fb^{-1} in the 0-jet analysis, while more than 100 fb^{-1} are needed for $m_A = 200$ GeV and 300 GeV.

Figure 4.27 shows the signal significance obtained as a function of the A-boson mass at fixed $\tan\beta$ and an integrated luminosity of 30 fb^{-1} for the two analyses considered. Note that for $\tan\beta = 60$, the signal significances obtained in both analyses are above 5σ for the whole mass range.

The fact that the highest sensitivity is found in the region around $m_A = 130$ GeV is also observed in the analysis which makes use of b-tagging [54]. One should

remark that for an integrated luminosity of 10 fb^{-1} and more, the b-tagging is expected to be fully functional. Thus the discovery reach presented here for the mentioned integrated luminosity can be further improved by the b-tagging requirement.

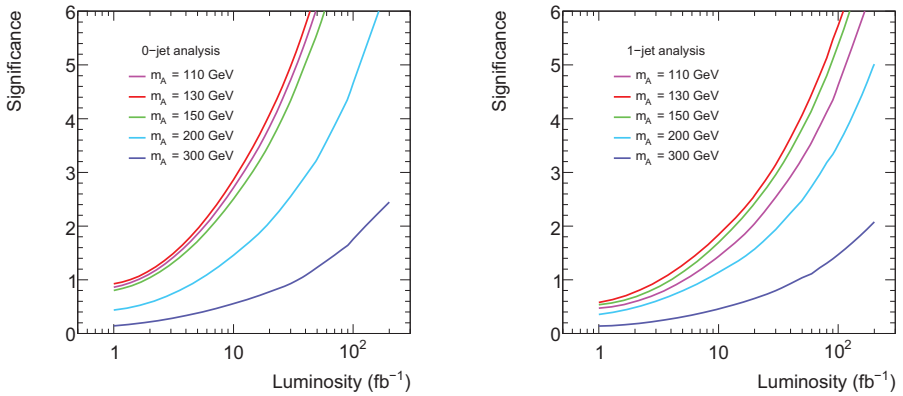

Figure 4.26: Signal significances as a function of the luminosity for different m_A values and fixed $\tan\beta = 30$. The results are obtained for both analysis branches using the fixed-mass approach.

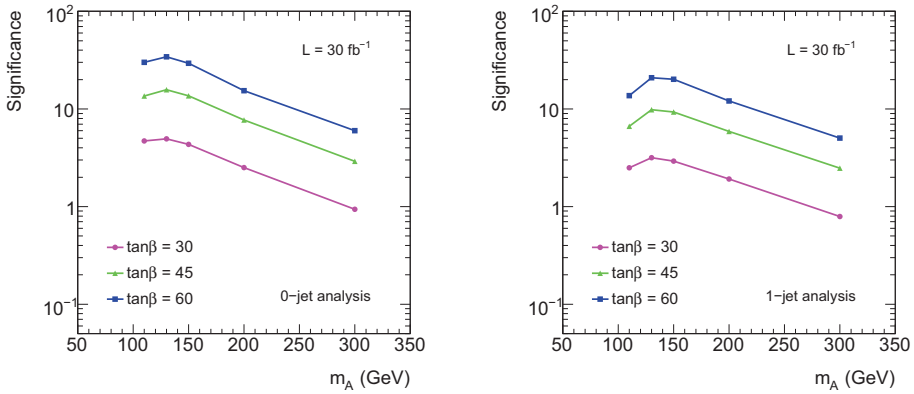

Figure 4.27: Signal significance as a function of the A-boson mass for different values of $\tan\beta$ at an integrated luminosity of 30 fb^{-1} for 0-jet (left) and 1-jet (right) analysis.

4.9.2 Results with Floating-Mass Fits

We study in this Section the look-elsewhere effect, also known as "trials factor", which needs to be taken into account in order to perform a search in the whole mass range with no prejudice on the Higgs boson mass, as will be the case with real data.

To evaluate the look-elsewhere effect, the A-boson mass is left as a free parameter running from 100 GeV to 500 GeV during the fitting procedure on the resulting toy Monte Carlo pseudoexperiments. The only constraints on the fit parameters are to have a positive signal amplitude and in addition, the A-boson width is required to be between 1 GeV and 20 GeV, range expected for this parameter when $\tan\beta = 30$.

Figure 4.28 shows the distributions of the best-fit mass obtained for the signal-plus-background pseudoexperiments with $m_A^{\text{true}} = 130$, 150 and 200 GeV, $\tan\beta = 30$ and an integrated luminosity of 30 fb^{-1}. We can observe how, with no a priori knowledge of the Higgs resonance mass, the values for the mass obtained from the fits are concentrated in the regions corresponding to the true Higgs mass generated in the toy Monte Carlo. In this way, we demonstrate that the signal-plus-background fits deliver in most of the cases the correct Higgs mass. Note the small accumulation of events at $m_A = 300$ GeV, which corresponds to the initial guess for the mass. The stability of the fit procedure can be further improved by means of the signal-free control data samples (e^+e^- final state, see Ref. [54]).

Figure 4.29 shows the distributions of pulls for the three masses considered and the two analysis branches, 0-jet and 1-jet analysis. For the A-boson mass parameter in our fits, the pulls are defined as:

$$\text{Pull}(m_A) = \frac{m_A^{\text{fit}} - m_A^{\text{true}}}{\epsilon(m_A^{\text{fit}})} \tag{4.17}$$

where m_A^{fit} and $\epsilon(m_A^{\text{fit}})$ are the values of the A-boson mass and its error obtained as parameters of the fit performed with the signal-plus-background function. Note that the distributions of the obtained pulls have mean values ~ 0 and σ values ~ 1, as expected.

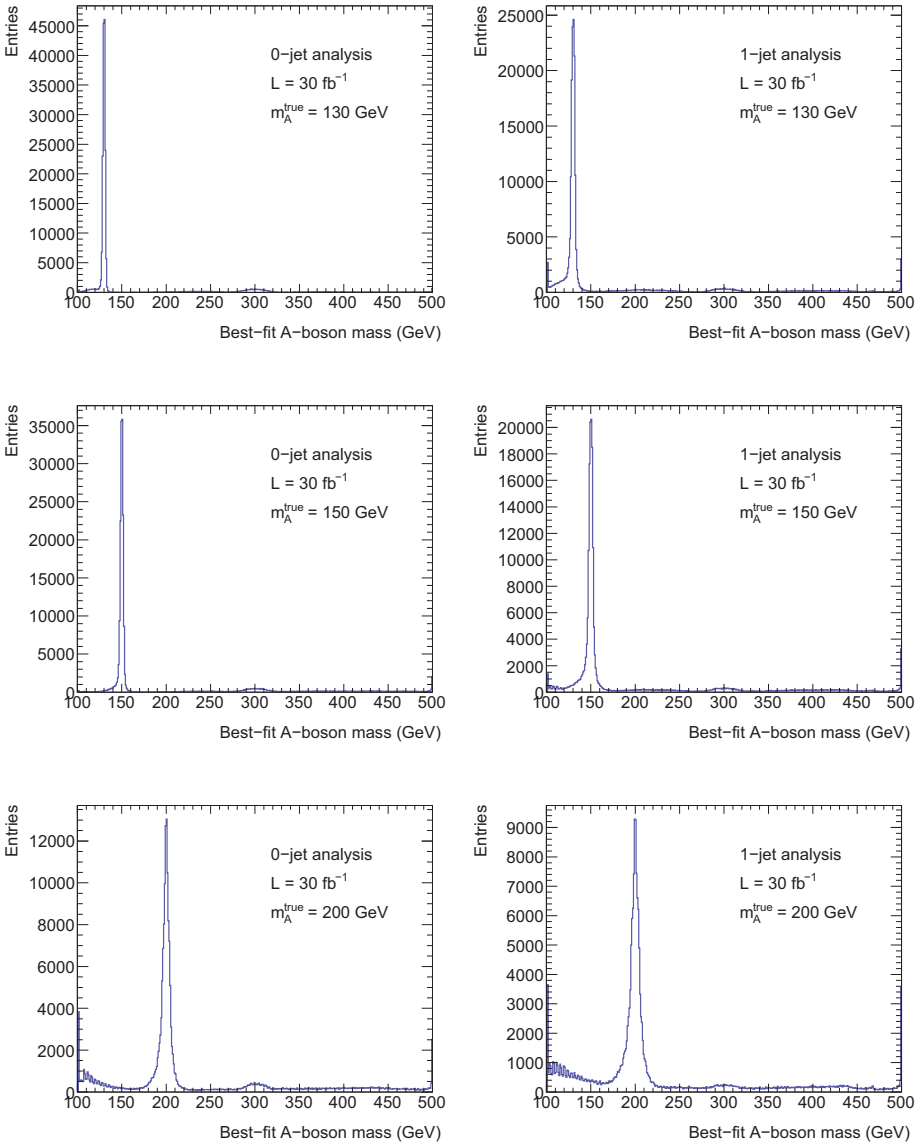

Figure 4.28: Distributions of the best-fit A-boson mass performed in the signal-plus-background pseudoexperiments for the 0-jet (left) and 1-jet (right) analysis, for $m_A^{\text{true}} = 130$ GeV (top), 150 GeV (center) and 200 GeV (bottom), $\tan\beta = 30$ and an integrated luminosity of 30 fb^{-1}.

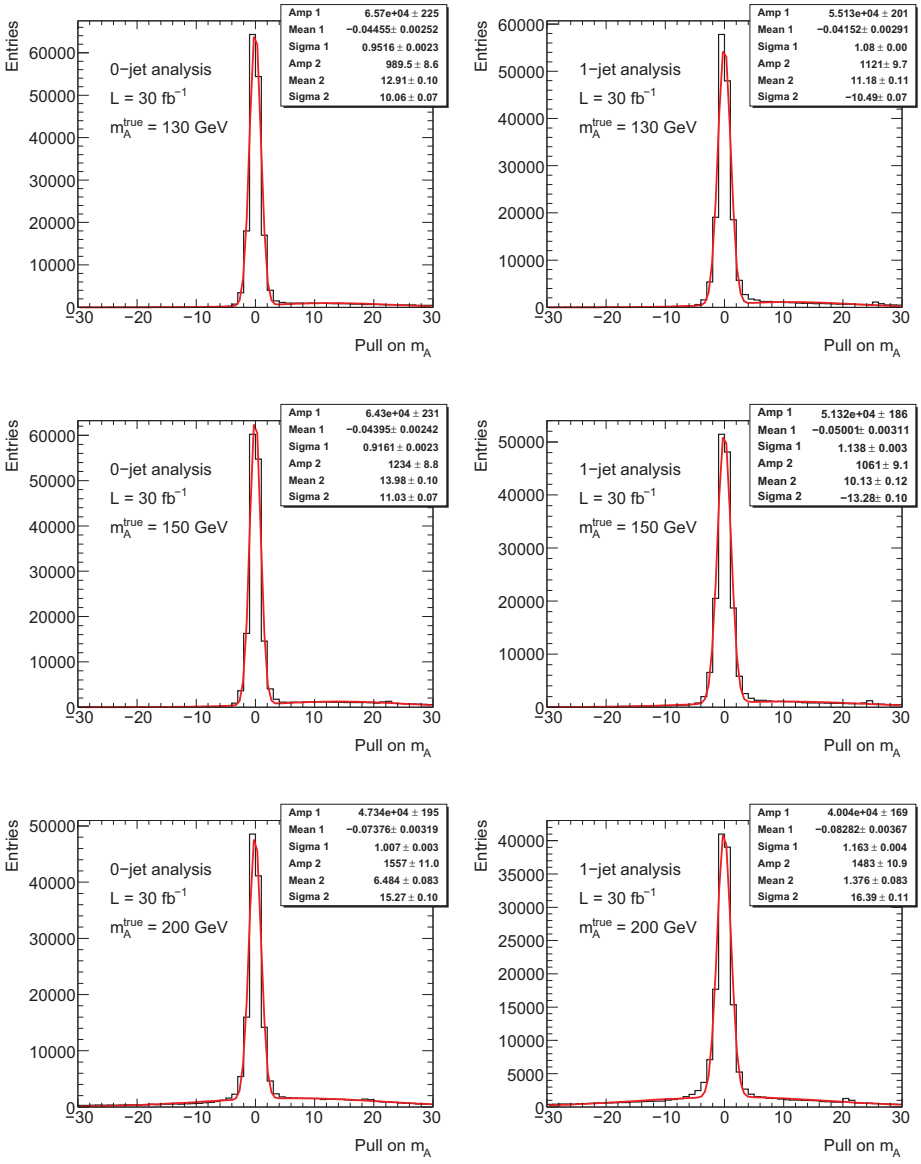

Figure 4.29: Distribution of m_A pulls for the 0-jet (left) and 1-jet (right) analysis, for $m_A^{\text{true}} =$ 130 GeV (top), 150 GeV (center) and 200 GeV (bottom), $\tan\beta = 30$ and an integrated luminosity of 30 fb^{-1}. The distributions have been fitted to a double Gaussian.

Other control test of the floating-mass fit procedure is the comparison of the best-fit *A*-boson width with the true one. The width parameter on the signal-plus-background fits is running from 1 GeV to 20 GeV, region where the reconstructed width is predicted to be for all the masses considered. In fact, the fit results are a measure of how well the width of the Higgs resonance can be reconstructed from data.

Figure 4.30 shows the distributions for the signal-plus-background best-fit of the *A*-boson width for three different masses: 130 GeV, 150 GeV and 200 GeV. The luminosity chosen for these plots corresponds to a 5σ significance in the fixed-mass approach.

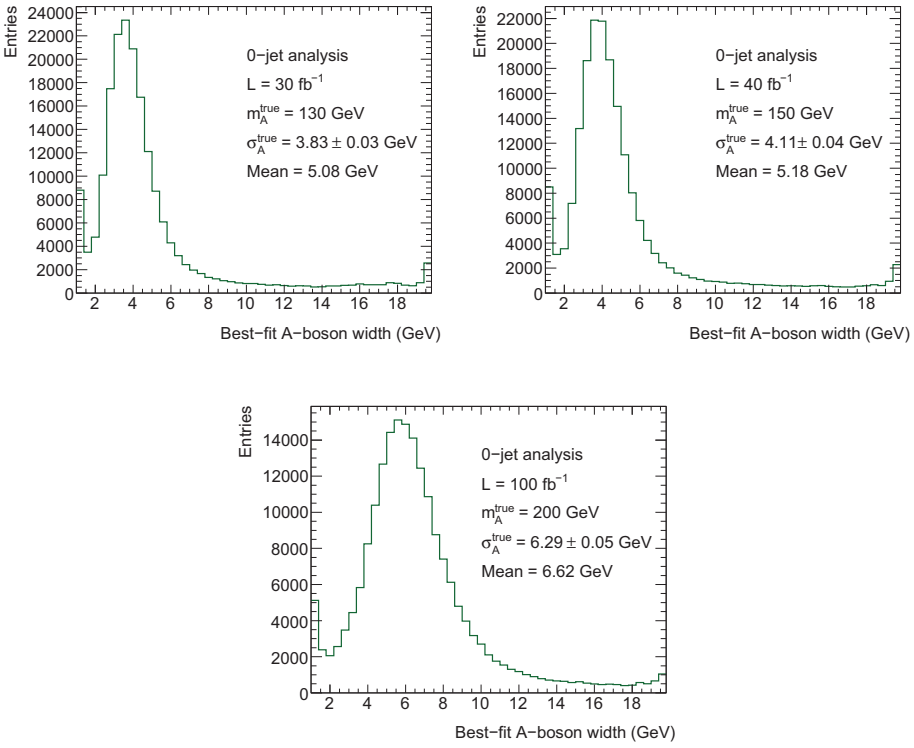

Figure 4.30: Distributions of the best-fit *A*-boson width performed in the signal-plus-background pseudoexperiments for three different masses, 130 GeV, 150 GeV and 200 GeV, at $\tan\beta = 30$ and using the 0-jet analysis.

The maxima of these distributions are very close to the input values used for toy Monte Carlo generation. Also note that the peaks observed at the edges of the mass window (1 and 20 GeV) are an expected artefact of the fitting procedure.

In addition, it is also important to mention that the mass and width values obtained for the background-only histograms have flat distributions, as expected. This way, the fluctuations of the background are fitted with the signal-plus-background function as a signal excess uniformly in the whole mass range. In this case, the best-fit of the A-boson width is distributed uniformly in the whole mass window, as no signal is present when generating the pseudoexperiments. These control checks are very important to confirm that all the region is properly scanned and the fits are free of possible bias effects.

Figure 4.31 shows the distributions of pulls for the width parameter, that is:

$$\text{Pull}(\sigma_A) = \frac{\sigma_A^{\text{fit}} - \sigma_A^{\text{true}}}{\epsilon(\sigma_A^{\text{fit}})} \tag{4.18}$$

where σ_A^{fit} and $\epsilon(\sigma_A^{\text{fit}})$ are the values of the A-boson width and its error obtained as parameters of the fit performed with the signal-plus-background function. As in the distributions of pulls for the mass parameter, values close to 0 are obtained for the mean and values close to 1 are obtained for the σ.

Note that the tails in Figure 4.30 are not present in Figure 4.31 due to the fact that when σ_A values away from the true Higgs width are obtained they are affected by larger errors.

As in the case of the fixed-mass approach, we used the probability of a Type-II error to compute the signal significance, obtained from the fraction of background-only pseudoexperiments whose log Likelihood Ratio is larger than the median of the log Likelihood Ratio for signal-plus-background. The p-value obtained is then converted via use of the inverse error function into significance, expressed in units of σ, the standard deviation of a Gaussian distribution.

Figure 4.32 shows some examples of log Likelihood Ratio distributions using the floating-mass approach for $m_A = 130$ GeV and 150 GeV at two different integrated luminosities.

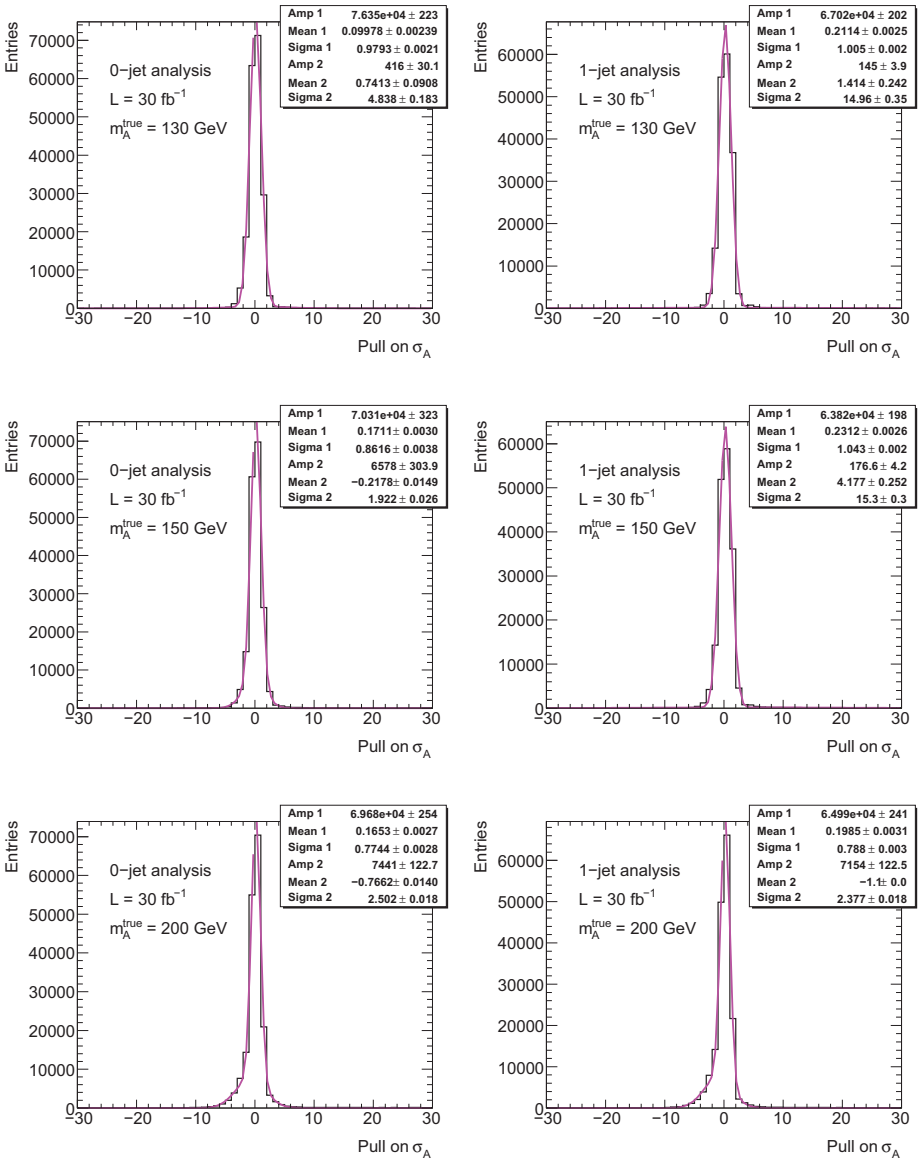

Figure 4.31: Distribution of σ_A pulls for the 0-jet (left) and 1-jet (right) analysis, for $m_A^{\text{true}} =$ 130 GeV (top), 150 GeV (center) and 200 GeV (bottom), $\tan\beta = 30$ and an integrated luminosity of 30 fb^{-1}. The distributions have been fitted to a double Gaussian.

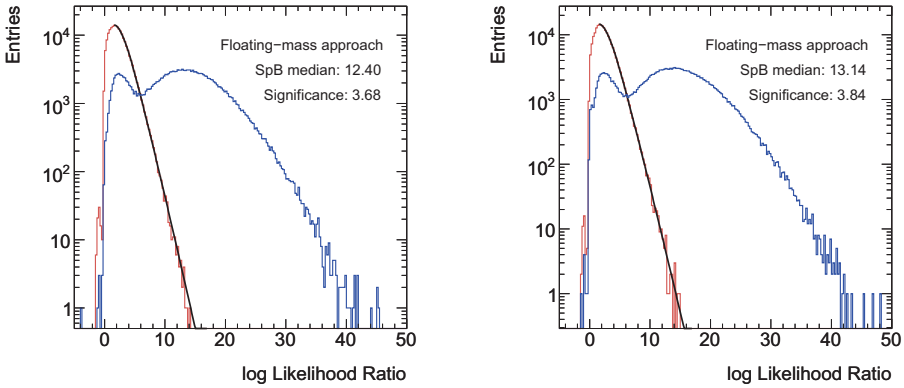

(a) $m_A = 130$ GeV, $\mathscr{L} = 30$ fb^{-1}. (b) $m_A = 150$ GeV, $\mathscr{L} = 40$ fb^{-1}.

Figure 4.32: Log Likelihood Ratio distributions for background-only (red line) and signal-plus-background (blue line) pseudoexperiments computed for the 0-jet analysis using the floating-mass approach. A combination of Gaussian and exponential function is fitted to the background-only distributions in order to extrapolate the end of the tail and provide an accurate estimation of the signal significance.

The tails of the background-only distributions are again extrapolated to higher log Likelihood Ratio values to provide an accurate estimation of the signal significance. The distributions shown have been obtained for the 0-jet analysis, where a higher significance is reached compared with the 1-jet analysis for any given luminosity. Note that the shapes for background-only and signal-plus-background are different than for the fixed-mass approach (see Figure 4.23). The background-only distribution is not as sharp as in the fixed-mass approach since upward background fluctuations anywhere in the mass range can be wrongly interpreted as a signal. The signal-plus-background distribution shows two peaks, the left one corresponding to the fits where the signal excess is not properly found and the fit is more similar to the background-only case. In particular, for $m_A = 130$ GeV we obtain a signal significance of 3.68 for an integrated luminosity of 30 fb^{-1}, compared to 5.01 in the fixed-mass approach.

Figure 4.33 shows the signal significance as a function of the luminosity for the floating-mass approach. In particular, less than $\mathscr{L} = 60$ fb^{-1} would be needed to reach a 5σ discovery for $m_A = 130$ GeV, $\tan\beta = 30$ in the 0-jet analysis. As

expected, better discovery significance can be obtained as the luminosity increases, although the results are not as good as with the fixed-mass approach (Figure 4.26).

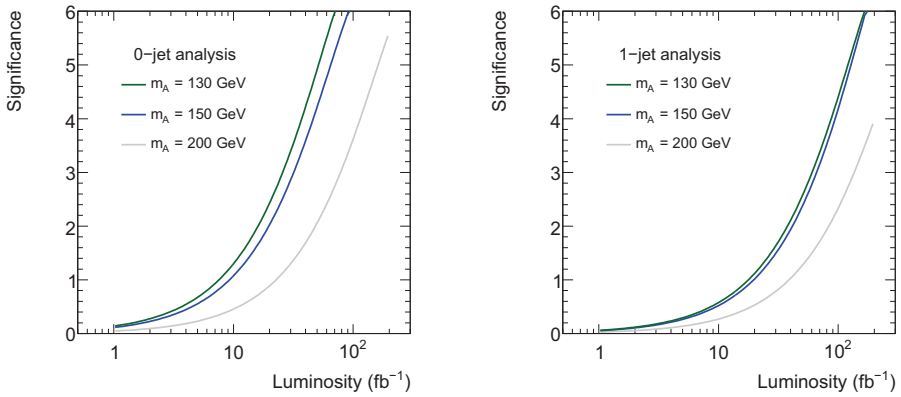

Figure 4.33: Signal significances as a function of the luminosity for different m_A values and fixed $\tan\beta = 30$. The results are obtained for both analysis branches using the floating-mass approach.

Figure 4.34 shows the ratio between the signal significance obtained with the floating- and the fixed-mass approach as a function of the luminosity for different masses.

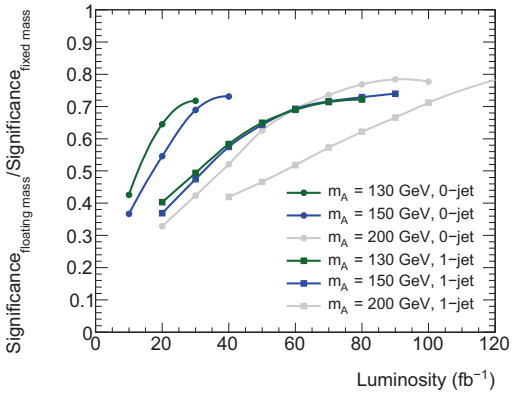

Figure 4.34: Ratio between the significances obtained for the floating- and fixed-mass approach for three different masses, $\tan\beta = 30$ and both analysis branches as a function of the integrated luminosity.

The significances obtained with the floating-mass become more similar to the fixed-mass results as the integrated luminosity increases, obtaining a ratio greater than 0.7 at the luminosity needed to achieve a 5σ significance in the fixed-mass approach. Even with no assumption on the value of the Higgs mass, the technique illustrated here can successfully detect a significant excess of signal events.

Finally, Figure 4.35 shows the difference between the reconstructed and true A-boson mass for three different mass points as a function of the true A-boson mass. These plots have been obtained at $\mathscr{L} = 30$ fb^{-1} for the two analyses considered. The error bars correspond to the median fit error and the pink band covers the width of the Gaussian fit performed on the best-fit mass distributions.

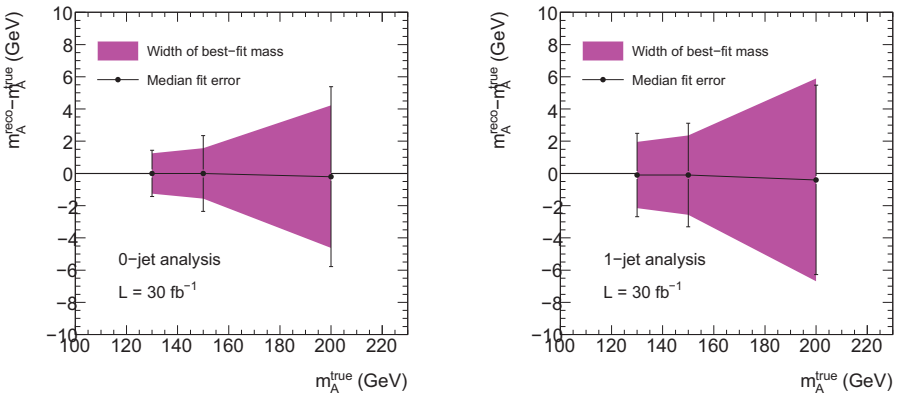

Figure 4.35: Difference between the reconstructed mass (m_A^{reco}) and the true A-boson mass (m_A^{true}) as a function of m_A^{true} computed for an integrated luminosity of 30 fb^{-1}. Results are shown for the 0-jet (left) and the 1-jet (right) analysis.

4.10 Exclusion Limits Estimation

To determine the regions of the parameter space where the Higgs boson does not exist, we need to establish the exclusion limits achievable with this analysis. The exclusion limits have been evaluated using the probablility of a Type-I error, that is, the number of signal-plus-background toy Monte Carlo pseudoexperiments whose

log Likelihood Ratio is below the median of the background-only log Likelihood Ratio distribution.

For that, the fits of Eq. (4.16) are performed to the pseudoexperiments generated under the background-only hypothesis, having m_A as a fixed parameter (fixed-mass approach). The signal-plus-background fits are performed on the background-only toy Monte Carlo pseudoexperiments under two assumptions: in the first fit, the signal normalization is left as a free parameter while in the second fit, it is fixed to the expected value in this analysis. Therefore, the Likelihood Ratio is computed as:

$$\mathrm{LR} = \frac{\mathrm{L}(N_\mathrm{s}\ \text{free})}{\mathrm{L}(N_\mathrm{s}\ \text{predicted})} \tag{4.19}$$

This way, we evaluate the probability that a downward fluctuation of a hypothesized signal is large enough to be interpreted as background-like. The p-value is computed with the median of the Likelihood Ratio distribution, p_med, and the point in the parameter space where $p_\mathrm{med} = 0.05$ gives the 95% CL upper limit. The obtained results are shown in the next Section.

4.11 Discovery Potential and Exclusion Limits

The discovery significance has been computed using the background-only and signal-plus-background log Likelihood Ratio distributions obtained from toy Monte Carlo pseudoexperiments. The signal significances obtained for several m_A at fixed $\tan\beta = 30$ and an integrated luminosity of 10 fb^{-1} and 30 fb^{-1} are summarized in Table 4.9. The significance has been obtained using the fixed-mass approach for the two analysis branches considered.

Table 4.10 shows the integrated luminosities needed for a 5σ discovery and a 95% confidence level exclusion for both analysis branches and their combination. According to these results, only very few fb^{-1} are needed to achieve a 95% confidence level exclusion, that is, less than 10 fb^{-1} for $m_A \lesssim 200$ GeV and $\tan\beta = 30$.

Table 4.9: Signal significances obtained for different m_A points at $\tan\beta = 30$ and an integrated luminosity of 10 fb^{-1} and 30 fb^{-1} using the fixed-mass approach.

m_A (GeV)	Signal significance					
	$\mathscr{L} = 10$ fb^{-1}			$\mathscr{L} = 30$ fb^{-1}		
	0-jet	1-jet	comb.	0-jet	1-jet	comb.
110	2.7	1.4	3.0	4.7	2.5	5.3
130	2.9	1.8	3.4	5.0	3.1	5.9
150	2.5	1.7	3.0	4.3	3.0	5.2
200	1.5	1.1	1.9	2.6	1.9	3.2
300	0.6	0.5	0.8	0.9	0.8	1.2

Table 4.10: Integrated luminosities (in fb^{-1}) needed for a 5σ discovery and 95% CL exclusion computed for the 0-jet and 1-jet analysis as well as for their combination. Different A-boson masses have been used at $\tan\beta = 30$.

m_A (GeV)	$\mathscr{L}$ (fb^{-1}) for a 5σ discovery			$\mathscr{L}$ (fb^{-1}) for a 95% CL exclusion		
	0-jet	1-jet	comb.	0-jet	1-jet	comb.
110	33.6	118.6	26.0	2.3	12.8	1.8
130	30.0	75.5	21.6	2.1	8.2	1.5
150	40.0	86.3	27.3	2.7	9.2	2.0
200	117.1	201.1	73.9	8.0	21.5	5.4
300	840	1150	500	55.7	123.0	36.0

For this analysis we found the same trend in the curves to obtain a 5σ discovery and a 95% CL exclusion limits within the (m_A, $\tan\beta$) plane as obtained with the analysis which makes use of the b-tagging in the event selection [54]. The obtained exclusion and discovery reach is only about two times weaker compared to the analysis with the b-tagging requirement, which demonstrates the feasibility of the presented analysis with the early data.

Figure 4.36 shows the contour in the (m_A, $\tan\beta$) plane for the 5σ significance for three integrated luminosities, 10, 30 and 100 fb^{-1} and both analysis branches. For both 0-jet and 1-jet analysis, the earliest 5σ discovery can be achieved for $m_A \sim 130$ GeV at fixed $\tan\beta$ and luminosity. Similar values of $\tan\beta$ are needed to reach a 5σ significance for the A-boson masses around 110 and 150 GeV while weaker constraints can be set on $\tan\beta$ at higher masses. In the whole mass range

studied, the 0-jet analysis covers a larger region of the parameter space than the 1-jet analysis.

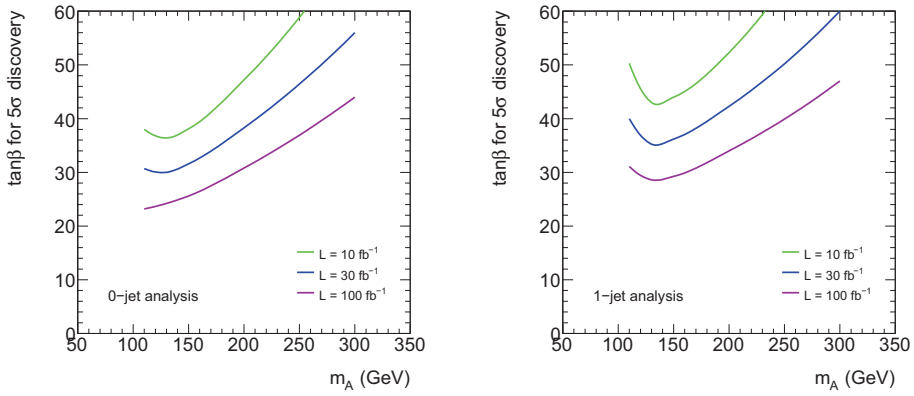

Figure 4.36: Values of $\tan\beta$ needed to achieve a 5σ discovery as a function of the A-boson mass at three different integrated luminosities (10, 30 and 100 fb^{-1}) for the 0-jet (left) and 1-jet (right) analysis.

Figure 4.37 shows the contour in the (m_A, $\tan\beta$) plane to obtain a 95% CL exclusion for three integrated luminosities, 1, 10 and 30 fb^{-1} and both analyses. Note that with only 1 fb^{-1} a big part of the parameter space can already be excluded with this analysis. At that luminosity, $\tan\beta > 60$ can be excluded for $m_A < 200$ GeV with the 1-jet analysis and $\tan\beta > 35$ can be excluded for $m_A \approx 150$ GeV with the 0-jet analysis. At higher luminosities, the exclusion power in each analysis branch increases with sensitivity in the $\tan\beta > 20$ for 0-jet analysis at 30 fb^{-1}.

Figure 4.38 presents the results obtained after the combination of both analyses, allowing for a better sensitivity. Concerning the discovery reach, with 10 fb^{-1} the A/H signal could be observed at $\tan\beta > 35$ at low m_A, improving to $\tan\beta > 20$ with 100 fb^{-1}. For lower integrated luminosity (up to 1 fb^{-1}), where the b-tagging performance may still not be optimal, one can exclude the $\tan\beta$ values of 30 in the low mass region, and $\tan\beta > 60$ for masses $m_A = 300$ GeV. Note that with such a luminosity, better limits can be set compared to the current Tevatron results. These values are improving with 30 fb^{-1}, excluding $\tan\beta > 15$ for low Higgs masses and $\tan\beta > 30$ at $m_A = 300$ GeV.

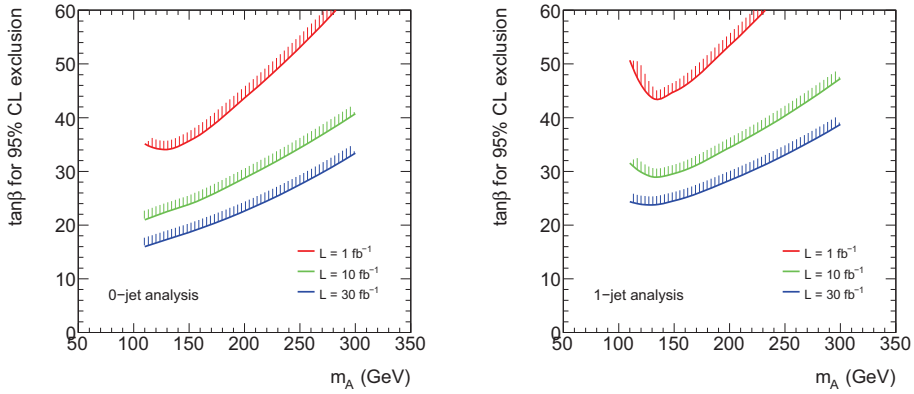

Figure 4.37: Values of $\tan\beta$ needed to achieve a 95% CL exclusion as a function of the A-boson mass at three different integrated luminosities (1, 10 and 30 fb^{-1}) for the 0-jet (left) and 1-jet (right) analysis.

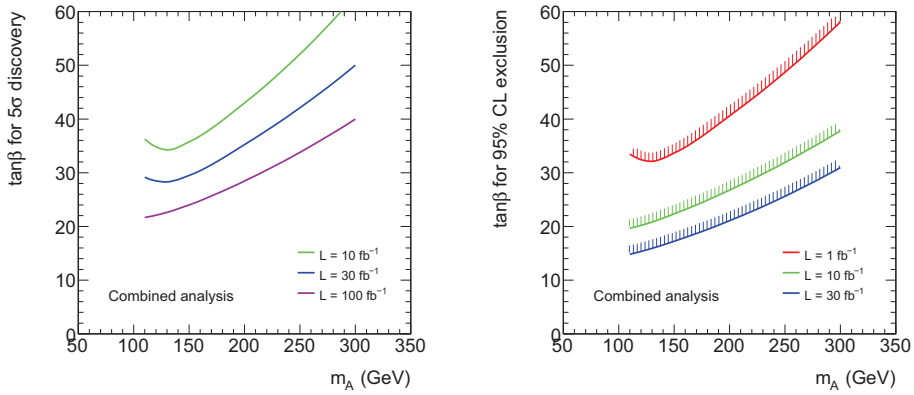

Figure 4.38: Values of $\tan\beta$ needed to achieve a 5σ discovery (left) and a 95% CL exclusion (right) as a function of the A-boson mass for three different integrated luminosities, combining both analyses.

4.12 Conclusions

This Chapter is devoted to the discovery potential of the MSSM $h/A/H \to \mu\mu$ in the ATLAS experiment, making use of the event selection criteria agreed in the collaboration and also used in Ref. [54] with the only exception that the jet b-

tagging is not required. Such an analysis can be very useful for the first ATLAS data taking, with low luminosity (up to 1 fb^{-1}) when the b-tagging still does not have the optimal performance. The event selection criteria require at least two muons of opposite charge, with $p_{\text{T}} > 20$ GeV and $|\eta| < 2.7$. Muons are required to be isolated to discard the ones coming from hadronic showers. After the muon preselection, events with large $E_{\text{T}}^{\text{miss}}$ are rejected. After that, a cut on jet multiplicity is applied, taking into account jets with $p_{\text{T}} > 20$ GeV within $|\eta| < 2.5$. The analysis is split in two branches according to the jet multiplicity, with no requirement on the jet flavor.

The main background comes from the Z-boson resonance, which is more than two orders of magnitude higher than the other backgrounds in this analysis ($t\bar{t}$, ZZ and WW) after all event selection criteria have been applied. Several Higgs boson masses (from 110 to 400 GeV) and $\tan\beta$ values have been considered.

Signal significance has been evaluated by means of the log Likelihood Ratio from background-only and signal-plus-background toy Monte Carlo pseudoexperiments. The results presented in this Chapter show that 5σ significances can be achieved at 30 fb^{-1} for $\tan\beta = 30$ and $m_A = 130$ GeV and also that better significances are obtained for larger $\tan\beta$ values. Signal significance has been obtained as a function of the integrated luminosity, the A-boson mass and $\tan\beta$.

Relatively low luminosity (less than 6 fb^{-1}), at the beginning of ATLAS data taking, is needed to set a 95% CL exclusion limits for values up to $\tan\beta = 30$ for A-boson mass ≤ 200 GeV.

In summary, the presented studies show that this analysis is feasible with very early ATLAS data, before the b-tagging is fully performing, and provides sensitivity to the Higgs boson discovery and exclusion in a wide region of the MSSM parameter space. However, once the b-tagging algorithm is available, the exclusion and the discovery reach will be improved by applying the b-tagging requirement for the event selection.

5 Conclusions

"Nothing in life is to be feared, it is only to be understood. Now is the time to understand more, so that we may fear less."
— Marie Curie (1867 - 1934)

The work presented in this Thesis is devoted to studies which makes use of muons in the ATLAS experiment. Signatures characterized by these particles are present in a wide variety of physics processes involved in precision Standard Model measurements as well as in several Beyond the Standard Model theories. Furthermore, muons provide a clean experimental detection which is exploited in ATLAS achieving a very good performance.

This Thesis is split in two parts which treats the muons at different energy regimes: low-p_{T} muons which can be triggered with the Hadronic Tile Calorimeter and the MSSM neutral Higgs boson search by means of muons in the high-p_{T} range.

Although the main purpose of TileCal is to detect hadronic jets, in the first part of the Thesis is shown that low-p_{T} muons can be detected efficiently with the calorimeter. The typical energy deposition pattern can be distinguished with a relatively simple algorithm called TileMuId using the calorimeter geometrical segmentation. TileMuId identifies muons by looking for moderate energy depositions in the calorimeter cells following a projective trajectory. In particular, this algorithm can be very useful for muons with $p_{\mathrm{T}} \approx 3 - 4$ GeV, where the Muon Spectrometer shows a low efficiency or in the $|\eta| \approx 0$ region where the Muon Spectrometer efficiency is reduced.

TileMuId has been implemented in the Read-Out Driver (ROD) Digital Signal Processors (DSPs) so that the information about the presence of muons is sent with the raw data for all the events passing the Level-1 trigger. At HLT, dedicated algorithms apply TileMuId separately using the cell energy and the preprocessed information in the ROD which is stored in the raw data.

Results from Monte Carlo data show that the efficiency of the ROD-based version of TileMuId is 60% in the $p_{\mathrm{T}} \geq 4$ GeV. TileMuId is fully operational in the ATLAS cosmics runs, where promising results are obtained with real data, and it is implemented in the ATLAS Muon Trigger Slice. Two trigger chains in the trigger menu for the 10^{31} cm^{-2}s^{-1} run period (2009-2010) are based in TileMuId.

The second part of the Thesis is dedicated to the analysis of the MSSM neutral Higgs boson in the $h/A/H \rightarrow \mu\mu$ channel. Despite the low cross-section for this channel, the very clean experimental signature based on dimuons together with advanced analysis techniques used show very promising results and good prospects for a MSSM Higgs discovery. This signal is produced at the LHC via gluon-gluon fusion or in association with b-jets and the most important background comes from the Z-peak tails in the Drell-Yan $Z \rightarrow \mu\mu$ process.

This analysis has been traditionally studied with constraints on b-tagged jets in the final state. However, the original contribution in the analysis presented here is that the search is performed with no flavor requirement in the event selection. In consequence, this analysis can be performed with the very first LHC data, before the b-tagging is fully operational.

The approach used here for significance and exclusion limit computation is based on log Likelihood Ratios obtained from fixed-mass and floating-mass fits. Results show that a discovery is feasible with low integrated luminosity (~ 10 fb^{-1}) and constraining limits can be set in the MSSM parameter space with only 1 fb^{-1}.

6 Resumen

"La verdadera ciencia enseña, sobre todo, a dudar y a ser ignorante."

— Miguel de Unamuno (1864 - 1936)

6.1 Introducción

6.1.1 El Experimento ATLAS

El CERN, acrónimo de *Conseil Européen pour la Recherche Nucléaire*, es en la actualidad el laboratorio de Física de Partículas más grande del mundo. Está situado en la frontera entre Francia y Suiza, cerca de Ginebra. Fundado en 1954, actualmente está formado por 20 estados miembros europeos y un gran número de paises no miembros participan en sus experimentos. Grandes descubrimientos se han llevado a cabo en los experimentos del CERN como el descubrimiento de las partículas $W^{\pm}$ y Z.

El LHC [1] (siglas de *Large Hadron Collider*) o Gran Colisionador de Hadrones es el nuevo colisionador protón-protón cuya puesta en funcionamiento está prevista a finales de 2009. Situado a 100 m bajo tierra en el antiguo tunel de LEP, tiene una longitud de circunferencia de 27 km. Ha sido diseñado para alcanzar una energía de colisión en centro de masas de 14 TeV y una luminosidad de 10^{34} cm^{-2}s^{-1}. Se han construido seis grandes experimentos para estudiar las colisiones en el LHC: ALICE [2], ATLAS [3], CMS [4], LHCb [5], LHCf [6] y TOTEM [7].

ATLAS (*A Toroidal LHC ApparatuS*) es un experimento de propósito general, diseñado para explotar todo el potencial de descubrimiento de nueva física del LHC. Por tanto, se ha optimizado el detector para que sea sensible al mayor rango posible de la masa del Higgs. Otros objetivos son la búsqueda de partículas supersimétricas, así como el estudio de la violación de *CP* en física del quark b y estudios detallados del quark top. ATLAS es un experimento de simetría cilíndrica, cuyas dimensiones son 44 m de longitud y 22 m de diámetro y un peso de 7000 Tm que sigue la típica estructura de un experimento de física de altas energías.

El detector interno [8] mide con gran precisión la posición de las partículas cargadas y curvatura de las trazas. Consta a su vez de tres subdetectores que ordenados desde la parte más interna a la más externa son el detector de Pixels, el *SemiConductor Tracker* (SCT) y el *Transition Radiation Tracker* (TRT).

Los calorímetros, cuya función principal es medir la posición y energía de los jets de partículas, son dos: un calorímetro de argón líquido (conocido como *Liquid Argon* [10]) con una parte central electromagnética y sus extremos hadrónicos y un calorímetro hadrónico de tejas que rodea al anterior conocido como TileCal [11].

El espectrómetro de muones [12] se utiliza para medir la posición y trayectoria de estas partículas. Está dividido en cuatro partes: *Monitored Drift Tubes* (MDTs), *Cathode Strip Chambers* (CSCs), *Resistive Plate Chambers* (RPCs) y *Thin Gap Chambers* (TGCs).

Además ATLAS dispone de un sistema de imanes [13] para curvar las partículas cargadas y así medir su momento. Posee un solenoide central, un toroide en la parte asociada al barril y dos toroides en los extremos.

ATLAS cuenta con un sistema de trigger [14] basado en tres niveles para la selección de sucesos en tiempo real. Cada nivel de trigger refina las decisiones del nivel anterior aplicando criterios de selección adicionales. Así pues, partiendo de una frecuencia inicial de colisión de 40 MHz (con una frecuencia de interacción de $\sim 10^9$ Hz a una luminosidad de 10^{34} $\mathrm{cm}^{-2}\mathrm{s}^{-1}$), la frecuencia de sucesos seleccionados se reduce a ~ 100 Hz para su posterior almacenamiento en disco. El primer nivel de trigger está basado en hardware, mientras que el segundo y tercer nivel, también conocidos como trigger de alto nivel, están basados en software.

6.1.2 Motivaciones Físicas

El Modelo Estándar [28] es una exitosa teoría que describe las interacciones de los componentes de la materia a las escalas más pequeñas ($<10^{-18}$ m) y energías más altas ($\sim$ 200 GeV) disponibles. Es una teoría cuántica de campos que describe la interacción de fermiones puntuales de spin 1/2 mediada por bosones de gauge de spin 1. Los bosones surgen cuando se aplica una invariancia de gauge local a los campos fermiónicos, y son una manifestación del grupo de simetría de la teoría, que para el Modelo Estándar es SU(3)⊗SU(2)⊗U(1). Los fermiones fundamentales son leptones y quarks. Existen tres generaciones de fermiones, idénticas a excepción de su masa. El origen de esta estructura generacional, y la rotura generacional de simetría (es decir, la distinta masa para cada generación) permanece sin resolver. Para cada generación, existen tres leptones con carga eléctrica -1, el electrón (e), el muón (μ) y el tau (τ), y tres leptones eléctricamente neutros (los neutrinos ν_e, ν_μ y ν_τ). De modo similar, existen tres quarks con carga eléctrica $+2/3$, up (u), charm (c) y top (t), y tres con carga eléctrica -1/3, down (d), strange (s) y bottom (b). Las tres generaciones de quarks están mezcladas (es decir, los autoestados de masa no corresponden a los autoestados de interacción) y esta mezcla está parametrizada (pero no explicada) por la matriz de Cabibbo-Kobayashi-Maskawa (CKM).

Los quarks son tripletes del grupo de gauge SU(3) y por tanto transportan una "carga" adicional, llamada color, que es responsable de su participación en la interacción fuerte (Cromodinámica Cuántica o QCD). Ocho gluones median esta interacción; transportando a su vez carga de color y en consecuencia interactuando entre ellos mismos. Esto implica que el acoplamiento de QCD α_s es pequeño para grandes transferencias de momento pero grande para bajas transferencias, dando lugar al confinamiento de los quarks dentro de los hadrones neutros en color (como protones y neutrones). Al intentar liberar un quark se produce un jet de hadrones a través de la producción de pares quark-antiquark y bremsstrahlung.

En el Modelo Estándar, el grupo de simetría SU(2)⊗U(1), que describe la interacción electrodébil, se rompe espontáneamente a través de la existencia de un (postulado) campo de Higgs con valor esperado distinto de cero. Esto conlleva la existencia de bosones vectoriales masivos, el $W^\pm$ y el Z, que median la interac-

ción débil, mientras que el fotón del electromagnetismo permanece sin masa. Un grado físico de libertad permanece en el sector de Higgs, que podría manifestarse del modo más simple como un bosón escalar neutro H^0, no observado.

Los éxitos del Modelo Estándar han conducido a un creciente interés en sus limitaciones. En su versión más simplificada, el Modelo Estándar tiene 19 parámetros: tres constantes de acoplamiento, nueve masas de quarks y leptones, la masa del bosón Z que establece la escala de la interacción débil, cuatro parámetros de mezcla de la matriz CKM, y un parámetro que describe la escala de la violación de CP en la interacción fuerte. El parámetro restante se asocia con el mecanismo responsable de la rotura de la simetría electrodébil SU(2)⊗U(1) a U(1) del electromagnetismo. Esto se puede tomar como la masa del bosón de Higgs, ya que sus acoplamientos quedan determinados una vez conocida la masa. Dentro del modelo no existe orientación sobre la masa esperada del bosón de Higgs.

Supersimetría (*Supersymmetry*, SUSY) es una teoría de la que actualmente no hay evidencias experimentales. Ofrece el único mecanismo conocido en la actualidad para incorporar la gravedad en la teoría cuántica de interacciones de partículas y proporciona un elegante mecanismo de cancelación para las divergencias que afectan a la masa del Higgs, mientras que conserva todas las predicciones del Modelo Estándar y permite la unificación de los tres acoplamientos de las interacciones de gauge a gran escala. Modelos supersimétricos postulan la existencia de partículas supersimétricas para todas las partículas observadas hasta la fecha. Hay bosones supersimétricos de fermiones (squarks y sleptones), y fermiones supersimétricos de bosones (gluinos y gauginos). Hay también multiples bosones de Higgs. Habría, en consecuencia, un largo espectro de partículas hasta ahora no observadas, cuyas masas exactas, acoplamientos y cadenas de desintegración son calculables en la teoría dados unos ciertos parámetros. Desafortunadamente estos parámetros se desconocen; pero si supersimetría interviene en la rotura de la simetría electrodébil, las masas deberían estar comprendida en la region de 100 GeV - 1 TeV.

El *Minimal Supersymmetric Standard Model* (MSSM) es la extensión supersimétrica más simple del Modelo Estándar. El sector de Higgs está formado por 2 dobletes del Higgs que dan lugar a 5 estados físicos: un pseudoescalar neutro (A), dos escalares neutros (h y H) y dos bosones cargados ($H^{\pm}$).

Otras teorías han sido propuestas como la teoría de dimensiones adicionales, tecnicolor, etc. para dar respuesta a los interrogantes que quedan abiertos en el Modelo Estándar. Con este amplio abanico de teorías a nuestra disposición, son necesarios nuevos datos experimentales capaces de confirmar o descartar sus predicciones. Así pues, estamos a la espera de la nueva física que podría ponerse de manifiesto en la próxima puesta en funcionamiento de los experimentos del LHC diseñados para este fin.

6.2 Trigger de Muones

La primera parte esta tesis trata del desarrollo de un algoritmo de identificación de muones de bajo momento transverso utilizando la energía depositada en el calorímetro hadrónico de tejas TileCal. Este algoritmo, conocido como TileMuId [36, 37], ha sido diseñado para su uso en la selección de sucesos a segundo nivel de trigger de ATLAS.

TileMuId puede ser utilizado para confirmar los candidatos a muones procedentes de triggers basados en el espectrómetro de muones y reducir los posibles fakes causados por el ruido electrónico, proporcionando redundancia y robustez al sistema de trigger de muones de ATLAS.

Los muones de bajo momento transverso son de especial relevancia para seleccionar sucesos de física del quark b, así como la identificación de las partículas J/ψ y Υ.

6.2.1 Descripción e Integración del Algoritmo

TileMuId explota la capacidad de TileCal para detectar muones de bajo momento transverso, aprovechando su geometría proyectiva en η. Se define un candidato a muón cuando la deposición de energía en tres celdas, una en cada capa del calorímetro siguiendo una trayectoria proyectiva en η, es compatible con la de una partícula al mínimo de ionización (MIP).

Así pues, el algoritmo dispone de una serie de umbrales entre los cuales debe estar comprendida la energía depositada:

$$\text{Umbral}_{\text{inferior}} < E_{\text{celda}} < \text{Umbral}_{\text{superior}}. \tag{6.1}$$

El umbral inferior de energía se utiliza para eliminar el ruido electrónico y los sucesos de *minimum bias*, mientras que el umbral superior se usa para descartar las cascadas hadrónicas.

Se han desarrollado dos versiones de este algoritmo:

- TrigTileLookForMuAlg
- TrigTileRODMuAlg

Todo el software asociado al algoritmo, necesario para la simulación, decodificación y reconstrucción de los datos, así como para el acceso de los mismos a segundo nivel de trigger, ha sido escrito e integrado dentro del software general de ATLAS para tareas offline conocido como Athena [40]. TileMuId se ejecutará a segundo nivel de trigger en combinación con el detector interno. Ambos algoritmos han sido integrados en el sistema de trigger de muones de ATLAS [44]. Dos cadenas de trigger, mu4_tile y mu4_trod, han sido incluidas en el menu de trigger para $\mathscr{L} = 10^{31}$ cm^{-2}s^{-1}.

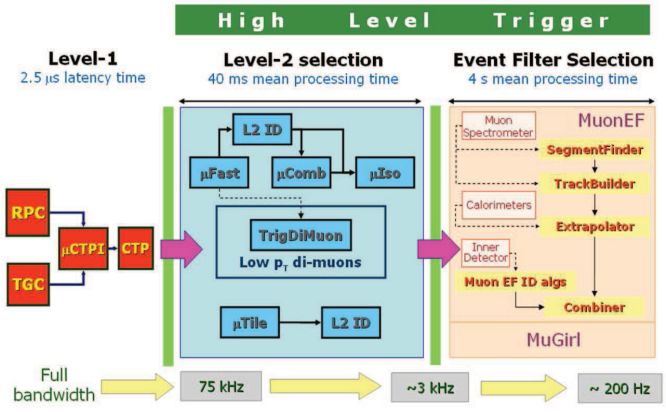

Figure 6.1: Esquema del sistema de trigger de muones de ATLAS.

6.2.2 Resultados con Datos de Simulación Monte Carlo

Se ha evaluado el rendimiento del algoritmo en términos de eficiencia y fracción de fakes con datos de simulación Monte Carlo. La eficiencia ha sido calculada como la fracción de muones correctamente identificados por el algoritmo sobre el número total de muones generados, mientras que la fracción de fakes corresponde a la fracción de candidatos a muones que no se corresponden con un muón de la simulación sobre el número total de sucesos. En las Figuras 6.2 y 6.3 se muestran la eficiencia y la fracción de fakes respectivamente.

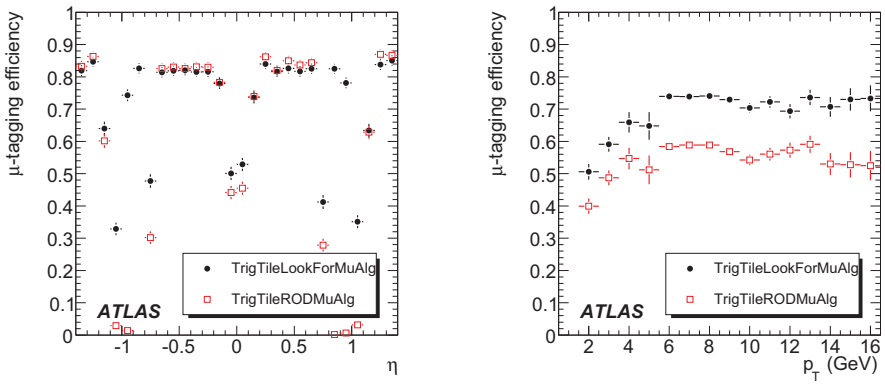

Figure 6.2: Eficiencia en función de η (izquierda) y p_{T} (derecha) para $b\bar{b} \rightarrow \mu(6)\mathrm{X}$.

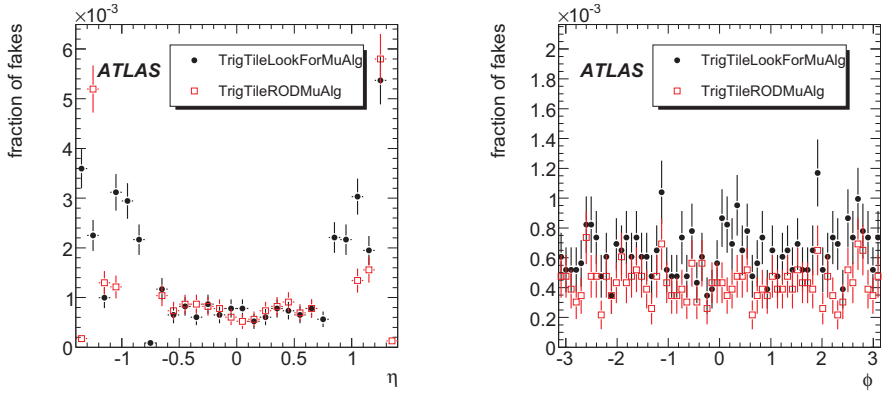

Figure 6.3: Fraction de fakes en función de η (izquierda) y ϕ (derecha) para $b\bar{b} \rightarrow \mu(6)\mathrm{X}$.

Para la ejecución de TileMuId a segundo nivel de trigger, se utilizan algoritmos de reconstrucción de trazas en el detector interno, tales como TrigIDSCAN [42] y TrigSiTrack [43], para hallar las trazas correspondientes a los muones identificados por TileMuId. En la Figura 6.4 se muestra la eficiencia de TrigTileLookForMuAlg ejecutado en solitario y en combinación con algoritmos de reconstrucción de trazas en el detector interno.

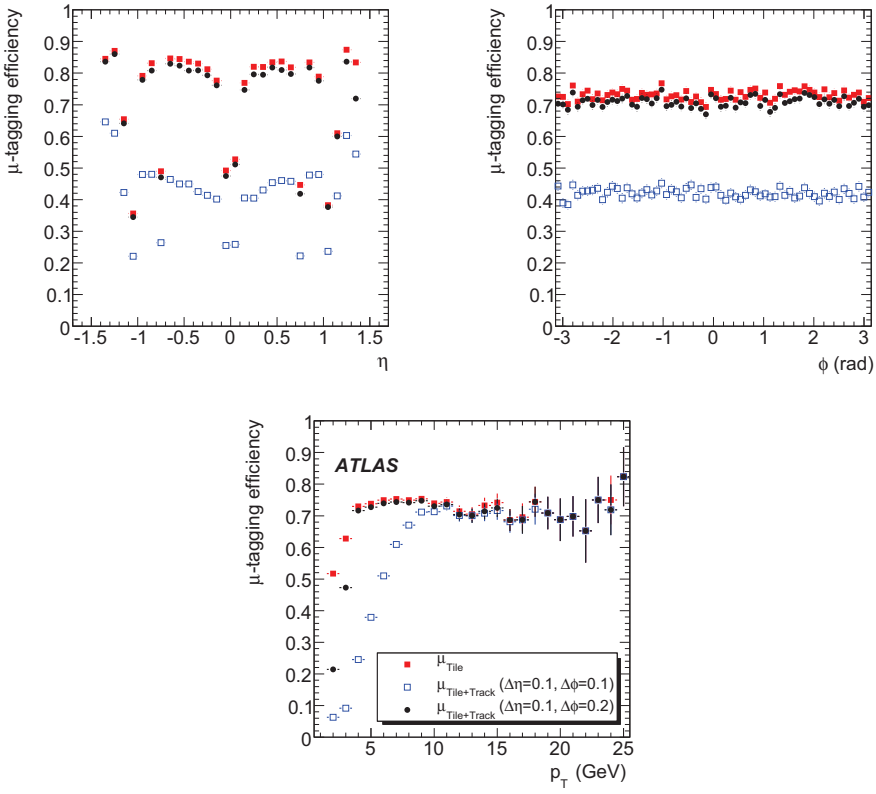

Figure 6.4: Eficiencia en función de η, ϕ y p_{T} para $b\bar{b} \rightarrow \mu(4)\mathrm{X}$.

Los resultados obtenidos tras la combinación con el detector interno utilizando sucesos de $b\bar{b}$ se muestran en la Tabla 6.1 (donde la pureza se define como la fracción de muones correctamente identificados sobre el total de muones proporcionados por el algoritmo), así como los resultados obtenidos para sucesos de $t\bar{t}$ a distintas luminosidades se muestran en la Tabla 6.2.

Table 6.1: Eficiencia, fracción de muones sin correspondencia en el detector interno (μ_{Tile} sin traza) y pureza para TrigTileLookForMuAlg para sucesos de $b\bar{b} \rightarrow \mu(6)$X.

	Tamaño del cono ($\Delta\eta \times \Delta\phi$)		
	(0.1×0.1)	(0.1×0.2)	(0.1×0.3)
$b\bar{b} \rightarrow \mu(6)$X			
Eficiencia (%)	59.59 ± 0.19	71.21 ± 0.17	72.43 ± 0.17
μ_{Tile} sin traza (%)	18.68 ± 0.21	2.81 ± 0.08	1.15 ± 0.05
Eficiencia para $p_{\text{T}} > 6$ GeV (%)	63.44 ± 0.19	73.55 ± 0.17	73.70 ± 0.17
Pureza para $p_{\text{T}} > 6$ GeV (%)	98.92 ± 0.71	98.90 ± 0.66	98.85 ± 0.66
$b\bar{b} \rightarrow \mu(6)$X a $\mathscr{L} = 10^{33}$ cm^{-2}s^{-1}			
Eficiencia (%)	57.92 ± 0.83	67.94 ± 0.79	68.93 ± 0.78
μ_{Tile} sin traza (%)	16.86 ± 0.90	2.49 ± 0.32	1.06 ± 0.21
Eficiencia para $p_{\text{T}} > 6$ GeV (%)	61.32 ± 0.86	70.08 ± 0.80	70.39 ± 0.80
Pureza para $p_{\text{T}} > 6$ GeV (%)	99.16 ± 3.22	99.05 ± 2.98	99.05 ± 2.99

Table 6.2: Fracción de sucesos identificados por TileMuId sobre el número total de sucesos.

	$N_{\text{TrigTileRODMuAlg}}/N_{\text{Total}}$	$N_{\text{L2\_mu4\_trod}}/N_{\text{Total}}$
$t\bar{t}$ (14 TeV) sin apilamiento	0.292 ± 0.003	0.273 ± 0.003
$t\bar{t}$ (10 TeV) con apilamiento (450 ns)	0.304 ± 0.007	0.280 ± 0.006
$t\bar{t}$ (10 TeV) con apilamiento (75 ns)	0.316 ± 0.007	0.278 ± 0.006
$t\bar{t}$ (10 TeV) con apilamiento (25 ns)	0.334 ± 0.007	0.271 ± 0.006

6.2.3 Resultados con Rayos Cósmicos

También se han analizado los resultados del algoritmo TileMuId obtenidos con datos reales del detector, rayos cósmicos, durante su fase de puesta a punto. En particular, se ha utilizado la versión del algoritmo ejecutado en los DSPs de las tarjetas ROD. Estos datos son muy útiles, ya que permiten testear el algoritmo integrado en la cadena de adquisición y por otra parte, se puede estudiar la respuesta del algoritmo bajo condiciones reales de ruido electrónico, estado del detector, etc.

En la Figura 6.5 se muestra la energía depositada por los muones en el calorímetro que sigue una distribución de Landau y su distribución en ϕ que muestra dos estructuras correspondientes a la parte superior e inferior del calorímetro.

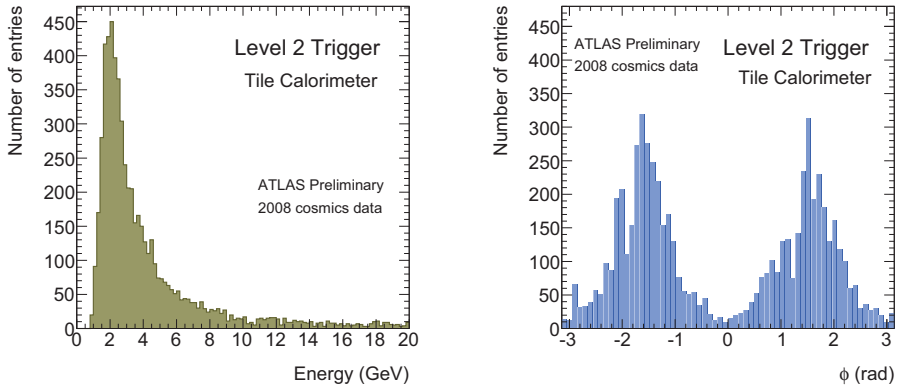

Figure 6.5: Energía depositada por los muones en TileCal (izquierda) y distribución en ϕ (derecha) para el run 91060.

En la Figura 6.6 se muestran los resultados obtenidos al combinar TileMuId con el algoritmo de reconstrucción de trazas en el detector interno TrigIDSCAN para el run 91900 con el campo magnético encendido, es decir, se requiere que los candidatos a muones identificados en TileCal tengan una traza en el detector interno.

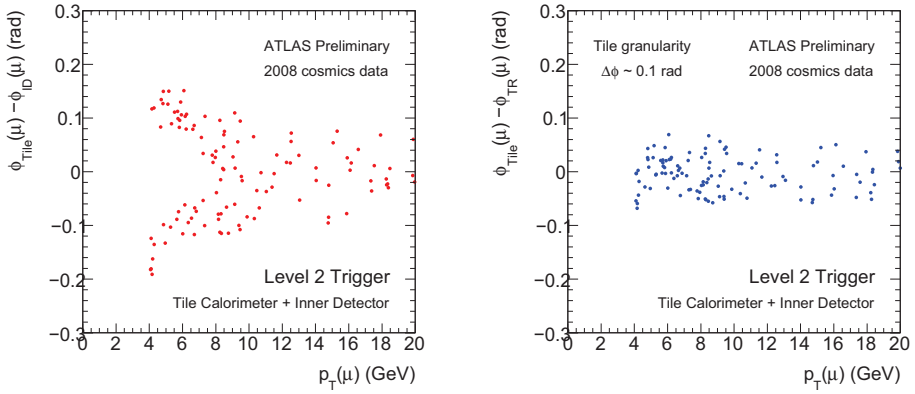

Figure 6.6: A la izquierda, diferencia entre la coordenada ϕ del muón identificado por TileMuId (ϕ_{Tile}) y la coordenada ϕ de la traza en el detector interno reconstruida por TrigIDSCAN (ϕ_{ID}) en función del p_{T} del muón medido por TrigIDSCAN. A la derecha, la traza hallada en el detector interno ha sido extrapolada al radio de TileCal debido al campo magnético.

6.3 Búsqueda del Bosón de Higgs del MSSM en ATLAS

La segunda parte de esta tesis trata del análisis del potencial de descubrimiento del bosón de Higgs neutro $h/A/H$ del MSSM en el experimento ATLAS. Para ello, se ha utilizado el canal de desintegración del bosón de Higgs a dos muones. El canal de desintegración elegido tiene la ventaja de ser muy limpio desde el punto de vista experimental y de proporcionar una resonancia del Higgs estrecha en comparación con otros canales de desintegración.

Este análisis se ha realizado en colaboración con los grupos de física del Higgs en el CERN, contribuyendo a los recientes estudios de *Computing System Commissioning* (CSC) [8] realizados sobre el rendimiento esperado del detector ATLAS con datos de colisiones protón-protón a una energía en centro de masas de 14 TeV. Estos estudios suponen una revisión de la física que se espera poder observar en ATLAS a una escala de energía del TeV respecto a los resultados ya publicados en el Technical Design Report [9].

6.3.1 Datos de Simulación Monte Carlo

La producción del bosón de Higgs en el MSSM se realiza por fusión gluón-gluón o en asociación con quarks b como se muestra en la Figura 6.7.

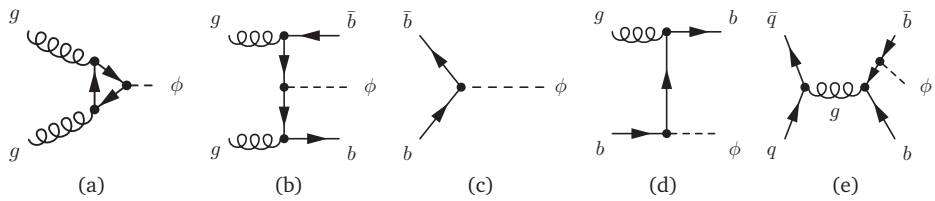

Figure 6.7: Diagramas de Feynman que contribuyen a la producción del bosón de Higgs en el MSSM. El diagrama (a) corresponde a la producción directa mientras que los diagramas del (b) al (e) contribuyen a la producción asociada al quark b. En estos diagramas ϕ representa a los distintos bosones de Higgs neutros del MSSM, h, H o A.

Los principales fondos considerados en este análisis son $Z \rightarrow \mu\mu$ (producción asociada con jets ligeros o jets originados a partir de un quark b), $t\bar{t} \rightarrow (W^+b)(W^-\bar{b}) \rightarrow (\mu^+\nu b)(\mu^-\bar{\nu}\bar{b})$ y la producción de bosones ZZ y WW.

6.3.2 Criterio de Selección de Sucesos

Para comparar con los resultados obtenidos utilizando *b-tagging* [54], los mismos cortes de selección se han aplicado en este análisis con la única diferencia de no requerir *b-tagging* para la selección de jets:

- **Corte 1**: se seleccionan aquellos sucesos con al menos dos muones de carga opuesta, $p_{\mathrm{T}} > 20$ GeV, $|\eta| < 2.7$ y aislados ($E_{\mathrm{T}}^{\mathrm{cone}\,0.4}/p_{\mathrm{T}}(\mu) < 0.2$). De este modo, se lleva a cabo una preselección de sucesos con muones de alto p_{T}, aislados para eliminar los muones procedentes de cascadas hadrónicas, potencialmente producidos en la desintegración del bosón de Higgs neutro $h/A/H$.
- **Corte 2**: se requiere $E_{\mathrm{T}}^{\mathrm{miss}} < 40$ GeV en el suceso. Este corte es muy potente para eliminar gran parte de los sucesos de $t\bar{t}$, caracterizados por una alta $E_{\mathrm{T}}^{\mathrm{miss}}$ debido a la presencia de neutrinos en la desintegración del quark top.
- **Corte 3**: se requiere que el número de jets < 2 con $p_{\mathrm{T}} > 20$ GeV y $|\eta| < 2.5$. Con este corte se elimina una parte considerable de los fondos procedentes de los procesos de $t\bar{t}$ y desintegración del bosón Z. A partir de este corte, el análisis se divide en dos ramas teniendo en cuenta el número de jets presente en el suceso: 0 y 1 jet.
- **Corte 4**: únicamente en el caso de los sucesos que contienen 1 jet se requiere que $|\sin\Delta\phi_{\mu\mu}| < 0.75$. Este corte es especialmente útil para eliminar los fondos ya que en los procesos de desintegración a dos muones, estos tienden a ser emitidos en direcciones opuestas, mientras que aquellos procedentes de distintas partículas no están correlacionados.
- **Corte 5**: se contabilizan los sucesos cuya masa invariante del sistema de dos muones $m_{\mu\mu}$ está contenida en una ventana $\Delta m_{\mu\mu} = m_A \pm 2\sigma_{\mu\mu}$, donde m_A es la masa del Higgs y $\sigma_{\mu\mu}$ su anchura reconstruida.

Los resultados obtenidos tras aplicar los cortes de selección discutidos anteriormente se resumen en las Tablas 6.3-6.5, que muestran el porcentaje de sucesos

aceptados tanto para las muestras de señal como de fondo. Las muestras de señal utilizadas en la Tabla 6.3 corresponden a varios valores de m_A, para $\tan\beta = 30$. En el caso de los fondos, aparte del número total de sucesos en todo el rango de masas (Tabla 6.4), se muestran los sucesos contenidos en una ventana $\Delta m_{\mu\mu}$ entorno a cada una de las masas del Higgs consideradas (Tabla 6.5).

Table 6.3: Sección eficaz efectiva para las muestras de señal (en fb) con $\tan\beta = 30$ tras aplicar cada corte de selección, obtenida para el análisis sin requerir *b-tagging*.

Corte	$b\bar{b}A \to \mu\mu$ (fb)					
	110 GeV	130 GeV	150 GeV	200 GeV	300 GeV	400 GeV
0.	182.97	112.43	72.85	27.58	6.22	1.78
1.	141.23	88.09	58.47	22.59	4.99	1.43
2.	133.34	82.51	53.62	20.40	4.33	1.17
3.	121.79	74.74	47.60	17.58	3.44	0.90
3a.	92.40	54.36	34.50	11.95	2.17	0.55
5a.	78.16	46.50	27.51	10.12	1.89	0.48
3b.	29.39	20.39	13.09	5.63	1.27	0.35
4b.	23.27	16.61	11.19	5.15	1.20	0.33
5b.	18.13	13.67	8.94	4.02	0.96	0.28

Table 6.4: Sección eficaz efectiva para las muestras de fondo (en fb) tras aplicar cada corte de selección, obtenida para el análisis sin requerir *b-tagging*.

Corte	Z+light jets (fb)	Z+b-jets (fb)	$t\bar{t}$ (fb)	$ZZ \to b\bar{b}\mu\mu$ (fb)	WW (fb)
0.	996845	47802	833000	109.324	40880
1.	733960	33523	5648	60.948	673
2.	732441	33146	1354	55.837	298
3.	667670	27724	228	26.169	276
3a.	526455	18006	28.65	7.243	204.40
3b.	141215	9718	199.30	18.927	71.95
4b.	93022	6116	117.40	10.768	49.87

En la Figura 6.8 se muestra las distribuciones de la masa invariante de los dos muones para todos los fondos y tres muestras de señal. Tras aplicar los cortes de selección, el fondo más importante, que prevalece en todo el rango de masas,

es Z+jets ligeros (incluso para las regiones a 200 GeV del pico del Z), el fondo Z+b-jets se halla más de un orden de magnitud por debajo en ambos casos, 0 y 1 jet.

Table 6.5: Sección eficaz efectiva para las muestras de fondo (en fb) en una ventana $\Delta m_{\mu\mu}$ alrededor de las masas que figuran en la Tabla 6.3.

m_A (GeV)	Z+light jets (fb)	Z+b-jets (fb)	$t\bar{t}$ (fb)	$ZZ \to b\bar{b}\mu\mu$ (fb)	WW (fb)
110	7857	227.63	2.18	0.164	15.53
130	2420	60.80	2.18	0.041	14.72
150	1035	22.56	1.25	0.014	19.62
200	373	4.68	1.87	0.014	11.45
300	107	1.05	0.93	<0.014	0.82
400	45	0.57	0.31	0.014	1.64
110	613	28.87	9.65	0.191	4.91
130	613	28.87	9.65	0.096	<0.82
150	291	13.34	8.41	0.027	4.09
200	126	4.59	4.05	<0.014	3.27
300	44	1.10	2.49	<0.014	0.82
400	20	0.24	0.31	0.014	<0.82

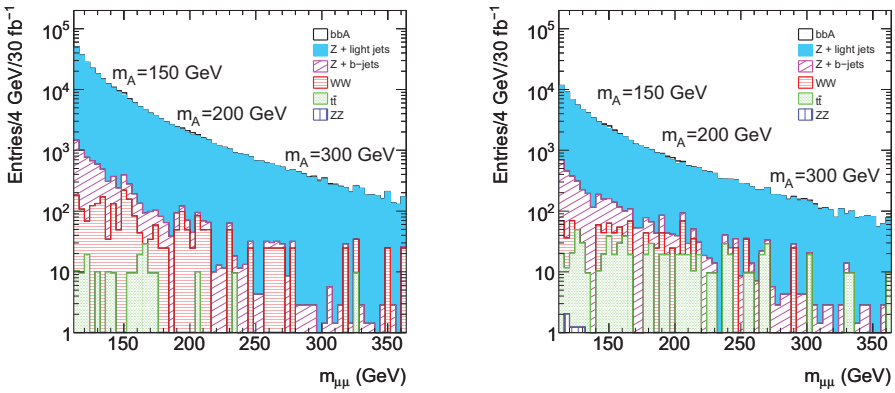

Figure 6.8: Masa invariante del sistema de dos muones para los fondos considerados y tres muestras de señal para masas $m_A = 150$, 200 y 300 GeV y $\tan\beta = 30$, con una luminosidad integrada de 30 fb^{-1}. A la izquierda se muestra el análisis para 0 jets y a la derecha para 1 jet.

6.3.3 Parametrización de las Distribuciones de Fondo

Se han ajustado las distribuciones de la masa invariante para el fondo a la siguiente función:

$$f_{\mathrm{B}}(x) = \frac{a_1}{x}\left[\frac{1}{(x^2 - M_Z^2) + M_Z^2\Gamma_Z^2} + a_2\, e^{-a_3 x}\right] \tag{6.2}$$

donde x es la masa invariante del sistema de dos muones. La función contiene un término Breit-Wigner para describir la resonancia del Z y una exponencial que describe el rango a masas altas.

6.3.4 Parametrización de las Distribuciones de Señal más Fondo

Una vez obtenida una forma funcional para modelar el fondo, también hay que utilizar una función para parametrizar la distribución de masa invariante de señal más fondo. La función seleccionada en este caso es la siguiente:

$$f_{\mathrm{SB}}(x) = f_{\mathrm{B}} + p_1 f_{\mathrm{S}} = f_{\mathrm{B}} + p_1 \frac{1}{\sigma_A\sqrt{2\pi}} \exp\left(-\frac{(x - m_A)^2}{2\sigma_A^2}\right) \tag{6.3}$$

donde x es la masa invariante del sistema de dos muones, f_{B} es el término que describe el fondo en la Ec. (6.2) y el exceso creado por la señal del bosón de Higgs se modela por f_{S}, que es una Gausiana centrada en la masa del boson A (m_A) y caracterizado por su anchura tras ser reconstruida (σ_A).

Los resultados de los ajustes realizados sobre las distribuciones de masa invariante para una señal de $m_A = 150$ GeV y $\tan\beta = 60$ se muestran en la Figura 6.9.

6.3.5 Cálculo de la Significancia

Para evaluar la significancia de nuestra señal, se ha generado un gran número de pseudoexperimentos en un intervalo de masa invariante de 100 a 500 GeV,

tanto para los casos de fondo en ausencia de señal como para señal más fondo, considerando distintos valores de m_A, $\tan\beta$ y luminosidad integrada. Cada pseudoexperimento es ajustado bajo dos hipótesis: fondo y señal más fondo. De estos ajustes, se obtiene el cociente de máxima verosimilitud.

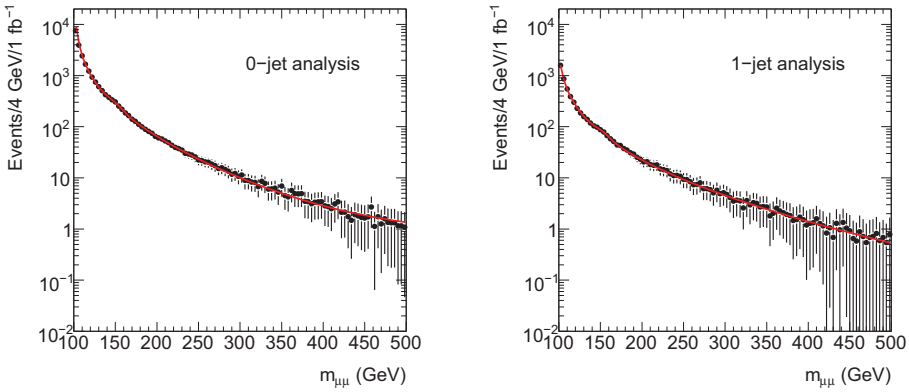

Figure 6.9: Ajustes realizados sobre las distribuciones de masa invariante para señal más fondo. La señal generada corresponde a $m_A = 150$ GeV y $\tan\beta = 60$.

La probabilidad de un error de tipo II se obtiene de la fracción de pseudoexperimentos de fondo cuyo cociente de máxima verosimilitud es mayor que la mediana de la distribución obtenida de los pseudoexperimentos de señal más fondo. El valor P es entonces transformado en significancia de una observación.

Los ajustes realizados bajo la hipótesis de señal más fondo se han llevado a cabo de dos modos distintos, dejando la masa como un parámetro fijo del ajuste o, en cambio, dejándola como un parámetro libre o flotante sobre todo el rango de masa invariante.

La Figura 6.10 muestra la significancia en función de la masa del bosón de Higgs para distintos valores de $\tan\beta$, a una luminosidad integrada de 30 fb^{-1}. Estos resultados han sido obtenidos utilizando los ajustes con masa fija.

La Figura 6.11 muestra la significancia en función de la luminosidad integrada para distintos valores de la masa del Higgs y con $\tan\beta = 30$. Los resultados han sido obtenidos utilizando los ajustes con masa flotante.

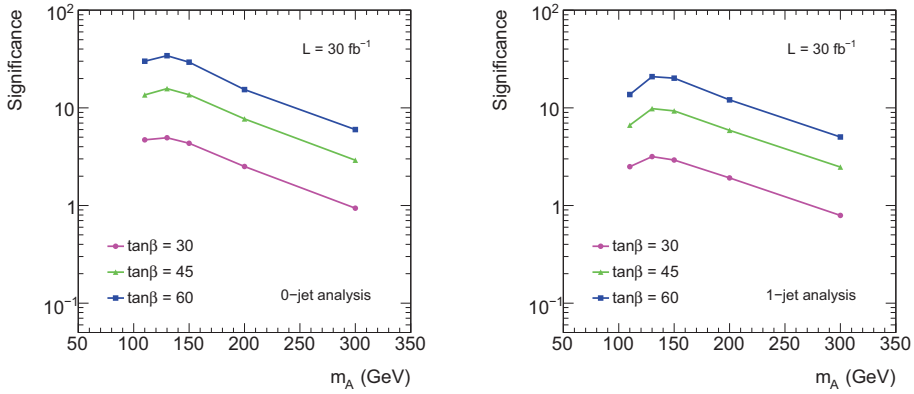

Figure 6.10: Significancia en función de la masa del bosón de Higgs para distintos valores de $\tan\beta$ con una luminosidad integrada de 30 fb^{-1}.

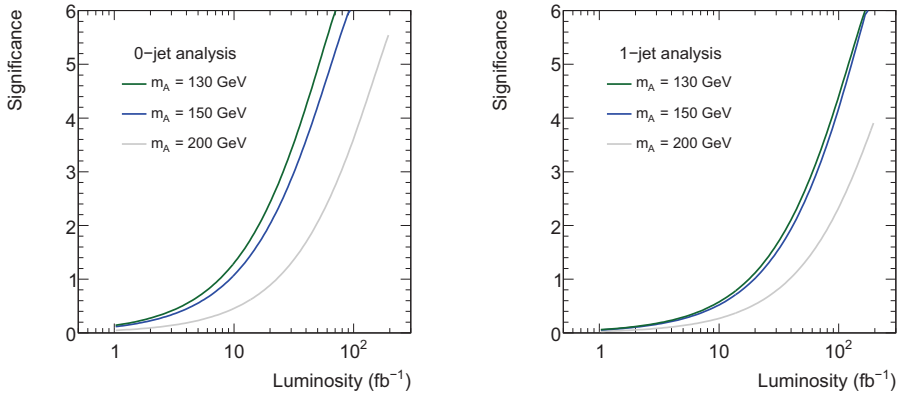

Figure 6.11: Significancias en función de la luminosidad integrada para distintas valores de m_A y $\tan\beta = 30$.

6.3.6 Cálculo de los Límites de Exclusión

Para determinar que regiones del espacio de parámetros pueden ser excluidas a un 95% CL, se genera un gran número de pseudoexperimentos de fondo, en ausencia de señal, y en cada uno de ellos se ajusta bajo la hipótesis de señal más fondo utilizando dos supuestos: por una parte, se deja como parámetro libre la normalización de la señal y fijandola al valor predicho en nuestro modelo. A partir

de aquí, se obtiene la razón de máxima verosimilitud y de este modo se evalúa la probabilidad de que fluctuaciones a la baja de una hipotética señal sean interpretadas simplemente como fondo. Los resultados obtenidos se encuentran en la siguiente Sección.

6.3.7 Potencial de Descubrimiento y Límites de Exclusión

La significancia de descubrimiento ha sido calculada utilizando para ello los ajustes sobre las distribuciones de fondo y señal más fondo obtenidas en los pseudoexperimentos dejando la masa como parámetro fijo en este caso. Las significancias obtenidas para distintas masas del bosón de Higgs, $\tan\beta = 30$ y luminosidades integradas de 10 fb^{-1} y 30 fb^{-1} se muestran en la Tabla 6.6.

Table 6.6: Significancias obtenidas para diferentes valores de m_A, $\tan\beta = 30$ y luminosidades integradas de 10 fb^{-1} y 30 fb^{-1}.

m_A (GeV)	Significancia					
	$\mathscr{L} = 10$ fb^{-1}			$\mathscr{L} = 30$ fb^{-1}		
	0 jets	1 jet	comb.	0 jets	1 jet	comb.
110	2.7	1.4	3.0	4.7	2.5	5.3
130	2.9	1.8	3.4	5.0	3.1	5.9
150	2.5	1.7	3.0	4.3	3.0	5.2
200	1.5	1.1	1.9	2.6	1.9	3.2
300	0.6	0.5	0.8	0.9	0.8	1.2

La Tabla 6.7 muestra las luminosidades integradas necesarias para alcanzar un descubrimiento de 5σ y una exclusión al 95% de nivel de confianza para las dos ramas del análisis consideradas y su combinación. A tenor de estos resultados, unos pocos fb^{-1} serían necesarios para obtener una exclusión al 95% de nivel de confianza en la mayoría de los casos considerados.

La Figura 6.12 presenta los resultados obtenidos tras la combinación de ambos análisis, obteniendo, en consecuencia una mayor sensibilidad. Cabe destacar que para las luminosidades estudiadas, se podrían establecer mejores límites de exclusión respecto a los resultados actuales proporcionados por Tevatron.

Table 6.7: Luminosidades integradas (en fb^{-1}) necesarias para obtener una significancia de descubrimiento de 5σ y una exclusión al 95% CL calculado para las dos ramas, 0 jets y 1 jet, del analysis así como su combinación. Para ello, se han utilizado diferentes masas del bosón de Higgs neutro A para $\tan\beta = 30$.

m_A	$\mathscr{L}$ (fb^{-1}) (significancia de 5σ)			$\mathscr{L}$ (fb^{-1}) (exclusión al 95% CL)		
(GeV)	0 jets	1 jet	comb.	0 jets	1 jet	comb.
110	33.6	118.6	26.0	2.3	12.8	1.8
130	30.0	75.5	21.6	2.1	8.2	1.5
150	40.0	86.3	27.3	2.7	9.2	2.0
200	117.1	201.1	73.9	8.0	21.5	5.4
300	840	1150	500	55.7	123.0	36.0

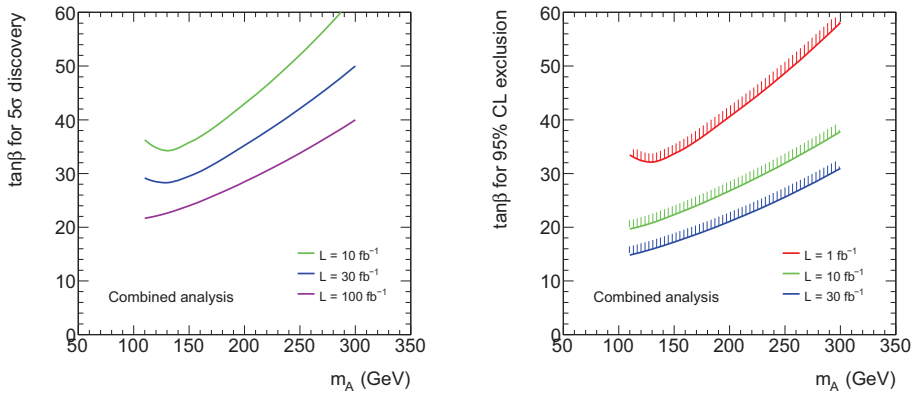

Figure 6.12: Valores de $\tan\beta$ necesarios para obtener una significancia de descubrimiento de 5σ (izquierda) y una exclusión al 95% CL (derecha) en función de la masa del bosón de Higgs neutro A para diferentes luminosidades integradas, combinando ambos análisis.

6.4 Conclusiones

Esta tesis consta de dos partes diferenciadas, ambas realizadas en el seno del experimento ATLAS: el desarrollo de un trigger de segundo nivel de muones basado en el calorímetro hadrónico TileCal y el análisis del potencial descubrimiento del bosón de Higgs neutro del MSSM en el canal de desintegración a dos muones.

La primera parte consiste en el desarrollo de un algoritmo de identificación de muones para su utilización a segundo nivel de trigger de ATLAS. El algoritmo, conocido como TileMuId, utiliza la energía depositada en el calorímetro hadrónico TileCal y su segmentación proyectiva en η para detectar muones de bajo p_{T} procedentes del punto de interacción. Estudios sobre la eficiencia y fracción de fakes del algoritmo han sido realizados e incluidos en Ref. [54]. Junto a estos estudios, se discute la combinación de TileMuId con algoritmos de reconstrucción de trazas en el detector interno, tales como TrigIDSCAN o TrigSiTrack. Fruto de este trabajo, dos cadenas de trigger (mu4_tile y mu4_trod) han dido definidas e incluidas en el menu de $\mathscr{L} = 10^{31}$ cm^{-2}s^{-1}. Así mismo, se muestran los resultados del algoritmo durante la adquisición de rayos cósmicos en la etapa de puesta a punto del detector, ejecutado en solitario o en combinación con el detector interno, ya completamente integrado en el sistema de trigger de ATLAS. Para concluir, este trigger proporciona robustez al sistema de trigger de muones de ATLAS y está preparado para ser utilizado con los primeros datos de colisiones protón-protón.

La segunda parte trata del estudio del potencial descubrimiento del bosón de Higgs neutro $h/A/H$ en el canal de desintegración a dos muones. El análisis se ha realizado con datos de simulación Monte Carlo para evaluar la significancia o en su caso los límites de exclusión susceptibles de ser obtenidos con los primeros datos del detector ATLAS. Dicho analisis se ha llevado a cabo durante el periodo de elaboración de [54], utilizando los cortes de selección de sucesos definidos por la Colaboración, con la singularidad de no utilizar los algoritmos de etiquetado de b-jets que pueden estar en fase de puesta a punto durante la adquisición de los primeros datos del detector. Así pues, se ha realizado un análisis alternativo, ya que no se impone requisito alguno en el sabor de los jets. En el análisis se ilustra un formalismo de máxima verosimilitud que nos permite calcular los valores de la significancia y trazar los límites de exclusión en el plano (m_A, $\tan\beta$). Para ello, se han generado un gran número de pseudoexperimentos para un amplio rango de masas (110 a 400 GeV) y valores de $\tan\beta$ (10 a 60) a diferentes luminosidades integradas. Para terminar, este análisis puede ser de gran utilidad para la búsqueda del bosón de Higgs neutro con los primeros datos de ATLAS.

Finalmente, ambas partes han sido desarrolladas en estrecha cooperación junto a diversos miembros de la Colaboración, durante la puesta a punto del detector.

Acknowledgments

In this last part, I would like to thank all the people that in many ways contributed and made this thesis possible, people that I had the fortune to meet during all these years. Working in such a large collaboration it is difficult, if not impossible, not to miss an important part of the people involved, so my apologies in advance.

I would like to express my gratitude to my supervisors, Emilio Higón and Juan Antonio Valls, for their support, valuable advice and trust during all these years. In the same way, I am deeply grateful to Antonio Ferrer and Victoria Castillo for their help, affection and encouragement. To Bruce Mellado and Sau Lan Wu, I am indebted for their precious support to carry out the second part of the thesis. With their help I learned very advanced techniques to perform such analysis. Thanks to Margherita Primavera and Masaya Ishino for all their help as well as all my gratitude to all the members of the Muon Trigger Slice WG. It has been a pleasure to work within this group and I really appreciate all the support received for the integration of our trigger. Thanks to Sandra Horvat and Dimitris Fassouliotis for their help and accurate comments for the analysis. Thanks to Victoria Castillo, Tomáš Davídek and Iacopo Vivarelli for all the useful comments and suggestions provided as referee of the thesis. All my gratitude to Bob Stanek, Ana Henriques and Irene Vichou in the coordination of the TileCal activities. Especially, I want to thank Alexander Solodkov his close collaboration and immeasurable help in TileCal. I really admire his wide understanding of very different TileCal parts, covering all the offline software aspects. Also in an especial way, I would like to express all my gratitude to Heuijin Lim. It has been a pleasure to work with her side by side in all the trigger part. She has been an excellent colleague doing a magnificent work and making always things easy. I really appreciate her talent and energy for pushing things up and devising ingenious plots, with who a learned a lot. And of course, I don't forget Giulio Usai and Jinlong Zhang, to complete the

TileMuId team, which have also been great colleagues. I am also deeply grateful to Bill Quayle, where I found a lot of help and valuable advice and suggestions during all the analysis. I want to thank all the collaboration and help that I always found in Oleg Solov'Yanov for the online software aspects. My acknowledgments to all the past and current members of the TileCal Valencia group during my PhD time, Jose Castelo, Esteban Fullana, Belén Salvachúa, Cristóbal Cuenca, Carmen Iglesias, Carlos Solans, Antoni Munar, Alberto Valero, Jalal Abdallah, Ali Abdallah, Eva Valladolid, Yesenia Hernández and Pablo Moreno for their close collaboration in so many things. Finally, to express my gratitude to my colleagues and friends at IFIC, Paco, Vera, Carlos, Loli, ...

Finalmente, quiero agradecer a mis padres y hermanos, Rocío y Rafa, todo el apoyo, cariño y comprensión que siempre he tenido. También a mi tío Amador, que es para a mi un ejemplo a seguir a todos los niveles. Por último, no tengo palabras para agradecer a Ximo su apoyo incondicional, que no para de sorprenderme, y se afianza y crece, si cabe, con el paso del tiempo.

A List of Acronyms

AD: Antiproton Decelerator

ADC: Analog to Digital Converter

ALICE: A Large Ion Collider Experiment

ALEPH: Apparatus for LEP Physics at CERN

ASIC: Application Specific Integrated Circuit

ATLAS: A Toroidal LHC ApparatuS

BCID: Bunch Crossing Identifier

BT: Barrel Toroid

CERN: *Conseil Européen pour la Recherche Nucléaire*

CKM: Cabibbo-Kobayashi-Maskawa

CMS: Compact Muon Solenoid

CNGS: CERN Neutrinos to Gran Sasso

CPU: Central Processing Unit

CRC: Cyclic Redundancy Check

CS: Central Solenoid

CSC: Cathode Strip Chamber

CSIC: *Consejo Superior de Investigaciones Científicas*

CTF3: Clic Test Facility

DAQ: Data AcQuisition

DELPHI: DEtector with Lepton, Photon and Hadron Identification

DMU: Data Management Unit

DONUT: Direct Observation of the NU Tau (FNAL Experiment)

DSDC: *Diseño de Sistemas Digitales y Comunicaciones*

DSP: Digital Signal Processor

EB: Extended Barrel

ECT: End-Cap Toroid

EF: Event Filter

EMEC: ElectroMagnetic End-cap (ATLAS Electromagnetic Calorimeter)

EWSB: ElectroWeak Symmetry Breaking

FCAL: Forward Calorimeter (ATLAS Hadronic Calorimeter)

FCNC: Flavor Changing Neutral Current

FEX: Feature EXtraction

FIFO: First Input First Output memory

FNAL: Fermi National Accelerator Laboratory

FPGA: Field Programmable Gate Array

HEC: Hadronic End-cap Calorimeter (ATLAS Hadronic Calorimeter)

HLT: High Level Trigger

HOLA: High-speed Optical Link for ATLAS

HV: High Voltage

HYPO: Hypothesis

ID: Inner Detector

IFIC: *Instituto de Física Corpuscular*

ISOLDE: Isotope Separation OnLine DEvice

ITC: Intermediate Tile Calorimeter

L1A: Level-1 Accept

L1ID: Level-1 Identifier

LAr: Liquid Argon

LB: Long Barrel

LHC: Large Hadron Collider

LHCb: the Large Hadron Collider beauty experiment

LHCf: the Large Hadron Collider forward experiment

LEIR: Low Energy Ion Ring

LEP: Large Electron-Positron collider

LINAC: LINear ACcelerators

LQ: Leptoquark

LSB: Least Significant Bit

LSC: Link Source Card

LSP: Lightest Supersymmetric Particle

LVDS: Low Voltage Differential Signaling

MDT: Monitored Drift Tube

MIP: Minimum Ionizing Particle

MSB: Least Significant Bit

MSSM: Minimal Supersymmetric Standard Model

n-ToF: Neutrons Time Of Flight

OC: Output Controller

OMB: Optical Multiplexer Board

OPAL: Omni-Purpose Apparatus at LEP

ORX: Optical Receiver

PMT: PhotoMultiplier Tube

PU: Processing Unit

QCD: Quantum ChromoDynamics

ROB: Read-Out Buffer

ROD: Read-Out Driver

RoI: Region of Interest

ROL: Read-Out Link

ROS: Read-Out System

RCC: ROD Crate Controller

RPC: Resistive Plate Chamber

SCT: SemiConductor Tracker

SDRAM: Synchronous Dynamic Random Access Memory

SLAC: Stanford Linear Accelerator Center

SLC: Stanford Linear Collider

SM: Standard Model

SPS: Super Proton Synchrotron

SUSY Supersymmetry

TBM: Trigger and Busy Module

TDAQ: Trigger and Data Acquisition

TDS: Transient Data Store

TGC: Thin Gap Chamber

TileCal: Tile Calorimeter

TileMuId: Tile Muon Identification algorithm

TM: Transition Module

TOTEM: TOTal Elastic and diffractive cross-section Measurement

TRT: Transition Radiation Tracker

TTC: Trigger and Timing Control

TTCrx: TTC Receiver

Ttype: Trigger type

UV: *Universitat de València*

VME: Versa Modula Europa bus

WLS: WaveLength Shifter

WWW: World Wide Web

Bibliography

[1] L. Evans and P. Bryant, JINST **3** (2008) S08001.

[2] The ALICE Collaboration, K Aamodt *et al.*, JINST **3** (2008) S08002.

[3] The ATLAS Collaboration, G. Aad *et al.*, JINST **3** (2008) S08003.

[4] The CMS Collaboration, S. Chatrchyan *et al.*, JINST **3** (2008) S08004.

[5] The LHCb Collaboration, A. Augusto Alves Jr *et al.*, JINST **3** (2008) S08005.

[6] The LHCf Collaboration, O. Adriani *et al.*, JINST **3** (2008) S08006.

[7] The TOTEM Collaboration, G. Anelli *et al.*, JINST **3** (2008) S08007.

[8] The ATLAS Collaboration, *ATLAS Inner Detector: Technical Design Report, 1*, CERN-LHCC-97-016, http://cdsweb.cern.ch/record/331063; *ATLAS Inner Detector: Technical Design Report, 2*, CERN-LHCC-97-017, http://cdsweb.cern.ch/record/331064.

[9] The ATLAS Collaboration, *ATLAS Calorimeter Performance: Technical Design Report*, CERN-LHCC-96-040, http://cdsweb.cern.ch/record/331059.

[10] The ATLAS Collaboration, *ATLAS Liquid Argon Calorimeter: Technical Design Report*, CERN-LHCC-96-041, http://cdsweb.cern.ch/record/331061.

[11] The ATLAS Collaboration, *ATLAS Tile Calorimeter: Technical Design Report*, CERN-LHCC-96-042, http://cdsweb.cern.ch/record/331062.

[12] The ATLAS Collaboration, *ATLAS Muon Spectrometer: Technical Design Report*, CERN-LHCC-97-022, http://cdsweb.cern.ch/record/331068.

[13] The ATLAS Collaboration, *ATLAS Magnet System: Technical Design Report*, CERN-LHCC-97-018, http://cdsweb.cern.ch/record/338080.

[14] The ATLAS Collaboration, *ATLAS Trigger Performance: Status Report*, CERN-LHCC-98-015, http://cdsweb.cern.ch/record/381430.

[15] J. Christiansen, A. Marchioro, P. Moreira and A. Sancho, IEEE Trans. Nucl. Sci. **43** (1996) 1773-1777.

[16] B.G. Taylor, *Timing Distribution at the LHC*, Presented at 8th Workshop on Electronics for LHC Experiments, Colmar, 9 - 13 September 2002. http://cdsweb.cern.ch/record/592719.

[17] S. Berglund *et al.*, JINST **3** (2008) P01004.

[18] *Technical Reference Manual for VP 110/01x VME Pentium III-M Single Board Computer*, http://atlas.web.cern.ch/Atlas/private/DIG/RCC/vp110_manual.pdf.

[19] P. Matricon, *The Trigger and Busy Module of the ATLAS LARG ROD System*, ATLAS EDMS document ATL-AL-EN-0054.

[20] J. Castelo *et al.*, *TileCal ROD Hardware and Software Requirements*, ATLAS Note ATL-TILECAL-2005-003, http://cdsweb.cern.ch/record/821482.

[21] P. Matricon, *A 9U Transition Module for the ROD Demonstrator*, ATLAS EDMS document ATL-AL-EN-0053.

[22] A. Ruiz, *HOLA specification*, ATLAS EDMS document 330901.

[23] V. González *et al.*, IEEE Trans. Nucl. Sci. **53** (2006) 2131-2138.

[24] D. La Marra, *OC (Output Controller) FPGA of the LArgROD board Description*, ATLAS EDMS document ATL-AL-EN-0056.

[25] A. Blondel, D. La Marra, A. Léger, I. Riu and A. Straessner, *VME and BUSY FPGA for the ROD motherboard*, ATLAS EDMS document ATL-AL-EN-0060.

[26] B. Laforge and G. Perrot, *TTC System Implementation for ATLAS Liquid Argon Detectors (V.2.2.2)*, ATLAS Note ATL-ELEC-2004-003, http://cdsweb.cern.ch/record/730568.

[27] J. Prast, *The ATLAS Liquid Argon Calorimeters Read Out Driver (ROD). The TMS320C6414 DSP Mezzanine board*, ATLAS EDMS document ATL-AL-CD-0009.

[28] The ATLAS Collaboration, *ATLAS Detector and Physics Performance: Technical Design Report, 2*, CERN-LHCC-99-015, http://cdsweb.cern.ch/record/391177.

[29] The DØ Collaboration, V.M. Abazov *et al.*, Phys. Rev. Lett. **103** (2009) 092001.

[30] The CDF Collaboration, T. Aaltonen *et al.*, Phys. Rev. Lett. **103** (2009) 092002.

[31] J. Charles *et al.*, Eur. Phys. J. **C41** (2005) 1-131.

[32] The Tevatron New-Phenomena and Higgs Working Group for the CDF and DØ Collaborations, arXiv:0903.4001.

[33] L. Vacavant and I. Hinchliffe, J. Phys. G: Nucl. Part. Phys. **27** (2001) 1839-1850.

[34] A. Henriques, G. V. Karapetian and A. Solodkov, *The Muon energy losses in the Tile calorimeter*, ATLAS Note ATL-TILECAL-95-068, http://cdsweb.cern.ch/record/683526.

[35] D. Costanzo, T. Del Prete, E. Mazzoni and C. Petridou, *Muon Trigger with TileCal. A Preliminary Investigation*, ATLAS Note ATL-DAQ-99-002, http://cdsweb.cern.ch/record/683798.

[36] G. Usai, *Feasibility study of a level two low p_T di-muon trigger based on Tile calorimeter*, ATLAS Note ATL-DAQ-2003-017, http://cdsweb.cern.ch/record/685454.

[37] G. Usai, Nucl. Instrum. Meth. **A 518** (2004) 36-38.

[38] B. Salvachúa *et al.*, JINST **2** (2007) T02001.

[39] C. P. Bee *et al.*, *The raw event format in the ATLAS Trigger & DAQ*, ATLAS Note ATL-DAQ-98-129, http://cdsweb.cern.ch/record/683741.

[40] The ATLAS Collaboration, *Athena. The ATLAS Common Framework. Developer Guide*, 2004.

[41] LHCb software architecture group, *GAUDI-Architecture design document*, CERN-LHCb-98-064, http://cdsweb.cern.ch/record/691746.

[42] M. Sutton *et al.*, *A Fast Tracking Algorithm for the ATLAS Level 2 Trigger*, ATL-DAQ-CONF-2006-018, http://cdsweb.cern.ch/record/995403.

[43] C. Schiavi *et al.*, *Fast Tracking for the Second Level Trigger of the ATLAS Experiment Using Silicon Detectors Data*, Presented at 51st Nuclear Science Symposium and Medical Imaging Conference, Rome, Italy, 16 - 22 Oct 2004. http://cdsweb.cern.ch/record/830388.

[44] S. Grancagnolo, *The ATLAS Muon Trigger vertical slice at LHC startup*. Presented at 12th International Workshop on Advanced Computing and Analysis Techniques in Physics Research, Erice, Italy, 03 Nov - 07 Nov 2008. http://cdsweb.cern.ch/record/1157977.

[45] R. Achenbach *et al.*, JINST **3** (2008) P03001.

[46] M. Boonekamp *et al.*, *Cosmic Ray, Beam-Halo and Beam-Gas Rate Studies for ATLAS Commissioning*, ATLAS Note ATL-GEN-2004-001, http://cdsweb.cern.ch/record/719263.

[47] H. Okawa, *Commissioning of the ATLAS Tile Calorimeter with Cosmic Ray and Single Beam Data*. Presented at 2008 Nuclear Science Symposium, Medical Imaging Conference and 16th Room Temperature Semiconductor Detector Workshop, Dresden, Germany, 19 - 25 Oct 2008. http://cdsweb.cern.ch/record/1139845.

[48] S. Schael *et al.*, Eur. Phys. J. **C47** (2006) 547-587.

[49] The DØ Collaboration, *Search for MSSM Higgs Boson Production in Di-tau Final States with L=2.2 fb^{-1} at the DØ Detector*, DØ Note 5740-CONF, 2008.

[50] The CDF Collaboration, *Search for Neutral MSSM Higgs Bosons Decaying to Tau Pairs with 1.8 fb^{-1} of Data*, CDF Note 9071, 2007.

[51] S. Heinemeyer, W. Hollik and G. Weiglein, Comput. Phys. Commun. **124** (2000) 76-89. See http://www.feynhiggs.de.

[52] M. Spira, Nucl. Instrum. Meth. **A 389** (1997) 357-360.

[53] S. Gentile, H. Bilokon, V. Chiarella and G. Nicoletti, Eur. Phys. J. **C52** (2007) 229-245.

[54] The ATLAS Collaboration, G. Aad *et al.*, arXiv:0901.0512.

[55] D. Rebuzzi, M. Schumacher *et al.*, *Cross sections for Standard Model processes to be used in the ATLAS CSC notes*, ATLAS Internal Note ATL-PHYS-INT-2009-003, http://cdsweb.cern.ch/record/1106527.

[56] M. Spira, arXiv:hep-ph/9510347.

[57] E. Boos and T. Plehn, Phys. Rev. **D69** (2004) 094005.

[58] J. Campbell, R.K. Ellis, F. Maltoni, and S. Willenbrock, Phys. Rev. **D67** (2003) 095002.

[59] T. Sjöstrand *et al.*, Comput. Phys. Commun. **135** (2001) 238-259.

[60] T. Gleisberg *et al.*, JHEP **0402** (2004) 056.

[61] S. Frixione, P. Nason and B.R. Webber, JHEP **0308** (2003) 007.

[62] E. Richter-Was, D. Froidevaux and L. Poggioli, *ATLFAST 2.0 a fast simulation package for ATLAS*, ATLAS Note ATL-PHYS-98-131, http://cdsweb.cern.ch/record/683751.

[63] C. Zeitnitz and T.A. Gabriel, Nucl. Instrum. Meth. **A 349** (1994) 106-111.

[64] A. Fasso, A. Ferrari, J. Ranft and P.R. Sala, *FLUKA: a multi-particle transport code*, CERN-2005-010, http://cdsweb.cern.ch/record/898301.

[65] S. Hassani *et al.*, Nucl. Instrum. Meth. **A 572** (2007) 77-79.

[66] S. Gentile, H. Bilokon, V. Chiarella and G. Nicoletti, *Data based method for* $Z \rightarrow \mu^+\mu^-$ *background subtraction in ATLAS detector at LHC*, ATLAS Note ATL-PHYS-PUB-2006-019, http://cdsweb.cern.ch/record/965385.